NONINVASIVE BIOMECHANICAL ASSESSMENT OF THE RUPTURE POTENTIAL OF ABDOMINAL AORTIC ANEURYSMS

by

Hong Jun Wang

B. S. in Electrical Engineering, WuHan University, P. R. China

M. S. in Mechanical Engineering, West Virginia University

Submitted to the Graduate Faculty of

the School of Engineering in partial fulfillment

of the requirements for the degree of

Doctor of Philosophy

University of Pittsburgh

2002

UNIVERSITY OF PITTSBURGH

SCHOOL OF ENGINEERING

This dissertation was presented

by

Hong Jun Wang

It was defended on

July 17, 2002

and approved by

Harvey S. Borovetz, Ph.D.

Michael S. Sacks, Ph.D.

Anne M. Robertson, Ph.D.

Marshall W. Webster, M.D.

David A. Vorp, Ph.D.
Dissertation Director

NONINVASIVE BIOMECHANICAL ASSESSMENT OF THE RUPTURE POTENTIAL OF ABDOMINAL AORTIC ANEURYSMS

Hong Jun Wang, Ph.D.

University of Pittsburgh, 2002

Abdominal aortic aneurysm (AAA) is a localized dilation of the infrarenal aorta. Ruptured AAA has a mortality rate of 95% and is ranked as the 13th leading cause of death in the US. The ability to reliably evaluate the susceptibility of a particular AAA to rupture could vastly improve the clinical management of AAA patients. Currently, no such reliable evaluation technique exists. The purpose of this work was to develop a noninvasive technique to evaluate the rupture potential of individual AAA.

To predict the wall strength distribution, experimentally determined wall strength data were used for construction of a mathematical model using multiple linear regression techniques. The developed model was then validated using data from a different group of specimens. The strength distributions for four different AAA were then generated using the validated model. The finite element method was used to estimate the wall stress distribution for all four AAA based on their realistic geometries (reconstructed from CT images) which included intraluminal thrombus (ILT). The measured systolic blood pressure was applied as the loading condition. Nonlinear hyperelastic constitutive models for AAA and ILT tissue were used, the latter being developed

here based on uniaxial tensile testing data. For each patient, a local Rupture Potential Index (RPI) distribution was calculated as local (nodal) wall stress divided by local wall strength.

The developed model contains four independent variable parameters: AAA size, patient's age, family history, local ILT thickness, and normalized local AAA diameter ($R^2 = 0.86$, $p < 0.001$). The model predicted the actual (measured) strength very accurately ($R^2 = 0.81$ for model validation). The wall strength values predicted for the four AAA studied ranged from 130 N/cm^2 to 306 N/cm^2, whereas the measured wall strength values ranged from 39 to 324 N/cm^2. The peak wall stress for the four AAA studied ranged from 19 N/cm^2 to 37 N/cm^2. The peak RPI values ranged from 0.15 to 0.55.

This patient-specific, computer-based, noninvasive RPI estimation technique could become an import and reliable diagnostic tool for AAA patient management. However, further clinical studies are needed to validate this technique.

ACKNOWLEDGEMENTS

The essence of wisdom is the ability to make the right decision on the basis of inadequate evidence.

Alan Gregg

With my ultimate gratitude, I surrender this work to God, who is the source of my knowledge and strength.

The results of this manuscript are the results of five years of hard work. The work is far from done. It is just a beginning. There are so many people who have been my inspiration and support during this time and I gratefully acknowledge them here.

Many thanks to my advisor, Dr. David Alan Vorp, for his guidance and support. Also I would like to thank his family - his wife Carolyn M. Vorp, and his son Justin David Vorp - for the encouragement and caring they gave to me when I needed them.

Special thanks to Dr. Harvey S. Borovetz, who provided me with endless support and encouragement during the course of my study at the University of Pittsburgh. Dr. Borovetz, you are my professional role model.

I would like to thank all the members of my dissertation committee who have challenged and helped me to do my best. Thanks to Dr. Marshall W. Webster for his clinical insights and enthusiastic support for this work. Thanks to Dr. Michel S. Sacks who has challenged me and helped me in many different ways. I thank Dr. Ann M. Robertson, for her insights and help.

Special thanks to Michel S. Makaroun, M.D., and Denise Marie Macy, RN, who helped me in every possible way to get the clinical tissue specimens so important to this study.

Thanks also to Dr. Stephen R. Wisniewski, who helped me with the statistical modeling, and to Dr. David B. Smith for allowing the use of his Biquintic Surface Smoothing software.

It has been a great joy and privilege to work in Dr. Vorp's Vascular Surgery and Vascular Biomechanics Research Lab, especially with so many talented and wonderful people. Thank you Stephanie M. Kute, for all the help and fun we had during our graduate studies. Thanks to Don A. Severyn, Jon R. Mears, Brian Schiro, Mohammed El-Kurdi, Dr. Elena DiMartino, Dr. Doug Halmilton and Jonathan Van de Geest. It has been fun working with all of you. Also thanks to Jeremy Suggs and Brian Wessel, two students who worked with me, providing me with a lot of critical help.

To a great degree, I would also like to thank Dr. Madhavan L. Raghavan, on whose earlier thesis work I have expanded.

Many thanks to my family back in China, whom I miss a lot, for their understanding and love. If nothing else, when I see them in the future, I can show them this manuscript.

On a personal level, I cannot thank Rev. Harry Jeffery Hopson too much for his unconditional support at all times.

Last but not least, I would like to express my great gratitude to all the patients I have worked with. Thank you for your selfless support. With my sincere heart, I do hope this work will benefit patients in the coming future.

"**To Ms. Frances Tisdale Dreisbach, who brought me to this brand new world, I dedicate this manuscript"**

This work was supported in part by grants from The Whitaker Foundation, NIH (#RO1 HL 060670-01A2), and The Pittsburgh Foundation, all to Dr. David Alan Vorp.

TABLE OF CONTENTS

LIST OF TABLES

LIST OF FIGURES

1.0 INTRODUCTION AND BACKGROUND

The word *aneurysm* originates from *aneurysma,* the Greek term for "dilation" or "widening". [1] Abdominal aortic aneurysm, usually referred to by the acronym AAA, is a local circumscribed dilation of the infrarenal segment of the abdominal aorta; i.e., between the renal arteries and the iliac bifurcation. **Figure 1** shows the typical anatomic location of AAA. The exact cause of this is still unknown. However, the manifestation of this disease is the destruction of the vital structural components of the aortic wall and formation of a focal dilation. [2]

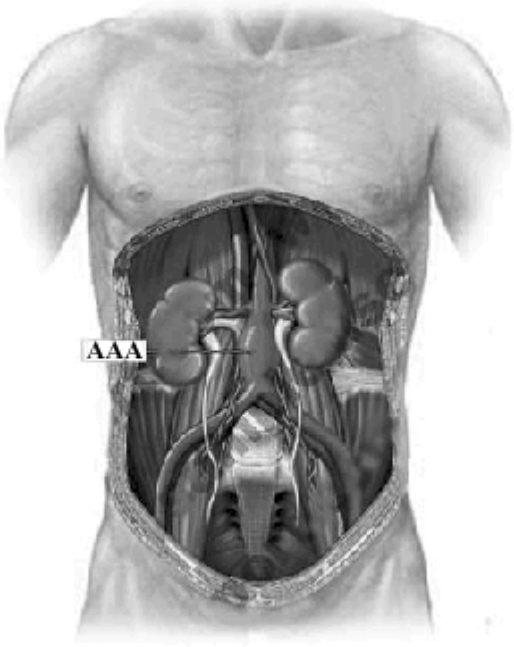

Figure 1 An artist's rendering of a AAA in its in situ position.

The normal abdominal aorta is about 2 cm in diameter. Typically, AAA dilates to anywhere between 4 cm to 10 cm in diameter. If left untreated, AAA will continue to dilate until it eventually ruptures. Ruptured AAA causes massive internal bleeding and in many cases death of the patient. Therefore, the main goal of AAA management is to prevent that from happening.

1.1 Epidemiology of AAA

Epidemiology deals with the frequency and distribution of the diseases within the population. Epidemiologic data shows that the mean age of patients with AAA is 67 years and men are affected more often than women by a ratio of 4:1. [3] AAA is present in approximately 2% of the elderly population, with approximately 200,000 new cases diagnosed each year, and 50,000 to 60,000 surgical AAA repairs performed annually. Ruptured AAA is responsible for approximately 15,000 deaths in the United States each year, making it the 13th leading cause of death in this country, similar in magnitude to emphysema, renal disease, and homicide. [4, 5]

During the last few decades, the incidence of AAA has increased. The reason for this might be due to an aging population and the introduction of modern imaging techniques that make large screening possible. From 1900 to 1996, life expectancy increased approximately 30 years, from less than 50 years to almost 80. The over-85 age group is the fastest growing segment of the population in this country. [6] The impact of this is the certainty of more aneurysms, because abundant data exist to show that the prevalence of AAA and rupture risk increases sharply with advancing age. One in 10 men older than 80 has at least some aneurysmal dilation in his aorta. [5, 7-9] Besides aging, other factors are involved, because the incidence of small AAA has increased almost 30- fold. [10] Certainly, better diagnosis and more frequent

imaging studies are involved, but it appears there has been a true increase in prevalence as well. [11] Thus, it is certain that in coming years vascular surgeons are going to deal with more patients with AAA in their practice, many of whom are elderly and high risk. [12]

1.2 Natural History of AAA

Upon development of the initial wall dilation, the natural history of AAA is to grow continuously until rupture. The pattern of growth is exponential and asymmetrical. [13-15] Smaller aneurysms expand more slowly than larger aneurysms. [15, 16] AAA tends to grow more in transverse dimension than in anterioposterior dimension. [17, 18]

To update the information on the natural history and the outcome of surgical repair of AAA, Hallin et al recently reviewed 132 papers with 54,048 patients examined between 1985 and 1997. [17] The result is summarized in **Table 1**.

Table 1 AAA growth rate and risk of rupture. Adapted from Hallin et al. [17]

Size, cm	Mean growth rate, cm/year	Rupture at 1 year of follow-up, % (No. of patients followed)	Rupture at 4 year of follow-up, % (No. of patients followed)
3.0-3.9	0.33	1 (108)	2 (43)
4.0-5.0	0.41	1.4 (212)	1.4 (146)
>5.0	0.51	8.5 (131)	22 (23)

The AAA expansion rate averaged 0.2-0.4 cm per year for aneurysms smaller than 4 cm, 0.2-0.5 cm/yr for aneurysms 4-5 cm/yr and 0.3-0.7 cm/yr for those larger than 5 cm. [17, 18] The risk of AAA rupture increases exponentially with maximum diameter. [17, 18] For AAA smaller than 5 cm, the rupture rate does not exceed 2%. For AAA larger than 5 cm, rupture rate can reach as high as 22% during a 4 year following up period. [17, 18]

The majority of aneurysms detected are less than 4.5 cm in diameter. [15, 16, 19] Predicting the rate of progression for individual patients is uncertain at best and further complicated by the fact that not all aneurysms expand. Those that do expand, do so in an irregular and unpredictable fashion. Moreover, even a small AAA can rupture. [20] Also, many unruptured large AAA have been detected in autopsies of patients who died of other causes. Because there are no proven medical interventions effectively limiting the growth of aortic aneurysms and surgery for abdominal aortic aneurysm is risky, patients with a small AAA are generally followed with repeated measurements of aneurysm diameter. Surgical repair is reserved for those aneurysms reaching a certain size (i.e., operating when the risk of complications exceeds the risk of surgery). The goal of treatment is timely surgical intervention before rupture occurs.

1.3 Interventional Repair of AAA

AAA may be asymptomatic or symptomatic. The symptomatic commonly complain of vague abdominal or back pain. Repair is generally recommended for symptomatic AAA patients because of the high risk of rupture. However, approximately 75% of AAAs are asymptomatic. [21] These are usually diagnosed on either routine physical examination or during other

unrelated procedures. For asymptomatic AAAs, surgical intervention usually takes place only when the maximum diameter of the aneurysm reaches 5 cm in diameter.

There are two types of AAA repair: *open (surgical) repair,* which is the traditional method (**Figure 2**), and *endovascular (minimally invasive) repair* (**Figure 3**), which is an alternative approach developed in the last decade. For open repair, a large incision is made from just below the sternum to the top of the pubic bone. The aneurysm is isolated from surrounding organs and tissues, and opened lengthwise along its anterior surface. The contained intraluminal thrombus (ILT) is removed and a prosthetic graft is sewn in place. If the aneurysm does not involve the iliac arteries, a straight tube graft is used. If the iliac arteries are also aneurysmal, or if a sufficient length of undilated aortic "neck" is not present above the iliac bifurcation, a bifurcated or inverted-Y-shaped graft is used. The aneurysmal sac is then trimmed and sutured closed around the graft, providing a natural tissue barrier over the prosthesis. With the graft now enclosed in the old aneurysm sac, the abdominal contents are allowed to return to their normal position. Finally, the muscular wall of the abdomen is sewn back together and the skin incision is sewn or stapled closed.

Open repair of AAA is a major surgical procedure that requires patients to be hospitalized typically for a week and to recuperate at home for several more weeks. The mean postoperative mortality for elective repair is approximately 5% and for emergency operations 47% (range 27-69%).[17] This technique has matured over the years and has proven to be excellent for low-risk patients. The major draw back of this approach is the compromised quality of life after surgery because of postoperative pain, the prolonged recovery period, and the high costs associated with both the surgery and the recovery.

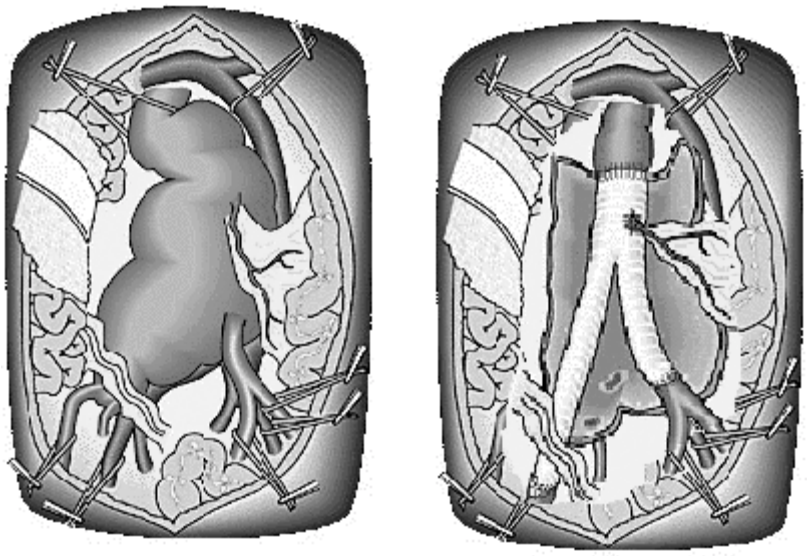

Figure 2 Illustration of the traditional open AAA surgical procedure.

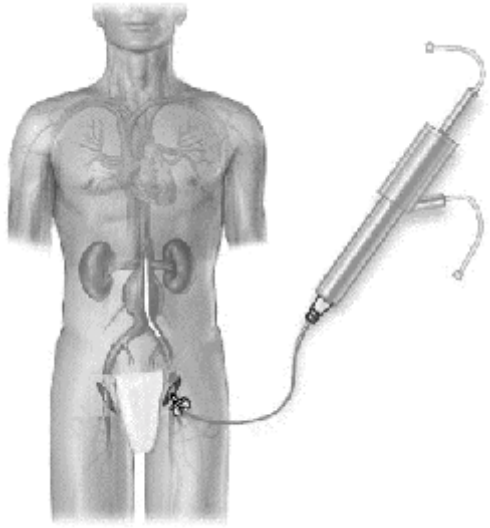

Figure 3 Illustration of minimally invasive endovascular repair of AAA.

An alternative approach that avoids the extensive tissue dissection associated with open repair is the endovascular repair procedure first reported clinically by Parodi in 1991. [22] For this procedure, two small femoral cutdowns are performed in the groin instead of a majorabdominal incision. Rather than disrupting abdominal organs and exposing the aorta, a stent graft device is introduced under fluoroscopic guidance through the femoral artery, proximally into the iliac artery then into the abdominal aorta (**Figure 3**). The stent graft device is typically made of a tubular polyester body to which attachment systems (most commonly stents or hooks) have been incorporated. Once the graft is in the appropriate position within the aneurysm, its proximal and distal ends are attached to the nonaneurysmal aortic "neck" using the attachment devices, and the delivery system is carefully removed. [23]

The potential advantages of endovascular AAA repair include reductions in mortality, morbidity, blood loss, hospital stay, intensive care unit utilization, and discomfort. [24] Recovery is faster with the endovascular approach than with the traditional approach. [25] Although at present the cost-effectiveness of endovascular treatment of AAA is debatable, especially in view of the high cost of the graft, endovascular treatment may turn out to be cost-effective in view of the shortened hospital stay. Even with this minimally invasive procedure, which is not devoid of risks and morbidity, careful selection of patients is key. [26] The mortality of patients undergoing endovascular repair is 1.9%. [27] In addition, endovascular repair is subject to post procedural complications, mostly due to endoleak or failure by fatigue loading of the device components. [26] Endoleak is a persistent blood flow outside the lumen of the endograft into the aneurysmal sac after deployment and may be caused by incomplete apposition of the attachment sites against the aortic wall, seepage through the graft body, or retrograde flow through patent

side branches (e.g., lumbar and inferior mesenteric arteries). Endoleaks are not infrequent and are reported in 15% to 52% of early post-implant CT scans in various studies. [28-32]

1.4 The Clinical Need of a Reliable Rupture Potential Assessment Technology

As discussed above, both open and minimal-invasive repair procedures are associated with significant risks and expense. Therefore, it is essential that only those patients who are of high risk of suffering AAA rupture be offered these procedures. However, the problem is that there is no current technique available to quantify the risk of rupture for individual AAA. The contemporary approach to AAA patient management is that once an AAA is diagnosed, the patient is followed by serial CT examinations to monitor the growth of the size of the AAA. The size of AAA is defined by its maximum transverse diameter, usually as measured on CT images. Once the aneurysm approaches 5-cm, surgical intervention is considered. [20, 33, 34] Of course, this is a general rule-of-thumb and does not necessarily suit every individual. In fact, it has been reported that up to 23% of AAAs rupture at a diameter <5 cm. [35, 36] On the other hand, a large number of elective AAA repairs are done to prevent rupture despite the fact that some of them might never rupture given the patient's life span. [37, 38] Therefore, the use of 5 cm diameter as a cut-off criterion in making the surgical decision is obviously an unreliable criterion. There is thus a clear need to understand and develop a reliable methodology to predict the susceptibility of a particular aneurysm to rupture.

1.5 Previous Research on Prediction of AAA Rupture

The ability of providing AAA patients the best care by making a timely decision lies in the ability to predict the propensity of their AAA to rupture. Predicting AAA rupture has been an intense area of research with increasing interests in recent years. There are basically two major approaches in predicting AAA rupture: the empirical approach and the biomechanical approach. The definitions of these approaches and the previous work associated with them are discussed further below.

1.5.1 The Empirical Approach

Earlier attempts to predict AAA rupture potential have used an empirical approach. In this approach, researchers analyzed empirical data on AAA patients; namely, the incidence of rupture and the apparent factors that seem to correlate with it. Clinical factors such as patient age, gender, blood pressure, AAA size, and presence or absence of intraluminal thrombus, have been assessed for possible correlation with the incidence of rupture. [14, 15, 19, 39, 40] Cronenwett et al. [15, 41] found that aneurysm size, diastolic hypertension and chronic obstructive pulmonary disease (COPD) are significant risk factors for AAA rupture. Brown et al. [42] found that the risk of rupture is associated with female sex, larger initial aneurysm diameter, current smoking, and higher mean blood pressure. Sterpetti et al. [19], Limet et al.[13], Bengtsson et al. [5, 43], Guirguis and Barber [44], and Chang et al. [14] suggested that the rate of AAA expansion could be a better indicator of rupture than AAA size itself. For example, Limet et al. [13] used the following exponential model to describe the expansion of AAA over time:

$$d_t = d_0 e^{\alpha t} \tag{1.1}$$

where d_0 is the initial diameter of AAA at the time of diagnosis, d_t is the AAA diameter at some time 't' after diagnosis and α is the "exponential" expansion rate. From a total 114 patients and 18 ruptured AAA, they found the critical value of $\alpha = 0.106$ year^{-1}. Guirguis and Barber [44] suggested a critical linear expansion rate of 0.3 cm/year as the cutoff value for selective treatment.

Other researchers used medical imaging processing methods to study AAA shape and size and related those parameters to rupture potential. Wolf et al. [40] measured the area ratio of thrombus to AAA sac from CT scans and suggested that thrombus is associated with AAA expansion rate and, consequently, rupture. Hatakeyama [45] delineated the risk factors for rupture of AAAs as evaluated by means of a combination of three-dimensional (3D) reconstruction and clinical data analysis. They obtained 3D-based data by means of computer-aided 3D reconstruction from computed tomography studies of AAAs. The data included the tortuosity of the aneurysm, maximum transverse diameter, length of the aneurysm, aneurysmal volume, aneurysmal surface area, largest aneurysmal cross-sectional area, ratio of transverse aneurysmal diameter to the length of the aneurysm (T/L), and amount of mural thrombus. All data were assessed by means of multivariate analysis for their predictive value for expansion or rupture of AAA. Their results showed that the most efficient predictors of aneurysmal rupture were a combination of annual expansion rate of maximum transverse diameter, diastolic blood

pressure, and T/L. Stebaek et al. [46] showed that a rapid increase of thrombus area may be a better predictor of AAA rupture than increase in maximal diameter.

Although these empirical approaches have helped shape the present clinical treatment of patients with AAA, their accuracy in predicting the risk of rupture of individual AAA is limited. As Hua [47] pointed out, the empirical approaches for rupture assessments are based on statistics from aggregate populations and are incapable of providing precise risk estimates for individual AAA.

1.5.2 The Biomechanical Approach

The biomechanical approach to predict AAA rupture is fundamentally different from any empirical approach in that it views the biomechanical status (stress and strength) of a given aneurysm as the determining factor behind its potential to rupture. This approach represents the manifestation of other critical factors, such as patient age, sex, blood pressure, AAA size, and AAA shape. The fundamental assumption is that AAA rupture is a mechanical phenomenon and occurs when the local acting stress in the wall exceeds the local strength of the wall. Therefore, for this approach, one must determine both wall stress and wall strength.

Most current biomechanical studies on AAA rupture have focused on assessing stresses. The simplest way of estimating AAA wall tension or stress is via the law of Laplace by assuming that the AAA geometry is cylindrical or spherical. [48, 49] A recent study was conducted to compare the AAA wall tension between a ruptured and a non-ruptured group of AAA using the law of Laplace. [36] They found that the mean wall stress of the ruptured AAAs was 4.96×10^5 N/m^2 as compared to 3.05×10^5 N/m^2 for the non-ruptured AAAs ($p < 0.008$). Based on this, they suggested that AAA wall tension is a significant predictor of pending rupture. Mower et al.

[50] demonstrated that the law of Laplace is inaccurate in predicting the complicated stress distribution that exists in aneurysm walls, and more sophisticated tools, such as the finite element (FE) method, are needed. Using 2D hypothetical axisymmetric models, Elger [51] demonstrated that the shape of the AAA profiles is an important determinant of the magnitude and location of the maximum wall stress. Hua et al. [47] demonstrated the critical importance of using detailed three-dimensional modeling of individual AAA to assess wall stress and rupture for individual AAAs. In addition, our laboratory [52] used hypothetical models to assess the influence of AAA geometry on 3D stress analysis. It was found that the increase in AAA diameter from 4 cm to 8 cm increased the peak wall stresses by 100% while change in shape from axisymmetric to highly asymmetric increased peak wall stress by more than 50%. To improve the technique of assessing wall stress distribution, our group first employed the actual, 3D, patient-specific AAA wall geometry and realistic material properties and boundary conditions for a more accurate estimation of wall stress distribution. [53] This initial work demonstrated that the wall stress distribution is quite complex and does not adhere to the commonly used law of Laplace. However, one limitation of this work was that it did not take into account the effect of the intraluminal thrombus. ILT is a three-dimensional fibrin structure incorporated with blood cells, platelets, blood proteins, and cellular debris, and is present in variable degrees between the flowing blood and the aortic wall in approximately 75% of all AAA. [54] Inzoli et al. [55], Di Martino et al. [56], and Mower et al. [57] each used FE methods and hypothetical geometries, and linear elastic material properties to demonstrate the influence of ILT on wall stress distribution. Both Mower and Inzoli used axisymmetric finite element models to determine influence of the size and mechanical properties of ILT on maximum AAA wall stresses. Inzoli et al. [55] reported that a large ILT that reduces the AAA lumen volume by 30% also results in a

30% decrease in maximum stress. Mower et al. [57] reported a 51% maximum stress reduction for large (filling the space between the normal diameter lumen and AAA wall) and stiff (elastic modulus of 1.0 MPa in the range of 0.01 to 1.0 MPa) ILT. Di Martino et al. [56] studied the effect of ILT shape (eccentricity) and mechanical properties on maximum wall stress. They showed that the stiffer and the more concentric shaped the ILT, the lower the wall stress. They also showed that the absence of ILT results in the highest values of circumferential aortic wall stress. All of these previous studies concluded that ILT can significantly influence AAA wall stress. However, one major limitation of these studies was their use of linear elastic material models for both the ILT and AAA wall. Based on clinical observation and ex-vivo testing results [58-60], our group showed that both of these tissues are nonlinearly elastic materials. Therefore, the current work will more rigorously investigate the influence of ILT on wall stress distribution (Specific Aim #1) by using patient specific models, realistic boundary conditions, and realistic nonlinear elastic material properties for both ILT and AAA wall.

The knowledge of the relationship between AAA tissue strength and aneurysm rupture is equally important. It is possible that decreases in tissue strength may actually precipitate rupture in many aneurysms. [52, 61] Despite its critical importance, little attention has been devoted to study the relationship between AAA tissue strength and aneurysm rupture. Data from our group shows that there is a significant decrease in the tensile strength of AAA (65 ± 9 N/cm^2) compared to nonaneurysmal tissue (121 ± 33 N/cm^2). [62] However, the significant standard deviations in this previous data suggest that the wall strength differs considerably from patient to patient. Studying paired wall specimens from different locations of AAA, our recent study showed that wall specimens from regions adjacent to a thick layer of ILT were significantly weaker than those from regions adjacent to a thin layer of ILT (138 N/cm^2 ± 19 N/cm^2 vs. 216

$N/cm^2 \pm 34\ N/cm^2$, $P < .05$). [62] To our knowledge, there is no report in the literature on prediction of local wall strength ***distribution*** in AAA. Therefore, the present study will also address this issue (Specific Aims #2 and #3).

With an improved estimation of wall stress distribution, and a newly developed method to predict wall strength distribution, we will be able to noninvasively predict a rupture potential index distribution for individual AAA (Specific Aim #4). This patient specific technique would be much more reliable than the general "5 cm diameter criterion". It would help surgeons make better decisions by operating on smaller aneurysms with high risk of rupture and by not operating on larger aneurysms with a low risk of rupture. The most important potential outcome of this approach is that AAA patients might receive higher quality care.

1.6 Hypothesis and Specific Aims

The overall goal of this work was to develop a technique that will allow us to evaluate of the propensity for rupture of an individual AAA by comparing local AAA wall stress with local AAA wall strength. The closer the wall stress at any point on a AAA is to the local wall strength, the higher the risk of rupture for that patient's aneurysm. A critical rupture index based on the local wall stress and strength might then be developed to predict the risk of rupture, replacing the current unreliable criteria. In order to move toward this goal, the following two hypotheses were explored in this work:

Hypothesis #1: The presence of ILT in AAA significantly effects the 3-D wall stress distribution and should be included in the stress simulation model.

Hypothesis #2: The local strength of the AAA wall may be adequately predicted by certain clinical, noninvasively measurable variables using multiple linear regression techniques.

Our group has previously developed and validated a noninvasive technique to estimate wall stress distribution acting on the AAA wall. [63] If hypothesis #1 proves correct, however, the current study will improve that previous technique by incorporating ILT into the stress analysis. In order to do this, the previous 3D reconstruction technique developed by our laboratory was modified to incorporate the ILT. Additionally, a constitutive model for ILT was developed and incorporated into the finite element analysis of AAA.

To address hypothesis #2, a statistical/mathematical model was developed to predict the patient-specific, spatial AAA wall strength distribution noninvasively. We used multiple linear regression techniques to develop a mathematical model for the local wall strength as a function of certain clinical, noninvasively measurable variables. Since the factors that influence AAA wall strength are poorly understood, we included as many variables which have been proven to be associated with wall strength, aortic wall microstructure, and/or AAA rupture potential. The dependent variable (wall strength) data and all dependent variables were collected experimentally. Significant parameters were chosen by multiple linear regression analysis techniques. After the model was constructed, a different data set was collected to validate the predictability of the model by comparing the predicted wall strength value with the measured value.

A Rupture Potential Index (RPI) distribution was calculated that compares, on a point by point basis, the local AAA wall stress to AAA wall strength. As the RPI value at any point

approaches 1.0, that part of the wall has a high likelihood of failure point and therefore the aneurysm has a high likelihood of rupture.

In summary, to address our hypotheses, and to develop a potentially useful new clinical technique to improve AAA patient management, the following three specific aims will be accomplished:

Specific aim #1: Study the effect of ILT on AAA wall stress distribution and improve our existing noninvasive method for the assessment of AAA wall stress distribution by incorporating ILT into the 3D structure and analyses if necessary.

Specific aim #2: Identify the significant, noninvasively measurable variables that are predictors of local AAA wall strength.

Specific aim #3: Develop and validate an adequate statistical model to predict the local strength of AAA wall.

Specific aim #4: Develop a noninvasive method for the estimation of the Rupture Potential Index (RPI) for individual AAA

2.0 GENERAL BIOMECHANICAL CHARACTERISTICS OF ILT

2.1 Introduction

Biomechanics is a branch of mechanics that is concerned with how biological materials respond to applied loads. In AAA biomechanics, we are concerned with the wall stress distribution under physiological loading. In order to capture or simulate the biomechanical response of an object, the biomechanical properties of the material(s) involved are prerequisites.

Besides the aneurysmal wall, most AAAs contain a solid mass of intraluminal thrombus (ILT). [54] ILT is a fibrin structure incorporated with blood cells, platelets, blood proteins, and cellular debris. [64] To explore Hypothesis #1 (see Section 1.6) and accomplish Specific Aim #1, the knowledge of the biomechanical behavior of both the AAA wall and ILT is necessary. Our group [62, 63] has previously reported the mechanical behavior of AAA wall. However, no rigorous studies have been performed to quantify the mechanical properties of ILT. The mathematical equation describing the mechanical behavior of a material is referred to as the "constitutive equation" for that material. The following three chapters (Chapters 2, 3, and 4) describe efforts towards deriving a constitutive equation for ILT.

In mechanics, the properties of a material result from its internal constitution and structure. Therefore, the first step for any constitutive formulation should be to study the general characteristics of that material; [65] that is to classify the material based on its composition and observed behavior. The general characteristics of the material would then dictate the approach

for developing suitable constitutive equations. For example, an approach taken for a solid material would be different for a material that is a fluid-solid mixture. Therefore, it is important to distinguish the relative fluid/solid composition of ILT. Another example is the ability of a material to preserve its density or volume upon deformation. A material with such ability is termed "incompressible". A previous study conducted by our lab investigated the incompressibility of ILT. [59] In that study, an ultrasound system with automated border detection (ABD) (Hewlett-Packard model 77035A, Andover, Massachusetts) was used to measure continuously the cross-sectional area enclosed by the aneurysm wall and the luminal surface throughout the cardiac cycle. The difference between the area of the two cross-sectional measurements at any point in time was taken as the area of intraluminal thrombus. The results showed that intraluminal thrombus area was nearly constant over the cardiac cycle, suggesting that the thrombus is virtually incompressible.

In the current chapter, additional work is described that provides further insights on the general material characteristics of ILT, including its composition, general structure, isotropy, heterogeneity, and viscoelasticity.

2.2 Methods

2.2.1 ILT Procurement

All procedures were carried out in accordance with guidelines of the NIH and the University of Pittsburgh Biomedical Internal Review Board. Study subjects were patients

undergoing surgical AAA resection. ILT was removed intact from the AAA and carried to our lab in heparinized PBS (10 NIH unit/ml). Tissue specimens were individually prepared as described in the sections below depending on the particular study.

2.2.2 Heterogeneity

If the material properties are identical at every location within a body, the body is said to be *homogeneous*. Alternatively, a body whose material properties change from point to point is said to be *nonhomogeneous* or *heterogeneous*. The material may be heterogeneous, but isotropic. To qualitatively study the homogeneity of ILT, we inspected the microstructural variation of ILT specimens from different regions or layers using scanning electron microscopy (SEM) techniques. Three samples - one from the luminal surface, one the medial layer, and one from the abluminal region close to the wall - were carefully cut and fixed in 2% paraformaldehyde with PBS for at least 48 hours. Samples were post-fixed in 1%OsO_4 to increase electron conductivity, then underwent dehydration and critical point drying. The dried specimens were mounted, sputter-coated with gold and visualized using a scanning electron microscope (Model S-2460N, Hitachi, Ltd., Tokyo, Japan). SEM images of specimens from the different regions were taken and studied for any microstructural differences that would suggest heterogeneity of the material.

2.2.3 Wet Density and Fluid Fraction

To measure the density of ILT, small (~ 5 mm length) specimens from different regions of the intact ILT were removed using a 6 mm punch. The weight of each specimen was then measured by a balance (Model SA-80, Scientech, Boulder, Colorado). To measure the volume,

the specimen was immersed in a graduated cylinder partially filled with PBS and the measured volume change within the cylinder was taken as the volume of the specimen. The wet density was calculated as wet weight divided by the volume of the specimen. The samples were desiccated by a speed vacuum centrifuge machine (Model # SPD111V, The Savant SpeedVac, Sunnyvale, CA), and the dry was weight then measured. The difference between the dry weight and the wet weight was taken as the fluid weight. The fluid weight fraction was calculated as the percentage of total wet weight. The fluid volume was then calculated from the fluid weight by assuming the density of the fluid is 1 g/cm^3. The volume fraction of fluid was calculated as the percentage of the total volume of the specimen.

2.2.4 Isotropy

If the constituents of the material of a solid body are oriented randomly, that part of the body will display essentially the same material properties in all directions. If a solid body is composed of such randomly oriented constituents, it is said to be *isotropic*. To investigate preliminarily the isotropic behavior of the ILT, both biaxial tensile testing and fibrin fiber orientation quantification of SEM images were performed on specimens from the luminal surface of the thrombus. For each specimen studied, four SEM images were taken and analyzed.

2.2.4.1 Scanning Electron Microscopy

Small samples were carefully cut from the luminal surface of the ILT. All the samples went through fixation, dehydration and critical point drying process as described in Section 2.2.2. The circumferential-radial orientation of each sample was carefully registered and preserved throughout the preparation. Obtained SEM images (512 x 512 pixels) were used for

subsequent fiber orientation quantification using the Fast Fourier Transform (FFT) algorithm available on the image analysis software Scion Image (Release Beta 4.0.2, Scion Corporation, Frederick, Maryland).

FFT has been widely used to quantify the collagen fiber orientation in skin [66] and bone [66-69], and also to explore the structure of other materials. [70] In short, the FFT algorithm transforms the image intensity function in gray scale from spatial to a frequency domain. The image in the frequency domain is referred to as a "power spectrum plot". Radial symmetry of the power spectrum plot would represent randomly-oriented constituents, and therefore an isotropic material. Any deviation from radial symmetry is indicative of some degree of anisotropy of the material. In the current work, the radial symmetry of the power spectrum plots for ILT were qualitatively assessed.

2.2.4.2 Biaxial Tensile Testing

To further investigate the material symmetry of ILT, biaxial tensile testing was studied on a single planar specimen obtained from the luminal surface of the intact ILT. The specimen was cut into a thin "sheet" of dimensions 2 x 2 cm and average thickness of ~ 1 mm. The specimen was mounted in a well-validated biaxial testing device within the laboratory of Dr. Michael Sacks [71] using suture line and surgical staples. The in-vivo circumferential and longitudinal directions coincided with the stretch axes of the biaxial device; i.e., x_1 and x_2, respectively. The test specimen was first preconditioned with 15 cycles of equi-biaxial loading (i.e., f_1:f_2 =1:1, where f_1 is the force loading in the x_1 direction and f_2 is the force loading in the x_2 direction) to a maximum strain of 0.10 at a strain rate of 0.01 s^{-1}. Next, an equal biaxial test was performed with a maximum load control of 50 g. All testing was performed with the specimen completely immersed in phosphate buffered saline bath (pH=7.4) at room temperature. The deformation

responses along the two axes under the equi-loading condition were compared to investigate the isotropic behavior of ILT.

2.2.5 Viscoelastic Behavior of ILT

A body is deformed when subjected to applied forces. If, upon the release of the applied forces, the body immediately recovers its original shape and size, then the material body is said to be *elastic*. The material that recovers its size and shape only gradually after the load is released is a *viscoelastic* material. When a viscoelastic material is suddenly deformed and then the strain is maintained constant afterward, the responding stress decreases with time. This phenomenon is called *stress relaxation*. On the other hand, if a viscoelastic material is suddenly stressed, and then the stress is maintained constant, the material continues to deform. This phenomenon is called *creep.* If the viscoelastic material undergoes a cyclic loading, the stress-strain relationship in the loading and unloading processes are different due to viscous energy loss. This is called *hysteresis*. The features of *hysteresis*, *stress relaxation*, and *creep* are collectively referred as the viscoelastic characteristics of the material. [72] To preliminarily investigate the viscoelastic behavior of ILT, stress relaxation, creep and cyclic loading tests were all performed on ILT material and described in the following subsections.

2.2.5.1 Stress Relaxation

A thin sheet of ILT was obtained freshly from the luminal surface of a thrombus harvested and prepared as described as in Section 2.2.1. A single uniaxial specimen was then cut from the sheet as a narrow strip with dimensions 2 x 20 mm and average thickness of ~ 1 mm. The specimen was mounted in the well-established tensile testing machine in our laboratory

which is fully described elsewhere. [60] A 10% stretch was suddenly applied to the sample and then maintained constant. The resistive force offered by the sample was recorded. The resulting force-time data was fit to the following equation to study the stress relaxation response of ILT [72]

$$F = (F_0 - F_\infty)e^{-\frac{t}{\tau_\varepsilon}} + F_\infty \quad (2.1)$$

where F_0 is the initial responsive force after the load was applied to the specimen, F_∞ is the equilibrated force after decay, or relaxation, is complete, t is time, and τ_ε is the time constant for the decay. The parameter τ_ε characterizes the rate of decay of the force under constant strain. F_0 and F_∞ were obtained directly from the experimental (F, t) data. τ_ε was obtained via nonlinear least square regression of the model against the data. Nonlinear regression was performed using the software STATISTICA (v.*4.5*, Statsoft Inc., Tulsa, OK)

2.2.5.2 Creep

A single disk-shaped sample of ILT with thickness of ~ 2 mm was cut from the luminal surface of the intact ILT using a 6 mm diameter punch and then mounted in a creep testing machine designed by Dr. J.K. Suh. [73] The specimen was placed in a confined compression chamber with a porous filter on top. A 10-gram compressive load was applied suddenly to the filter and the axial deformation of the specimen was recorded for 45 minutes. The displacement-time (u_t – t) data was fit to the following model for the creep response of a viscoelastic biological material [72]:

$$u_t = u_\infty \left(1 - \left(1 - \frac{\tau_\varepsilon}{\tau_\sigma} \right) e^{-\frac{t}{\tau_\sigma}} \right) \tag{2.2}$$

where u_∞ is the equilibrated deformation, τ_ε is the relaxation time under constant strain determined from the stress relaxation study (Section 2.2.5.1), and τ_σ is *the time constant for creep relaxation* (i.e., under constant load), which characterizes the rate of the deformation. u_∞ was obtained directly from the experimental data. τ_σ was obtained via nonlinear least squares regression of the model against the (u_t – t) data.

2.2.5.3 Hysteresis

A specimen similar to that for the stress relaxation test was obtained and again mounted in our uniaxial tensile testing device. A cyclic loading of 10% strain was applied to the specimen at rate of 0.1%/s. The induced force was recorded over time and the data was converted to force – stretch (f – λ) data pairs as previously described. [60] For each cycle, the loading and unloading curves were identified separately, plotted on the same figure, and inspected for qualitative assessment of the hysteresis of the material.

2.3 Results and Discussion

2.3.1 Heterogeneity of ILT

The top panel of **Figure 4** shows the gross anatomy of an ILT freshly harvested from a patient undergoing AAA repair. Gross observation revealed that this and indeed most ILT appear to be composed of three distinct transmural layers. The first layer appears red and is nearest the lumen (the "luminal layer"). The second layer is situated in the medial region of the ILT and appears white (the "medial layer"). The third layer appears dark brown and is nearest the wall (the "abluminal layer"). The observation of laminated thrombus seems to support the theory of thrombus formation put forth by Duguid [74] as follows:

> *"Most aortic thrombi are composed mainly of fibrin, which when newly formed is loose in texture and somewhat ragged…, but which later becomes more compact.*
>
> *"In the aorta thrombosis tends to recur, with the formation of multiple deposits of elements derived from the blood mass, and the appearance produced are varied, depending not only on the size of the deposits but also on the time which elapses between their formation. With repeated thrombosis and organization thick accumulations of fibrous tissue may be produced, deeply embedded with them, layer of hyaline or 'fibrinoid' substance."*

SEM images (bottom panels of **Figure 4**) of the three different regions within an ILT specimen also demonstrated a marked difference between layers. In the luminal region (**Figure 4A**), fibrin fibers and red blood cells are clearly identifiable. The fibers are arranged into primary

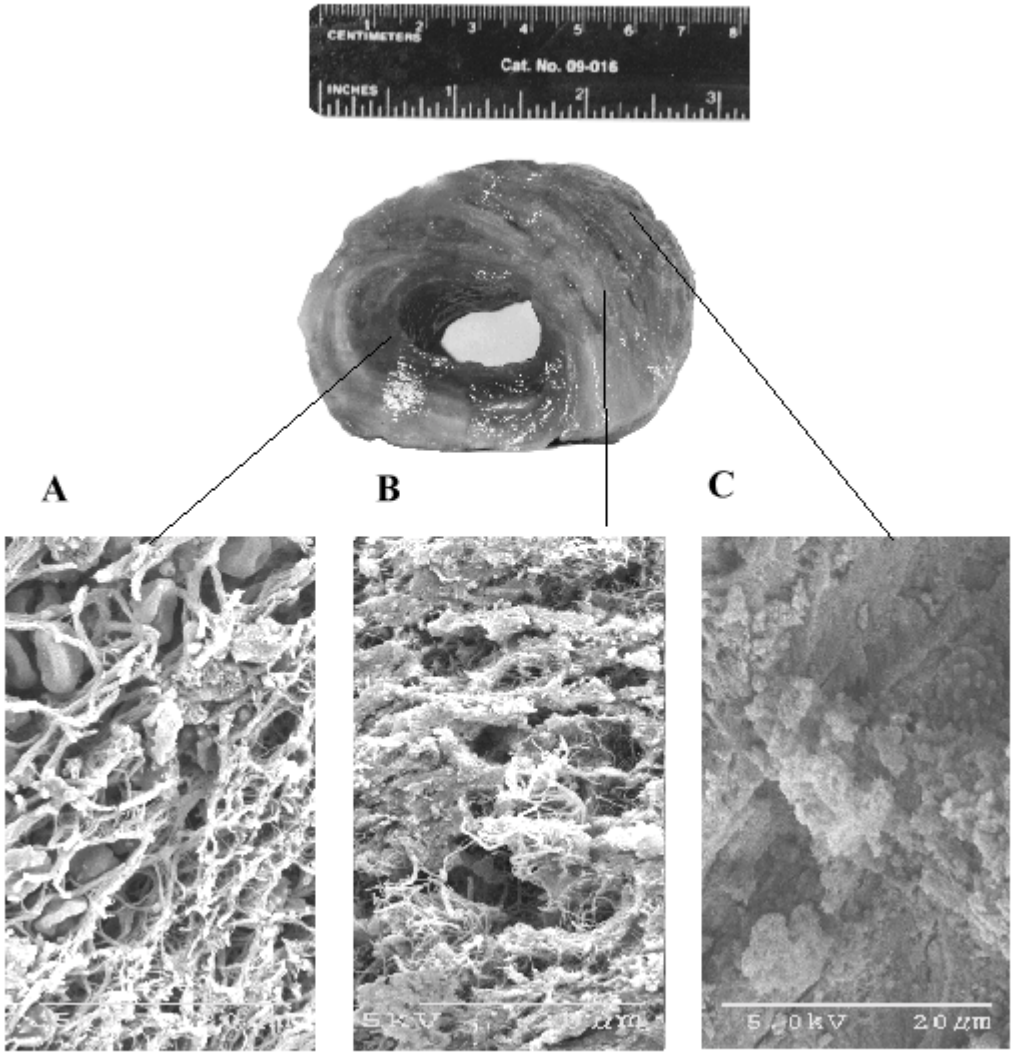

Figure 4 Top: A cross-sectional view of a typical intraluminal thrombus specimen. Bottom: Representative scanning electron micrographs from the three different regions - the luminal surface which is the newly formed ILT (A), the medial region (B), and the abluminal region near the AAA wall where the ILT is the most "aged" (C).

thick fibrin bundles and fine secondary structures cross-linking the primary bundles. The medial layer of the same ILT (**Figure 4B**) appears distinctly different as some of the fibers have been degenerated. All the fibrin fibers appear to be degenerated in the abluminal region (**Figure 4C**) where the ILT showed little or no structure at all.

2.3.2 Wet Density and Fluid Fraction

Six total ILT samples from three patients were studied. For each patient, one sample was obtained from the region close to the lumen (luminal region), the other from the region close to the wall (abluminal region). The calculated wet density, fluid weight ratio, and fluid volume ratio are listed in **Table 2**. The average (± SEM) wet density of ILT was found to be 1.11 ± 0.03 g/cm^3 , and the averaged fluid weight fraction was 78.6 ± 1.5 %. The average fluid volume fraction was 87.2 ± 1.8 %. Given the accuracy of the measurement, ILT might be a little greater in density than water. Overall, water makes up 50 to 70 per cent of the weight of the human body. [75] A similar water content has been found for aortic tissues. Fisher and Llaurando [76] showed that the water content (fluid weight ratio) for canine abdominal aorta is 70.4 + 0.4 %. Under dynamic in vivo loading conditions, fluid might move in and out of tissue. The friction interactions resulting from this interstitial fluid flow causes its viscoelastic behavior. [77] The percentage of fluid content in ILT provides a baseline understanding of the biomechanical behavior, i.e., highly viscoelastic or nearly viscoelastic.

Table 2 Measured wet density and fluid fraction for ILT

	Region	Wet Density (g/cm^3)	Fluid Weight Ratio (%)	Fluid Volume Ratio (%)
ILT 1 (PT#1)	Abluminal	1.05	84.8	88.8
ILT 2 (Pt #1)	Luminal	1.19	76.2	90.9
ILT 3 (Pt #2)	Abluminal	1.00	75.3	78.9
ILT 4 (Pt #2)	Luminal	1.07	77.8	90.9
ILT 5 (Pt #3)	Luminal	1.08	80.9	87.5
ILT 6 (Pt #3)	Abluminal	1.18	76.5	86.4
Mean		1.11	78.6	87.2
Standard Error		0.03	1.5	1.8

2.3.3 Isotropy

2.3.3.1 Microstructural Evaluation of ILT via SEM and Power Spectral Analysis

Three total ILT specimens from three different patients were studied. Each specimen was taken from the luminal surface. **Figure 5A** shows a representative SEM image. The fibrin fibers are clearly identifiable and appear to be distributed in a random manner. **Figure 5B** is the power spectrum plot of **Figure 5A**. The other 11 SEM images and power spectrums were similar to

these. The radial symmetry of the power spectrum plots suggests that the fibrin fibers are indeed distributed randomly along each direction, and that ILT is isotropic in terms of microstructure.

2.3.3.2 Biaxial Testing

Figure 6 shows the deformation (stretch) response for the single equi-biaxial tension experiment on ILT from the luminal surface. Because the data shows an equal stretch response under equal applied forces along the two axes, this suggests that ILT is mechanically isotropic.

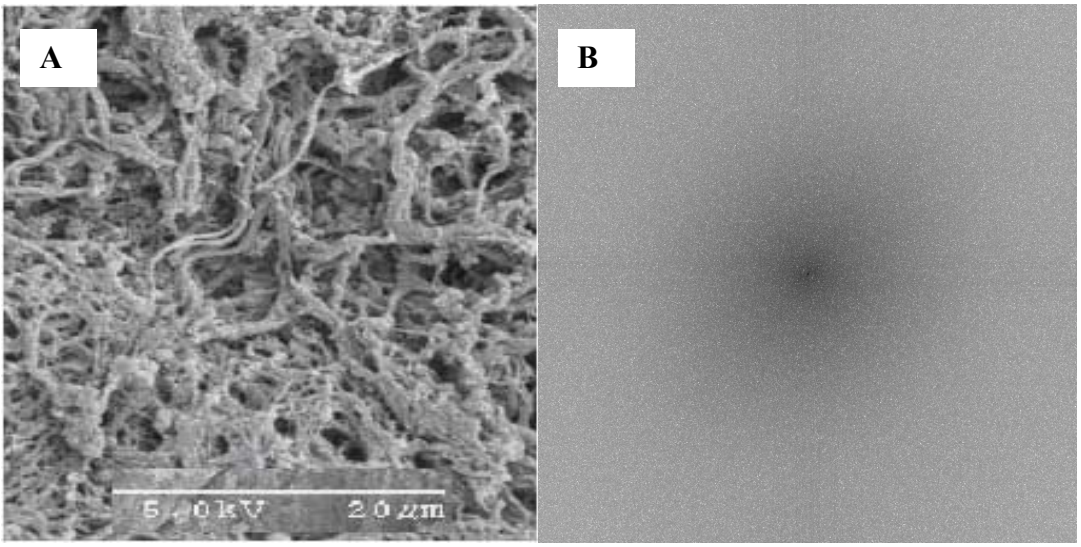

Figure 5 Evaluation of the microstructure of ILT. A: Representative SEM image of ILT from the luminal surface. The random orientation of the fibers suggests isotropy of ILT. B: Power spectrum of the image in (A) obtained by Fast Fourier Transformation. The radial symmetry of the power spectrum further suggests isotropy of ILT.

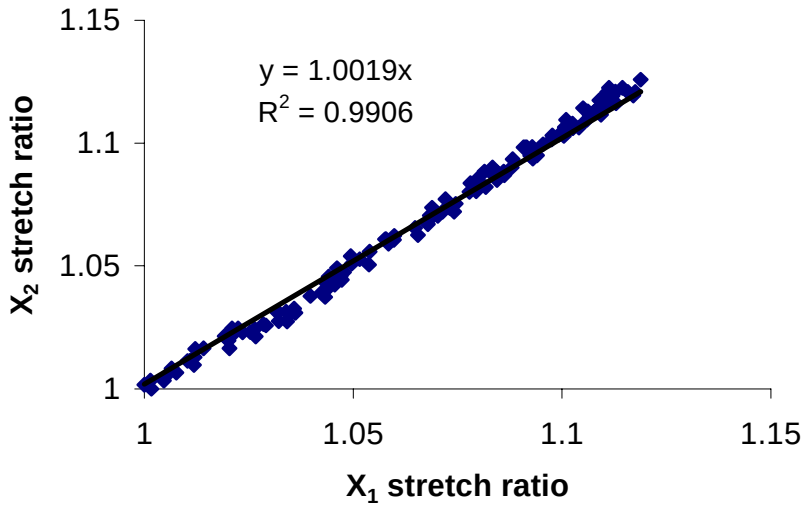

Figure 6 The stretch response of an ILT specimen in the circumferential (X_1) and longitudinal (X_2) directions under equi-biaxial loading conditions.

2.3.4 Viscoelasticity

As shown in Section 2.3.2, fluid makes up about 87% of ILT by volume. Furthermore, the SEM images in **Figures 4** and **5** suggest that ILT is rather porous. Under deformation, fluid moves in and out of ILT, the friction interactions resulting from this interstitial fluid flow causes its viscoelastic behavior. [77] The results of our experiments to evaluate preliminarily this behavior is below.

2.3.4.1 Stress Relaxation

Figure 7 shows the stress relaxation behavior of the single ILT specimen tested while under 10% strain loading. The peak initial force (F_0) was 37 N. The force decayed with time until it reached a steady state value (F_∞) of 32 N. The nonlinear regression of the data against

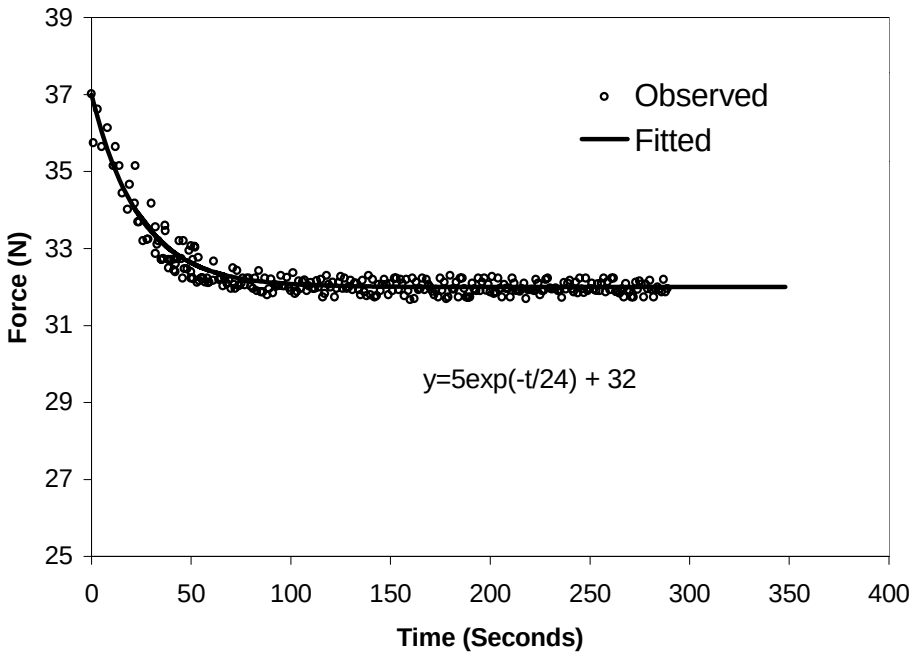

Figure 7 Uniaxial stress relaxation behavior of ILT under 10% elongation.

equation 2.1 found that τ_ε = 24 seconds. Therefore, the stress relaxation equation for this ILT specimen is given by

$$F = 5e^{-t/24} + 32 \quad (2.3)$$

where t is in seconds and F in N. The fact that $\tau_\varepsilon \neq 0$ and $F_0 \neq F_\infty$ indicates that ILT does exhibit stress relaxation under constant extension.

The stress relaxation behavior of ILT is not surprising considering the large fluid content of the material (Section 2.3.2, **Table 2**) and the characteristics of the microstructure (Section 2.3.1, **Figure 4**). The instant response of reaction force is due to the incompressibility of thematerial (i.e., water). The interconnected fibrin network will continue to rearrange itself under constant displacement until an equilibrium force is reached, and this process is characterized by the stress relaxation observed in **Figure 7**. At approximately 100 seconds, the reaction force begins to reach an asymptotic (equilibrium) value. This result is comparable with relaxation data for aorta reported by Fung (~100 seconds) [72] and the stress relaxation data for bovine coronary arteries reported by Humphrey (~200 seconds). [78]

2.3.4.2 Creep

Figure 8 shows the creep behavior of a single ILT specimen tested under 10g loading. The instant deformation of the material was about 12 μm. The specimen then continued to deform until it reached a steady state displacement (u_∞) of 30 μm. The nonlinear regression of the data against equation 2.2 found that $\tau_\sigma = 1250$ seconds. Therefore, the creep equation for this ILT specimen is given by

$$u_t = 30\left(1 - 0.9808\, e^{-\frac{t}{1250}}\right) \quad (2.4)$$

where t is in seconds and u_t in μm. The fact that $\tau_\sigma \neq 0$ indicates that ILT does exhibit creep under constant loading.

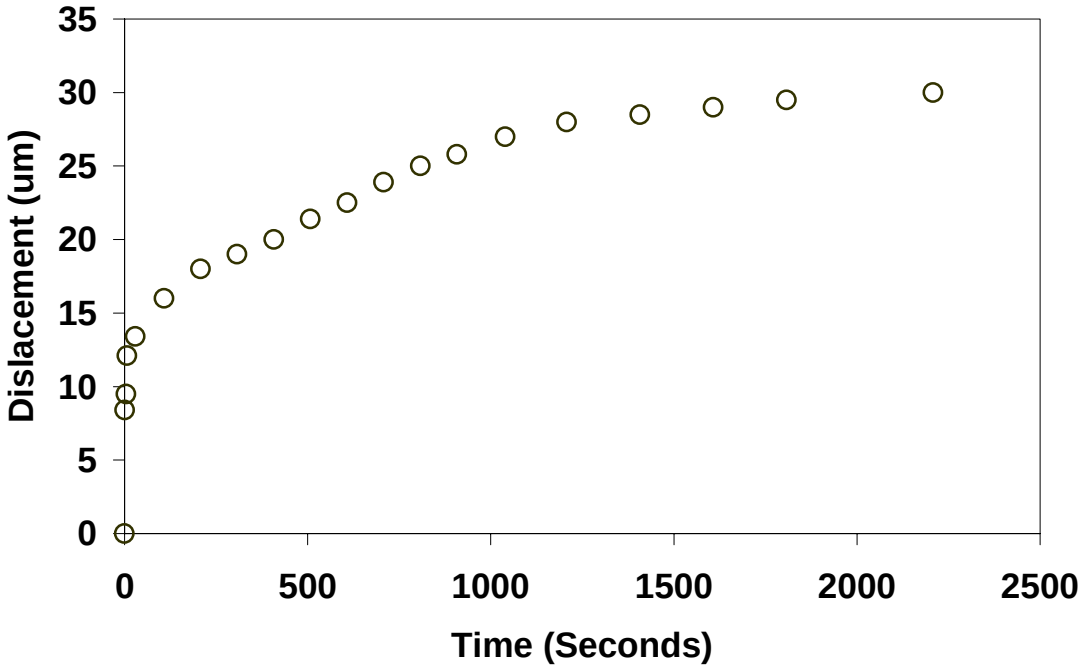

Figure 8 Creep response of ILT under a constant compressive load (10 g).

The initial response, i.e., the sudden displacement after load placement is due to elastic deformation and the fluid escaping through the filter. After that, the fibrin network deforms to generate the pressure needed to balance out the applied axial load. It is noted by comparing **Figures 7** and **8** that the creep process lasts longer than stress relaxation. This is typical for soft

tissues. [72] The result that τ_σ =1250 seconds is comparable with the creep response for dog carotid artery as reported by Fung ($\tau_\sigma \approx 1000$ seconds). [72]

2.3.4.3 Hysteresis

Figure 9 shows the loading and unloading curves of a single ILT specimen during one cycle of loading at 10% strain. It is clear that these two curves do not overlap each other and that there is significant viscous loss. The area enclosed between the two curves corresponds to this energy loss and demonstrates that ILT exhibits hysteresis

2.4 Limitations

The information on the general biomechanical characteristics of ILT obtained in this chapter was only intended to guide the design of a uniaxial tensile testing protocol (Chapter 3) and to facilitate constitutive modeling (Chapter 4). It was not our purpose to rigorously study the biaxial or viscoelastic properties of ILT, for example. More rigorous experiments should be conducted in the future to fully investigate the mechanical behavior of ILT under all possible loading conditions.

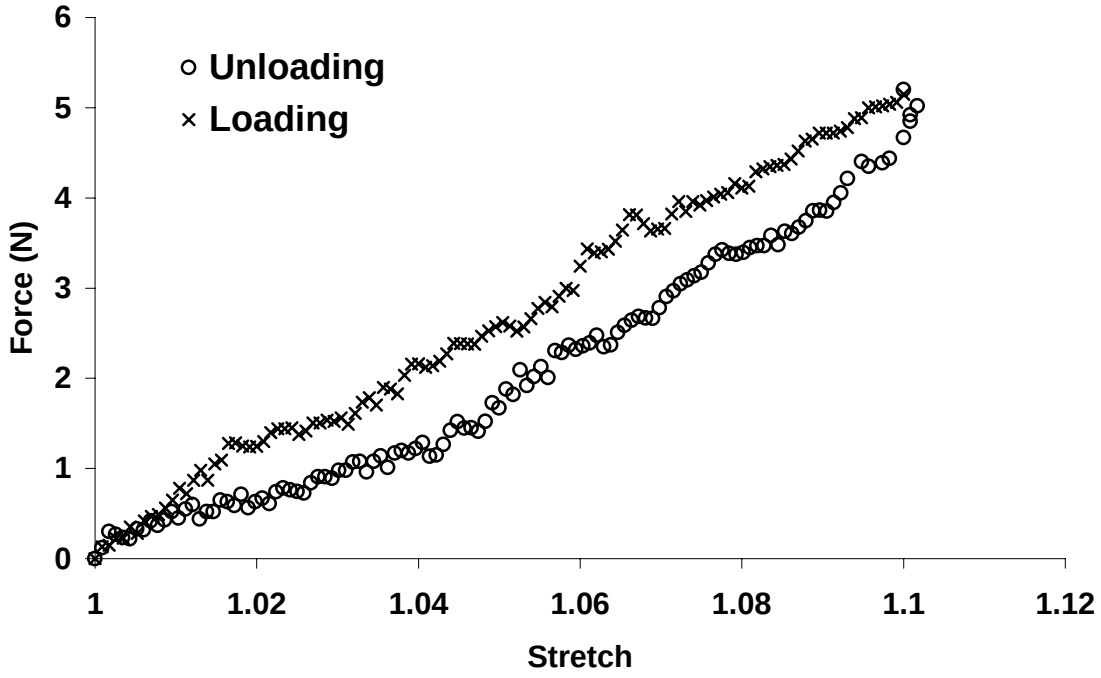

Figure 9 Ex-vivo force-stretch response of ILT during one cycle of loading in uniaxial tension. Note the hysteresis; i.e., the area enclosed by the loading and unloading curves that is indicative of viscous energy loss.

Like all experimental methods, there are limitations and sources of error related to the studies described in this chapter. In the determination of wet density and fluid fraction, only six samples total were tested. Additionally, specimens were not dabbed dry after washing in heparinized PBS. This could contribute error to the fluid fraction measurements. Moreover, the accuracy of our volume measurement method may have caused error in calculating wet density of ILT. In the isotropy study, all the specimens were obtained from luminal surface. Specimens from other regions might behave differently. Only one ILT specimen was subjected to biaxial

testing. Again, only one ILT specimen each was used to study stress relaxation and creep, and both were obtained from the luminal region. More complete studies would include a larger number of samples and samples from different regions of the ILT. However, since the purpose of these studies was simply to collect preliminary data to facilitate experiment design of uniaxial tensile testing, and since our results were comparable with other studies, we believe that the data collected is sufficient.

2.5 Summary and Conclusion

The distribution, orientation and interconnection of the ILT constituents give rise to its mechanical properties. The laminated structure of ILT (**Figure 4**) likely dictates heterogeneous material properties for this material. However, within a single laminate, or layer, it is possible that the material properties are isotropic as suggested by the data presented in Section 2.3.3. Therefore, our initial observations suggest that ILT exhibit heterogeneity and layer-wise isotropy. Subsequent data reported in the next chapter also support this observation.

ILT experiences stress relaxation under constant extension, creep under constant compression, and hysteresis during cyclic loading. Therefore, ILT behaves as a viscoelastic material.

In conclusion, the present data and previous data from our laboratory suggested that ILT is an incompressible, heterogeneous, isotropic, viscoelastic material. These findings were very important in terms of guiding us with more rigorous biomechanical testing and subsequent constitutive modeling as described in the following two chapters (Chapter 3 and Chapter 4).

3.0 BIOMECHANICAL TESTING OF ILT

3.1 Introduction

In order to incorporate ILT into 3D-stress analysis of AAA (Specific Aim #3), a constitutive model of ILT is necessary. A constitutive model is a mathematical description of the biomechanical behavior of a material. A constitutive model development for ILT is the focus of Chapter 4. However, correct constitutive modeling of any material needs to begin with experimental data collection. With this in mind, the goals of this chapter were to: 1) design the proper mechanical testing protocol to capture the nonlinearly elastic response of ILT; and 2) to utilize the designed protocol to test freshly obtained ILT specimens.

Throughout a single cardiac cycle, the AAA wall and contained thrombus undergo large, dynamic deformation. [59] Further, the ILT within AAA is viscoelastic (recall Chapter 2). Therefore, to simulate the physiological response of AAA in vivo, ILT should be modeled as a viscoelastic material capable of undergoing large deformation. However, since the goal of the present study is to develop a clinical tool to predict the rupture potential of AAA, the "worse case scenario", or maximum stress distribution in the wall under static systolic pressure is our primary interest. Hence, the elastic behavior instead of viscoelastic behavior of ILT is the interest of present study.

To the best of our knowledge, there have been no previous studies reporting the nonlinear elastic behavior of ILT. In fact, the only study in the literature regarding the elastic behavior of ILT was done by Di Martino et al. [56] In that analysis, Hooke's law was utilized, but this is valid only for linearly elastic materials that undergo small strains. Therefore, it is apparent that in order to perform an accurate stress analysis of AAA, a rigorous study first needed to be performed to evaluate the nonlinearly elastic properties of ILT.

A detailed description of the experimental design, experimental procedure and results are provided in the following sections.

3.2 Methods

3.2.1 Sample Procurement

Intact ILT was obtained from open AAA reconstruction and rinsed as described in Section 2.2.1. Thin (~0.6 mm) "sheets" of ILT were obtained from both the luminal and medial regions of each thrombus. ILT from the abluminal layer near the AAA wall was too degenerated to be removed and tested. Narrow strips of specimens with typical dimension of 10×2 mm were cut from each thin "sheet" oriented along both longitudinal and circumferential directions. Paired specimens from the same "sheet" of ILT oriented along both directions were tested as described below to further investigate the isotropic behavior of ILT. Paired specimens from different layers of the same ILT but with the same orientation were tested to further determine whether the ILT is homogenous material or not.

All specimens were either tested immediately or refrigerated at 4^{o}C and tested within 24 hours of harvest The latter specimens were equilibrated to room temperature by immersion in fresh warm saline before testing. The specimens were kept wet with saline during the entire process.

3.2.2 Uniaxial Tensile Testing

The details of the ex-vivo uniaxial testing device used for this work have been described elsewhere. [60] In short, each long, thin ILT specimen was held between two clamps and a small amount of Cyanocrylate glue. The clamps were attached via straight, rigid tees to two translational brackets, the motion of which was controlled by a computerized microstepping motor. At the end of one tee, a 1kg load cell (Model 311430-04; Sensotec, Columbus, OH) was mounted to measure the force imposed during the testing. The "zero force" state of the specimen was determined by adjusting the length of the specimen until a small amount (< 15 g) of force was noted. The length, thickness and width of the specimen at the Zero-force State were measured at the center of the specimen using a dial caliper. The product of width and thickness was used as the reference cross-sectional area. An open pump circuit was used to drip room-temperature saline on the specimen to keep it wet during the test.

3.2.2.1 Evaluation of Strain Rate

As discussed in Chapter 2, ILT in-vivo exhibits characteristics of a viscoelastic material. Therefore, the total response of the tissue under extension is not only dependent on the amount of deformation but also on the *rate* of deformation, i.e., the strain rate. To determine the *elastic*

component of the response of ILT or any other soft tissue, one needs to utilize the proper strain rate while tensile testing so that the stress-relaxation of the material is accounted for.

To determine the strain rate needed for tensile testing of ILT in the present work, a multiple step stress relaxation test was performed. A single ILT specimen obtained as described in Section 3.2.1 was mounted in our ex-vivo tensile testing device and the "zero force" state achieved. A step load was then applied to the specimen resulting in 10% strain increments. The specimen was held at each level of strain for 250s as this was shown to be sufficient to reach an asymptote. The process was repeated several times, each time applying an additional 10% strain. For each strain step, the force-time (*F*-t) data was modeled by the mathematical function

$$F_{(t)} = F_0 - \frac{(F_0 - F_\infty)t}{t + \tau} \tag{3.1}$$

where F_0 is the force immediately after the step increase in strain, F_∞ is the asymptotic stress value at equilibrium (i.e., as $t \rightarrow \infty$), and τ is the time at which the stress decays by 50%. For each step, F_0 was directly measured so that τ and F_∞ were determined by nonlinear regression against the F- t data. One way to determine the strain rate necessary for tensile testing would be to divide the increment in strain for a given step by the time that it takes for the force to reach the value F_∞. Theoretically, this response time is ∞. Practically, however, data can only be collected over a finite period of time. One way to compromise is to use the time that is required for the force to decay by a reasonable percentage. In the present work, we assumed that 90% decay is sufficient.

Substituting $F = F_0 - 0.90(F_0 - F_\infty)$ in Equation 3.1 and rearranging, we find

$$t_{90\,\%} = \frac{0.90}{0.10}\tau = 9\tau \tag{3.2}$$

Using equation 3.2, $t_{90\%}$ was calculated for a given set of data (i.e., for a given step in strain) once τ was determined from the least square regression procedure. For each step, the strain rate was estimated as the increment in strain for that step divided by $t_{90\%}$. For our current application, the strain for each step was 10%. Therefore, the strain rate ($\dot{\varepsilon}$) calculated from each step was

$$\dot{\varepsilon} = \frac{10\%}{t_{90\%}} \tag{3.3}$$

Since the strain rate calculated in this manner will, in general, be different based on the data from each step in strain, the minimum value of strain rate calculated was used for all subsequent tensile tests of ILT.

3.2.2.2 Preconditioning

One thing that we found in Chapter 2 was that ILT exhibits hysteresis; i.e., the loading and unloading curves do not overlap each other. This is a typical viscoelastic behavior of any kind of soft tissues including ILT. To minimize the effect of hysteresis and obtain repeatable loading curves, Fung [72] suggested that prior to mechanical testing, the specimens be subjected to cyclic loading and unloading until a nearly repeatable cyclic behavior is achieved. Then the specimen is said to have been *preconditioned*. The number of cycles is taken as the number of cycles for preconditioning process. All specimens tested were preconditioned for the same number of cycles by loading to 10% strain and unloaded repeatedly at the constant strain rate determined as described in Section 3.2.2.1.

3.2.2.3 Tensile Testing

Each ILT specimen was mounted in the tensile testing device as described in Section 3.2.2.1. The zero force sate was achieved and the original dimensions were measured also as described in Section 3.2.2. Then the specimen underwent preconditioning as described in Section 3.2.2.2. Following preconditioning, each specimen was loaded to failure at the same strain rate determined in Section 3.2.2.1, and the tensile force was recorded at 1 Hz using the data acquisition software LabView (version 5.0, National Instrument, National Instruments Corporation, Austin, TX).

3.2.3 Data Analysis

The recorded data was converted to stress-stretch ($\sigma - \lambda$) data using a customized Excel macro written by Dr. M.L. Raghavan. [53] The change in specimen length (and hence λ) for each increment of recorded load was determined from the strain rate determined in Section 3.2.2.1 and the original length measured as in Section 3.2.2. The normal Cauchy (σ) stress in the direction of extension is defined as the applied load (f) per unit deformed area (A) of the specimen:

$$\sigma = \frac{f}{A} \tag{3.4}$$

Since the material is incompressible, i.e., the volume of the specimen does not change with time, the current area can be shown to be equal to [53]

$$A = \frac{A_0}{\lambda} \tag{3.5}$$

The Cauchy stress or the true stress is then calculated as

$$\sigma = \frac{f}{A_0}\lambda \tag{3.6}$$

The Cauchy stress-stretch (σ-λ) curve was plotted for each of the ILT specimens tested. The ultimate strength was defined as the maximum stress prior to failure. The maximum tangential stiffness was defined as the maximum slope of the stress-stretch curve before specimen failure. Wilcoxon paired test was used for the paired sets of specimens to determine significant differences in the various parameters ($p<0.05$) between region pairs (luminal vs. medial) and direction pairs (longitudinal vs. circumferential). The Student t-test was used to determine significant differences in the various parameters ($p<0.05$) between region groups (luminal vs. medial) and direction groups (longitudinal vs. circumferential). In all cases, $p < 0.05$ was used to determine significance.

3.3 Results and Discussion

3.3.1 Strain Rate

Figure 10 shows the recorded force-time data for the step-wise relaxation test described in Section 3.2.2.1. Using equation 3.3, we calculated the strain rate for each step of strain (**Table 3**). To be conservative, the minimum value of ***0.1411%/sec*** was selected as the strain rate for all preconditioning and tensile tests.

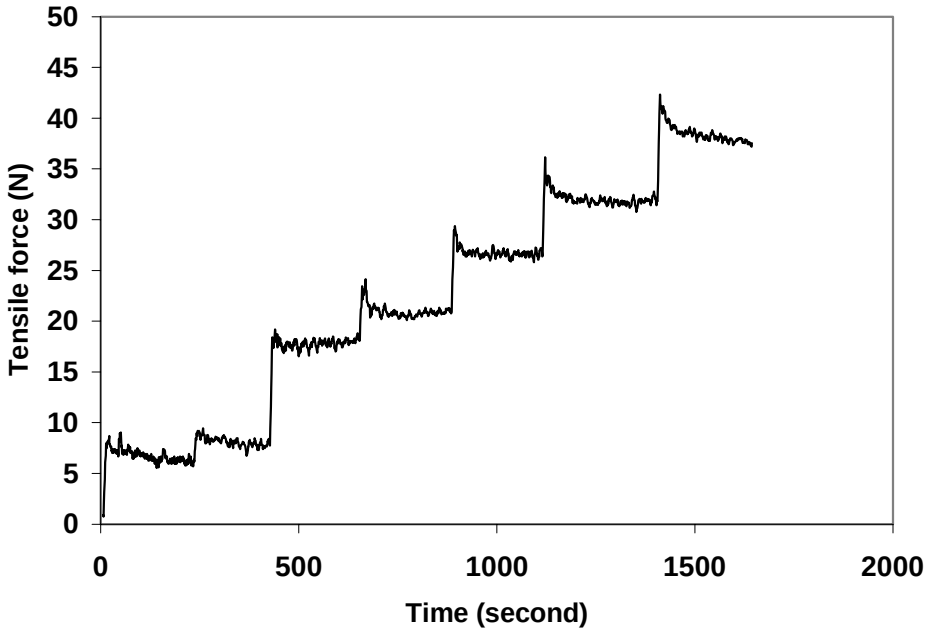

Figure 10 Multiple stress relaxation steps on a single ILT specimen for determination of strain rate. 10% elongation was applied at each step.

Table 3 Strain rate calculation according to equation 3.3.

Strain	Calculated Strain Rate, %/sec
10%	0.2561
20%	0.3423
30%	0.2641
40%	0.1567
50%	0.1425
60%	0.1411
70%	0.1524

3.3.2 Preconditioning

Figure 11 shows the preconditioning data from one ILT specimen. It is clear that after 5 loading cycles, the loading and unloading curves did not change and that preconditioning was completed. Therefore, all the ILT samples tested in this chapter were preconditioned using 5 cycles.

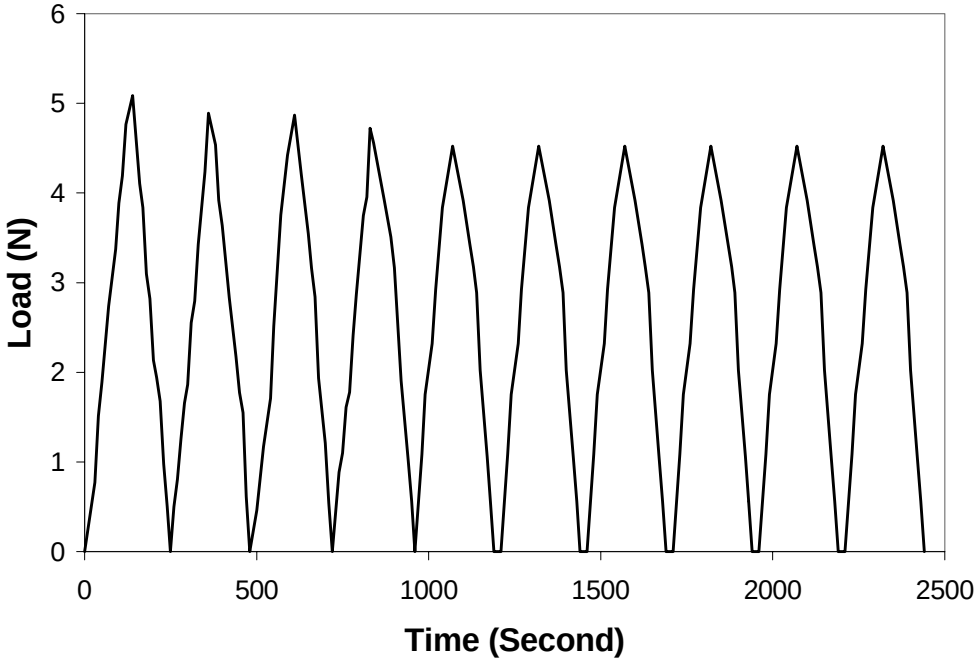

Figure 11 Preconditioning of a single ILT specimen. After 5 cycles, the loading and unloading curves are unchanged and preconditioning is complete.

3.3.3 Tensile Testing

Fifty specimens from 14 different patients were used for tensile testing. Patients were aged 69 ± 2 years (mean ± SEM) with an AAA diameter of 5.6 ± 0.2 cm. Among the 50 specimens, 28 (14 longitudinally oriented and 14 circumferentially-oriented with seven longitudinal-circumferential pairs taken from the same ILT) were from the luminal layers and 22 (11 longitudinally oriented and 11 circumferentially-oriented, with seven longitudinal-circumferential pairs taken from the same ILT) were from the medial layers.

Figure 12 shows a typical set of T-λ data from the uniaxial tensile testing, while **Table 4**

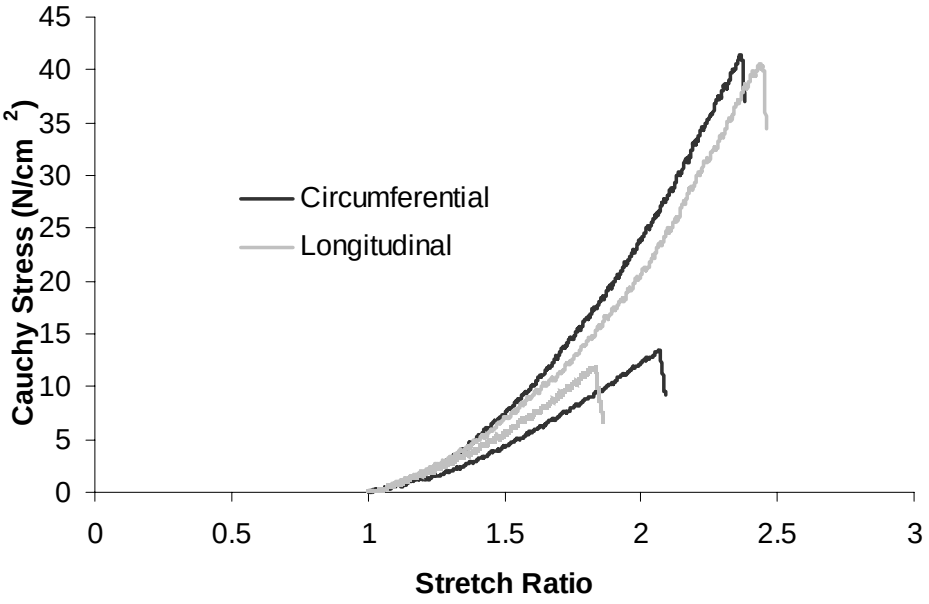

Figure 12 Typical set of circumferential and longitudinal stress-stretch curves for ILT samples taken from the luminal region (upper set of curves) and the medial region (lower set of curves). All data were obtained from the same ILT (same patient).

Table 4 Mechanical properties of ILT from the luminal and medial regions in both circumferential and longitudinal orientations

Region	Orientation	Stiffness (N/cm^2)	Strength (N/cm^2)
Luminal Layer	Longitudinal (n=14)	54 ± 7	52 ± 7
	Circumferential (n=14)	57 ± 7	54 ± 7
Medial Layer	Longitudinal (n=11)	33 ± 7	30 ± 7
	Circumferential (n=11)	27 ± 4	22 ± 5

orientation. The luminal layer is significantly stiffer and stronger than the medial layer in both directions ($p<0.01$), which is consistent with our structural heterogeneity observations detailed in shows stiffness and strength values for all the specimens tested, grouped by location and Section 2.3.3. Both the Student t-test and the Wilcoxon paired test (for the seven-paired sets of specimens) show there is no significant difference in terms of the strength and stiffness of ILT specimens between longitudinal and circumferential orientations for either luminal or medial specimens ($p>0.5$). This data would support our previous observation that ILT is mechanically isotropic (recall Section 2.3.3).

3.3.4 Limitations

Since it was not the objective of this work to model the physiological response of ILT during cyclic hemodynamic loading, the viscoelastic response of the material was not evaluated. Only the elastic response was measured. Therefore, any application of our data to dynamic simulation should be treated with caution. More complex simulations of the physiological response of ILT and AAA to the cyclic hemodynamic loading in vivo would require a totally different experimental design to capture the viscoelastic behavior of ILT. However, for the purpose of the current study (i.e., developing a constitutive model for ILT under static deformation), the uniaxial data reported here provides sufficient information.

As stated in Section 3.1, the purpose of biomechanical testing of ILT was to facilitate constitutive modeling (Chapter 4), the fundamental goal in constitutive modeling is the ability to predict the mechanical behavior of the material under any loading sate. Ideally, we should provide the information on all possible deformations. For the current study, due to the complex geometry of AAA and ILT, even under a static blood pressure loading, some part of AAA wall and ILT might undergo compression. The uniaxial tensile testing results provided here only provide the information on the tensile behavior of ILT. The compressive behavior of ILT was not evaluated. More rigorous experiments, including biaxial or tri-axial tensile and compression tests [72], should be conducted in the future to fully investigate the mechanical behavior of ILT under all possible loading conditions.

Of course, like all experimental methods, there are also limitations and sources of error with the tensile testing itself. For example, it was assumed that the ILT specimens had a constant thickness and width (and therefore area) over their length. However, only one measurement was taken for each specimen, and these were made at the center far away from the deformation

caused by the clamps. As a tensile testing specimen elongates, the central cross sectional area becomes smaller due to "necking" as the specimen deforms into a "dog bone" shape. Since the cross sectional area varies from the middle to the ends, the current area calculation based on Equation 3.5 might introduce error to the stress calculation (Equation 3.6). Manual measurement of width and thickness using a dial caliper may also contribute some degree of error. Other sources of errors might include the accuracy of the load cell itself (± 1.5 N), the temperature under which the experiments were conducted (i.e., room temperature vs. body temperature), ex vivo instead of in vivo, etc.

Finally, the strain rate evaluation was based on one representative ILT sample. A larger number of specimens should have been tested and the lowest strain rate calculated from all of those would be more appropriate. However, we were conservative and used the lowest value calculated for the specimen tested.

4.0 CONSTITUTIVE MODEL DEVELOPMENT FOR ILT

4.1 Introduction

A constitutive model is a mathematical characterization of a material's intrinsic relationship between force and deformation (or stress and strain), and along with appropriate governing equations, can describe the mechanical behavior of the material under specific conditions. It is unreasonable to expect that any constitutive relationship will adequately describe all behavior of a material under all conditions. It was with this in mind, we carefully designed our uniaxial tensile testing experiments in Chapter 3 to extract the static, uniaxial elastic response of ILT. In this chapter, basic mechanical principles and methods are used to model the uniaxial tensile testing data obtained in Chapter 3. First, the general principles of mechanics are introduced, then those are applied to our uniaxial tensile testing data to obtain a specific constitutive equation to mathematically describe the uniaxial tensile behavior of ILT.

4.1.1 Need for a More Suitable Model for ILT

In the field of soft tissue modeling, the most common malpractice is what Fung [79] pointed out:

> *" The main difficulty (of modeling soft tissue) lies in the customary use of the infinitesimal theory of elasticity to media which normally exhibit finite deformation."*

Although Fung wrote this nearly 35 years ago, the inappropriate use of infinitesimal elasticity has continued, including in the case of AAA mechanics. According to da Silva et al. [80], the diameter of the AAA changes dramatically from its load-free configuration to diastolic pressure. A previous study by our group using in-vivo ultrasound measurements indicated that the diameter of the lumen through ILT in AAA varies by ~ 8% over the cardiac cycle (i.e., from diastole to systole). [59] It stands to reason, therefore, that the ILT undergoes well over 10% strain from its load-free configuration. Clearly, *ILT can not be modeled as a linearly elastic material* based on infinitesimal deformation theory. Nonetheless, several previous finite element simulations of AAA have evaluated the effect of ILT on AAA wall stress [55-57] using such a model. No previous model that included ILT into finite element stress simulations of AAA utilized a nonlinearly elastic material model. Just as using a large strain hyperelastic model for the AAA wall provided a significantly different (and likely more accurate) wall stress distribution than a linearly elastic model, [81] a more accurate model for ILT would likely result in the same.

In addition to being a nonlinearly elastic material undergoing large deformation, and as discussed in detail in Chapter 2, ILT can be treated as incompressible, heterogeneous, and isotropic. Therefore, any constitutive model developed for ILT will need to take into account these features.

4.2 Methods

4.2.1 Constitutive Model Development

For the uniaxial tensile testing, the specimen is extended along one axis (say x_1) while being allowed to freely deform in the other (e.g., x_2 and x_3) directions. The displacement field for such a deformation is given by,

$$\begin{aligned} x_1 &= \lambda_1 X_1 \\ x_2 &= \lambda_2 X_2 \\ x_3 &= \lambda_3 X_3 \end{aligned} \tag{4.1}$$

where λ_1 is defined as the ratio of the deformed length of ILT specimen (L) to the original length (under zero force state) L_0 ,

$$\lambda_1 = \frac{L}{L_0} \tag{4.2}$$

The other two λ_I's are defined in a similar manner. The deformation gradient **F** for this case is then given by,

$$F = \frac{\partial x}{\partial X} = \begin{pmatrix} \lambda_1 & 0 & 0 \\ 0 & \lambda_2 & 0 \\ 0 & 0 & \lambda_3 \end{pmatrix} \tag{4.3}$$

Since the material is incompressible,

$$\det[F] = \lambda_1\lambda_2\lambda_3 = 1 \tag{4.4}$$

Because the material is isotropic, the "2" and "3" directions must incur the same amount of strain, i.e., $\lambda_2 = \lambda_3$. Combined with equation 4.4, this requires that

$$\lambda_2 = \lambda_3 = \frac{1}{\sqrt{\lambda_1}} \tag{4.5}$$

The left Cauchy-Green deformation tensor, ***B***, is then given as:

$$B = FF^T = \begin{pmatrix} \lambda_1^2 & 0 & 0 \\ 0 & \frac{1}{\lambda_1} & 0 \\ 0 & 0 & \frac{1}{\lambda_1} \end{pmatrix} \tag{4.6}$$

To simplify the notation, we drop the subscript convention and allow $\lambda_1 = \lambda$. Then

$$B^{-1} = \begin{pmatrix} \frac{1}{\lambda^2} & 0 & 0 \\ 0 & \lambda & 0 \\ 0 & 0 & \lambda \end{pmatrix} \tag{4.7}$$

The first and second invariant are given by

$$I_1 = \lambda^2 + \frac{2}{\lambda} \tag{4.8a}$$

$$I_2 = 2\lambda + \frac{1}{\lambda^2} \tag{4.8b}$$

Since the tissue is under uniaxial tension, by definition the Cauchy stress tensor is given by

$$T = \begin{pmatrix} \sigma & 0 & 0 \\ 0 & 0 & 0 \\ 0 & 0 & 0 \end{pmatrix} \tag{4.9}$$

where σ is the normal Cauchy stress in the "1" direction.

Hyperelasticity theory states that for any solid there exists a strain energy function W which depends only on the deformation. The general strain energy function form for an isotropic, incompressible, hyperelastic material can be written as [82]

$$W = W[I_B , II_B] \tag{4.10}$$

where I_B and II_B are the first and second invariants of the left Cauchy-Green deformation gradient tensor $\boldsymbol{B}$. For a hyperelastic, incompressible, and isotropic material, the constitutive equation can be expressed as[83]

$$T = -pI + 2W_1 B - 2W_2 B^{-1} \tag{4.11}$$

where T is the Cauchy stress tensor, and W_1 and W_2 are defined as:

$$W_1 = \frac{\partial W}{\partial I_1} \qquad W_2 = \frac{\partial W}{\partial I_2} \tag{4.12}$$

The goal is to determine a specific functional form of W for ILT. Applying this functional form of W to equation 4.11 will then yield the constitutive equation for ILT.

The general form of W in equation 4.10 may be expressed as a Taylor series expansion as:

$$W = \sum_{i+j=1}^{N} c_{ij}(I_1 - 3)^i (I_2 - 3)^j \qquad (4.13)$$
$$= c_{10}(I_1 - 3) + c_{01}(I_2 - 3) + c_{11}(I_1 - 3)(I_2 - 3) + c_{02}(I_1 - 3)^2 + c_{20}(I_2 - 3)^2 + ..$$

where the c_{ij} are material parameters. The expansion is in terms $(I_1 - 3)$ and $(I_2 - 3)$ because at zero strain, $W = 0$ while $I_1 = 3$ and $I_2 = 3$. The search for the specific form of W involves finding which combination of the terms in equation 4.13 fits the experimental data best; i.e., whether W depends on both invariants, or whether the dependence is linear or nonlinear based on our uniaxial tensile testing data.

For a nonlinear material, uniqueness of the specific functional form is unlikely. In fact, given a sufficient number of material parameters, almost any functional form will fit the experimental data. However, we have to keep in mind that the purpose of determining the functional form of W in the current work is for computational stress analysis. More complex functional forms will lead to exponentially increasing computational times, sometimes to a point where it is impossible to implement the calculation. Therefore, besides having the criteria for a good fit to the experimental data, the process of identifying a specific functional form of W should also yield a model with as few parameters as possible. In general, the fewer the material parameters, the more desirable and physically meaningful the model. For example, the simplest W for rubber is the neo-Hookean strain energy function; i.e., $W = c_{10}(I_1 - 3)$. To find the specific

functional form of W for ILT, one approach is to start with the simplest form, and then add additional terms until the corresponding constitutive equation fits the experimental data sufficiently. In the present work, instead of using such a "trial and error" method, a similar approach to that used by Humphrey and Yin [84] for modeling passive cardiac tissue was employed. First, the strain energy function for ILT was assumed to be a function of either I_1 or I_2, alone; i.e.,

$$W = a_1(I_1 - 3) + a_2(I_1 - 3)^2 + a_3(I_1 - 3)^3 + \ldots \tag{4.14a}$$

$$W = c_1(I_2 - 3) + c_2(I_2 - 3)^2 + c_3(I_2 - 3)^3 + \ldots \tag{4.14b}$$

If we assume that $W = W(I_2)$, equation 4.11 is written as:

$$T = -pI - 2W_2 B^{-1} \tag{4.15}$$

For the uniaxial tension case, Equations 4.7 and 4.9 may be substituted into Equation 4.15 to yield

$$\sigma = -p - 2\frac{W_2}{\lambda^2} \tag{4.16a}$$

$$0 = -p - 2W_2\lambda \tag{4.16b}$$

From Equation 4.16b, we find that $p = -2W_2\lambda$, substiuting this into equation 4.16a and solving for W_2, we then find

$$W_2 = \frac{dW}{dI_2} = \frac{\sigma}{2(\lambda - \frac{1}{\lambda^2})} \tag{4.17}$$

Equation 4.17 and 4.8b were used to convert our experimental σ-λ data obtained in Chapter 3 to W_2 - (I_2-3) data**. Figure 13** shows a plot of the data and corresponding linear fit for a representative ILT specimen. Since the data has a linear fit, the first and the second terms of Equation 4.14b would be appropriate for this material if $W = W(I_2)$.

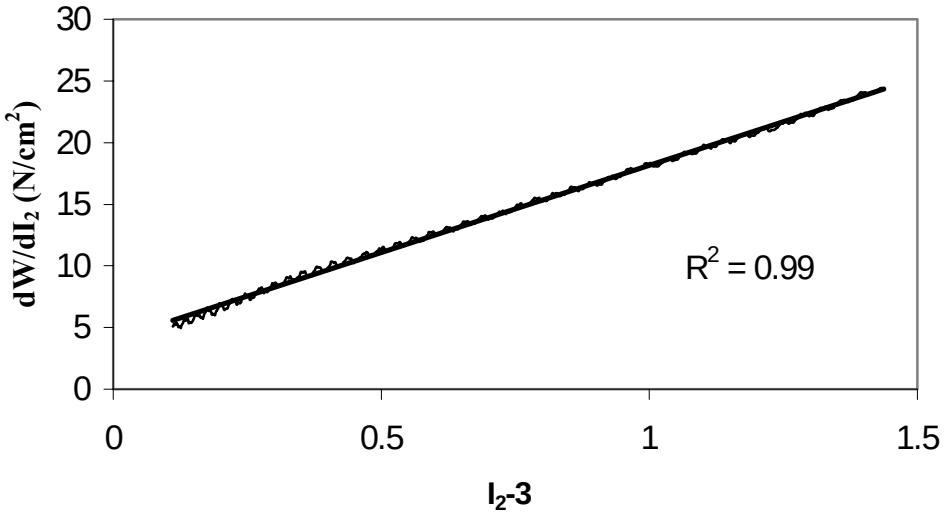

Figure 13 The W_2 - I_2 relationship for a representative ILT specimen. The high R^2 value of the regression suggests a linear relationship.

If we assume that $W = W(I_1)$, equation 4.11 is written as:

$$T = -pI + 2W_1 B \tag{4.18}$$

For the uniaxial tension case, Equations 4.6 and 4.9 may be substituted into Equation 4.18 to yield :

$$\sigma = -p + 2W_1\lambda^2 \tag{4.19a}$$

$$0 = -p + 2\frac{W_1}{\lambda} \tag{4.19b}$$

From Equation 4.19a, we find that $p = 2W_1/\lambda$. Substituting this into Equation 4.19a and solving for W_1, we then find:

$$W_1 = \frac{dW}{dI_1} = \frac{\sigma}{2\left(\lambda^2 - \frac{1}{\lambda}\right)} \tag{4.20}$$

Equation 4.20 and 4.8a were used to convert our experimental σ-λ data obtained in Chapter 3 to W_1 - (I_1-3) data. **Figure 14** shows a plot of the data and corresponding linear

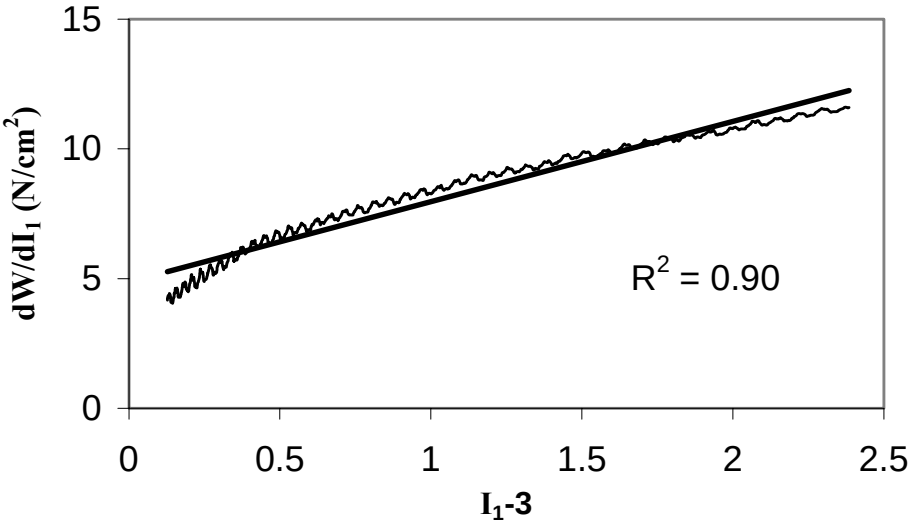

Figure 14 The W_1 - (I_1-3) relationship from the same specimen as in Figure 13.

model fit for the same specimen as in **Figure 13**. Since this data clearly does not demonstrate a linear relationship, as determined both by visual inspection and linear regression, either W is a higher order function of I_1 alone, or W is a function of I_1 and I_2. For the purpose of this work, for simplicity, we chose W to be a second order function of $(I_2\text{-}3)$. For this, we may write,

$$\frac{dW}{dI_2} = c_1 + c_2(I_2 - 3) \tag{4.21a}$$

$$W = c_1(I_2 - 3) + c_2(I_2 - 3)^2 \tag{4.21b}$$

where c_1 and c_2 are two model parameters that describe the mechanical behavior of ILT. Rearranging equation 4.17 gives,

$$\sigma = 2\frac{dW}{dI_2}\left(\lambda - \frac{1}{\lambda^2}\right) \tag{4.22}$$

Finally, substituting equations 4.21a and 4.8b into equation 4.22, we obtain the stress-stretch relationship for ILT under uniaxial tension:

$$\sigma = 2\left[c_1 + c_2\left(2\lambda + \frac{1}{\lambda^2} - 3\right)\right]\left(\lambda - \frac{1}{\lambda^2}\right) \tag{4.23}$$

Equation 4.23 may then be used along with our tensile testing data from Chapter 3 to evaluate the constitutive properties for ILT, c_1 and c_2, as described below.

4.2.2 Material Parameter Evaluation

Nonlinear regression of our uniaxial tensile testing data (i.e., the σ-λ data collected in Chapter 3) against Equation 4.23 allowed determination of c_1 and c_2. This regression was performed two ways. First, we performed the regression separately on all 50 sets of σ-λ data obtained from individual specimens. Secondly, we performed the regression once on all combined σ-λ data (i.e., for all 50 specimens) from each group to get "group" material constants, which represent a more generalized estimate of ILT mechanical properties. The statistical software package, STATISTICA (v.*4.5*, Statsoft Inc., Tulsa, OK) was used for the Quasi-Newton nonlinear regression and all statistical analyses. Comparison of the best-fit estimates for c_1 and c_2 between groups from different regions was performed by one way ANOVA. Both the Student t-test and the Wilcoxon paired test were used to compare the material parameters between different orientations. Statistical significance was assumed for $p < 0.05$.

4.3 Results

Regression analyses on all 50 data sets from Chapter 3 reached convergence. The final best-fit parameters were independent of the starting value input and had an average standard error of approximately 0.05% of the estimated value. In all cases, the model fit the experimental data very well ($R^2 > 0.98$). **Figure 15** shows the fit of the model to a single specimen's tensile testing data. **Figure 16** shows the group data (mean $\pm$ SEM) and the group fit for the luminal layer. **Table 5** shows both the mean values of the best fit material parameters c_1 and c_2 for each

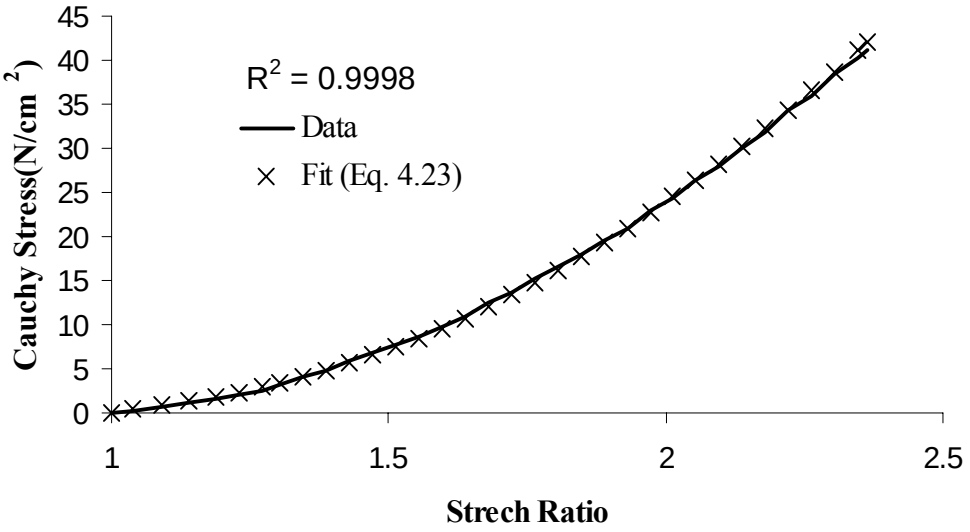

Figure 15 Uniaxial tensile testing data for one representative ILT specimen from the luminal layer and fit to the constitutive model given by equation 4.23.

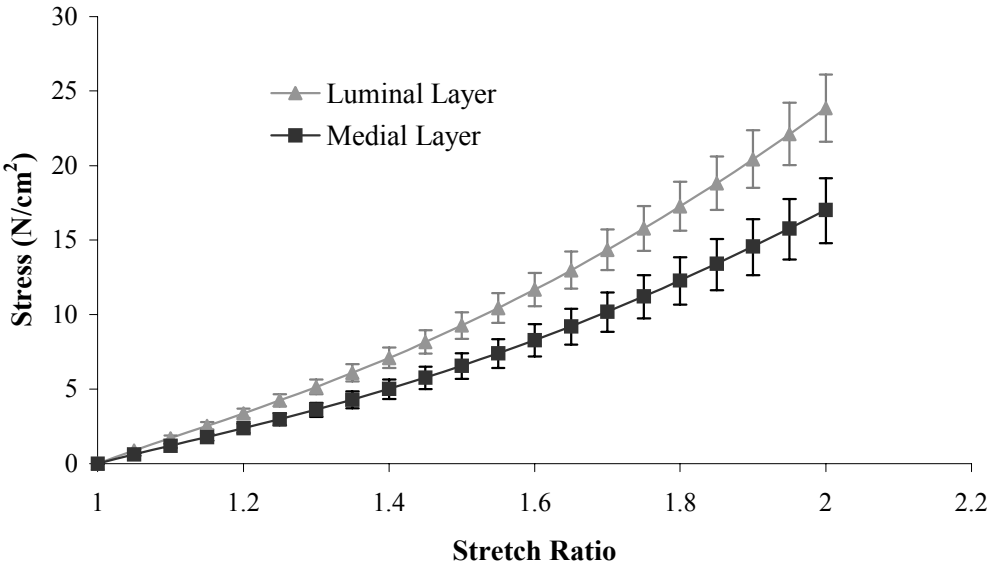

Figure 16 Group data (mean ± SE) from the luminal and medial layers along with fit to the constitutive model given by equation 4.23.

location and orientation group, and also the single best fit values for each group with the data combined into a single data set.

Both the Student t-test and the Wilcoxon paired test (for the 7 paired sets of specimens) showed that there is no significant difference in c_1 and c_2 between longitudinally and circumferentially-oriented specimens from either the medial layer or the luminal layer. However, ANOVA tests did indicate that both c_1 and c_2 were significantly greater for specimens from the luminal layer compared to their like-oriented counterparts from the medial layer.

Table 5 Material constants derived from Eq. (4.23) for both methods of regression, average of all individual fits (presented as mean ± SEM) and group fits.

Region	Orientation	c_1 (N/cm^2)		c_2 (N/cm^2)	
		Average	Group	Average	Group
Luminal Layer	Longitudinal (n=14)	2.89 ± 0.39	3.12	3.10 ± 0.45	3.39
	Circumferential (n=14)	3.19 ± 0.45	3.62	2.93 ± 0.36	3.55
Medial Layer	Longitudinal (n=11)	2.06 ± 0.33	2.77	1.77 ± 0.28	2.11
	Circumferential (n=11)	2.21 ± 0.48	1.8	2.57 ± 0.43	2.38

4.4 Discussion

As stated in Section 4.1.1, ILT does experience large deformation in-vivo. [59] Therefore, ILT is materially nonlinear as indicated by the uniaxial testing results in **Figure 12**. Previous work on biomechanical modeling of ILT was done by Di Martino et al. [56] based on the infinitesimal theory of deformation. In their work, a simple Hookean, linearly elastic model was used to fit the data obtained from tensile testing of ILT and obtain the Young's modulus, which is not appropriate for ILT biomechanics. We believe that the nonlinear hyperelastic model developed here will provide a more accurate prediction of the biomechanical behavior of ILT and, therefore, more accurate AAA wall stress estimates.

The mechanical behavior and material properties of longitudinally- and circumferentially-oriented ILT specimens do not appear to be different (**Table 5**). Though biaxial testing would be necessary to confirm this, these results suggest that ILT is an isotropic material. Comparing the mechanical behavior and properties of ILT from luminal vs. medial layers suggests that this material is not homogeneous (**Table 5**). This finding is consistent with our observation of the structure of ILT (**Fig. 4).** The luminal region appears more structurally stable than the medial layer, and this is reflected in their mechanical properties.

4.5 Limitations

As with all constitutive models, there are certain assumptions and limitations that should be kept in mind. Again, this two-parameter hyperelastic model for ILT only applies to the static tensile loading conditions. Any application besides such conditions should be treated with

caution. The assumption that ILT is isotropic when deriving our constitutive model should be evaluated by more rigorous biaxial tensile testing. Nevertheless, preliminary findings reported in Chapter 2 showed that the microstructure (Section 2.3.3.1) and biomechanical behavior (Section 2.3.3.2) are consisted with an isotropic material. Moreover, the uniaxial biomechanical properties reported in **Table 5** of this chapter also support this assumption. As we showed in Chapter 3 and the current chapter, ILT differs not only from and patient to patient, but also from region to region. However, a thin layer of ILT may be more homogenous than a thick layer. Finally, the constitutive parameters determined here are for the luminal and medial layers only. As discussed in Chapter 3, because of its degenerative nature, the abluminal layer of ILT could not be tested. Therefore, data was not available from which to determine the constitutive properties for that layer. The small number of samples used for this study is also a limitation. More data are needed to establish the variation of the biomechanical behavior of ILT within the general AAA population. The use of data from uniaxial tensile tests to develop the three dimensional functional form of the strain energy density functional form of the strain energy density function and to estimate the parameters may be another limitation. All of these limitations should be kept in mind when one use the results obtained in this chapter.

4.6 Conclusion

Characterizing a suitable constitutive model for ILT is a step toward developing a method that would allow accurate estimation of wall stress in intact AAA. The model we provide here contains only two material parameters and can be easily incorporated in common, commercially available finite element software packages (e.g., ANSYS, ABAQUS, etc.). This

will allow more accurate estimation of the in-vivo AAA wall stress distribution, and in turn may enable clinicians to evaluate more precisely the severity of individual AAA rather than using generalized criteria such as maximum AAA diameter.

5.0 3D RECONSTRUCTION OF AAA GEOMETRY WITH ILT

5.1 Introduction

5.1.1 Motivation/Purpose

As shown in **Figure 17,** the actual geometry of AAA is quite irregular. It is primarily this "irregularity" that gives rise to the unique stress distribution pattern in each AAA. However, the actual geometry of individual AAA is too complex to be reliably approximated with simple analytical representations. Earlier computational investigations on wall stress in hypothetical, idealized AAAs have failed to predict wall stress accurately. This leads to the conclusion that using the actual geometry in evaluating wall stress distribution is necessary. [49-52, 55]

Our group developed and demonstrated a noninvasive methodology to estimate AAA wall stress distribution based on 3D reconstructed AAA geometry from patient's CT images. [81, 85] The results showed a great improvement in the accuracy of wall stress evaluation compared to earlier studies. However, the presence of ILT was not included in that study. Therefore, the goal of this work was to improve our existing technique to reconstruct real AAA geometry including ILT. In this chapter, a modified procedure is described to include ILT into the "virtual" 3D model of a patient specific AAA.

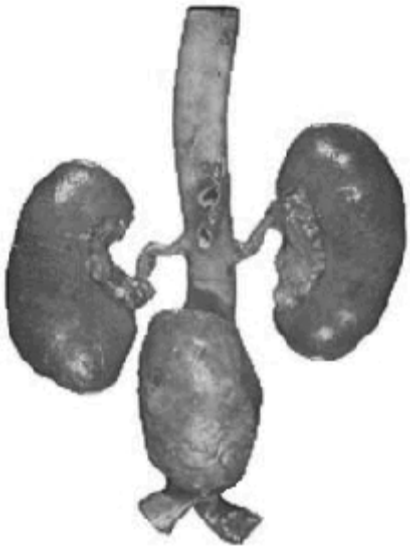

Figure 17 An excised AAA from an autopsy sample (htttp://www.vascularsurgery.com).

5.1.2 Previous Work/Background on 3D Reconstruction of AAA

AAAs are typically viewed by ultrasound, or computed tomography (CT), as such diagnostic imaging is often desired before preoperative evaluation. 3D reconstructed AAA models have been used for more complete visualization of the AAA (see the following web sites: http://everest.radiology.uiowa.edu/nlm/aaa/; http://www.engineering.uiowa.edu/~raghavan/; http://www.pitt.edu/~vorp/) [81, 85-87], for planning of endovascular repair procedure (see the following web site: http://www.medicalmedia.com) [88-92] and to study the biomechanical stresses acting on the aneurysm wall. [85, 93-97] Investigators at Stanford University described their initial efforts to create computational solutions for three-dimensional (3-D) pulsatile blood flow in a model of the entire aorta, including AAAs. [98] They have also developed computational methods to quantify blood flow and vessel wall mechanical behavior of normal

human thoracoabdominal aortas and aneurysmal abdominal aortas using 3D reconstruction techniques. [97, 99] Our group and other groups have developed a 3D reconstruction technique for AAA using CT data and mathematical techniques.[81, 85] With the advent of endovascular surgery, imaging and 3D reconstruction techniques are changing rapidly. Leotta et al. developed a 3-D AAA reconstruction technique from ultrasound images. [100] Recently, magnetic resonance imaging (MRI) including magnetic resonance angiography (MRA) techniques have also been used to view the reconstructed AAA before surgery and after endovascular repair. [101, 102] In spite of the different imaging techniques, the 3D AAA surface reconstruction were all generated in a manner similar to our technique described below; i.e., by assembling a sequence of 2D outlines traced on individual 2D cross-sectional images which are registered in 3D space.

5.2 Methods

Physicians have been using information from medical imaging to study, diagnose and plan treatment for illness involving internal organs for many years. For AAA patients, the computed tomography (CT) has become the imaging modality of choice. Therefore, our 3D reconstruction technique is based on CT images. In this section, the methods describing the imaging, image analysis, 3D reconstruction and solid modeling are presented. The procedure is similar to the one described by Raghavan et al. [53] but modified to include the ILT and patient-specific wall thickness.

5.2.1 Imaging Protocol

Since four of the patients studied by Raghavan et al. [53] were reanalyzed in this work, the reader is referred to this previous dissertation for full detail on the imaging protocol. In short, consenting patients with AAA who were scheduled for routine CT exam were taken to the Abdominal Imaging Center at the University of Pittsburgh Medical Center and scanned using a General Electric spiral CT scanner (Model 9800, high-speed advantage ^{TM}). Prior to scanning, 120 ml of standard nonionic contrast agent was administrated at 4 ml/sec to the patient to enhance image quality. To avoid artifact due to AAA motion, subjects were asked to hold their breath during the period of the scan, which was approximately 30 seconds. Cross sectional images from the suprarenal abdominal aorta to the external iliac arteries with collimation (slice interval) of 3 mm and helical pitch of 1.5:1 were obtained. Three readings of "arm cuff" blood pressure were obtained immediately before and immediately after the imaging procedure. The six measurements were averaged to yield a single blood pressure (systolic, diastolic and mean) for each patient. This information was used as described in Section 6.3 to determine the loading condition of each AAA.

5.2.2 Image Processing

The goal of image processing was to isolate and extract the two-dimensional boundary of the AAA wall and the lumen from each cross-sectional image of an AAA patient. This process is often referred as "segmentation". **Figure 18** shows a sample cross-sectional image. The area of interest is inside the square area. The bright region in the middle of the area of interest is the

blood and contrast-filled lumen, while the wall is appears as the bright circular structure around the lumen. The dark area between the lumen and the wall is ILT.

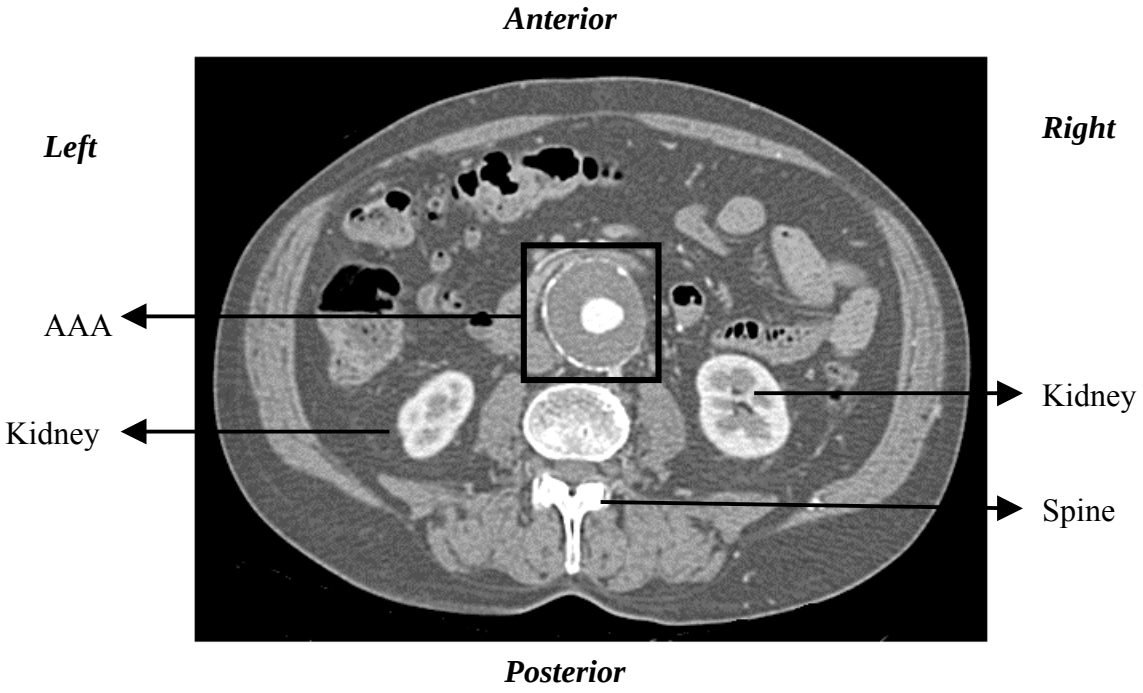

Figure 18 A sample cross-sectional CT image of a representative subject with AAA. See text for detail.

Each cross-sectional CT image was created with a 512 x 512 pixel resolution and stored in DICOM format on a console in Division of Radiology Informatics, Department of Radiology, University of Pittsburgh Medical Center. A typical AAA required 40 to 70 image slices to span its entire length. Image sets of each patient were uploaded to a network workstation, then transferred via the Internet to a PC in the Computational Vascular Biomechanics Lab for further

processing. Each image was tagged with a header file that includes patient and image information. **Figure 19** shows a sample of such a header file, which is actually specific to the image shown in **Figure 18.** Since CT scan images displayed on a computer screen are represented by a collection of pixels, it is necessary to know a pixel-to-mm conversion factor in order to translate it into real dimensions. This factor is included on each header file for each image. For the image represented by **Figure 18** and the header file of **Figure 19**, the conversion factor is 0.765625 mm per pixel.

Segmentation of each individual CT slice was done using the software Scion Image (Version 4.0.1, 1998 Scion Corporation, Frederick, Maryland). **Figure 20** shows an example of the process. Different anatomic components shown have distinct densities and appear with a corresponding grayscale (or brightness) in the CT image. Since a contrast medium was injected into the blood flow, the lumen typically had a very high grayscale, often in the range of 225 – 255. Making use of the contrast difference, the boundary of the lumen was extracted with aid from an automatic procedure called "grayscale thresholding" which displays only the objects in the image that have a selected range of grayscale (**Figure 20 B**). After the lumenal boundary was identified and isolated, the X-Y coordinates of 60-100 discrete points on the boundary were exported to an ASCII file with a numerical extension designating the Z location of the slice. The Z value for the first image, just distal from the most distal renal artery was taken as Z = 0. The Z value for each subsequent slice was determined by the "Slice Thickness" value listed in the header file for the prior image (see **Figure 19**, units in mm). Extraction of the inner AAA wall boundary was performed in a similar manner as that for the lumen. However, a closed boundary often could not be automatically extracted from the images after thresholding because of a failure of the grayscale thresholding to distinguish this surface at all points (**Figure 20B**). In these

instances, a closed boundary was drawn manually to delineate the inner wall boundary (**Figure 21A**).

Figure 19 An example of the header file attached to each DICOM image. This particular example is specific to the image in Figure 18.

```
Study Date:  20001120
Study Time:  164333.000000
Modality:  CT
Study Description:  ABDOMEN W/WO
Series Description:
Operator's Name:  LC

Patient's Name:  XXXXXXXX
Patient ID:  *********
Additional Patient History:  AAA

Contrast/Bolus Agent:  150 CC CONRAY
Slice Thickness:  3.000000

Study ID:  33881
Series Number:  3
Acquisition Number:  1
Image Number:  29

Rows:  2621952
Columns:  2621952
Pixel Spacing:  0.765625\0.765625
Bits Allocated:  2621456

     file
'D:1.2.124.113532.128.147.145.11.20001120.174227.1270974.dc
m'
min= -2000, max= 2464
```

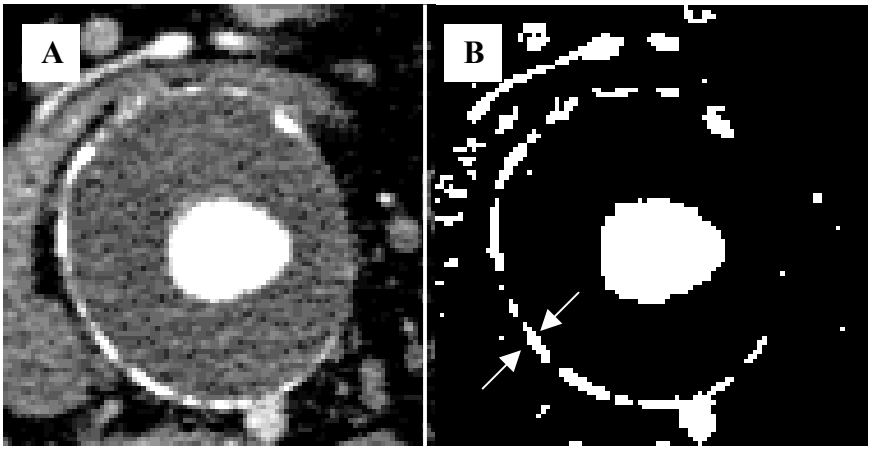

Figure 20 Example of segmentation of the AAA wall and lumenal boundaries from CT scan images. A) The original CT image; B) the image after gray scale thresholding (the arrows indicate the locations of measured wall thickness for this particular slice).

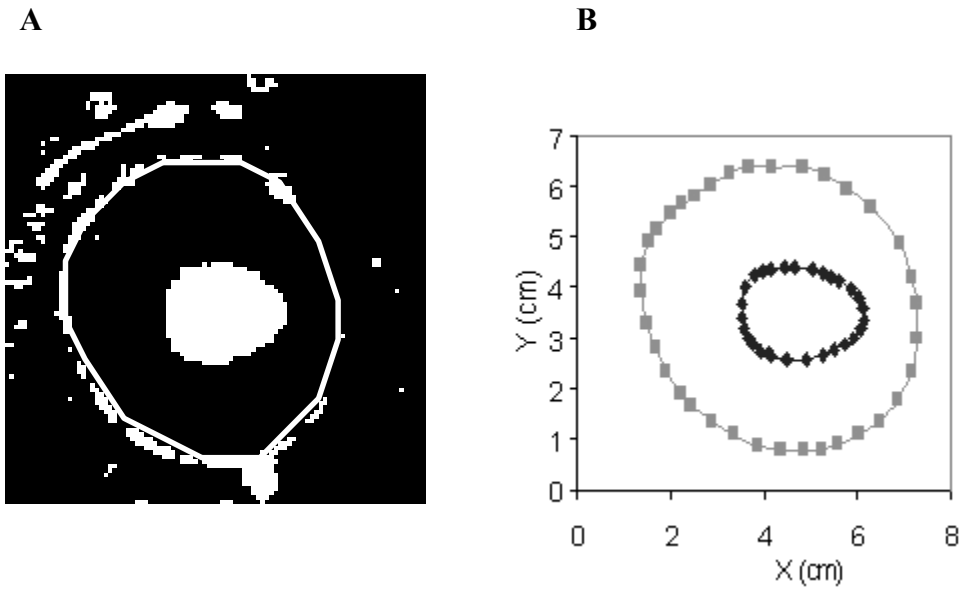

Figure 21 Example of manual assistance with boundary detection. A). Manually drawn inner wall boundary. B). Cartesian coordinate output of the two boundaries.

Figure 21 B shows the output of X-Y data points which describe the outlines of our example inner wall and lumen. Ideally, one would measure the wall thickness at each location around the perimeter. However, it was found to be very difficult to differentiate the boundary of the inner and the outer AAA walls on the CT images. Therefore, an alternative approach was taken as follows. Three total wall thickness measurements were made on three different image slices in regions were the wall was clearly defined from the surrounding tissues, see **Figure 20 B**. The wall thickness for a particular AAA was taken as the average of these three measurements.

5.2.3 2D Smoothing, Local ILT Thickness, and Local Diameter Calculation

Notice that the rough outlines represented by the coordinate points in Figure **20B** do not resemble the smooth outlines shown for the CT image in Figure 19. A smoothing procedure was therefore necessary to remove this artificial roughness. The "raw" boundary point data were imported to a custom Mathematica (v. 3.0 Wolfram research, Inc. Champaign, IL) program adapted from that written by Raghavan [53] for 2D smoothing in order to eliminate the "noise" generated during digitization. In brief, the centroid of the wall outline was determined by averaging the X-Y coordinates for all points. With this point as the center, the program first converts the "raw" inner wall data and lumenal surface data to cylindrical coordinate (r-θ) data, then linearly interpolates the radial (r) coordinate at equal intervals of θ. The r-θ data was converted back to a new set of X-Y data to produce a smoothed set of 2D data points representing the inner wall and lumenal surface for each image "slice" of AAA. The Mathematica code that was used for this purpose can be found in **APPENDIX A**.

As described in Chapter 9, it is necessary to evaluate the local ILT thickness and local AAA wall diameter for the purpose of AAA wall strength determination. The thickness of ILT at a given value of θ on a particular slice was taken as the difference between the value of r interpolated as described above for the wall outline and r for the luminal surface outline at that value of θ. The local diameter of AAA for a given slice was taken as twice the average of all values of r of the inner wall outline.

5.2.4 3D Smoothing

The smoothed X-Y data points of the inner wall and their corresponding Z locations were combined to create one complete, 3D set of X-Y-Z data. This data set represented the location of a finite number of discrete points lying on the inner surface of the AAA wall and took the form of a "point cloud". Similarly, a point cloud was also produced for the lumenal surface. **Figure 22A** shows these two point clouds for a single representative AAA with ILT.

Since the discrete 3D data points in the point clouds were not a mathematical representation of the surfaces themselves, the points were imported to a public domain software NUAGES (v4.1, INRIA, Sophia Antipolis Cedex, France) for 3-D surface reconstruction. In this "triangularization" procedure, the points were connected into finite numbers of triangles, which were then connected to form the 3D surfaces shown in **Figure 22 B**. Rendering of this surface shows rough edges (**Figure 22 B**) which does not represent the natural (in-vivo) AAA surface such as that shown in **Figure 17**. Therefore, a validated surface smoothing technique - the biquintic finite element (BQFE) technique developed by Smith et al. [103] - was used to smooth both the AAA wall and lumenal surfaces (**Figure 22C**). Full detail of the BQFE technique may be found in Smith et al. [103]

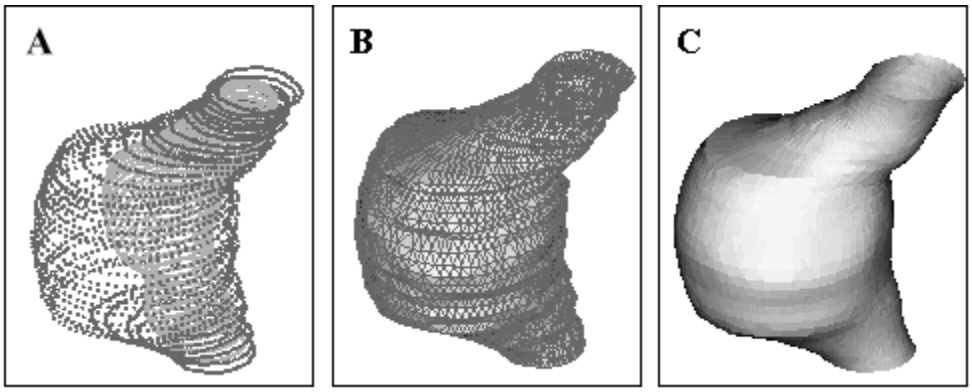

Figure 22 The point clouds for both the inner AAA wall and lumen assembled from the smoothed data from a series of CT scan images (A). A "triangulation" routine connects the points into triangles to form the preliminary 3D surfaces (B). This rough surface is smoothed to yield the "virtual AAA" (C).

5.2.5 Solid Modeling – "Virtual AAA"

The smoothed lumenal and inner wall surfaces described above were used for creation of the final 3D "virtual AAA" model including ILT as follows. Both the smoothed AAA inner wall and lumenal surfaces were converted back into point cloud representation and input to the solid modeling software Pro-Engineer (Release 2.0, Parametric Technology Corporation, San Jose, CA) for 3D solid reconstruction. First, a solid was constructed using the smoothed inner wall surface. This solid was then "cut" by another solid constructed using the luminal surface. The

space formed between the luminal and inner wall surfaces was the volume representing the solid mass of ILT. The thickness of the AAA wall was then created by extruding the inner wall outwardly to the wall thickness measured for each AAA as described in Section 5.2.2. A uniform wall thickness was assumed for each AAA. The complete 3-D reconstructed geometry of AAA (**Figure 23)** was exported to the meshing software PATRAN (MSC/PATRAN Version 9.0, MSC Software Corporation, Los Angels, CA) for finite element preprocessing as described in Chapter 6.

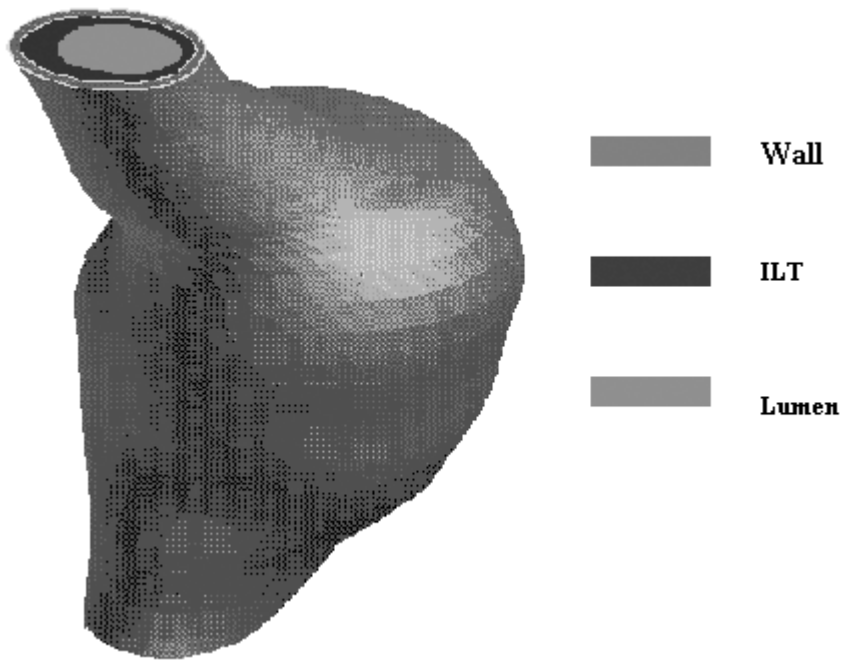

Figure 23 The "Virtual AAA" with a constant, patient specific wall thickness and included ILT.

5.2.6 Geometric Characterization of AAA

For each reconstructed AAA, four geometric parameters were measured: total AAA volume, total ILT volume, the total AAA surface area (i.e., of the inner AAA wall), and the lumenal surface area. The total volume of AAA was calculated in PATRAN as the volume contained within the 3D reconstructed inner wall surface. The volume of ILT was also calculated using PATRAN as the volume contained between the 3D reconstructed inner AAA wall and the 3D reconstructed lumen. The ILT volume ratio was defined as the ILT volume divided by the total AAA volume. Similarly, the surface area of the inner AAA wall and lumenal surfaces were also calculated using PATRAN and taken as total AAA surface. The ILT surface area ratio was defined as the ILT surface area divided by the total AAA surface area.

5.3 Results

Four different AAA were reconstructed. Each of these AAA were studied previously, ignoring the ILT. [63] Three of the patients were male and one was female. Their age ranged from 73 to 86, and the maximum AAA diameter ranged from 6.0 cm to 6.4 cm (**Table 6**). The reconstructed "virtual" AAA including ILT is shown for each subject in **Figure 24**. Note that each geometry is quite irregular and different from patient to patient. The ILT in AAA #1 covered only the lower half of the aneurysm, whereas AAA #2 and AAA #4 were fully covered by ILT. AAA #3 had a very small amount of ILT that covered only a part of the upper half of the aneurysm. The geometric features of AAA and contained ILT varied widely among selected subjects and are given in **Table 7**.

Table 6 Information on subjects whose AAA were reconstructed and subsequently analyzed in this study.

Patient	Gender	Age	Systolic Pressure* (mmHg)	AAA Diameter (cm)	Wall Thickness* (mm)
1	M	85	120 (115, 120, 125, 120, 116, 124)	6.0	1.95 (1.95, 1.92, 1.98)
2	M	86	128 (123, 128, 125, 132, 130, 130)	6.1	1.84 (1.93, 1.72, 1.87)
3	F	74	155 (150, 155, 160, 150, 165, 150)	6.4	1.75 (1.80, 1.83, 1.62)
4	M	73	128 (130, 125, 128, 135, 120, 130)	6.4	1.86 (1.82, 1.84, 1.90)

* Systolic pressure and wall thickness values were given as mean followed parenthetically by individual measurements.

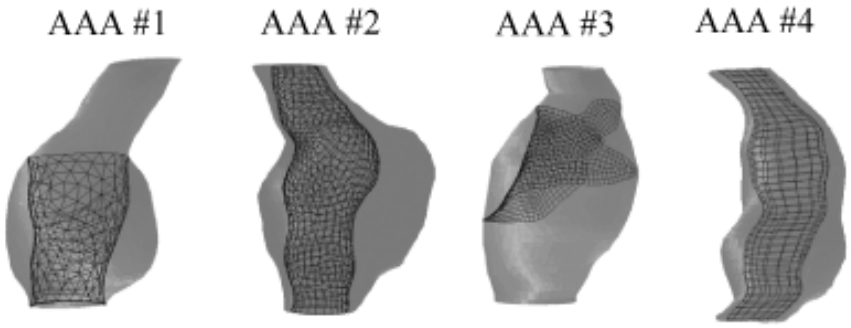

Figure 24 Four reconstructed virtual AAA models. The lumen through the ILT is indicated by the black mesh, so that the material between the mesh and AAA wall is ILT.

Table 7 Geometric features of the four AAA and contained ILT.

AAA#	Length (cm)	Wall Surface (cm^2)	AAA Volume (cm^3)	ILT Surface Ratio	ILT Volume Ratio
1	14.0	144	142	0.41	0.47
2	8.8	150	156	0.54	0.66
3	9.2	168	209	0.29	0.12
4	15.0	241	266	0.72	0.49

5.4 Discussion

Using the techniques described in this chapter, for the first time, we were able to reconstruct a real 3D AAA geometry including ILT in a noninvasive and patient specific manner. This will facilitate investigation of hypothesis #1 that states that the inclusion of ILT will greatly improve the accuracy of computational stress analyses of AAA, and therefore improve the accuracy of predicting the rupture potential for individual patients. However, there remain several limitations that should be kept in mind. For example, wall thickness was assumed to be uniform. This is most likely not the case in vivo. The thickness of the wall has a great influence on the stresses within the AAA wall. [47, 63] Future work should address this issue by adopting a different imaging modality that will provide a clear distinction between the inner and outer wall. A second limitation is that the semi-automatic segmentation technique is time consuming and prone to user error. Thirdly, some parts of the AAA wall are calcified but were ignored in the 3D-reconstruction procedure. These calcified plaques have irregular

geometries and distinct mechanical behavior from the wall and ILT. This also should be addressed in future studies.

Additionally, not all AAAs start immediately below the renal arteries or extend all the way to the iliac bifurcation. Indeed, in some patients, the suprarenal aorta and iliac arteries are also dilated and should be included in the 3D reconstruction. For this reason, a more robust definition of the AAA should be adopted in future studies.

During the cardiac cycle, AAA geometry varies due to pulsation of the wall. Therefore, the cross-sectional images of AAA on CT images are not a snapshot at a certain time point, but rather an average over the period of time throughout which the image data was collected. As a result, the reconstructed AAA geometry is not the geometry at one state or instant in time. To improve this, gated imaging is recommended. For example, gated MRI can synchronize with the ECG signal and capture the cross-sectional view of AAA at a particular time in the cardiac cycle; e.g., when the abdominal aorta is at its end-diastolic or end-systolic stages.

Because AAA tissue does not contrast strongly against its background or surrounding tissue, user interface is required for the segmentation process which makes it a laborious task. As a result, user dependent errors are inevitable. On average, it takes about 8 hours for an experienced user to complete the segmentation process. What is needed is a technique that can both accurately and effortlessly segment images. A technique called “adaptive snakes” has been proposed to address this issue and applied on segmentation of the kidney. [104] The feasibility of using that technology for application to AAA segmentation should be included in future studies.

The main drawback of 3D reconstruction from CT images is that 2D texture does not represent 3D features of the CT data set. As a result, the produced images do not accurately reflect the information of the data set. This is illustrated by the rough edges in **Figure 22B**. To

remedy this, a surface smoothing technique (such as the BQFE technique used in the current work) must be used to generate a smoothed, realistic geometry, such as in **Figure 22C**. The parameters in a surface smoothing algorithm control the degree to which the smoothing of a 3D reconstruction occurs. For the BQFE technique used here, the optimal parameter values have been set and validated using phantoms. [53, 103] However, in reality, the smoothing parameters might differ from case to case due to the unique features of each AAA geometry and of each imaging procedure. In addition, most of the current smoothing techniques are unable to handle structures with branches or bifurcation, and therefore can not be used for AAA which extend to iliac arteries, for example. To mitigate this, effort has been devoted to producing 3D geometries directly from the CT data set. [105, 106] One such method uses a 3D deformable surface to segment the CT data set, and only requires human intervention to designate a seed point. [106] An example of the application of this technique for the reconstruction of the lumenal surface of AAA can be found at the following web site: http://www.comp.leeds.ac.uk/comir/research/epsrcAAA/AAA.htm.

Most AAA walls are calcified. [107-109] The presence of calcified plaques would likely affect the wall stress magnitude and distribution [55]. Therefore, they should be included in the reconstructed AAA and this should be addressed in future studies.

Despite the stated limitations, the modifications made to the 3D reconstruction protocol have extended the state-of-art by allowing inclusion of AAA wall thickness and ILT. The latter feature is of course, necessary to address Hypothesis #1.

6.0 BOUNDARY CONDITIONS AND REFERENCE CONFIGURATION

6.1 Introduction

The physical interactions of a body with any surrounding entities or forces form the "*boundary conditions*" of a problem in mechanics. Like all other organs in the body, AAA is not isolated but rather connected to and interacting with its surrounding environment. Since the stress analysis is only based on the reconstructed, isolated AAA geometry as shown in **Figure 24** in Chapter 5. All the interactions of interest will be included in the model in the form of boundary conditions.

For any finite element stress analysis, there are two types of boundary conditions involved: loading conditions and physical constraints. Load-type boundary conditions can be displacement (deformation) or any physical force applied to the body. Constraint-type boundary conditions are typically contacts between the body and its environment, which inhibit the translation or rotation of a certain part of the body.

Boundary conditions depend on the physical environment of the body we are simulating and the aim of the analysis. The physiological environment of AAA is complex and dynamic. As shown in **Figure 1**, AAA is tethered to the renal arteries on its proximal end and iliac arteries on its distal end. On its inside, pulsate blood flow subjects the blood contacting surface to changing pressure and shear force. On the outside, AAA may be in contact with adjacent structures, such as the vertebral column, veins and other surrounding tissue. Ideally, all the interactions would

enter into a stress analysis model in the form of boundary conditions. However, in reality, one would choose boundary conditions based on the physical environment of the body we are simulating and also on the aim of the analysis.

In the finite element method, one starts with an unloaded and undeformed "reference" configuration. Under the applied loading and boundary conditions, the body deforms and reaches a new equilibrium state. During this process, strain is calculated with respect to the unloaded configuration. Therefore the strain is zero when the stress is zero, and vice versa. Thus, identification of the true reference configuration is very important for stress analyses. The 3D reconstructed AAA geometries obtained from CT scan images described in Chapter 5 were not at their load free reference configuration.

In this chapter, we review the assumptions made in choosing the boundary conditions and reference configuration for our finite element analysis.

6.2 Systolic Pressure as Applied Boundary Condition

Throughout a single cardiac cycle, the blood flow conditions within a AAA changes substantially. [94] As a result, the distribution of intraluminal pressure and shear stress changes both spatially and temporally within the AAA. Ideally, one would simulate this via a fluid-structure interaction to obtain a correctly coupled solution. However, this would result in great mathematical complexity and enormous computational times. This would be unacceptable considering the goal of the present study is to move toward a clinically useful tool to predict the rupture potential of AAA. Since the "worse case scenario", or maximum stress distribution in the wall is of more interest to us than the actual variation of stress during the cardiac cycle, and since

Peattie et al. showed that the intraluminal pressure in AAA does not vary spatially by more than 1 mmHg, [94, 110] the systolic pressure was applied to the inside of AAA as a uniform quasi-static pressure boundary condition. Since the blood pressure must be measured noninvasively, cuff pressure was obtained for each patient studied as described in Section 5.2.1. It is noted that the difference between arm-cuff blood pressure measurement and direct invasive measurement within the distal aorta has been found to be insignificant. [59]

6.3 Displacement Constraints

It is speculated that AAA might be under some degree of axial tension due to tethering. However, quantitative information on the "tethering force" is not available. Until this data is available, we take the traditional approach as taken by other researchers [47, 49, 50, 55-57, 63], i.e., fixing both ends of AAA in the longitudinal direction and allowing free expansion along the radial direction.

As indicated by some CT scan images, the vertebral column is located close to the posterior surface of AAA. In some cases, vertebral bodies might actually come into contact with the AAA wall. In fact, one symptom of AAA is back pain, which could be caused by this interaction. However, direct contact of AAA with the vertebral column and other surrounding tissues were neglected in this study. The error introduced by this simplification should be addressed in future investigations.

6.4 Reference Configuration and Residual Stress

Recall from Chapter 5 that the 3D reconstruction procedure from CT images results in a configuration under some degree of load; i.e., aortic pressure. The "CT configuration", therefore, is not load free. Even if the AAA were reconstructed in the absence of blood pressure (say a reconstructed geometry from excised AAA), there may still be some stress within the AAA wall. This kind of stress is referred as *residual stress* found commonly in many soft tissues. As described by Bergel:[111]

> *"When an artery is split open longitudinally it will unroll itself.... This surely indicates some degree of stress even when there is no distending pressure."*

Fung, Vossoughi, Humphrey and their colleagues [72, 112-115] have all contributed to the improved understanding of residual stress in arteries. Humphrey [114] et al. proposed an "inversion" technique to account for the residual stress in arteries. In this approach, a residual stretch ratio was calculated by enforcing equilibrium in the unloaded intact configuration. The calculated residual stretch ratio then was used to convert the unloaded intact configuration into a stress-free configuration. However, one needs to know the existing residual stress in order to use this technique. Currently there is no information on the residual stress or strain in the AAA wall. Therefore, residual wall stress was neglected in the current study. Future studies should determine the degree of residual stress in AAA wall and the degree of errors introduced in wall stress estimations incurred by neglecting it.

One approach to estimate the reference configuration might be to assume that the "CT configuration" corresponds to the configuration of AAA under mean aortic pressure. Applying a negative mean blood pressure to the luminal surface of the CT configuration would yield a geometry that would be similar to the AAA in the load free configuration. However, this

approach is not feasible in practice. First, the application of the negative pressures typically results in instability (element "collapse"), and a non-converging analysis. Second, the pseudo elastic constitutive equations developed both for the AAA wall and the ILT were from the loading curve of these tissues. They would not apply to the "unloading" situation.

Another approach would be to assume that the CT configuration is the load free configuration. This approach has been taken by our group and others to study stress distribution on 3D reconstructed cardiovascular organs. [63, 116] Lacking of a suitable alternative, we took the second approach and assumed that the CT configuration is the load free configuration during stress analyses. The error introduced by this assumption will be estimated in Chapter 7.

6.5 Effect of Shear Stress

Besides providing a pressure load, the flowing blood within AAA will also impart a shear stress to the luminal surface. Some interesting studies have attempted to estimate the shear stress and pressure distribution in AAA. [94, 110, 117, 118] The reported maximum shear stress due to turbulent or non-turbulent flow is between approximately 5×10^{-5} and 40×10^{-5} N/cm^2,[94, 110, 117, 118] which is five to six orders of magnitude lower than the normal wall stresses due to blood pressure (i.e., 10 to 50 N/cm^2). [81] For the purpose of the present study, therefore, the effect of shear stresses on AAA wall stress was neglected.

6.6 Summary

In summary, the boundary conditions used in the present study were the uniform systolic pressure applied to the luminal surface of AAA acting outwardly and the longitudinal displacement constraints at all the points on the proximal and distal edges of the AAA wall. In addition, one point located on the proximal edge of AAA model was fixed in all six degrees of freedom to inhibit free body motion. Both the wall shear stresses acting on the inside and the contact constraints acting on the outside of the AAA were neglected.

7.0 FINITE ELEMENT SIMULATION

7.1 Introduction

The finite element method is the most powerful numerical technique available today for the analysis of complex structural and mechanical systems. In the finite element method, one divides the domain of interest into a finite number of non-overlapping but contiguous domains, called *elements*. Each element is of finite size. Instead of solving the problem for the entire body in one operation, one formulates the equations for each element and combines them into a system of simultaneous equations. This approach reduces a complex problem into a series of tractable small problems. Moreover, the finite element method reduces partial or ordinary differential equations into a system of algebraic equations, which are easier to solve. [119] The finite element method has been used extensively for stress analysis of many different types of structures, including bridges [120], automotive [121] and aerospace components [122], medical devices [123], bone [124] and cardiovascular structures [63, 114, 116, 125].

Stress analysis of AAA through the use of finite element models has also been carried out by our laboratory as well as by others. [36, 47, 50-52, 55-57, 63, 81, 126] Earlier efforts to estimate AAA wall stress used hypothetical geometries, linear elastic material properties, and/or simplified analytical methods. [36, 47, 50-52, 55-57, 63, 81, 126] In 1987, Stringfellow et al used the law of Laplace to determine the wall stresses in a hypothetical AAA by idealizing its geometry as cylindrical or spherical. [49] A simplified two-dimensional stress analysis was also

performed to evaluate the effect of aorta-aneurysm geometry on the wall stresses. Similar two-dimensional analyses were reported by Inzoli et al, Mower et al, and Elger et al. [50, 51, 55] More recent investigations with hypothetical 3D models of AAAs indicated that wall stress is greatly dependent on the detailed local geometry variation (asymmetry, local curvature, wall thickness, etc.) as well as the size of the aneurysm. [47, 127] For this particular reason, 3D reconstructed patient specific models were advocated to improve the accuracy of AAA wall stress estimation [126]. The state-of-the–art in this regard was previously developed by our group, [81] and uses the actual 3D abdominal aortic wall geometry, blood pressure measured individually during CT scanning, and a nonlinear mathematical model developed specifically for AAA tissue based on experimental data. Thubrikar [126] has also been using 3D reconstructed patient specific AAA geometry for stress analysis. However, the major limitation of the existing technique is that it neglects the presence of ILT, which, according to the current Hypothesis #1, is a significant contribution to the structure of AAA.

The mechanical role of ILT on wall stress distribution has been controversial. Dobrin [48] suggested that the presence of ILT neither reduces the luminal pressure exerted on the AAA wall nor offers a retractive force. Based on this, he suggested that ILT has no effect on AAA wall stress. Schurink et al. [128, 129] and Thubrikar et al. [130] reported that thrombus does not reduce the pressure near the aneurysmal wall and thus will not reduce the risk of aneurysm rupture. Contrary to this, stress analysis of the aneurysm through the use of models by us and others [55-57, 131] have suggested that presence of ILT reduces stress in the AAA wall. However, one limitation of these studies is that they have either assumed the mechanical properties of ILT [50, 55] or utilized a simple linearly elastic model for this material. [56, 57, 127] We have demonstrated that ILT undergoes large strain in-vivo. [58] The inaccurate

assumption of ILT as linear elastic material based on infinitesimal deformation prevented a more accurate evaluation on the effect of ILT on AAA wall stress.

The goal of this Chapter was to address Hypothesis #1 by investigating the effect of ILT on wall stress distribution and magnitude in realistic, patient-specific models of AAA. If it turns out that the presence of ILT does influence the wall stress distribution, we will advance the existing technology by developing the methods to include ILT in the stress analysis. If it does not influence the wall stress distribution, we will provide the rational to continue to neglect the presence of ILT. To accomplish this, we compare the wall stress between models with and without ILT on the patient specific models developed in Chapter 6, and use the constitutive model determined in Chapter 5 for ILT.

7.2 Methods

For any finite element simulation, there are three steps involved: preprocessing, solution and post-processing. Preprocessing is the process of constructing the finite element models and includes the following sub-tasks: 1) discretizing the geometry into a finite element mesh using the chosen element type; 2) assigning material properties to the corresponding elements; 3) applying appropriate loading and boundary conditions; and 4) choosing the appropriate analysis type. In the solution step, the simultaneous equations that the finite element model generates are solved. The solution is calculated at specific points on the elements. In order to view the solution information, the post-processing step displays and stores the deformation and stress fields on the body. In some instances, one might also want to manipulate or process the results according to

specific interests. For example, exporting the results to another software to plot variables of interest at certain nodes may be done during the post-processing step.

In the current study, the commercial software packages PATRAN and ABAQUS were chosen as the preprocessor and solver, respectively. Post-processing was also done within ABAQUS. These methods as used in this work are described below, followed by the results of application to the four AAA reconstructed in Chapter 5.

7.2.1 Preprocessing

7.2.1.1 Mesh Creation

The 3D "virtual AAA" (i.e., the mathematical description of the AAA geometry generated by methods described in Chapter 5, and shown in Figure 22) were discretized into a "finite element mesh". In meshing a body for finite element analysis, one must chose the desired element type and element size as input to the software.

7.2.1.1.1 Element Type Selection

Since both wall and ILT were modeled as solid structures, not surfaces, continuum (solid) elements instead of shell elements were chosen as the candidates for the element type. The solver ABAQUS allows the choice of three types of continuum elements; namely, tetrahedral, wedge (triangular prism) element, and hexahedron (brick) elements. Each type of element possesses the option of using either *first-order* (linear) or *second-order* (quadratic) interpolation functions, i.e., they can be formulated on the assumption that displacements vary either linearly or quadratically over the domain.

Linear element (first order element) would contain no calculation error when used to model a prismatic bar under constant tensile load; in this case, the assumed displacement matches the actual displacement. If the same bar were subjected to a uniformly distributed body force, however, the actual displacement varies quadratically and a calculation error would exist. As a result, an extremely fine mesh may be needed to obtain accurate estimates and convergence would be slow. [132] Second order elements provide higher accuracy than first order elements. They capture stress concentrations more effectively and are better for modeling irregular geometric features. The price one must pay is the cost of computation because of the dramatic increase in number of nodes compared with first order elements. For AAA stress analysis, the geometry is very complex and the surfaces are highly curved. We therefore chose second-order instead of first order elements in our simulations.

One powerful benefit of using the software PATRAN as a preprocessor is that a finite element mesh is automatically generated. The irregular geometries of the wall and ILT cannot be meshed by brick elements or wedge elements without yielding ill-shaped elements, e.g., badly distorted (flat) elements. Ill-shaped elements are prone to having inaccurate surface normals, collinear vertices and similar singularities and cause convergence problems during the solution phase. [133] To get around this problem, the 3D tetrahedral elements were chosen to adapt to the irregular geometry of both AAA wall and ILT.

Many problems involve the prediction of the response of almost incompressible materials. When the material is incompressible, the solution to a problem cannot be obtained in terms of the displacement history only, since a purely hydrostatic pressure can be added without changing the displacements. ABAQUS addresses this problem by treating the pressure stress as an independently interpolated, basic solution variable, coupled to the displacement solution. This

results in the "mixed formulation" and *hybrid elements*. Hybrid elements must be used if the material is fully incompressible even if they are significantly more expensive than their regular nonhybrid counterparts. [132] Since both wall and ILT exhibit incompressible behavior, we chose *the hybrid elements* for meshing both materials.

In summary, the *second order hybrid tetrahedral* element was chosen as the most suitable for meshing both AAA wall and the contained ILT. The chosen element type allows usage of hyperelastic material models, including those given by Equation 4.25 for ILT and that developed previously for AAA wall. [81, 134]

7.2.1.1.2 Element Size/Mesh Refinement

The reconstructed 3D "virtual AAA" generated in pro-Engineer was exported to the pro-processing software PATRAN for meshing. By varying the chosen element size, it was possible to mesh the model with a varying total number of elements. The refinement of the finite element mesh is critical in optimizing the accuracy of the result with respect to computational time. Since the actual solution is obtained on a discrete number of nodes, the higher the number of nodes (and therefore the number of elements), the closer the finite element solution is to the "exact" solution. On the other hand, if the mesh refinement is too fine, the computational requirements may become excessive. Often, mesh refinement beyond a certain degree would not effect the accuracy of the solution appreciably. Therefore, refinement should be an optimum between accuracy and computational expense. As a result of this requirement, the element size used will be different for each specific case. The exact number of elements needed for each AAA studied was determined as follows. Five different finite element models with different degrees of mesh refinement were created for each case by varying the global average element size from 0.5cm, 0.25 cm, 0.1 cm, 0.08 cm, to 0.05 cm. All the models were otherwise identical (i.e., the same

boundary conditions and material properties). Each model was then analyzed as detailed below, and a global, averaged von Mises stress (σ_{avg}) was calculated from:

$$\sigma_{avg} = \frac{\sum_{1}^{N} \sigma_i}{N} \tag{7.1}$$

Here N is the total number of nodes in each model, and σ_i is the von Mises stress at node "i" . The mesh was considered refined when there was no significant change (<1%) in this global average stress value.

7.2.1.2 Material Properties

The constitutive equation and material properties of ILT described in Chapter 4 and the constitutive equation and material properties of AAA wall developed previously by our group can be directly input into ABAQUS, which provides a general strain energy function for hyperelastic materials as:

$$W = \sum_{i+j=1}^{N} C_{ij} (I_1 - 3)^i (I_2 - 3)^j \tag{7.2}$$

Here N is the order of the mathematical function, Cij are material parameters, and I_1 and I_2 are the first and second invariants of the deformation gradient tensor, respectively.

For the AAA wall, we take N=2 to be consistent with the strain energy function determined by Raghavan and Vorp [134]. The strain energy function can then be written as

$$\boldsymbol{W} = C_{10}\,(\mathrm{I}_1\text{-}3) + C_{20}\,(\mathrm{I}_1\text{-}3)^2 \qquad (7.3)$$

All other $C_{ij} = 0$. Similarly, in accordance with Equation 4.23, the functional form of W for ILT can be written as

$$\boldsymbol{W} = C_{01}\,(\mathrm{I}_2\text{-}3) + C_{02}\,(\mathrm{I}_2\text{-}3)^2 \qquad (7.4)$$

Again, all other $C_{ij} = 0$. Population mean values of each of the material parameters (i.e., C_{10} and C_{20} for AAA wall, C_{01} and C_{02} for ILT) were determined from previous experimentation (recall Chapter 4 and Table 4) and assigned to each model (**Table 8**). Previous and ongoing studies in our lab revealed that use of population mean values does not affect the wall stress result in a significant manner. [53, 63, 135]

Table 8 The material properties used in this study for AAA wall [52] and ILT (recall Chapter 4) based on ex-vivo tensile testing.

	AAA Wall (n=61) Equation 7.3		**ILT (n=42)** Equation 7.4	
	C_{10} (N/cm^2)	C_{20} (N/cm^2)	C_{01} (N/cm^2)	C_{02} (N/cm^2)
Population Mean	17.4	188.1	2.6	2.6
Standard Error	1.5	37.2	0.28	0.26

7.2.1.3 Analyses Type

Just as there are many element types and features to chose from, there are large classes of stress analysis procedures available in ABAQUS, including static or dynamic analysis, and linear or nonlinear analysis. In this section, the different analysis types are defined and the rational for the type chosen is provided.

A finite element simulation problem can be divided into two types of response: static or dynamic. Dynamic problems are those in which inertia effects are significant and have been taken into account. In the problem at hand, AAA is a structure that undergoes dynamic deformation during the cardiac cycle. However, we are only interested in the peak wall stress that is more due to the systolic pressure than to the history of the pressure. Therefore, for the current treatment, the inertial effects were neglected and only the static response of AAA under systolic pressure was simulated.

The finite element method may be used to analyze both linear and nonlinear systems. In linear structure analysis, the stiffness of the structure remains constant. However, as described in Section 3.3, most biological systems including AAA exhibit structural nonlinearity. For example, the structural stiffness of ILT increases with deformation (recall Section 3.3.3, **Figure 12**). This type of nonlinearity is referred as material nonlinearity. Nonlinear stress analysis problems can contain two other sources of nonlinearity: boundary condition nonlinearity and geometric nonlinearity. If a structure experiences large deformations, its changing geometric configuration can cause the structure to respond nonlinearly. For the present application, AAA does undergo large deformation in vivo. Therefore, geometric nonlinearity was taken into account by utilizing the nonlinear large deformation algorithm within ABAQUS.

Many common structural features exhibit nonlinear behavior that is cause-dependent including contact. For example, a tension-only cable is either slack or taut; a roller support is either in contact or not in contact. It is possible to model such boundary condition status changes. However, as described in Chapter 6, the contact between the AAA outer surface and spine or adjacent other internal organs was neglected in the present study. Instead, the loading condition (systolic blood pressure) and displacement restraint at both ends were assumed not to change with deformation. Therefore, it was not necessary to account for any boundary condition nonlinearity.

In summary, nonlinear static analysis was chosen as the analysis type. This was accomplished by invoking the NLGEOM and STATIC parameters on the *STEP option in ABAQUS simulation. A sample ABAQUS program is attached in **APPENDIX B**.

7.2.2 Analysis -- Solving Nonlinear Problems

The boundary conditions for each model was assigned according to the description in Chapter 6. The measured individual systolic pressure was applied to the luminal surface of the model acting outwardly. The longitudinal displacement constraints at all the points on the proximal and distal edges of AAA wall. In addition, one point located on the proximal edge of AAA model was fixed in all six degrees of freedom to inhibit free body motion.

After the finite element model for each AAA studied was constructed, the preprocessing file was transferred to ABAQUS for stress analysis. For nonlinear problems, ABAQUS uses a quasi-Newton iterative solution technique [132] and the load is applied incrementally over time. At the end of each time increment or iteration, the difference between the total applied load and the structure's internal force (i.e., *residual force*) is calculated and compared to a preset tolerance

value. Most nonlinear engineering calculations are sufficiently accurate if the error in the residual is less than 0.5%. In all our analyses, we used this value as the convergence criterion. [132] That is, an approximate equilibrium configuration was assumed to be reached when the residual force was less than 0.5% of the applied load and the next increment was carried out. The process was repeated until 100% load was reached, after which the analysis was considered "converged".

ABAQUS provides the option between "automatic" time step control and direct user control. For the automatic time step control method, the user suggests only the size of the first increment of the simulation, after which ABAQUS automatically adjusts the size of increments. ABAQUS writes increment summaries to a status (.sta) file. In all the cases, automatic time stepping was used and was sufficient to attain convergence. The pressure load was gradually increased to 100% of the systolic pressure with an initial pressure of 1% of the subject's systolic pressure. **APPENDIX C** shows an example status file entitled AAA.sta.

7.2.3 Post Processing

In this phase, the results of the analysis were reviewed, and the relevant information is retrieved and processed. For both Specific Aim #1 and #4, some measure of wall stress is necessary. Since we are interested in AAA rupture, it was natural to consider various failure theories.

There are several failure criteria in multiaxial stress states, including: *the maximum principle stress criterion (Rankin's)* criterion; *the maximum principle strain (St. Venant's)* criterion; *the maximum shear-stress (Tresca)* criterion; and the *distortional energy density (von Mises)* criterion. [136]

The maximum principal stress criterion (Rankie's) criterion states that the failure occurs when the maximum principal stress reaches a value equal to the tensile strength of the material. It is often used to predict failure of brittle materials such as concrete. [26] *The maximum principle strain (St. Venant's)* criterion states that failure begins when the maximum principle strain at a point reaches a value equal to the yield strain of the material. It correlates closely with the maximum principle stress criterion and is also used to predict fracture of brittle materials. [137] *The maximum shear stress* (Tresca) criterion states that failure begins when the maximum shear stress at a point equals the maximum shear stress at yield in uniaxial tension or compression. Tresca is a conservative criterion used for predicting the failure of ductile metals. [137] The *distortional energy density (von Mises) criterion* states that failure begins when the distortion strain energy density at a point equals the distortion strain energy density at yield in uniaxial tension (or compression). To choose an appropriate criterion, one has to rigorously study the pattern of failure on the region of the materials where it fails, usually by microscopic methods. However, this analysis has not been done on AAA tissue. Traditionally, the von Mises criterion has been used in soft tissue failure prediction in the literature. [52, 53, 63, 81, 116] Since there is no evidence showing that the pattern of rupture is tear-, split-, or dissection- type, there is no reason to adopt the maximum principle strain, the maximum principal stress or the maximum shear stress criteria. Therefore, to keep with precedence, [52, 55, 81] we use the von Mises criterion to predict AAA rupture. The von Mises stress is defined at any point as

$$\sigma = \sqrt{\frac{1}{2}\left[(\sigma_1 - \sigma_2)^2 + (\sigma_2 - \sigma_3)^2 + (\sigma_3 - \sigma_1)^2\right]} \tag{7.5}$$

where σ_1, σ_2, and σ_3 are the three principle stresses at that point.

For studying AAA rupture, the inner surface of AAA wall was selected as the surface to calculate and display the results because, in general, the peak stress is expected to reside on the inner surface instead of the outer surface. For each AAA studied, therefore, the von Mises stress distribution was determined and displayed along the inner AAA wall surface.

Finally, a contour plot of stress distribution was generated for each AAA using the visualization software Tecplot (Version 8.0, Amtec Engineering, Inc., Bellevue, Washington). A 3D stress plot animation was also generated for that patient in AVI (Advanced Visual Interfaces) format which can be easily viewed and transferred through Internet.

7.2.4 Case Studies – Effect of ILT on Stress Distribution

All four AAA that were reconstructed as detailed in Chapter 5 were selected for the stress simulation. To carry out Specific Aim #1, two analyses were carried out for each patient. One was with the 3D reconstructed ILT included in the geometry, the other was without the ILT. The Wilcoxon matched pairs test was used to compare the peak wall stress between the two models of each patient.

To understand how stress is affected by the presence of ILT, the ILT volume ratio, and ILT surface ratio computed for each case in Chapter 5 (see **Table 6**) were correlated to the change of peak wall stress between the case with ILT versus the case without. The Spearman Rank Order Correlation method was used to calculate the correlation coefficients and p-values for each comparison. A p-value less than 0.05 was considered as statistically significant.

7.3 Results

7.3.1 Stress Analysis Results

The mesh refinement process is summarized in **Table 9** for each AAA studied. All finite element stress analyses using the refined meshes indicated by the final step of **Table 9** reached convergence. Von Mises stress distributions are shown in **Figure 25** for each AAA with and without ILT included in the analysis. Compared with the companion models neglecting ILT, the peak weak wall stress in the model including ILT is decreased to varying degrees (P = .067 by Wilcoxon paired test; **Table 10).** Patient #2 and #4 have the largest amount of ILT and also experienced the most profound decrease in peak wall stress. In all cases, the presence of ILT markedly altered wall stress distribution. Incidentally, the magnitude of von Mises stress in ILT is much lower than the stress in the wall (**Table 10**). The peak stresses in ILT for the four AAAs ranged from 8% to 32% of the peak wall stress.

7.3.2 Correlation Between Peak Wall Stress and Geometric Parameters

The Spearman rank correlation coefficient for peak wall stress reduction (**Table 10**) versus both ILT surface ratio and volume ratio (recall **Table 7**) as well as the associated p-values are listed in **Table 11**. Though the p-values do not indicate statistical significance ($p > 0.05$), there appears to be a clear correlation between the degree of peak wall stress reduction ($\rho = 0.60$) and both ILT volume ratio and ILT surface ratio ($\rho = 0.80$).

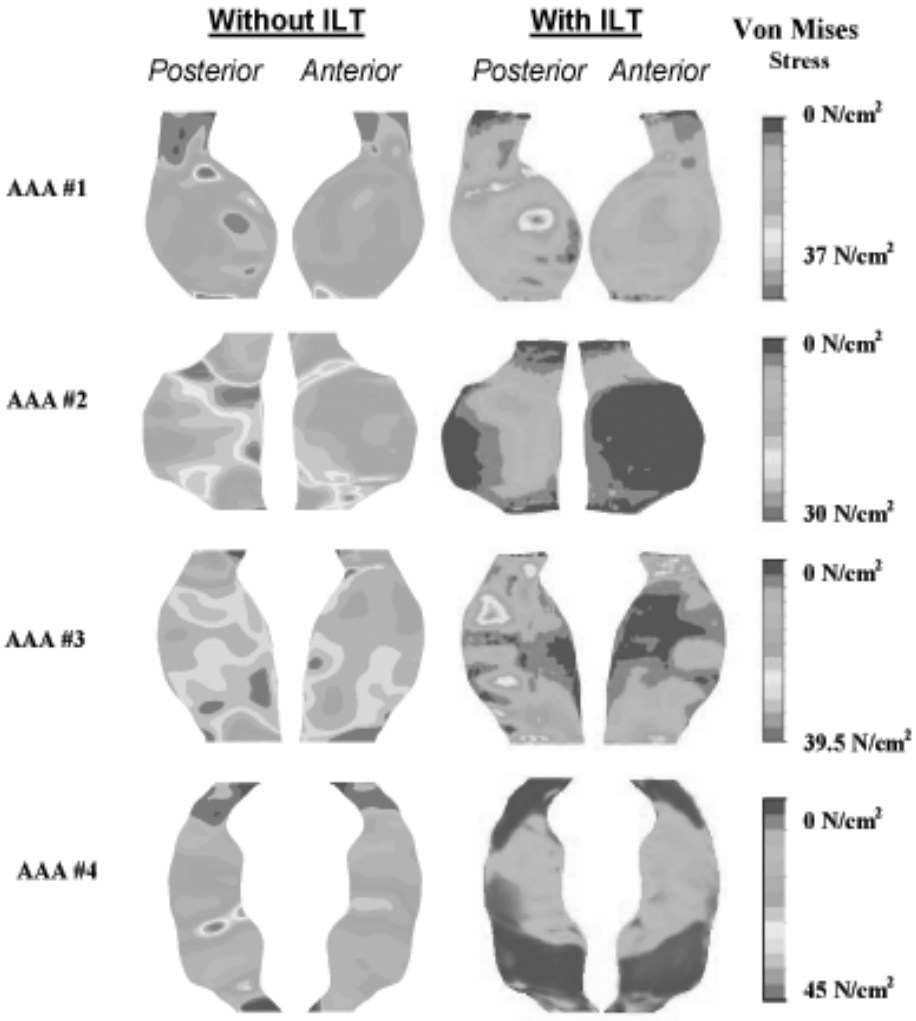

Figure 25 Comparison of 3-D wall stress distribution between AAA models with and without ILT. The individual color scales to the right indicate von Mises stress. Both the posterior and anterior views are shown for each case.

Table 9 The number of nodes (N) and the corresponding global average stress (σ_{Avg}) calculated using Equation 7.1. Five steps of refinement were carried out for each model. The global average stress of the last step (Step #5) is less than 1% different than that of the previous step.

AAA #1				AAA #2			
With ILT		Without ILT		With ILT		Without ILT	
N	σ(N/cm^2)	N	σ(N/cm^2)	N	σ(N/cm^2)	N	σ(N/cm^2)
1760	11.1	1540	20.2	1932	5.0	1360	16.5
4600	10.3	2632	19.8	4560	4.8	2542	15.3
7800	9.9	3240	19.3	7342	4.4	3820	15.1
9620	9.6	4620	18.7	8248	4.3	4254	14.8
10210	9.5	6500	18.5	10128	4.3	4796	14.6

AAA #3				AAA #4			
With ILT		Without ILT		With ILT		Without ILT	
N	σ(N/cm^2)	N	σ(N/cm^2)	N	σ(N/cm^2)	N	σ(N/cm^2)
3596	29.9	1264	30.2	2496	11.3	1846	20.5
3612	26.0	2306	28.6	3976	10.7	2450	19.1
5246	25.8	3520	28.0	6530	9.8	3824	8.3
6820	25.4	4128	27.2	9604	9.8	4982	17.6
7564	25.2	4620	27.0	11208	9.7	5460	17.4

Table 10 Peak wall stress for each patient with and without ILT, the percent decrease in peak wall stress due to the presence of ILT, and the peak ILT stress for the models that included ILT

Patient	Peak Stress Without ILT (N/cm^2)	Peak Stress* With ILT (N/cm^2)	Decrease of Peak Stress (%)	ILT Peak Stress (N/cm^2)	Peak ILT Stress to Peak Wall Stress (%)
1	36	34	6	11	32
2	30	19	36	5	26
3	40	37	6	3	8
4	44	25	43	8	32

* P = .067 by Wilcoxon paired test compared to AAA without ILT

Table 11 Spearman rank correlation coefficients indicating correlation between peak wall stress decrease and ILT volume ratio and ILT surface ratio for the four AAA models studied. No statistically significant correlation was observed ($p > 0.05$).

	Spearman ρ	p-level
Peak Stress Reduction vs. ILT Surface Ratio	0.80	0.1999
Peak Stress Reduction vs. ILT Volume Ratio	0.60	0.4000

7.4 Discussion

7.4.1 Possible Role of ILT in AAA Stress Distribution

Compared with the models that neglected ILT, the peak wall stress in the models including ILT has led to varying degrees of decrease in wall stress (**Table 10**). For AAA#1, the peak stress was 36 N/cm^2 without ILT and 34 N/cm^2 with ILT, a 6% decrease. For AAA#2, peak wall stress reduced from 30 N/cm^2 without ILT, to 19 N/cm^2 with ILT, a 36% decrease. For AAA#3, peak wall stress was 40 N/cm^2 without ILT, and 37 N/cm^2 with ILT, a 6% decrease. For AAA #4, peak wall stress reduced from 45 N/cm^2 without ILT, to 28 N/cm^2 with ILT, a 38% decrease. Also quite apparent is the difference in wall stress distribution between models. Patients #2 and #4 have large amount of ILT, therefore experienced the most marked decrease in peak wall stress. However, it is important to keep in mind that decrease in AAA wall stress does not necessarily mean lower risk of rupture.

The results of the stress analyses support Hypothesis #1, that the presence of ILT affects the magnitude and distribution pattern of wall stress in AAA. The degree of reduction in peak wall stress, and possibly the beneficial effect on AAA rupture, is dependent on the amount and specific configuration of ILT. In other words, ILT might decrease wall stress significantly in some cases, but not all cases. This observation accentuates the importance of evaluating the wall stresses in AAA on a patient-by-patient basis.

7.4.2 Advantages and Limitations of the Stress Analysis Technique

7.4.2.1 Advantages

To our knowledge, this is the first study to evaluate AAA wall stress in actual, 3D reconstructed AAA with ILT. Our approach also differs from previous studies of others in the following three important ways:

- A realistic patient-specific 3D virtual AAA model was used instead of hypothetical models.
- Nonlinearly elastic constitutive models developed specifically for AAA tissue and ILT were used instead of linearly elastic models.
- Patient specific values of AAA wall thickness were utilized instead of one value for all AAA models.

This patient specific approach allowed us to explore Hypothesis #1 and answer the question of how ILT affects AAA wall stress distribution for a given patient. More importantly, since the presence of ILT does affect wall stress magnitude and distribution, the developed technique of including ILT provides a more accurate stress analysis for a given AAA. Therefore, it represents the state-of-the-art in the field of 3D-stress analysis of AAA.

7.4.2.2 Limitations

Though our stress analysis technique represents the state-of-the-art in this field, it does have several limitations in terms of accuracy and clinical practicality. All these limitations may compromise the accuracy of our stress analysis technique and should be addressed in future studies. The accuracy of any stress analysis using the finite element method depends on the

accuracy of the three inputs to the model: geometry, boundary conditions and material properties. The limitations of each of these components are discussed in this section.

Limitations on geometry were discussed in Chapter 5, Section 5.4. In summary, these are:

1. The reconstructed AAA was not at its zero load configuration, but rather at some conglomerate or average of the configurations during the cardiac cycle.
2. The presence of calcified plaques was neglected in the reconstruction process. The presence of calcified plaques would likely affect the wall stress magnitude and distribution as has been shown by others for both AAA [55] and arterial tissue in general. [138] Indeed, several radiology studies showed that the degree of calcification of AAA wall is related to the stability and rupture potential of AAA. [107-109]
3. The wall thickness was assumed to be constant throughout each AAA, which is likely not the case. However, no information is available to allow inclusion of an accurate, spatially-varying wall thickness, so it was therefore assumed constant. Raghavan [53] evaluated the effect of wall thickness on peak wall stress by using three different wall thickness values: t_{mean} (group mean measured from 132 AAA wall specimens during tensile testing), $t_{mean - CI}$ (lower 99% confidence level for that population), and $t_{mean + CI}$ (upper 99% confidence level for that population). The results showed that the error in peak wall stress within 99% confidence is on the order of 8.6%. The constant wall thickness assumption should be further evaluated and improved upon.

Limitations on material properties include the following:

1. ILT was assumed to be a homogeneous material in the stress analyses. However, as determined in Chapter 4 (see Table 4), this is not the case.
2. Both ILT and wall were treated as isotropic materials based on preliminary uniaxial and biaxial testing data (recall Section 2.3.3 and Section 4.3). More rigorous studies are needed to determine whether these are indeed isotropic materials.
3. The material constants used in the models were population means instead of patient-specific values. It has been shown by Raghavan and Vorp [63] and Di Martino et al [135] that using population means for the material properties for the AAA wall and ILT does not appreciatively alter the AAA wall stress distribution. Raghavan and Vorp [63] reported that using the assumption that the wall material parameters of a particular aneurysm are equal to the mean values determined from the patient population results in less than 4% error for at least 95% of the patient population. Di Martino et al [135] reported that the use of mean ILT properties as opposed to the exact patient-specific parameters results in up to a 10% error in peak wall stress prediction. Those studies suggest that the AAA wall stress simulation is fairly insensitive to the errors in the estimation of patient-specific material parameters. More specifically, the results imply that one can use mean values of material properties of AAA wall and ILT for a patient specific model to reliably evaluate wall stress distribution without introducing significant error.

As for boundary conditions, we neglected tethering forces at both ends of the AAA. The aorta, like most arteries, is under some degree of longitudinal tension in vivo. [139] However, quantitative information on the longitudinal strain of the AAA wall in vivo is not available. Contact of the AAA with the spine and other internal organs has also been neglected to simplify

the simulation. It was also assumed that the systolic pressure is uniformly distributed at the entire luminal surface. It is possible that the pressure varies due to the variation of luminal cross-sectional area. Using an artificial AAA phantom setup, Peattie et al. [94] measured the pressure at various location of AAA due to laminar and turbulent flows. They showed that the pressure at the region of maximum diameter was 3% higher than that at the undilated region. However, this study did not consider the presence of ILT. Fluid mechanical studies that model blood flow in aneurysm with ILT may shed light in this direction.

A more important assumption employed here was that the virtual AAA configuration reconstructed from CT data (which will be referred to as Ω_{CT}) is the load-free configuration (Ω_0). Since AAA in vivo pulsates due to it being under cyclic pressure loading during the cardiac cycles, and since the CT image data is collected over several minutes, Ω_{CT} is actually an "average" configuration and certainly not unloaded. To evaluate the error resulting from this assumption, we performed some computational studies using hypothetical AAA. First, a hypothetical geometry was created in a manner similar to that previously described [52, 135] to simulate the load free reference configuration, Ω_0 of some hypothetical AAA. The hypothetical virtual AAA was created in PATRAN, included ILT, and was asymmetric in shape. Nonlinear hyperelastic models were used for both ILT and AAA wall. Then, the following analyses was performed.

A hypothetical mean aortic pressure of 100 mmHg (for the case of the blood pressure of 120/80 mmHg for a typical patient) was input as the internal force boundary condition along with the usual longitudinal displacement boundary conditions**.** This process is depicted in **Figure 26A** to **Figure 26B**. The deformed shape resulting from the mean pressure loading is assumed to represent the CT configuration Ω_{CT}. A systolic pressure of 120 mmHg was then applied to both

Ω_0 (from A to C in **Figure 26**) and Ω_{CT} (from B to D in **Figure 26**), and the stress distributions were determined for each resulting case in the same manner as described in Section 7.2.

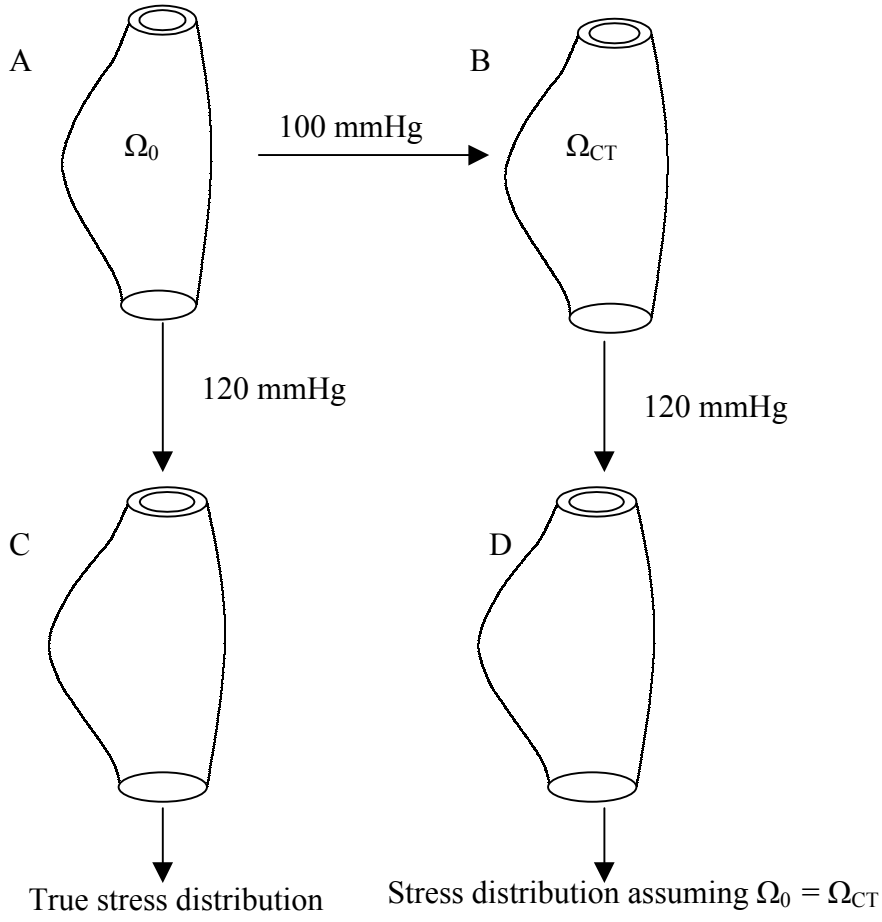

Figure 26 Steps taken to evaluate the error of assuming that $\Omega_{CT} = \Omega_0$. A) Hypothetical AAA at its load free configuration Ω_0. B) The CT configuration, Ω_{CT}, assumed to be obtained from loading Ω_0 with mean arterial pressure. C) Configuration of AAA after loading Ω_0 with systolic pressure (to obtain the true stress distribution). D) Configuration of AAA after loading Ω_{CT} with systolic pressure to obtain an estimated stress distribution. The approach described in this chapter is analogous to the step from B to D.

Figure 27 shows the comparison between the two stress distributions. The two cases have similar patterns of stress distribution, but the use of the CT configuration overestimated the peak wall stress by 8.0 % (from 17.96 N/cm^2 to 19.52 N/cm^2). The range of error introduced ranged from 2.0% at some nodes to 10% at others. However, whether this error could be greater in the case of irregular actual AAA geometry is unknown and hence requires further evaluation.

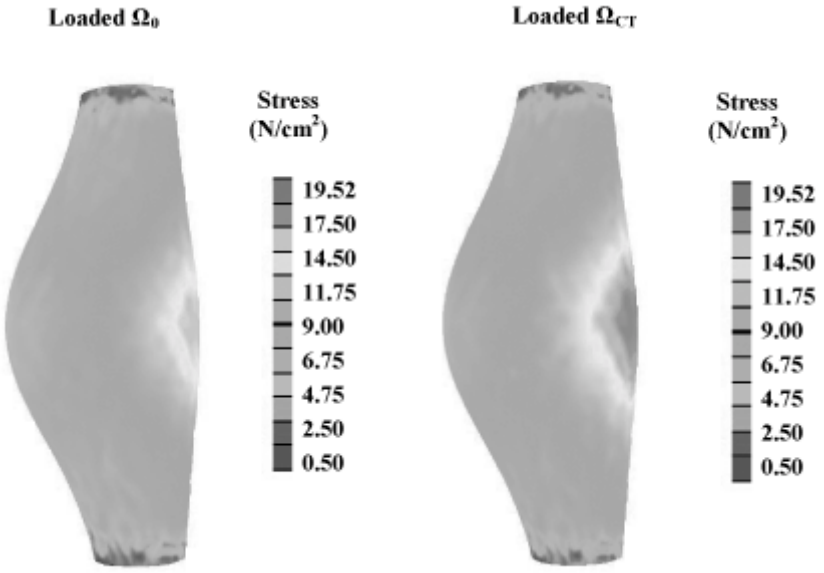

Figure 27 Von Mises stress for the case for which Ω_0 was loaded (i.e., step A-C in Figure 26, or the true stress distribution) and for the case which Ω_{CT} was assumed stress free and loaded (i.e., step B-D in Figure 26, as was done in this work). The peak stress was overestimated by this assumption by 8.0 % (17.96 vs. 19.52 N/cm^2).

As for any computer simulation, there is always a trade off between the accuracy and the simplicity of the model. In order to use this technique as a potential clinical tool, it must be simple and user friendly. However, the current protocol (from image digitization, 3D reconstruction, FEM modeling and FEM analysis) is very time consuming. In addition, several custom-written software programs were used which demand a lot expertise. Future efforts should focus on making the technique more user friendly (i.e., window based, simple operation) and less time consuming.

Further, our model does not address the possible existence of residual stress, which can have a large effect on ILT and AAA wall stress distribution. [140]

Finally, the correlation of peak wall stress with geometric parameters (**Table 11**) is insufficient due to the small sample size. More studies on patient specific models need to be conducted before a concrete conclusion can be drawn.

8.0 STATISTICAL MODELING OF LOCAL AAA WALL STRENGTH

8.1 Introduction

Like the failure of any other material, AAA rupture occurs when wall stress exceeds the ultimate strength of local wall tissues. In order to evaluate the rupture potential for an individual AAA, both wall stress and wall strength need to first be evaluated. In the preceding chapters, we modified a noninvasive technique to evaluate the wall stress distribution by taking into account the presence of ILT. This was in support of the first hypothesis, that ILT significantly influence AAA wall stress distribution. In this Chapter, we will address the second hypothesis, that AAA wall strength distribution might be evaluated noninvasively by certain clinical measurable variables on a patient-specific basis.

8.1.1 Structure of the Aortic Wall

The abdominal aorta serves as a conduit transmitting blood to the lower body. Like all blood vessels, it is comprised of three distinct layers - the intima, media and adventitia (**Figure 28**). The intima, or innermost layer, consists of a monolayer of endothelial cells attached to a narrow layer of connective tissue. The media consists of structural units made of smooth muscle cells surrounded by concentric lamellae of elastin and collagen imbedded in a ground substance rich in proteoglycans. Collagen and elastin are the major extracellular matrix proteins responsible for aortic structural integrity. [141] They impart the extensile and tensile properties

to the aorta, respectively. [142] Under normal conditions, the precise arrangement of elastin and collagen are critical to the mechanical properties of the aorta. Medial smooth muscle cells and adventitial fibroblasts synthesize these proteins. Repair and remodeling are necessary for vessel growth and structural integrity. This is regulated by the interaction between synthesis and degradation of these proteins. In AAA, disturbances in this intricate biochemical balance result in weakening and enlargement of the aorta. [143]

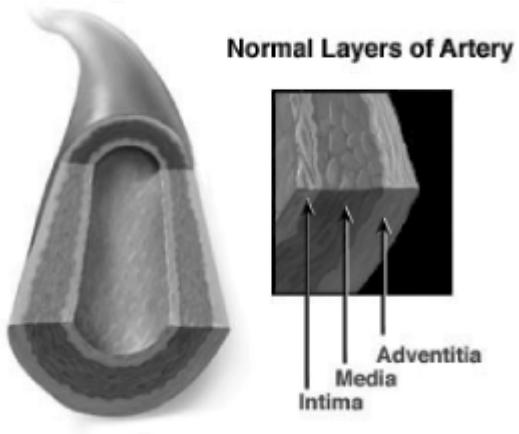

Figure 28 Structure of the normal artery (http://www.heartcenteronline.com).

The extracellular matrix provides a structural framework essential for the functional properties of vessel walls. [144] The three dimensional organization of the two major structural components, elastin and collagen, synthesized during fetal development are optimal for normal function. [144] It is well known that AAA tissue experiences modifications as it develops and enlarges. [145, 146] Medial lamellar units are destroyed, and the elastin and collagen are degraded. [145, 146] Data from our group showed that there is also a significant decrease in the

tensile strength of the AAA compared to nonaneurysmal tissue. [60, 62, 134] Specifically, it was found that the strength of AAA was 86.4 ± 10.2 N/cm^2 as compared to 201.4 ± 40.0 N/cm^2 for nonaneurysmal control aorta. [60] The significant standard errors in this previous data suggest that the wall strength differs from patient to patient, and it might be significantly different even from location to location in the same aneurysm. Therefore, we believe that an accurate assessment of wall strength distribution for a particular AAA is just as important as that for the stress distribution.

8.1.2 Potential Factors Associated with AAA Wall Strength

To prove Hypothesis #2, we utilized statistical techniques to build a model correlating local wall strength with certain clinical measurable parameters. An important aspect of such an approach is selecting the statistically significant predictors or independent variables to be used in the model. Sometimes previous experience or underlying theoretical considerations can help specify the set of variables that should be used in a particular situation. Usually, however, the problem consists of selecting an appropriate set of potential predictors, then using statistical evaluation to determine if all the candidate predictors are necessary, only a part of them are necessary, or additional predictors are needed to adequately predict the response variable.

Factors that influence AAA wall strength are poorly understood. Therefore, determining which clinical variables are associated with local wall strength is not an easy task. Our approach was to include all the appropriate clinical variables which have been shown to be associated with aortic wall strength and/or AAA rupture potential, and which are patient- and/or location-specific.

8.1.2.1 AAA Size as a Potential Predictor

As a AAA develops and enlarges, medial lamella units are destroyed, and the main structural proteins responsible for providing structural integrity to the aorta (namely elastin and collagen) are degraded. [145, 147] As detailed above, data from our group shows that there is also a significant decrease in the tensile strength of the AAA compared to nonaneurysmal tissue. [60] The evidence that larger AAAs have higher risk of rupture [5, 13, 17, 20, 35, 42-44, 54, 148-151] might also suggest that the failure strength of AAA wall reduce progressively as AAA enlarges. For all of these reasons, AAA size was selected as one of the potential predictors of wall strength.

8.1.2.2 Patient's Age as Potential Predictor

Epidemiological studies have shown an increased prevalence of abdominal aneurysm with advancing age. [5, 16, 152-155] Histologic examination of AAA reveals a disrupted thin media with a lack of elastic fibers, fibrosis, and thickening of the adventitia and neointima. [156] The elastin content is decreased, [157-160] whereas collagen content has been reported as increased with respect to nonaneurysmal aortic tissue. [145, 156, 157, 159] These changes may due to the reported increased proteolytic activity of collagenase [145, 161] and elastase. [161, 162] However, at the same time, lower antiprotease activity has been detected in AAA vs. nonaneurysmal aorta. [163] Together these factors will alter the microstructure of the aorta (e.g., raise the collagen-to-elastin ratio), resulting in changes to the biomechanical properties of the tissue.

In healthy arteries, the synthesis and degradation of collagen and elastin are carefully regulated by a balance between the activation and/or inhibition of proteases and their inhibitors.

[144] In the process of aging, this balance is temporally destroyed through the induction of matrix metalloproteinase gene expression or the secretion of enzymes by inflammatory cells. [144] Smooth muscle cells, the most numerous cells in vascular walls, have a high ability to respond to injury through their ability to synthesize extracellular matrix molecules and protease inhibitors. [48, 143, 164-168] However, the three dimensional organization of the newly synthesized extracellular matrix including collagen is never functionally optimal compared to the original matrix.

It has been shown that the collagen content of the arterial wall increases with age, and the elastin content decreases with age. [169-175] **Table 12** summarizes these and other changes. Since elastin mainly contributes to the compliance of the aorta, and collagen contributes to the tensile strength of the aorta, [142] it is quite possible that age influences the tensile strength of the aorta via the associated microstructural changes.

Table 12 Change of aorta with aging. From Lakatta et al. [171]

Diameter ↑
Wall thickness
  Intima
    ↑ Thickness-VSM cells and matrix
    ↑ TGFβ; ↑ MMPII levels and activity; ↑ ICAM expression
  Media
    ↑ Thickness
    VSM cells
    ↑ Size; ↓ number
    Δ In intracellular intermediary filaments
  Matrix
    ↑ Collagen amount; ↑ Crosslinking 2° nonenzymatic glycation
    ↑ Fibronectin
    Elastin - fragmented and calcified
Exaggerated wound repair response

For these reasons, we believe that AAA wall strength might also be associated with the patient's age, and this was selected as one of the candidate predictors for our statistical model.

8.1.2.3 Patient's Gender as a Potential Predictor

Epidemiological studies have shown a lower prevalence but higher risk of rupture of AAA in women than in men. [5, 153, 154, 177] The AAA frequency among men is between two and four times higher than among of women in the same age group. [5] Epidemiologic studies have also shown that females develop cardiovascular diseases and abdominal aortic aneurysms later in life than males. [5, 9, 178] These studies may suggest that there is a difference between the nature of the vessel between males and females that put men at higher risk for abdominal aneurysm than women.

In healthy arteries, stiffness increases with age as a result of an increase in the collagen-to-elastin ratio of the walls, with men having stiffer arteries than women. [178] Bengtsson and Sonesson's studies confirmed that there is a sex-related difference in diameter and compliance of the infernal abdominal aorta in age matched healthy population. [5, 178] The diameter was smaller in females than in males ($p < 0.01$). In males, the increasing of stiffness with age was greater and exponential compared to the linear fashion in females. [178] It is also noted that for the age-matched healthy subjects, the male aorta is stiffer than the female aorta. [178] In a different study, Sonesson et al. showed that the decrease in abdominal aortic aneurysm wall distensibility with age occurs at an earlier age in men and suggested that the abdominal aorta in men is more prone to degenerative changes which leads to weakening of the wall. [179]

For all these reasons, we believe that gender is a potential predictor of AAA wall strength.

8.1.2.4 Local ILT Thickness as a Predictor

The intima and subintimal media in infrarenal aorta are not nourished by the vasa vasorum. [48, 180, 181] The oxygen supply from the lumen is critical to the viability of the infrarenal aortic wall. The presence of ILT might serves as a barrier to the oxygen supply from the lumen, thereby causing hypoxia and weakening of the aortic wall. [62] In support of this idea, we recently performed a computational oxygen diffusion simulation that demonstrated the effect of ILT thickness on the oxygen supply to the smooth muscle cells in the AAA wall (**Figure 29**). [127] Normally functioning smooth muscle cells require a supply of 21×10^{-10} μmol/min/cell. [182] However, according to our results in **Figure 29**, the presence of even a thin, 3mm ILT layer causes diminished oxygen supply (less than 4×10^{-10} μmol/min/cell) which might cause hypoxia in the wall. [127] This was confirmed by subsequent experimental measurements and immunohistochemistry studies. [183] In this latter work, we measured the actual pO_2 level in the wall adjacent to either a thick or a thin (or absent) layer of ILT (**Figure 30**). The immunohistochemistry studies showed the association of ILT with local hypoxia and inflammation (**Figure 31**), as well as neovascularization in the wall (**Figure 32**). [183] Together, all of these results suggest that there is a strong correlation between the thickness of ILT and hypoxia, inflammation, and neovascularization in the adjacent AAA wall. We also measured, perhaps as a consequence of the hypoxia, inflammation and neovascularization, a strong correlation between the ILT thickness and adjacent wall strength (**Figure 33**). For all these reasons, ILT thickness was included as a predictor for local wall strength.

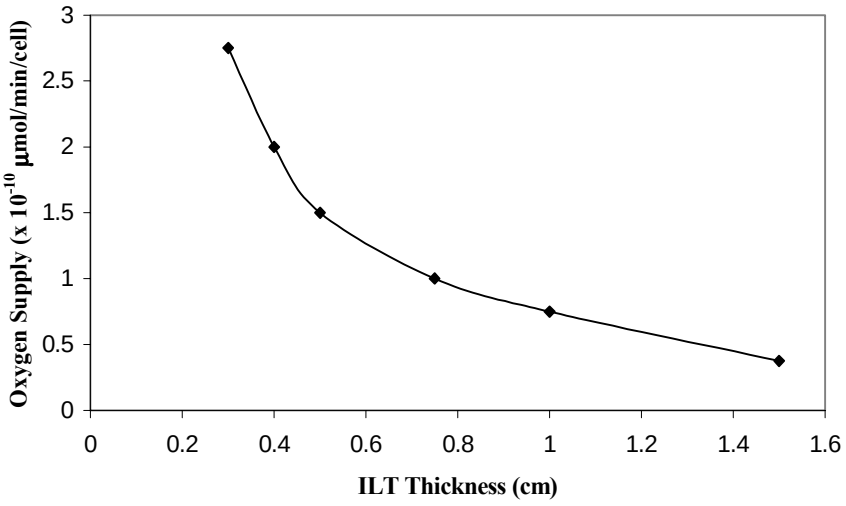

Figure 29 Effect of ILT thickness on oxygen supply to SMC in the AAA wall. Figure from Vorp et al. [127]

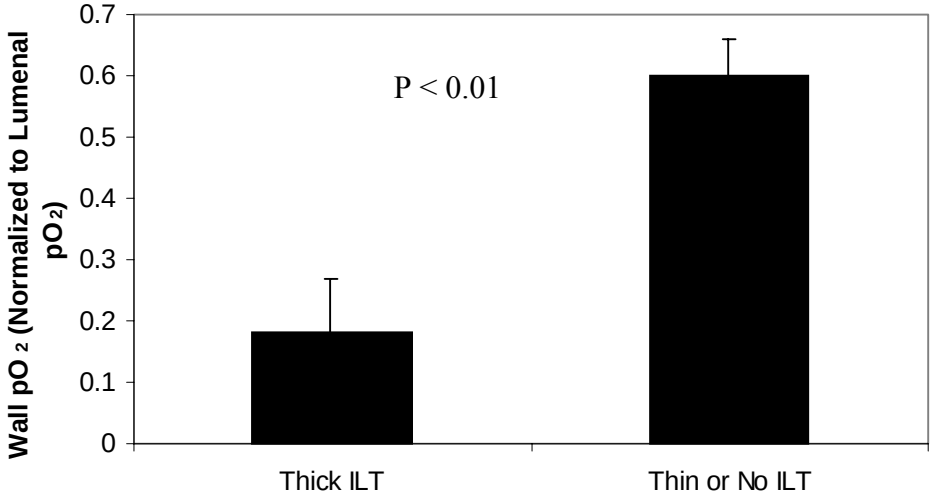

Figure 30 In vivo pO_2 measurements for AAA wall adjacent to thick AAA wall and to thin (< 4 mm) or no ILT. Figure from Vorp et al. [183]

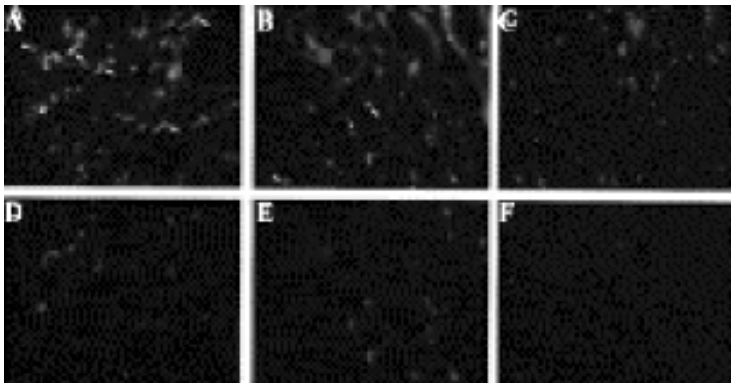

Figure 31 Immunohistochemistry staining on wall specimen section from thick ILT group (A and D), thin ILT group (B and E), and primary-deleted negative control (C and F). Hoescht-stained nuclei appear blue, whereas ORP-positive cells appear green and CD45-positive cells appear red. Figure from Vorp et al. [183]

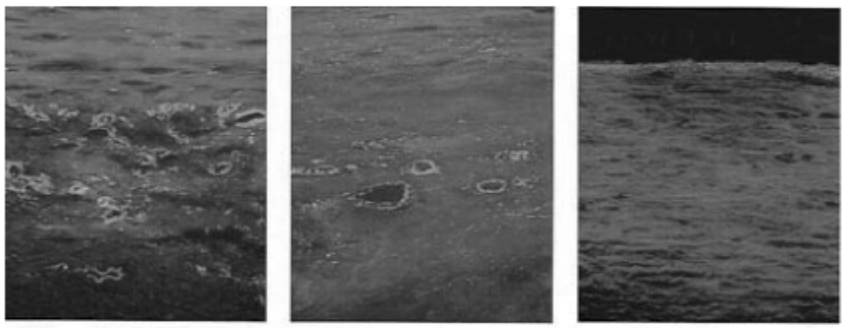

Figure 32 Neovascularization in wall with adjacent thick ILT, thin ILT, and nonaneurysmal control. New vessels were identified via staining for von Willebrand factor, which is a protein marker for endothelial cells. Figure from Vorp et al. [183]

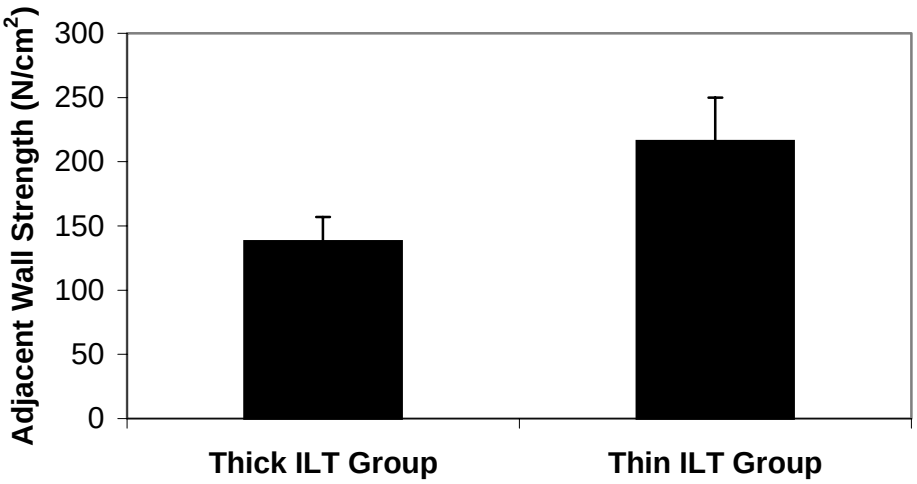

Figure 33 Association of wall strength with ILT thickness. Figure from Vorp et al. [183]

8.1.2.5 Local Diameter as a Predictor

It is well known that the AAA wall undergoes a change in microstructure as it enlarges, including the content and structure of elastin and collagen. [145, 147] In general, the larger the AAA diameter, the lower the structure protein content. This is likely due to an increase in proteolytic enzymes as the AAA enlarges. [184] In addition, the presence of the "5-cm diameter criterion" for assessing rupture risk is that the probability of AAA rupture increases with increasing diameter. Taken together, these suggest that an increase in AAA wall dimension (i.e., AAA diameter) is associated with a decrease in wall strength.

To explore this, we performed a preliminary paired study of AAA wall specimens from the same AAA, but obtained from region with a larger diameter vs. a small local diameter. A total of seven separate patients with AAA (age 73.4 ± 2.4 years; 6.9 ± 0.7 cm AAA diameter)

supplied these paired wall specimens for tensile strength testing. The results are shown in **Figure 34**.

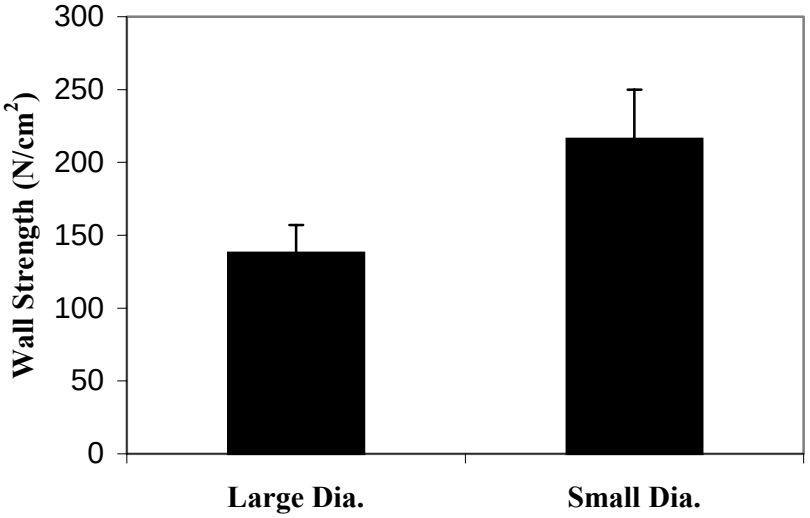

Figure 34 Comparison of tensile strength for wall specimens from a larger diameter region versus a smaller diameter region for paired samples. Significant difference was noted by means of the paired t test (N = 7, $p < 0.05$).

The paired t test indicates that the AAA wall specimens from the larger diameter regions were significantly weaker than specimens from the smaller diameter regions (138 N/cm^2 ± 19 N/cm^2 vs. 216 N/cm^2 ± 34 N/cm^2, $p < .05$).

Based on the above arguments and our preliminary experimental findings, we included local cross-sectional diameter as a potential predictor of local wall strength.

8.1.2.6 Patient Smoking Status as a Potential Predictor

Ultrasound screening surveys and case-control studies have demonstrated a strong epidemiological association between cigarette smoking and AAA. [7, 152, 177, 185-187] Smoking has also been associated with rapid AAA enlargement and rupture, [188, 189] and it was reported that there is a 5-fold increase in AAA rupture risk for cigarette smokers, versus non-smokers. [188] While the strength of the association and the presence of a dose response suggest a causal relation, etiologic mechanisms are unclear. [177] One possible mechanism for this is that continued absorption of chemicals from smoking may have effects on the proteolytic and fibrinolytic activities of the AAA wall, and also on smooth muscle cell metabolism. [189]

Studies by Pellegrini et al. and Wang et al. showed that smoking does alter specific aspects of endothelial function and enhances the acute endogenous fibrinolytic capacity in vivo. [190, 191] Smoking is also related to elevated proteolytic activities in lung tissue [192, 193] and altered SMC function in arteries. [194] Aortic stiffness is increased in smokers compared with nonsmokers. [195]

For these reasons, we believe that smoking may have a marked influence on AAA wall weakening. In this study, therefore, the patient's smoking status was selected as a potential predictor of AAA wall strength.

8.1.2.7 Family History as a Potential Predictor

Familial tendency of AAA has been demonstrated in several studies. [196-201] In a large case-control study by Darling et al. [196], 15 percent of AAA patients reported this disease in at least one first degree relative as compared with 1.8 percent of controls (odds ratio = 9.7). A similar study by Johansen and Koepsell [199] reported that 19 percent of the cases had at least

one first degree relative with an AAA in comparison with only 2.4 percent of controls (odds ratio = 11.6). Other studies have estimated the prevalence of AAA among family members of AAA patients without comparison to an explicit control group. In these studies, 11-20 percent of cases were found to have at least one first degree relative with an AAA. [197, 198, 200, 201] To our knowledge, no studies exist that examine the influence of family history on AAA wall microstructure or biomechanical properties. However, because of the strong familial tendencies in AAA disease, we believe that family history should be included as a potential predictor of AAA wall strength.

8.1.2.8 Other Potential Predictors

There are many other parameters, including hypertension, coexisting pulmonary disease, AAA configuration (ILT volume, the ratio of ILT and AAA volume, etc.), and AAA expansion rate, that may be associated with AAA wall weakening. [14, 15, 46, 53, 108, 127, 148, 174, 202-204] However, the purpose of this study was not to determine what causes AAA wall weakening, or to determine the most influential variables relating to AAA wall strength. Rather, the purpose was to develop an AAA wall strength prediction model based solely on some easily obtained clinical variables. Ideally, the best model is the one that uses the least number of predictors but provides the greatest predictive power. An increased number of predictors demand an increased sample size which might not be practical. Our approach here was to start with a limited number of candidate predictors resulting from some clinical or experimental observations. Relying on regression analysis results and significance tests, we then can decide if more variables are needed or if redundant variables need to be removed from our model. If it turns out that using all seven

candidate parameters can not predict local AAA wall strength accurately, the other potential predictors will be considered.

8.1.2.9 Summary

In summary, we chose the following seven clinically measurable variables for our model for local AAA wall strength: patient's age, gender, smoking status, family history, AAA size, local AAA diameter and local ILT thickness. Among these variables, patient's age, gender, smoking status, family history and AAA size would give a base-line strength for each individual patient. The other parameters (local AAA diameter and ILT thickness) would account for local variations of wall strength in an individual AAA.

8.2 Methods – Statistical Model Construction and Validation

There are two steps in statistical modeling: 1) constructing the model to quantify the relationship of one or more independent variables to the dependent variable; and 2) validating the constructed model by comparing a set of observed values to the model-predicted values. The detailed methods used for each of these steps in our model development procedure for local AAA wall strength are described below.

8.2.1 Data Collection

For any model construction or validation procedure, the first step should be data collection. In the present study, the necessary data includes each of the chosen independent

variables (patient's age, gender, smoking status, family history, AAA size, local AAA diameter, and local ILT thickness), and also the dependent variable (local wall strength). In the following subsections, we describe the method used for such data collection.

8.2.1.1 Measurement of Patient-Specific Independent Variables

Consenting patients undergoing traditional AAA repair surgery at the University of Pittsburgh Medical Center were selected for this part of the study. All procedures were carried out in accordance with NIH guidelines and the University of Pittsburgh biomedical Internal Review Board. General information on the patient (e.g., patient's age, sex, smoking status, family history, and AAA size) was obtained from the patient's hospital chart.

8.2.1.2 Measurement of Local Independent Variables and Local Strength

At the time of surgery, and just after cross clamping, a wedge of ILT with a piece of wall attached was cut and removed from the intact aneurysm (**Figure 35**). The aneurysm was then cut open and the remaining ILT was removed. Both the wall specimen with ILT attached as well as the remaining ILT were immediately immersed in a container of PBS until the time of testing. All the samples were tested immediately or stored at 4^{o}C and tested within 24 hours.

At the time of testing, the wedge was inserted back to the whole thrombus (**Figure 35A**) and sliced into cross-sections (**Figure 35B**). A thin strip of circumferentially-oriented wall (typical dimension of 0.2 x 1.5 cm) was cut from the edge of the wedge-shaped wall sample (**Figure 35 C**). Measurements of the local parameters for each such wall specimen, i.e., local diameter and local ILT thickness, were made on the cross-section. Measurements of two

randomly chosen, orthogonal cross sectional diameters were taken and averaged to provide the local diameter for each circumferentially-oriented wall sample (**Figure 35 B**). ILT thickness measurements were taken at each end of attached wall sample and the average was taken as local

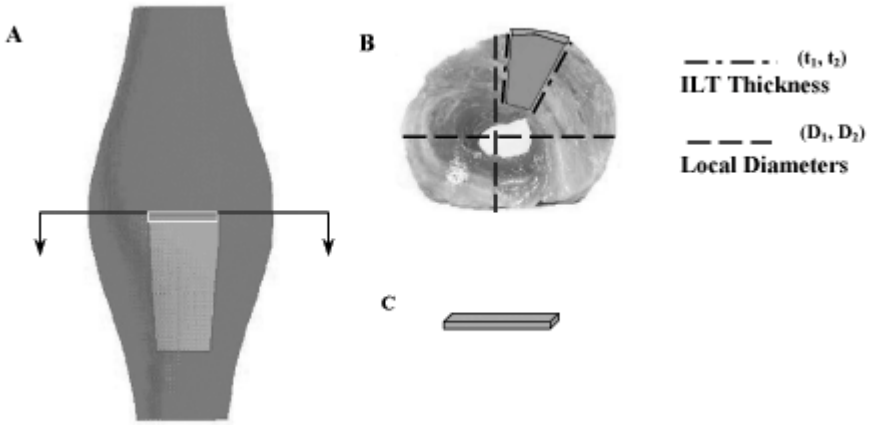

Figure 35 Schematic of AAA wall sample preparation and local parameter measurement. A wedge-shaped sample of ILT was cut and removed with a piece of wall attached (A). Then the whole thrombus was removed from the aneurysm as is routine in open surgical repair. The wedge-shaped ILT were put back in the whole thrombus and sliced into cross-sections, as shown in (B). The local ILT thickness and local diameter were then measured on the cross-section. A slice of circumferentially-oriented wall specimen was harvested from the wedge-shaped sample edge (C).

ILT thickness for the specimen (**Figure 35 B**). The local diameter measurement and local ILT thickness for each sample were carefully logged.

The AAA wall specimens were then individually mounted and tested to failure in our uniaxial tensile testing device as described in Section 3.2. The only exception was that no preconditioning was performed before pulling the sample to failure since we were not interested in quantifying the elastic behavior of the tissue. Data analysis was also carried out as described in Section 3.2. The peak value of stress attainable by each specimen (i.e., its tensile strength) was recorded. Only specimens that failed at points remote from the clamps were analyzed and reported in this study. Data from unsuccessful tests (i.e., due to slipping from, or failure at the clamps) were discarded.

8.2.2 Statistical Model Construction -- Multiple Linear Regression

Multiple linear regression is one statistical tool for evaluating the possible relationship of one or more independent variables to a single continuous dependent variable. [205] In this sense it allows the construction of a mathematical model relating the independent variables to the dependent variable. This tool and its utilization in the present work are described here. All the following analyses were done using the statistical software package NCSS ™ (Version 2001, NCSS, Kaysville, Utah).

8.2.2.1 Fundamentals of Multiple Linear Regression

For a simple linear relationship between the independent and dependent variables, one can write as a mathematical model: [205]

$$Y = \beta_0 + \beta_1 x_1 + \beta_2 x_2 + \ldots + \beta_k x_k + \varepsilon \quad (8.1)$$

where Y is the *dependent variable* (i.e., localized strength of AAA wall), the X_i are the dependent variables (i.e., the seven potential predictors of local wall strength), β_i are the individual constants of proportionality, and ε is the error or *residual* which describes the discrepancy between the model-predicted value and the *observed* (i.e., experimentally measured) *value*. In the current situation, we would write

$$Y = \beta_0 + \beta_1 * \text{ILT} + \beta_2 * \text{AGE} + \beta_3 * \text{SIZE} + \beta_4 * \text{DIA} + \beta_5 * \text{HIST} + \beta_6 * \text{SMK} + \beta_7 * \text{SEX} + \varepsilon \quad (8.2)$$

where the β_i are regression coefficients, ILT is the measured thickness of the attached ILT, AGE is the patient's age, SIZE is the maximum diameter of the aneurysm, DIA is the local AAA wall diameter, HIST is the patient's family history of AAA, SMK is the smoking status of the patient, and SEX is the gender of the patient.

8.2.2.2 Assumptions of Multiple Linear Regression

The following assumptions are implied when using multiple regression analysis: 1) The relationship between Y and each Xi is linear; 2) the "constant variance" assumption states that the variance of Y is constant for any fixed combination of X's; 3) the "normality" assumption states that for any fixed combination of X's, the residual term ε is normally distributed; 4) the independence assumption states that each observation is independent and uncorrelated with any other; 5) all independent variables are assumed to be independent of each other; and 6) all special

causes, outliers (rare or unusual observation that appears at one extreme of the data range) due to one-time situations have been removed from the data. Each of these assumptions is defined and discussed below.

8.2.2.2.1 Linearity

Multiple linear regression assumes that Y is a linear function of $X_1, X_2, \ldots X_k$ as shown in equation 8.1. The residual term ε in equation 8.1 reflects the difference between the observed value of Y and the model-predicted value. A simple and effective way to detect any existing nonlinear relationship in regression analysis is by examining the residuals. The ith residual is defined as

$$\varepsilon_i = Y_i - \bar{Y}_i \qquad (8.3)$$

where Y_i is the observed value and $\bar{Y}_i$ is the model-predicted value. This is most easily evaluated by a scatter plot of the residuals versus both Y and X_i which are called residual plots. Any nonlinear patterns that appear in the residual plots indicate a deviation from the linearity assumption. If a nonlinear pattern is detected, the model must be modified by adding a quadratic term, taking logarithms of Y and/or X, or some other appropriate transformation. [206]

8.2.2.2.2 Constant Variance (Homoscedasticity)

The residuals are assumed to have constant variance across all values of X. Like for the linearity assumption, nonconstant variance can be detected on a scatter plot of the residuals versus Y and/or X_i. If the residual plots show a horizontal band of points without any systematic

trends (i.e., a rectangular shape around zero value), the constant variance assumption holds. On the other hand, if a residual plot shows an increasing or decreasing wedge, nonconstant variance exists and must be corrected. A few of the general patterns that may emerge from a plot of residuals vs. predicted values are shown in **Figure 36.** [207] **Figure 36 A** illustrates the type of pattern to be expected when the linearity and constant variance assumptions hold: a horizontal

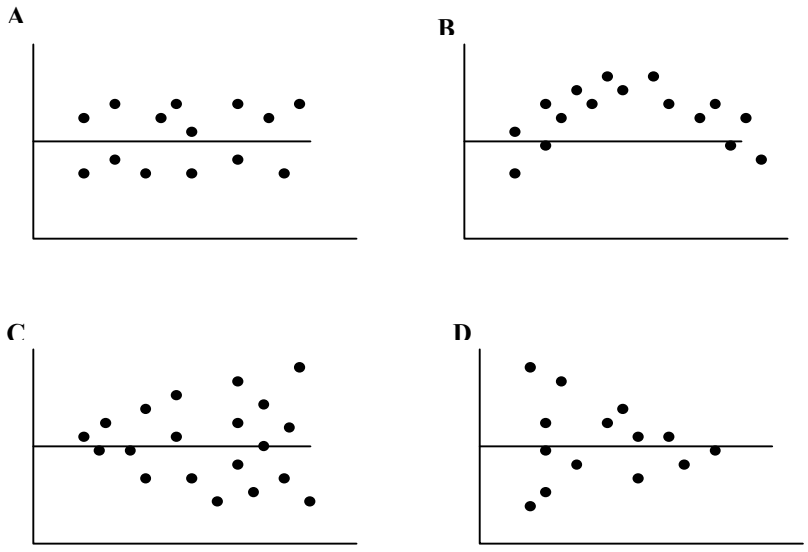

Figure 36 Typical residual plots as a function of predicted value Y for hypothetical data. (Adapted from [207]) Data satisfy both the linearity and constant variance assumptions. B) Data depart from linearity. C) Residual variance increase with Y. D) Residual variance increase with Y.

band of points with no hint of any systematic trends. **Figure 36B** shows a systematic pattern to be expected when the data depart from the linearity, indicating a need for curvilinear terms in the regression model. **Figure 36C** represents the pattern when the residual variance increases directly with Y. **Figure 36D** represents the pattern when the residual variance increases directly

with Y be expected when the linearity. When nonconstant variance is detected, a variance-stabilizing transformation such as the square-root or logarithm may be used.

8.2.2.2.3 Normality

When hypothesis tests and confidence limits are to be used (i.e., as in our case, where we wish to test the hypothesis that an individual potential predictor is statistically significant), the residuals are assumed to follow the normal distribution. If the residuals are not normally distributed, then the t-tests on regression coefficients, the F-tests, and any interval estimates are not valid. Therefore, this is a critical assumption to check. The normality of the residuals can be visually evaluated by graphical displays, such as normal probability plots of residuals and/or the histogram of the residuals. If the residuals are normally distributed, then the data points of the normal probability plot will fall along a straight. Major deviations from this ideal situation reflect departures from normality. **Figure 37A** illustrates a sample probability plot that could be expected when normality assumption holds; i.e., the majority of the residuals lie about a straight line. One or two residuals far away from the line may be indicative of outliers, not nonnormality. **Figure 37B** shows a pattern to be expected when the data depart from the normal distribution.

A more formal approach is to use the Normality (a.k.a., omnibus) test based on *skewness* and *kurtosis*. Skewness measures the direction and degree of asymmetry of the residual histogram. (**Figure 38**). A value of zero indicates a symmetrical distribution. A positive value indicates skewness (longtailedness) to the right of the mean (**Figure 38A**) while a negative value indicates skewness to the left (**Figure 38B**). Values between -3 and +3 are typical of a normal or

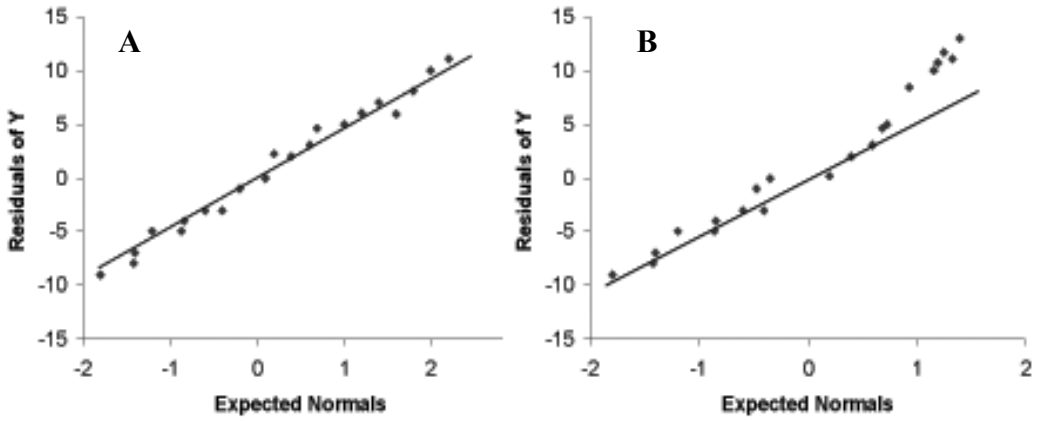

Figure 37 Example normal probability plots based on hypothetical data. A) In this case, the data follows a straight line; therefore, the normality assumption is met. B) In this case, the data deviates from a straight line; therefore, the normality assumption is not met.

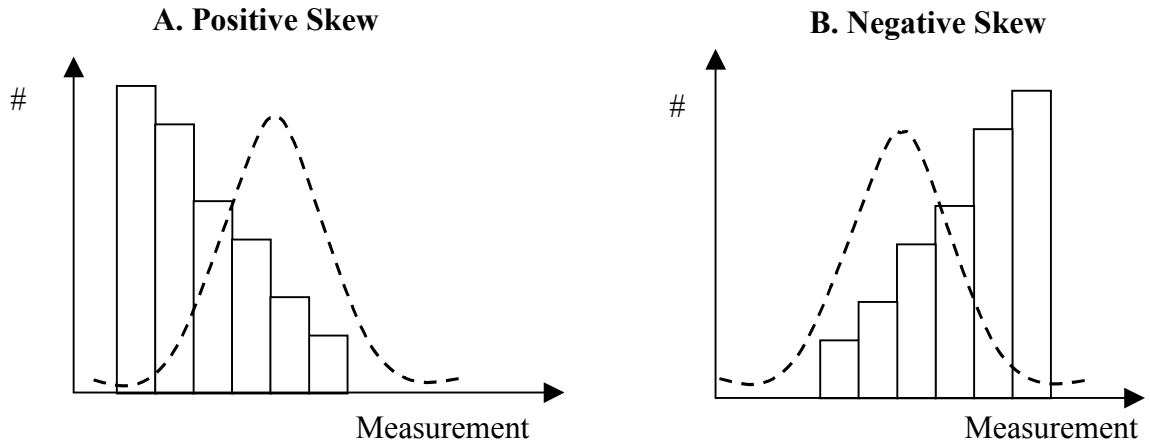

Figure 38 Histograms of positive and negative skewed distributions. A) positive and B) negative skewed distributions. The dotted line represents the normal distribution.

near-normal distribution. Kurtosis measures the heaviness of the tails of a distribution relative to the middle of the distribution, or the flatness of a distribution. The usual reference point in kurtosis is the standard normal distribution that has a kurtosis value of three. If the kurtosis statistic equals three and the skewness is zero, the distribution is perfectly normal. However, values between 2 and 4 are typical of a normal or near-normal distribution. **Figure 39** shows two distributions with the same skewness but opposite kurtosis. **Figure 39A** shows a distribution with Kurtosis larger than three, which means the distribution is skinnier than normal. **Figure 39B** shows a distribution with Kurtosis less than three, which means the distribution is flatter than normal. The statistical software NCSS calculates the skewness and kurtosis values automatically.

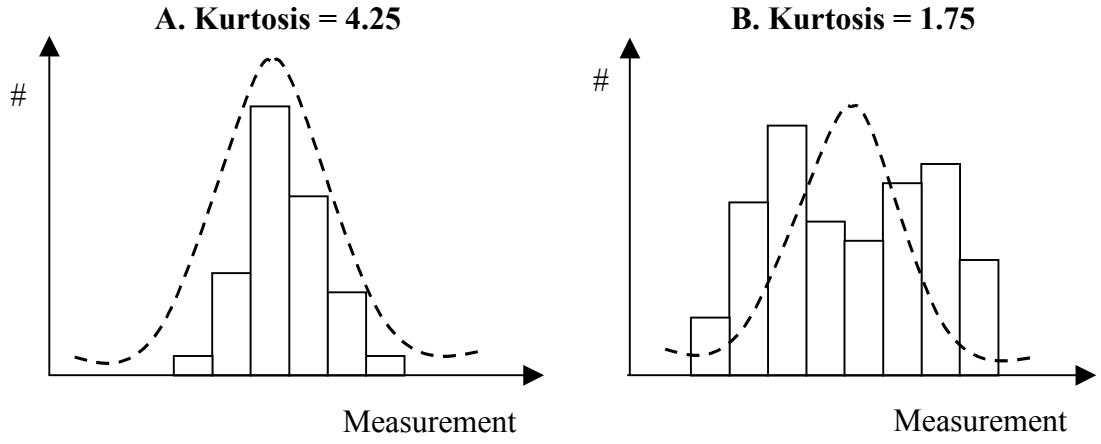

Figure 39 Two histograms which have approximately the same skew but markedly different kurtosis; i.e. A) greater than three and B) less than three. The dotted line represents the normal distribution curve.

Generally, remedies for non-normality involve transformation of the data. In particular, incorrect functional forms for the predictive model, outliers and violations of the constant variance assumption can cause the error terms to be non-normal. Appropriate transformation (e.g., the logarithm transformation) of the dependent variables often correct the non-normality problems after removing outliers.

8.2.2.2.4 Independence /Autocorrelation

The independence assumption states that residuals are uncorrelated with one another, which implies that the Y's (dependent variable observed values) are also uncorrelated and independent of one another (*independence assumption*). [207] If this assumption is met, it is said that there exists no *autocorrelation* among the observed data, and simple linear regression techniques can then be used to compute the regression coefficients. The presence of autocorrelation makes statistical inference invalid. Estimated values of regression coefficients, their standard error, and the p values are not reliable in this case. Any hypothesis tests or confidence limits that require the use of the t or F distribution would be also invalid. [208] Autocorrelation is usually violated when the observations are taken over time. For the present study, since observations taken from the same subject might be related, it is quite possible that the residuals are correlated with each other (e.g., all positive for one patient and all negative for another). If that is the case, autocorrelation exists and must be corrected.

To detect the presence of autocorrelation among the data (i.e., check the independence assumption), a formal statistical test called the Durbin-Watson test can be used. [208] It tests the

null hypothesis that autocorrelation is present by using the Durbin-Watson statistic d, which is calculated as follows:

$$d = \frac{\sum_{i=2}^{k} (\varepsilon_i - \varepsilon_{i-1})^2}{\sum_{i=1}^{k} \varepsilon_i^2} \qquad (8.4)$$

The testing procedure operates as follows:

-- If $d < d_L$, reject the null hypothesis. No autocorrelation exists;

-- If $d > d_U$, do not reject the null hypothesis . Autocorrelation does exits;

-- If $d_L < d < d_U$, the test is inconclusive.

The values of (d_L, d_U) for different percentage points have been tabulated by Durbin and Waston. This table can be found in most standard statistical textbooks. [208]

When the Durbin-Watson statistic indicates that autocorrelation exists, modeling techniques that adjust for autocorrelation, e.g., mixed models, [209] must be used.

8.2.2.2.5 Multicollinearity

When the independent variables in a regression model are interrelated or are dependent on each other, multicollinearity is said to exist among them and the independence assumption is violated. In essence, multicollinearity reflects the redundancy of the independent variables. Multicollinearity can create inaccurate estimates of the regression coefficients, inflate the standard errors of the regression coefficients, deflate the partial t-tests for the regression coefficients, give false insignificant p-values (shows insignificant when it is actually significant),

and degrade the predictability of the model. Multicollinearity affects both statistical inference (how we interpret the model) and the model's forecasting ability.

To detect the collinearity in the data, one should first inspect the correlation matrix. Any high correlation value between two variables (i.e., R > 0.5) reveals correlation between the two parameters. Unfortunately, multicollinearity is not always detectable in this way. Two alternate methods can be used to detect multicollinearity: the *variance inflation factors (VIF) method* and the *condition number method.* [207] VIF is calculated as [207]

$$VIF_i = \frac{1}{1 - R_i^2} \tag{8.5}$$

where the R_i^2s are the R^2 obtained when the ith variable is regressed on the remaining independent variables (i = 1, 2, …, n, where n is the number of independent variables). A VIF value of 10 or more for large data sets indicates a collinearity problem since the R_i^2 with the remaining X's is 90 percent. For small data sets, even VIF values of 5 or more can signify collinearity. A large condition number can also indicate collinearity. The condition number is the largest eigenvalue of the correlation matrix divided by each corresponding eigenvalue of the correlation matrix. An eigenvalue of zero or close to zero indicates that an exact linear dependence exists. Condition numbers greater than 1000 indicate a severe collinearity problem while condition numbers between 100 and 1000 indicate a mild collinearity problem. [207] Condition numbers between 0 and 100 indicate no collinearity problem.

The best solution to the multicollinearity problem is to remove the redundant variables. One approach is to remove one or more of the highly correlated variables. However, one must be careful not to remove an independent variable that is important in describing and predicting

the dependent variable. The second possible solution is to add more observations to the data used in building the regression model so that the multicollinearity is (possibly) lessened. A proper scaling technique might also help eliminate the collinearity. [207]

8.2.2.2.6 Outliers and High Influential Points

There are two types of possible problematic observations in the collected data, *outliers* and *high influential points*. An observation that is well separated from the rest of the data is called an *outlier*. Outliers have residuals that are large relative to the residuals for the remainder of the observations. An observation that cause the regression result to be substantially different from what it would be if the observations were removed from the data set is called a *high influential point*. The existence of outliers and high influential points will cause serious distortions in the regression calculations and yield misleading decisions, inference, and regression coefficients, and may cause nonconstant variance, nonnormality, or other problems with the regression model. Therefore, they should always be detected and removed before one can make any interpretation and decision based on modeling.

The first step in this process is detection; i.e., to determine if an X or Y observation is an outlier with respect to their mean values. The second step is to determine whether such outliers are influential. In order to identify outliers in X space, *the hat diagonal*, also known as *leverage,* is used. Consider the following regression model

$$Y_i = \beta_0 + \beta_1 X_{i1} + \beta_2 X_{i2} + \ldots + \beta_p X_{ip} + \varepsilon_i \qquad (8.6)$$

The *hat matrix* for the **X** space, for example, is defined as

$$\mathbf{H} = \mathbf{X}(\mathbf{X}'\mathbf{X})^{-1}\mathbf{X}' \quad (8.7)$$

Where X is the array of observed values of the independent variables.

$$\mathbf{X} = [1, X_{i1}, X_{i2}, \ldots, X_{ip}], \quad i = 1,2,\ldots, n$$

n is the total number of observations. The diagonal elements $\mathbf{H_{ii}}$ of the hat matrix **H** is defined as the hat diagonal. Each observation of X is associated with a hat diagonal value. Any observation with hat diagonal greater than two times the number of coefficients in the model divided by the number of observations (i.e., > 2p/n, p is the number of coefficients and n number of observations) is considered an outlier in the **X** space.

To determine outliers in Y space, one can examine the ith residual ε_i, or *the Studentized Residual*. The Studentized Residual is a modification of the standard residual defined as

$$r_i = \frac{\varepsilon_i}{s\sqrt{1 - H_{ii}}} \quad (8.8)$$

where r_i is the Studentized residual for each observation; ε_i is the regression residual; *s i*s the standard deviation; and H_{ii} is the ith diagonal element of the hat matrix **H** in equation 8.7. Dividing ε_i by $s\sqrt{(1-H_{ii})}$ instead of *s* guarantees that the n populations of all possible student residuals have equal variances and are of the same relative magnitude. The Studentized residual is so named because it approximately follows a Student's t distribution with n-p-1 degrees of freedom, if the data follow the normal distribution assumption of multiple regression. Therefore, if the absolute value of the studentized residual is greater than the t statistic value for n-p-1

degrees of freedom at 95% confidence interval $t_{(n-p-1,\ 0.025)}$, this residual is considered to be large at $\alpha = 0.05$ level, and the ith observation is considered to be an outlier with respect to its Y value.

After we have concluded that the ith observation is an outlier with respect to its X or Y value, we can determine whether the ith observation is a high influential point by calculating *Cook's Distance measure*, D_i:

$$D_i = \left(\frac{r_i^2}{p} \right) \left(\frac{H_{ii}}{1 - H_{ii}} \right) \tag{8.9}$$

where r_i is the studentized residual, p is the number of independent variables, and H_{ii} is the ith hat diagonal. D_i is an overall measure of how an observation impacts the regression coefficients and is related to the ith studentized residual as well as the hat diagonal. To decide whether the ith observation is high influential point or not, the following test that compares Di with the standard F-statistic is carried out: [208]

1. If $D_i < F_{(p,\ n-p,\ 0.80)}$ (the 20th percentile of the F-distribution having p and n-p degrees of freedom), then the ith observation should not be considered influential.
2. If $D_i > F_{(p,\ n-p,\ 0.50)}$ (the 50th percentile of the F-distribution having p and n-p degrees of freedom), then the ith observation should be considered influential.
3. Anything between (i.e., $F_{(p,\ n-p,\ 0.50)} < D_i < F_{(p,\ n-p,\ 0.80)}$) is considered inconclusive.

Once problematic observations are identified, one has to decide what to do about these observations. If it was caused by incorrect measurement or erroneous recording, the observation should be corrected (if it can be corrected), and the regression analysis should be rerun. If the observation can not be corrected, then it should be dropped from the data set. If no explanation can be found for an influential outlying observation, it might not be appropriate to drop this observation from the data set.

In summary, we examined the hat diagonal to detect outliers in X space, studentized residuals to detect outliers in Y space, and Cook's D to detect high influential points.

8.2.2.3 Model Selection

To select the best regression equation, one first needs to define the initial model which has all the potential predictors. In this study, the initial model consists of all the potential predictors discussed in Section 8.1.2. (i.e., patient's age, gender, smoking status, family history, AAA size, local wall diameter, and local ILT thickness). Then, starting from the initial model, one can work towards selecting the model which includes all the significant predictors and more importantly, the one which fits the data well.

The second step is to define criterion that describes how well the regression model fits the data. There are several statistical measures of model adequacy. Among them, the coefficient of determination R^2 is probably the most popular, and is defined as the ratio of *the model sum of squares* divided by *the total sum of squares*:

$$R^2 = \frac{SS_{Model}}{SS_{Total}} = \frac{1 - \sum (y_i - \hat{y}_i)^2}{\sum (y_i - \bar{y})^2} \tag{8.10}$$

where y_i is the observed (measured) value, $\hat{y}_i$ is the response value predicted by the model, $\bar{y}$ is the average of all the observed y_i's. The total sum of square SS_{Totoal} is the sum of deviations of observed values y_i's from the mean $\bar{y}$. It represents the total variation of y_i's before accounting for the linear effect of the independent variables. SS_{Model} is the sum of squares due to regression. It represents the variation explained by the model. Therefore, the R^2 value may be interpreted as the proportion of the total variability in y_i's that is explained by the combination of the

predictors. If R^2 is near 1, then the model explains all of variation in y_i's. For linear regression, a value of R^2 near zero indicates no linear relationship between the y_i's (the dependent variables) and the independent variables. In the current study, we employed $R^2 = 0.80$ as a criterion for model acceptance.

It should be noted that a large value of R^2 does not necessarily imply that regression model is a good one since adding a variable to the model will always increase R^2, regardless of whether or not the additional variable is a statistically significant predictor. Thus, models that have large values of R^2 may yield poor predictions of the dependent variable. Again, it is important to test whether each individual variable is significant or not. If it is not, one may consider that variable redundant and remove it from the model. The final, best model is the one that is both statistically significant ($p < 0.05$) and with a reasonable R^2 value ($R^2 = 0.80$).

To examine whether the model explains a significant amount of variation in Y, an F statistic test was also conducted. If the overall p-value is greater than a pre-selected significance level criterion, the combination of all the independent variables can not predict the variation in Y. In this work, we chose $p < 0.05$ as the criterion for model acceptance.

Not all the potential predictors in the initial model are necessarily significant. The third step in selecting the best, final model is to specify a strategy to eliminating the insignificant predictors or selecting the significant ones. To determine if an individual variable is a significant predictor or not, tests on individual regression coefficients are carried out. The testing of the significance of individual variables is equivalent to testing whether removing of this parameter will cause significant decrease in R^2. The criterion chosen here for removing individual insignificant variables is the associated p value. If the p value for a certain variable is less than some critical value (taken as 0.10 in current study), it means that removing this individual

parameter from the model would not reduce R^2 significantly. The variable is then considered insignificant and may be removed from the model. Removing all of the insignificant variables from the model has two advantages: it yields a simpler model, and it provides a better predictability. However, in some cases, a variable may be retained in an equation because of its scientific importance in a given problem, even though the sample regression coefficients are statistically insignificant. [206] For example, our group has shown that the presence of ILT causes a local hypoxic condition and wall weakening. [183] AAA wall adjacent to a thick layer of ILT is weaker and exhibits greater degrees of cellular hypoxia and inflammation with respect to wall specimens from the same AAA but adjacent to a thinner layer of ILT. Therefore, even if local ILT thickness was found to be statistically insignificant, we would tend to keep it in our model since it is considered scientifically significant.

The strategy described above and which we used to refine the model is called the step down procedure. [207] The procedure is described schematically by the flow chart in **Figure 40**. We applied this technique on a set of data collected as described in Section 8.2.1 specifically for the purposes of model construction.

8.2.3 Statistical Model Validation

After the model construction procedure was complete, the next step was to use a second, different data set to cross validate the developed model. If the developed model can also predict the local wall strength well for the second data set, it is then believed to have the desired predictability and we might apply the model to predict the local AAA wall strength in vivo. The cross validation procedure used here is described schematically by the flow chart in **Figure 41** and explained in detail below.

8.2.3.1 Patient Selection and Data Collection

Since any predictive model is applicable only within the range of data used for model construction, care was taken so that the characteristics of the patients and specimens in the validation group were inside the region of the data observed from the original data set. Local wall strength, local ILT thickness, local diameter, maximum diameter, patient's age, and patient's family history of AAA were collected as per Section 8.2.1. The new set of data was then used to validate the predictability of the developed model.

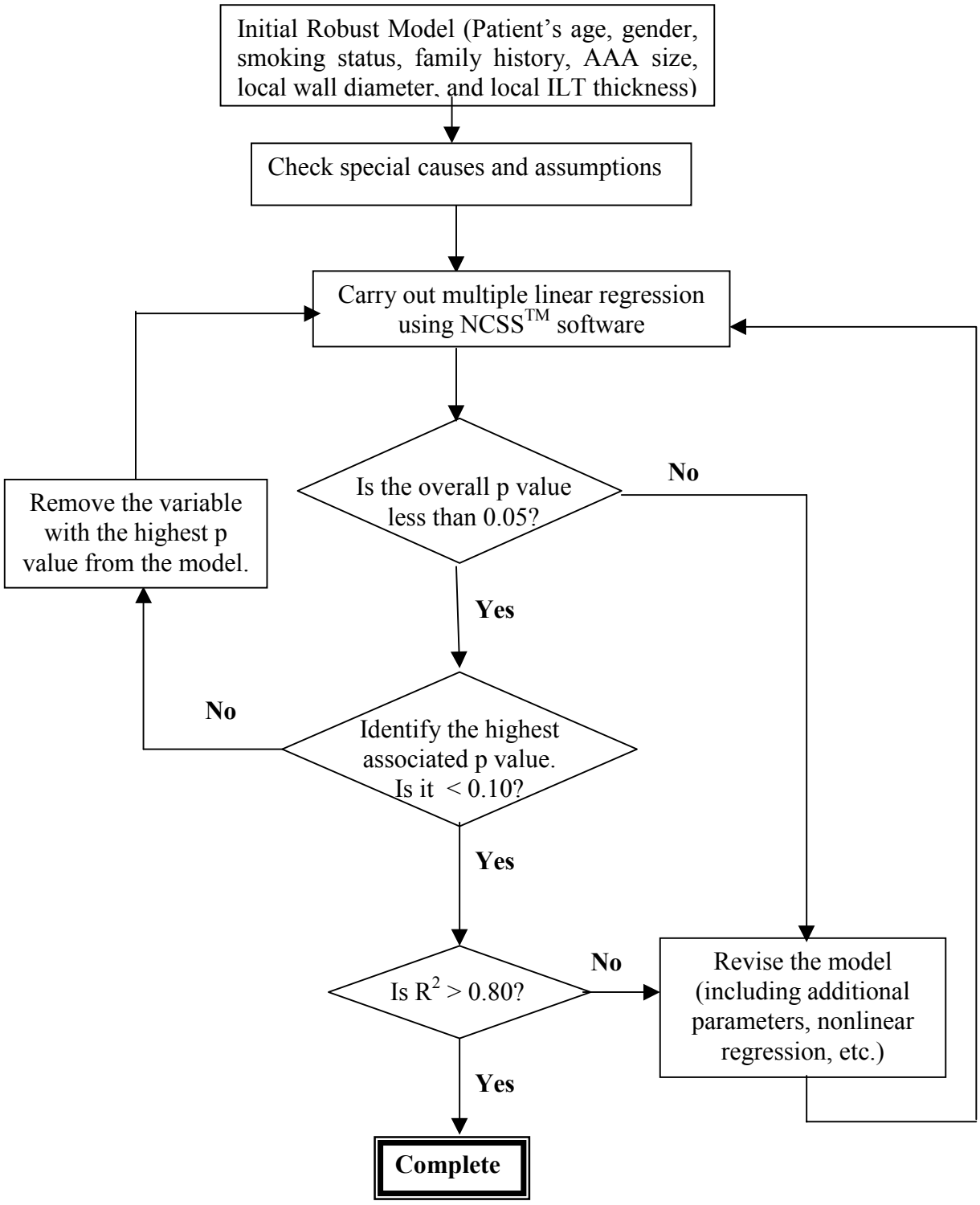

Figure 40 Procedure for model selection using the step down procedure.

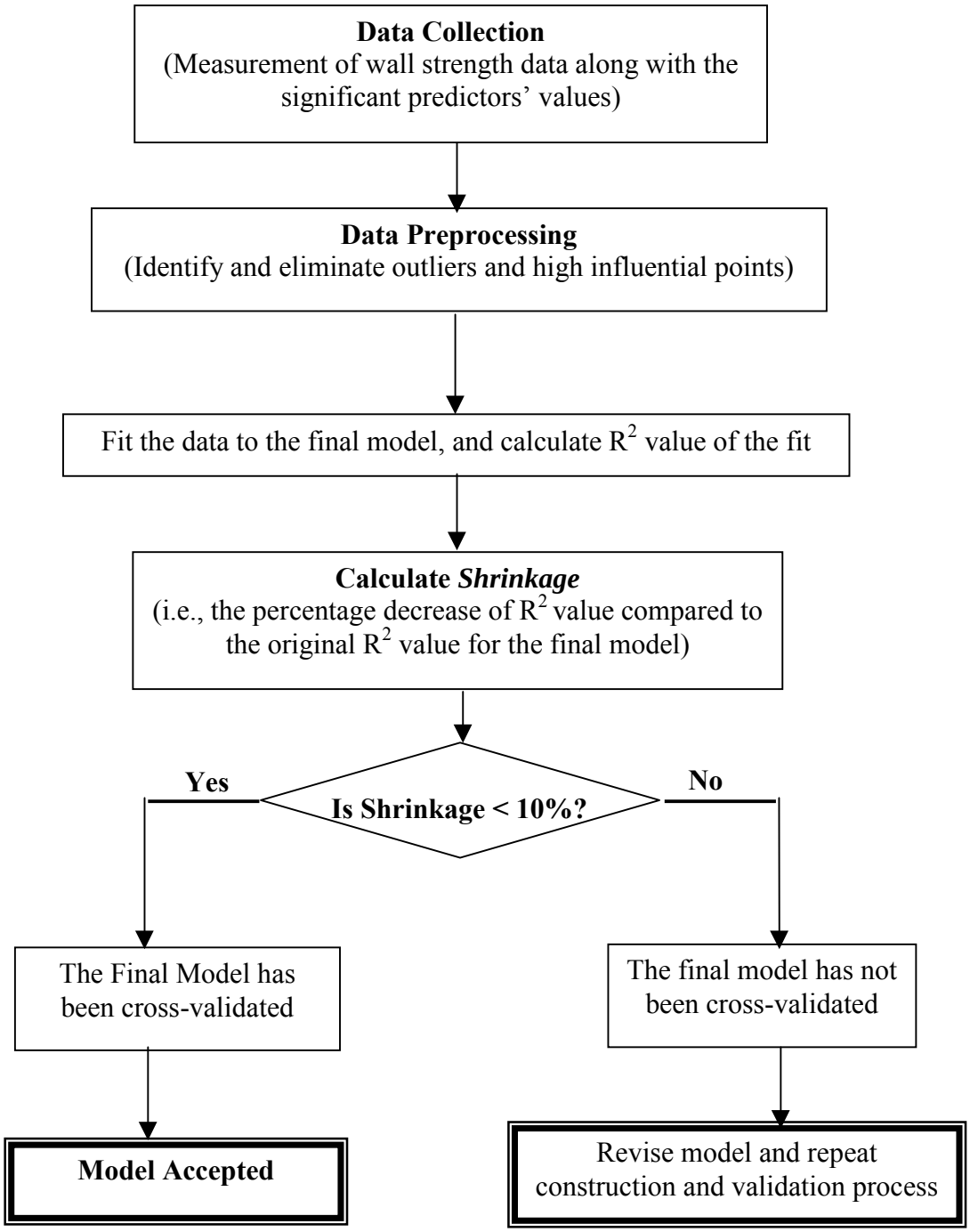

Figure 41 Procedure for model validation

8.2.3.2 Problematic Value Detection

Like any other data set, the validation data set might have contained extreme values, i.e., outliers and influential points, due to various reasons. Using a data set containing problematic data to validate a statistical model would yield an inaccurate judgement on the models' predictability. Therefore, the validation data set was inspected for outliers as described in Section 8.2.2.2.f and all detected problematic data were removed.

8.2.3.3 Cross Validation

The final model resulting from Section 8.2.2 was then applied to the processed data set to predict the wall strength value for each specimen based on its independent variable values. These predicted values were then plotted against the observed (experimentally measured) values. This scatter plot provided qualitative, visual information on the agreement between the observed and predicted values. To quantify the predictability of the model, the R^2 value was again calculated according to equation 8.10.

The manner in which regression coefficients are computed guarantee that they will provide an optimal fit with respect to the least square criterion *for the set of data* from which the model was constructed. If the purpose of the model is to predict a different set of data, the regression coefficients are no longer optimal. Hence, an R^2 value representing the fit of that model to the new data set will not be as large as the R^2 value from the original data set. This phenomenon is called *shrinkage*]. If the amount of shrinkage is less than 10% of the original R^2 value obtained in model construction, then the model is said to be *cross-validated*. [210, 211]

8.3 Results

8.3.1 Model Construction

Eleven consenting patients undergoing traditional AAA repair surgery at University of Pittsburgh Medical Center participated in the model construction phase of the study. Among them, seven were male and four females, four non-smokers and seven smokers. Four patients had family history of AAA. Their age ranged from 56 to 81, and the maximum AAA diameter ranged from 4.0 cm to 7.2 cm. From those 11 patients, a total of 40 AAA wall specimens were obtained and tested. 34 out of the total 40 tensile tests were successful. The other six tests were considered unsuccessful either because those specimens slipped from or tore at the clamps. Recorded strength ranged from 39 to 324 N/cm^2. ILT thickness ranged from 0 to 1.8 cm. Local diameter ranged from 2.1 to 6.85 cm. A summary of the tensile testing results and relevant patient information is tabulated in **Table 13**. The recorded strength value and measured model parameter values for each individual specimen is listed in **APPENDIX D.**

8.3.1.1 Data and Model Adequacy

8.3.1.1.1 Correlation and Collinearity

The correlation matrix for the multiple linear regression using all 7 predictors is shown in **Table 14**. This table indicates a strong positive correlation (R = 0.74) between the variables SIZE and DIA. To eliminate correlation, a new parameter, NORD, was defined as the local diameter normalized by the size of the aneurysm, and introduced. The variable DIA was replaced by NORD. The regression equation previously given by equation 8.2 then becomes

$$Y\ (STRENGTH) = \beta_0 + \beta_1 * ILT + \beta_2 * AGE + \beta_3 * SIZE + \beta_4 * NORD + \beta_5 * HIS + \beta_6 * SMK + \beta_7 * SEX + \varepsilon \quad (8.11)$$

Table 13 Summary of the 11 patients and of the results of the 34 tensile testing experiments used for the model construction phase. Of these 11 patients, 7 were male, 4 were smokers and 3 had family history. (See individual specimen data in Appendix D).

	Strength (N/cm^2)	ILT (cm)	Local Dia. (cm)	Size (cm)	Age (yrs)
Mean	145	0.71	4.1	5.3	69
Standard Error	12	0.08	0.22	0.3	3
Minimum	39	0	2.10	4.0	56
Maximum	323	1.78	6.85	7.2	81
Count	34	34	34	11	11

Table 15 shows the correlation matrix for the subsequent multiple linear regression using the new predictor variable NORD along with the other six variables. In this case, no correlation coefficient is larger than 0.50. Therefore it appears that transforming local diameter (DIA) into normalized diameter (NORD) eliminates the correlation between the variables SIZE and DIA.

Table 16 shows the regression report on multicollinearity. According to the criteria discussed in Section 8.2.2.e, i.e., all VIF are less than 5 and all condition numbers are less than 100, this report indicates that no collinearity conditions exist between the predictor variables.

Table 14 Correlation matrix from regression report using equation 8.2

	AGE	DIA	HIS	ILT	SEX	SIZE	SMK	Y
AGE	1.00	0.30	-0.14	-0.06	-0.37	0.05	0.45	0.21
DIA	0.30	1.00	-0.22	0.11	0.17	***0.74***	0.30	-0.26
HIS	-0.14	-0.22	1.00	-0.19	-0.15	-0.33	0.28	-0.52
ILT	-0.06	0.11	-0.19	1.00	-0.01	0.02	0.26	-0.17
SEX	-0.37	0.17	-0.15	-0.01	1.00	0.53	-0.23	0.14
Size	0.05	***0.74***	-0.33	0.02	0.53	1.00	0.18	0.23
SMK	0.45	0.30	0.28	0.26	-0.23	0.18	1.00	-0.04
Y	0.21	-0.26	-0.52	-0.17	0.14	0.23	-0.04	1.00

Table 15 Correlation matrix from regression report after transforming the data using equation 8.11

	ILT	SIZE	AGE	NORD	HIS	SMK	SEX	Y
ILT	1.00	0.02	-0.06	0.17	-0.19	0.26	-0.01	-0.17
SIZE	0.02	1.00	0.05	0.23	-0.33	0.18	0.53	0.23
AGE	-0.06	0.05	1.00	0.44	-0.14	0.45	-0.37	0.21
NORD	0.17	0.23	0.44	1.00	-0.06	0.33	-0.23	-0.51
HIS	-0.19	-0.33	-0.14	-0.06	1.00	0.28	-0.15	-0.52
SMK	0.26	0.18	0.45	0.33	0.28	1.00	-0.23	-0.04
SEX	-0.01	0.53	-0.37	-0.23	-0.15	-0.23	1.00	0.14
Y	-0.17	0.23	0.21	-0.51	-0.52	-0.04	0.14	1.00

Table 16 Multicollinearity diagnosis report for equation 8.11

Variable	VIF	Condition Number
ILT	1.46	1.00
SIZE	2.37	1.21
AGE	1.98	1.95
NORD	1.52	1.98
HIST	1.87	3.41
SMK	2.3	6.15
SEX	2.03	12.33

Table 17 Detection of problematic values by regression diagnostics statistics.

Sample	Hat Diagonal	Studentized Residual	Cook's D
1	0.2067	1.1932	0.0464
2	0.1711	-0.2432	0.0015
3	**0.2555**	1.9124	0.1569
4	0.2843	-0.8597	0.0367
5	0.2136	-0.3690	0.0046
6	0.2215	-1.7276	0.1062
7	0.1921	-0.4713	0.0066
8	0.1645	-0.0826	0.0002
9	0.1562	0.0520	0.0001
10	0.1640	-1.0674	0.0279
11	**0.2257**	-2.0249	0.1494
12	0.2271	1.3086	0.0629
13	0.1622	1.6027	0.0622
14	0.1679	1.4607	0.0538
15	0.3319	1.5481	0.1488
16	0.3546	0.4817	0.0159
17	0.3572	0.3673	0.0094
18	0.2311	0.6372	0.0153
19	0.2476	-0.7608	0.0238
20	0.2640	1.0211	0.0468
21	**0.2901**	1.9287	0.1900
22	0.1923	-1.3041	0.0506
23	0.2269	-1.0097	0.0374
24	0.2573	-0.4010	0.0070
25	0.2442	-0.3815	0.0059
26	0.2204	0.2425	0.0021
27	0.2071	0.1009	0.0003
28	0.2451	-0.1631	0.0011
29	0.2882	-0.6007	0.0183
30	0.2539	-0.3913	0.0065
31	0.2696	-0.4645	0.0100
32	0.2233	-0.2083	0.0016
33	0.2340	-0.7573	0.0219
34	0.2485	-0.3890	0.0063

8.3.1.1.2 Outlier and Influential Point Detection

For the initial model (Equation 8.11) and the data collected for the purpose of model construction (**Table 13** and **Appendix D**), the number of observations is n = 34 and the number of coefficients p = 7. Based on the criteria described in Section 8.2.2.2.f, observations with hat diagonals greater than 2*7/34 = 0.418 are considered outliers in X space. Any observations with the absolute value of Studentized residual greater than $t_{(34-7-1,\ 0.025)}$ = 1.910 are considered as outliers in Y space. Any observations with Cook's D greater than $F_{(7,\ 34-7,\ 0.50)}$ = 2.44 are considered as influential points. **Table 17** shows the values of the hat diagonal, Studentized residual, and Cook's D for all 34 data points. Based on the above criteria, three outliers in X space (#3, #11, and # 21) were detected and are highlighted in **Table 17**. These observations were deleted from the data set and the new data set was then fit against equation 8.11.

8.3.2 Residual Analysis – Assumption Check

In this section are the results of checking all the assumptions relating to multiple linear regression, namely constant variance, linearity, normality, and multicollinearity, as per Section 8.2.2.2.

8.3.2.1 Constant Variance

The error term in equation 8.11 is assumed to have a constant variance across the data range and a mean of 0. Plots of residual versus predicted values and versus each predictor are shown in **Figure 42** to **49**. In each case, the residuals are distributed randomly about 0 and no apparent trends appeared. Therefore, we conclude that the constant variance assumption is satisfied in this model.

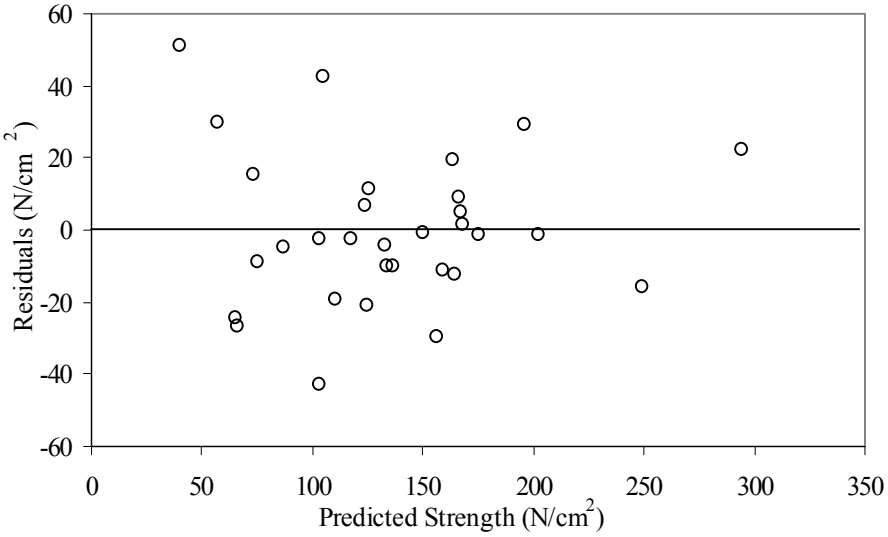

Figure 42 Scatter plot of residual vs. predicted strength. No apparent pattern exists with random distribution about Residual = 0 (line). This indicates that the constant variance and linearity assumptions are valid for the regression model.

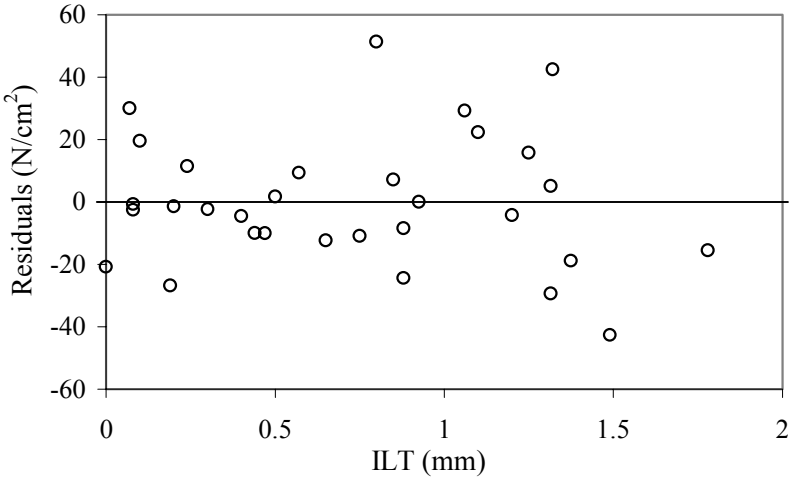

Figure 43 Scatter plot of residual vs. ILT. No apparent pattern exists with random distribution about Residual = 0 (line).

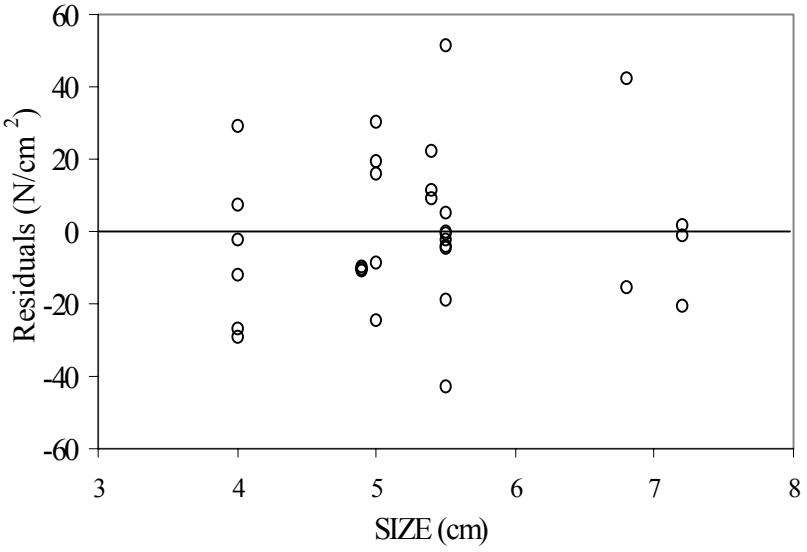

Figure 44 Scatter plot of residual vs. SIZE. No apparent pattern exists with random distribution about Residual = 0 (line).

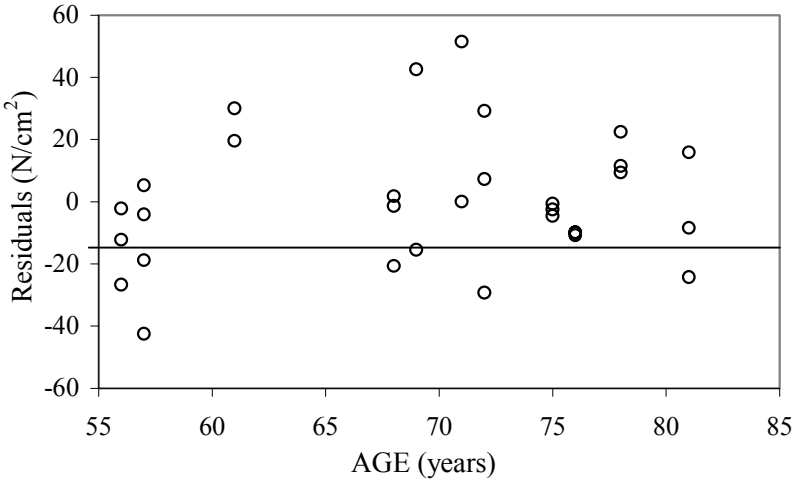

Figure 45 Scatter plot of residual vs. AGE. No apparent pattern exists with random distribution about Residual = 0 (line).

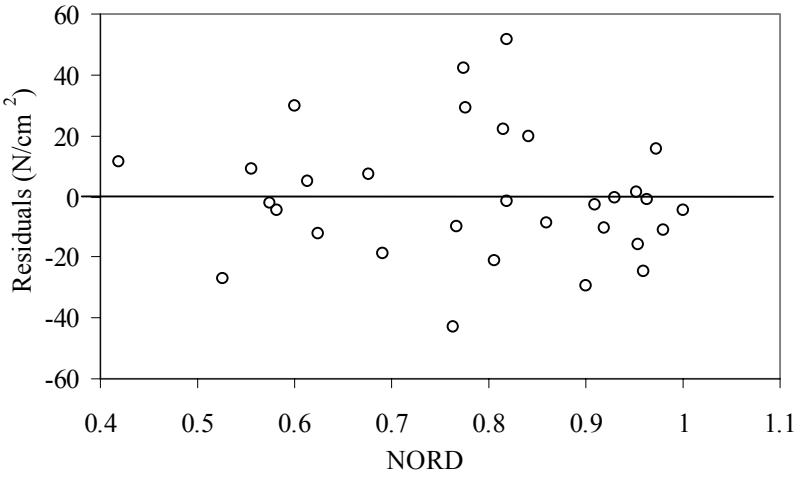

Figure 46 Scatter plot of residual vs. NORD. No apparent pattern exists with random distribution about Residual = 0 (line).

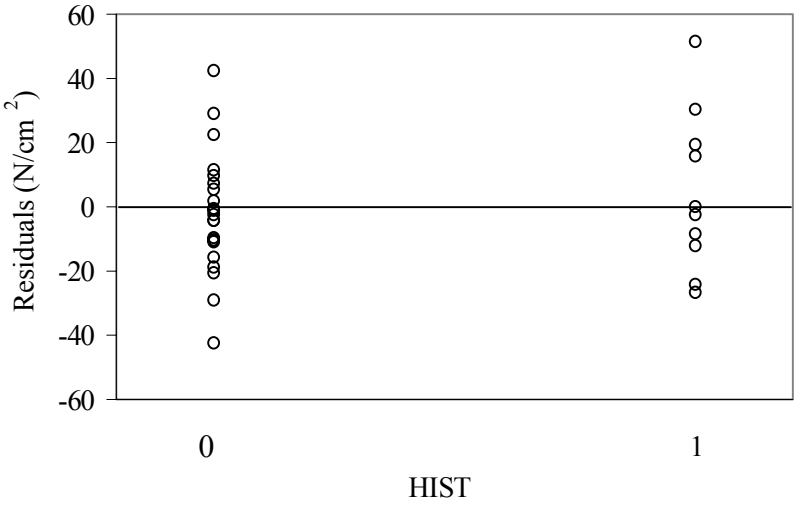

Figure 47 Scatter plot of residual vs. HIST. No apparent pattern exists with random distribution about Residual = 0 (line).

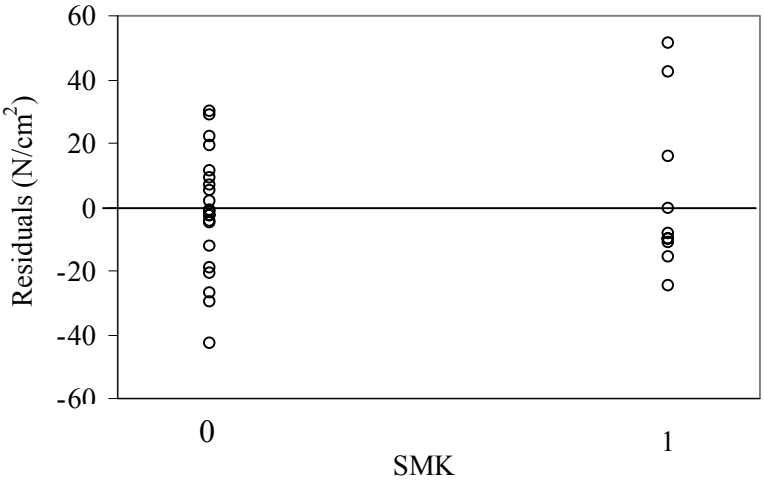

Figure 48 Scatter plot of residual vs. SMK. No apparent pattern exists with random distribution about Residual = 0 (line).

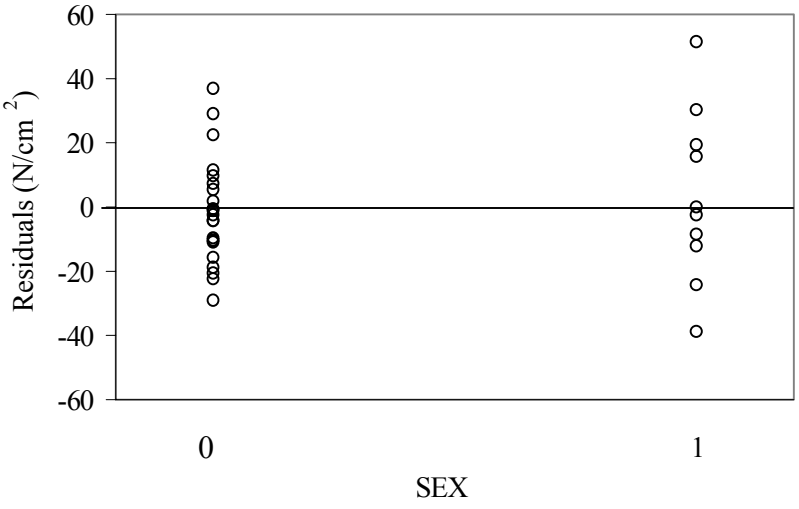

Figure 49 Scatter plot of residual vs. SEX. No apparent pattern exists with random distribution about Residual = 0 (line).

8.3.2.2 Linearity check

As described in Section 8.2.2.2.a, to check the linearity assumption, scatter plots of the residuals versus Y and each independent variables plotted in Section 8.3.2.1 were examined for any nonlinear pattern. It is clear that there is no systematic pattern in any of the residual plots. Therefore, the constant variance assumption is satisfied in this model.

8.3.2.3 Normality Check

As discussed in Section 8.2.2.2.c, the normality assumption states that the error term or residual in Equation 8.11 follows a normal distribution. A histogram of the error term is shown in **Figure 50**. It shows that the residual values follow a normal distribution.

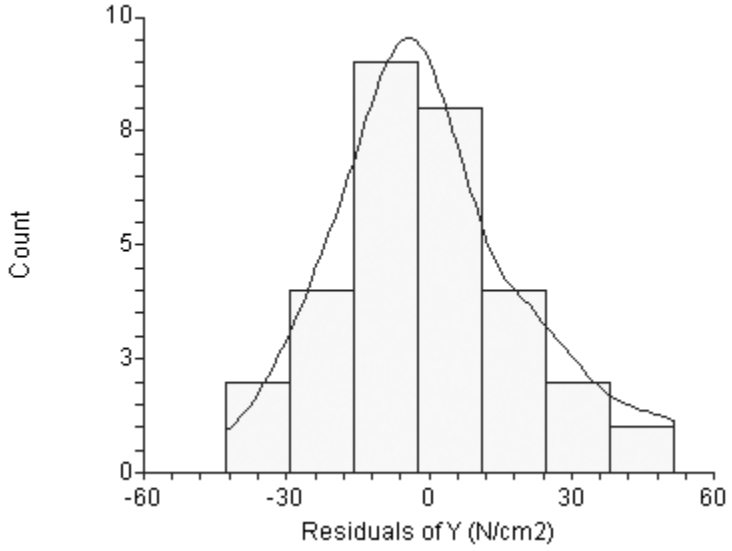

Figure 50 Histogram of the residuals for the regression results based on equation 8.11.

The normality plot in **Figure 51** shows that all the data points fall along a straight line, which also suggests that the normality assumption is met. The skewness and kurtosis of the observed data are shown in **Table 18**. The fact that –3 < skewness < 3 and 2 < kurtosis < 4 indicates that the normality test is accepted and there is no evidence that the residuals are not normal.

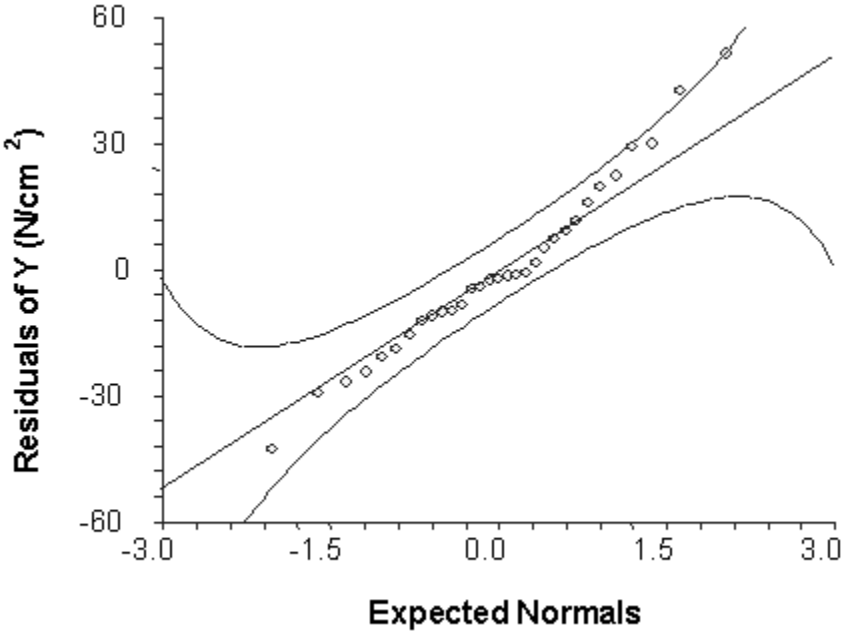

Figure 51 Normal probability plot of the residuals for equation 8.11. A linear pattern indicates that the underlying distribution of the data is normal. Confidence bands serve as a visual reference for departures from normality.

Table 18 Normality test results from the NCSS output.

Normality Tests Section		
Measure	**Value**	**Normality Accepted**
Skewness	1.22	Yes
Kurtosis	2.33	Yes

8.3.2.4 Independence or Serial Correlation

Using the method described in Section 8.2.2.2.d, for the number of observations n = 31 (after deleting 3 outliers), and number of estimated parameters p = 7, the Durbin and Watson table [212] gives $d_L = 1.09$, $d_U = 1.83$ at $\alpha = 5\%$ significant levels. The Durbin and Watson value determined by NCSS for this analysis is d = 1.3503, which lies in between the two critical values, d_L and d_U. Therefore, the test is inconclusive.

To determine if autocorrelation is a problem with our model, the residuals were grouped by each patient (**Figure 52)**. As discussed in Section 8.2.2.2.d, if the residuals for some patients are all negative, and other patients all positive, the residuals for individual patients are correlated and autocorrelation is a problem. As shown in **Figure 52**, the residuals of nearly all patients (9/11) are scattered about zero. Therefore, autocorrelation is not likely a problem for this study, and independence assumption is validated.

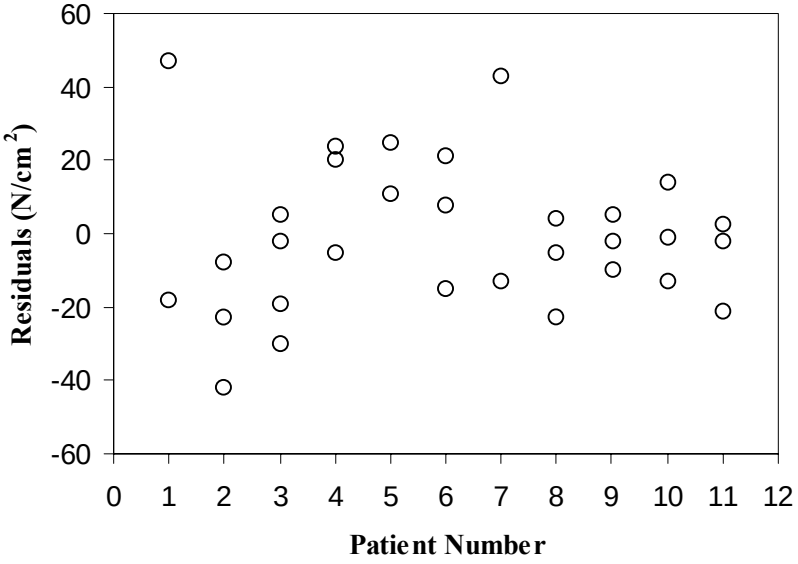

Figure 52 Based on the unrelated natural of the residuals for each individual patient, there is no strong evidence that the residuals in the same group are correlated.

8.3.2.5 Summary and Initial Model Regression

In summary, the assumptions of linearity, normality, constant variance, independence, multicollinearity, and no special causes related to multiple linear regression have been checked and satisfied for the current model.

Multiple regression results based on the model in equation 8.11 are listed in **Table 19**. Analysis of variance results are listed in **Table 20**. The overall R squared value is 0.8755, the overall p value is less than 0.0001.

Table 19 Regression analysis result output from NCSS for the regression of the data against the initial model, equation 8.11.

Independent Variable	Regression Coefficient	Standard Error	p value
Intercept	142.57	62.24	0.0315
ILT	-17.93	10.62	***0.1050***
Size	9.59	6.78	***0.1709***
AGE	3.08	0.73	0.0003
NORD	-284.56	35.91	0.0000
HIST	-81.21	12.45	0.0000
SMK	4.69	14.52	***0.7496***
SEX	-17.13	12.71	***0.1907***
R-Squared	0.88		

Table 20 Analysis of variance results from the regression output

Source	DF	Sum of Squares	Mean Square	F-Ratio	p Value
Intercept	1	564795	564795		
Model	7	93209	13316	23.12	0.0000
Error	23	13249	576		
Total	30	106458	3549		

The AAA wall strength model at this stage is written as:

$$\text{STRENGTH} = 142.57 - 17.93 * \text{ILT} + 9.59 * \text{SIZE} + 3.084 * \text{AGE} \quad (8.12)$$
$$- 284.56 * \text{NORD} - 81.21 * \text{HIST} + 4.69 * \text{SMK} - 17.13 * \text{SEX} + \varepsilon$$

This model is for strength in N/cm^2, ILT in cm, SIZE in cm. NORD has no units. HIST = 1 for patients with family history of AAA, 0 for no family history. Similarly, SMK = 1 for nonsmokers, and 0 for smokers, and SEX = 1 for females, 0 for males.

8.3.3 Model Refinement

The model described by equation 8.12 contains all seven suggested variables, though not all of them are necessary. According to **Table 18**, the variable with the highest p value is SMK with p = 0.95, the smoking status of the patient. The first step in model refinement as described in Section 8.2.3 and **Figure 35** is to remove this variable from the model. The new model is then written as

$$\text{STRENGTH} = \beta_0 + \beta_1 * \text{ILT} + \beta_2 * \text{AGE} + \beta_3 * \text{SIZE} + \beta_4 * \text{NORD} \quad (8.13)$$
$$+ \beta_5 * \text{HIST} + \beta_6 * \text{SEX} + \varepsilon$$

The linear regression results based on this new model are shown in **Table 21**.

Table 21 Regression report of equation 8.13 after SMK has been removed from the model given by equation 8.12.

Independent Variable	Regression Coefficient	Standard Error	p value
Intercept	130.25	48.25	0.0125
ILT	-16.18	8.96	0.0836
Size	10.33	6.26	0.1118
AGE	3.19	0.64	0.0000
ND	-283.17	34.98	0.0000
HIST	-79.01	10.22	0.0000
SEX	-18.16	12.07	0.1454
R-Squared	0.87		

According to **Table 21**, The remaining variables with the highest p-value is SEX ($p = 0.1454 > 0.05$). Therefore, SEX was removed from equation 8.13, and the new model becomes

$$\text{STRENGTH} = \beta_0 + \beta_1 * \text{ILT} + \beta_2 * \text{AGE} + \beta_3 * \text{SIZE} + \beta_4 * \text{NORD} + \beta_5 * \text{HIST} + \varepsilon \quad (8.14)$$

The linear regression results based on the model described equation by 8.14 are shown in **Table 22**. According to **Table 21,** the remaining variable with the highest p-value is SIZE ($p = 0.348 > 0.05$). Therefore, SIZE was removed from equation 8.14, and the updated model is then:

$$\text{STRENGTH} = \beta_0 + \beta_1 * \text{ILT} + \beta_2 * \text{AGE} + \beta_3 * \text{NORD} + \beta_4 * \text{HIST} + \varepsilon \quad (8.15)$$

Table 22 NCSS Regression report after SEX has been removed as a predictor; i.e., from the model given by equation 8.14.

Independent Variable	Regression Coefficient	Standard Error	p value
Intercept	113.58	48.14	0.0264
ILT	-16.10	9.19	0.0918
Size	5.10	5.33	0.3484
AGE	3.49	0.62	0.0000
NORD	-267.90	34.31	0.0000
HIST	-69.50	10.45	0.0000
R-Squared	0.86		

Table 22 shows the regression results after SIZE was removed from the model. All the p values in **Table 23** are less than our predefined criterion of p = 0.10. The ANOVA table for the data fit to this model is shown in **Table 24**, and indicates that the overall p value for this model is less than 0.0001. Likewise $R^2 = 0.86$, which is higher than our predefined criterion of $R^2 = 0.80$. With this, the step down procedure and hence model construction is completed. The final model contains four predictors: ILT, AGE, NORD and HIS. The final model is described as

Table 23 Regression report after SIZE has been removed as a parameter; i.e., from the model given by equation 8.15.

Independent Variable	Regression Coefficient	Standard Error	p value
Intercept	141.26	38.38	0.0011
ILT	-17.16	9.10	0.0707
AGE	3.39	0.61	0.0000
ND	-257.30	32.41	0.0000
HIST	-82.00	9.53	0.0000
R-Squared	0.86		

Table 24 Analysis of variance results from NCSS software for the model given by equation 8.15.

Source	DF	Sum of Squares	Mean Square	F-Ratio	p Value
Intercept	1	564794.60	564794.60		
Model	4	91361.79	22840.45	39.34	0.0000
Error	26	15096.50	580.63		
Total	30	106458.30	3548.61		

$$\text{STRENGTH} = 141.26 - 17.16 * \text{ILT} + 3.39 * \text{AGE} - 257.30 * \text{NORD} - 69.5 * \text{HIST} + \varepsilon \quad (8.16)$$

where ILT is the local ILT thickness in cm, AGE is patient's age (year), NORD is the local diameter normalized by the AAA size, and HIST is the family history of the patient (0 for no history, 1 for history).

Inspection of Equation 8.16 provides the following insights as to its physical meaning:

- As ILT increases one centimeter with all the other parameter fixed, the strength of the wall decreases 17.16 N/cm^2.
- A patient who is one year older than another otherwise identical patient with the same aneurysm, has a AAA that is globally stronger by 3.39 N/cm^2.
- As normalized local diameter increases by one, the wall strength decreases 257.30 N/cm^2.
- For two otherwise identical patients with identical AAAs, the one with family history has a AAA that is globally weaker by 69.5 N/cm^2 compared to the one without family history.

The narrow standard error of the estimated coefficients listed in **Table 23** indicates that the model has good predictability. Plotting observed values versus the predicted values of AAA wall strength (**Figure 53)**, we find that the model fits the original data very well ($R^2 = 0.86$, slope = 0.98). However, the ultimate goal of the model construction in this study is for prediction. The next section summarizes the works of using a different set of data to validate the equation 8.16.

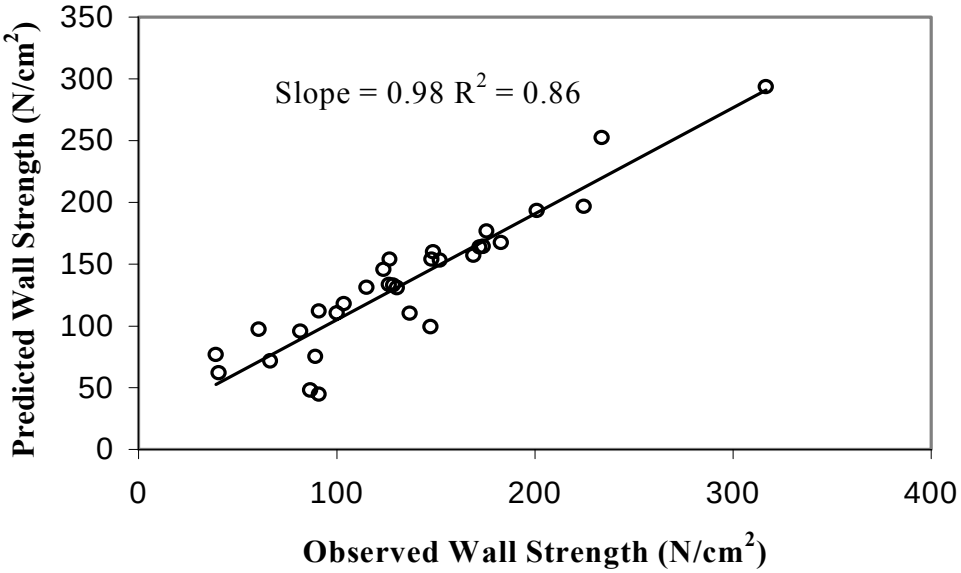

Figure 53 Predicted value of local wall strength vs. the observed value using the developed model, equation 8.16.

8.3.4 Model Validation

8.3.4.1 Subjects Selection

As described in Section 8.2.3.1, seven separate consenting patients undergoing traditional AAA repair surgery at the University of Pittsburgh Medical Center were selected to participate in the model validation phase. The characteristics of these patients and specimens are shown in

Table 25. Among the patients, 5 were male and 2 were females, one was non-smoker and six were smokers, and one patient had family history of AAA.

Table 25 Summary of the 34 tensile testing experiment results and the 7 patients for model validation.

	Strength (N/cm^2)	ILT (cm)	Local Dia. (cm)	Size (cm)	Age (yrs)
Mean	200	0.6	3.8	6.1	72
Standard Error	15.6	0.12	0.2	0.25	5
Minimum	70	0.02	2.1	4.0	62
Maximum	307	2	5.6	7.2	77
Count	21	21	21	7	7

A total of 21 successful wall strength measurements were collected along with the parameter values (ILT thickness, AAA size, patient's age, local diameter, normalized local diameter, patient's family history, smoking status, and gender) (**APPENDIX E**). Recorded strength ranged from 98 to 307 N/cm^2. ILT thickness ranged from 0 to 1.7 cm. Local diameter ranged from 3.2 to 6.8 cm. Since all parameter values in this validation group were inside the range of the values for the specimens in the model construction group, we were able to use the former values to validate our developed model; i.e., equation 8.16.

8.3.4.2 Problematic Data Detection

For the developed model (Equation 8.16) and new validation data set (**Table 24**, **Appendix E**), the number of coefficients (p) is 4, and the number of observations (n) is 21. Based on the methods described in Section 8.2.2.2.f, observations with hat diagonals greater than 2*4/21 = 0.3810 are considered outliers in X space, and any observations with an absolute value of Studentized residual greater than $t_{(21-4-1,\ 0.025)} = 2.120$ are considered outliers in Y space. Any observations with Cook's D greater than $F_{(4,\ 21-4,\ 0.50)} = 1.49$ are considered as influential points. **Table 26** shows the values of hat diagonal, Studentized residual, and Cook's D for all the data points. Based on above criteria, three outliers in X space (#7, #16 and # 19) were detected and are highlighted in **Table 26**. Those three observations were therefore deleted from the validation data set. The remaining 18 observations were used for model validation.

Table 26 Problematic observation inspection within the validation data set using linear regression techniques.

Sample	Hat Diagonal	Studentized Residual	Cook's D
1	0.3022	-1.4505	0.1822
2	0.1028	0.3354	0.0026
3	0.1558	0.1847	0.0013
4	0.3860	0.2013	0.0051
5	0.3518	-0.1449	0.0023
6	0.3428	-0.0507	0.0003
7	0.2338	**2.0211**	0.2493
8	0.1253	0.1972	0.0011
9	0.0959	0.4124	0.0036
10	0.2117	0.0595	0.0002
11	0.2035	0.1305	0.0009
12	0.1287	-0.2287	0.0015
13	0.1183	0.2293	0.0014
14	0.0703	0.4273	0.0028
15	0.2294	-0.7832	0.0365
16	**0.4027**	0.1319	0.0023
17	0.3864	0.4570	0.0263
18	0.4032	-0.4291	0.0249
19	0.1284	**-3.2235**	0.3063
20	0.1754	0.5632	0.0135
21	0.4458	1.1452	0.2110

8.3.4.3 Cross Validation

The observed wall strength values vs. those predicted using equation 8.16 are plotted in **Figure 54,** showing very nice agreement (R^2 = 0.81, slope = 0.97). Based on the original R^2 value of 0.86 (Section 8.3.3, **Figure 53**), shrinkage value of 8.2% was calculated as described in Section 8.2.3.3. Since it is less than 10%, we confirmed that the model is cross-validated.

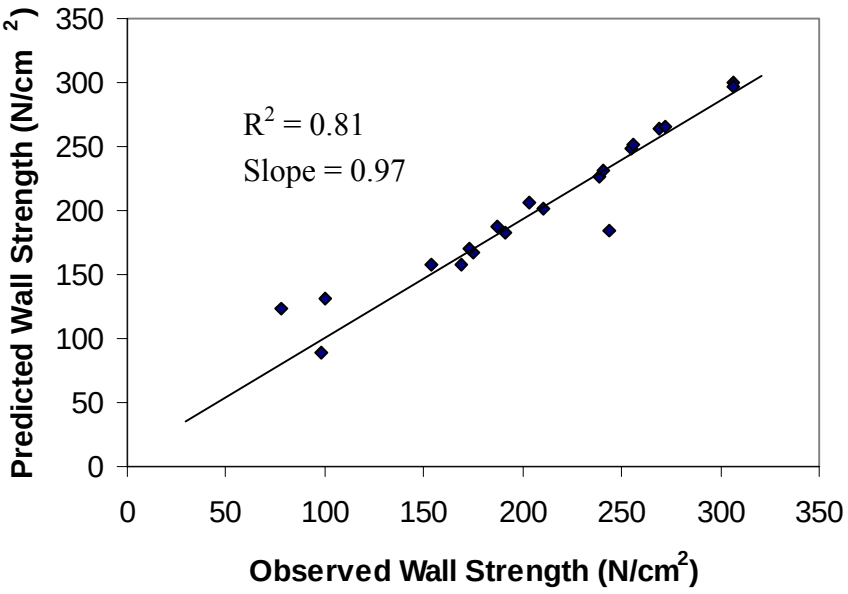

Figure 54 Observed values for local wall strength versus those predicted using Equation 8.16.

Table 27 summarizes all relevant information on the observed and predicted values of strength, the predictor values, and the predict error for the final model validation.

Table 27 Information on the validation of the final model based on 18 samples from 7 patients. Further information is available in Appendix E.

Sample #	Observed Strength (N/cm^2)	Predicted Strength (N/cm^2)	Error (N/cm^2)	ILT (cm)	AGE (year)	NORD	HIST
1	239	227	11	0.20	77	0.67	0
2	269	272	-2	0.15	77	0.53	0
3	98	91	7	0.60	66	0.71	1
4	175	181	-6	0.02	66	0.45	1
5	169	170	-1	0.02	66	0.49	1
6	255	253	2	0.14	77	0.59	0
7	191	177	14	0.60	77	0.81	0
8	307	314	-7	0.15	72	0.32	0
9	307	312	-5	0.18	72	0.33	0
10	204	203	0	0.25	72	0.68	0
11	256	259	-3	0.42	76	0.54	0
12	211	199	11	0.62	76	0.73	0
13	78	107	-29	1.10	76	1.00	0
14	173	167	7	1.37	62	0.62	0
15	241	241	0	1.50	62	0.37	0
16	272	273	-1	0.20	62	0.32	0
17	187	187	0	1.30	76	0.74	0
18	154	151	3	1.74	76	0.82	0

8.4 Discussion

From an engineer's point view, rupture of an individual AAA has to do with two factors: the local stress applied to the wall tissue and the strength of the wall tissue. In order to evaluate the risk of rupture for a given AAA, information on both local stress and local strength are necessary. For this reason, we proposed our Hypothesis #2, i.e., local wall strength could be predicted by certain clinical variables. To our knowledge, this is the first model that allows the prediction of local AAA wall strength distribution in a noninvasive manner. The final model contains four, non-invasively measurable predictors: local ILT thickness, normalized local diameter, patient's age, and patient's family history of AAA. ILT thickness, as well as local diameter and maximum diameter (which, combined, yield the normalized local diameter) can be measured from a patient's CT images and 3D reconstruction, while the patient's age and family history can be obtained from his or her hospital chart. Our results suggested that wall strength can be predicted accurately at any given location on the AAA. Combining this technology with our companion technology of 3D stress analysis described in Chapter 7 may provide clinicians with an improved index of the rupture potential for each individual AAA, which will in turn improve patient management.

There are several important observations that can be made from the statistical model developed in this chapter:

- Local AAA wall strength distribution for a given patient can be predicted adequately by the combination of the four predictors - patient's age, normalized local diameter, local ILT thickness, and patient's family history of AAA. The high R^2 value (R^2 = 0.86) and significant p value of the model ($p < 0.001$) suggest that the correlation between local AAA strength and the four predictors is strong. However, this does not

indicate any causal relationship between the predictors and local wall strength. Any conclusion of causal effect would need to be supported by further scientific evidence.

- Our results (see equation 8.16) suggest that AAA wall strength increases 3.39 N/cm^2 as age increases one year. At first, this may seem counter-intuitive considering the age-related changes of the aorta, including reduction of elastin [175] and increase in amount of newly synthesized collagen, which is weaker than the existing collagen [176]. Therefore, in spite of the increased amount of collagen, aortic wall still might be weakening with age. [158, 176] However, one must keep in mind that this was not a longitudinal study. That is, the data were not collected on the same patient over time. Of course, it is impossible to follow the patient over time and test the wall strength at different time points. Therefore, this model does not imply that AAA wall gets stronger over time for a given patient.
- The maximum size of AAA was removed from the model as a direct predictor because it was found to be insignificant (recall Section 8.3.3, **Table 22**). This also seems counterintuitive since it has been shown by previous studies (recall Section 8.1.2.1) that the risk of rupture increases as AAA enlarges, [5, 13, 17, 20, 35, 42-44, 54, 149-151] which suggest the failure strength of AAA wall reduces progressively as AAA enlarges. However, the influence of this parameter remained in the model since the local diameter was normalized by the maximum diameter of AAA. Local, normalized diameter was found to be a significant predictor (**Table 23**). This might be intuitive. In the region where the aortic wall is of normal caliber, the local normalized diameter is relatively low, and the strength would be high since the wall is not degenerated as compared to the dilated region. This is supported by the reported

scientific data [147, 167] that the microstructure of AAA tissue changes as it's size increases. It is also supported by our experimental data (Section 8.1.2.5, **Figure 34**) which showed that the wall strength is lower from the larger diameter region of AAA compared with the wall strength from the smaller diameter region.

- Local ILT thickness was also shown to be a significant predictor of local wall strength. Our results (see equation 8.16) suggest that as ILT increases one centimeter, the strength of the wall decrease 17.16 N/cm^2. This is consistent with our previous study that showed that presence of ILT inhibits oxygen supply to the smooth muscle cells (Section 8.1.2.4, **Figure 29, 30**), causes hypoxic condition (Section 8.1.2.4, **Figure 31**), promotes inflammatory response (Section 8.1.2.4, **Figure 31**), and neovascularization (Section 8.1.2.4, **Figure 32**), and therefore wall weakening. [183] The fact that ruptured AAAs have more ILT [213] may also support this observation.
- Family history was found to be a significant predictor of wall weakening ($p = 0.0001$). This is consistent with the clinical observations of the strong familial tendencies in AAA disease (Recall Section 8.1.2.7). [196-201] To illustrate the implication of this, consider two patients, one with a family history and the other without, who are identical otherwise; i.e., same age, same AAA size, same AAA geometry, and same ILT configuration. According to our results (Equation 8.16), the patient with family history experiences a decrease in wall strength of 69.5 N/cm^2 throughout his or her entire AAA. This suggests that family history is related to AAA wall weakening, and therefore may be related to AAA rupture. To explore this further, the mixed model multiple linear regression technique was used against all the patient's data, including the data for both the model construction and model

validation groups, to test if there is a significant difference between the two groups. [214] The results showed that wall strength is significantly different between the groups with and without family history of AAA ($p < 0.001$).

- Besides the parameters we used in our model, there might be some other factors that are highly related to local wall strength. However, one must keep in mind that the purpose of this work was to develop a statistical model to easily, reliably, and noninvasively predict local wall strength. We did not attempt to identify the underlying mechanisms or factors causing wall weakening. Though the model was found to be statistically significant with a large R^2 value, it does not mean that a causal link exists between the independent variables (predictors) and the dependent variable (wall strength). The results imply only that the predictors are associated with, not causal connections to the wall strength. We therefore believe that the chosen parameters are adequate and sufficient to predict the strength distribution for an individual patient's AAA.

As with any modeling technique, there are certain limitations that should be kept in mind. These limitations are listed below

- ***Sample procurement.*** Because of the restriction of the surgical procedure, all the specimens were taken from the anterior region of the AAA. This might have prevented a full evaluation of the influence of ILT thickness on local wall strength. Ideally, wall specimens from a given AAA with the same local diameter but different ILT thickness should be tested and the data included in the statistical model. However, this is not practical from surgical specimens, but possibly from carefully collected autopsy samples (which would, of course, have their unique limitations).

- ***Testing procedure.*** The wall strength measured by our experiments is not the true nodal (point) values of wall strength, but the average for all nodes encompassed by the sample. Therefore, to minimize the potential error, attempts were made to obtain specimens with minimal width and minimal variation in ILT thickness. Wall thickness and width were measured by using a dial caliper. Ideally, these dimensions would be obtained using a non-contacting method since contacting methods such as a caliper introduce errors that would yield inaccurate cross sectional area for the sample and, therefore, inaccurate wall strength. This might partially explain the outlier values observed in the model construction and model validation data sets. Additionally, local cross sectional diameter was measured as the average of two diameter measurements (recall Section 8.2.1.2, Figure 35). Thus, this only reflects the average of circumferential radius of curvature. A local, mean radius of curvature might be a more accurate and sensitive predictor since it takes into account two principle curvatures; i.e., circumferential and longitudinal. [85] Measurement of ILT thickness was done by averaging the thickness at both ends of the specimen. This is not true local ILT thickness per se. This is an inherited limitation because of the possible small size of ILT can be tested using our device.
- ***Data collection*** AAA size, patent's smoking status and family history were collected from the hospital chart. The accuracy of AAA size depends on the technique used to measure it (i.e., CT ultrasound, etc). Also the actual AAA size at the time of specimen collection might be different than that recorded in the patient's chart, depending on how long it was measured before surgery. The subjective nature of the patient's smoking status and family history also affects the statistical result. That is, the patient might not provide the truth about his or her smoking status, or be an ex-smoker and classify himself

or herself as a nonsmoker. Likewise, patients with family history might not be aware of this.

- ***Samples range*** Another obvious and important constraint of the statistical model is that its application is limited by the range of the original data from which it was constructed. The model construction data was extracted from 11 patients. As emphasized in section 8.2.3.1, any extrapolation outside the range of the original data is not trustworthy. For example, if one would like to predict the wall strength distribution for a AAA in a 75 year old patient who has a 7.5 cm AAA, we can not do so because it is outside our model's prediction range established in **Table 13**. In order to predict the wall strength distribution on any patient with any characteristics, many more patients with a wide variety of AAA (and hence wide range of predictor variables) would need to be tested and the model refined by incorporating that data.

In summary, we have developed a mathematical model, which allows us to estimate the local wall strength distribution noninvasively for a given patient and this is the subject of the next chapter. Despite the above limitations, the model has $p < 0.001$ and $R^2 = 0.86$. This indicates that the combination of the four predictors (patient's age, normalized local diameter, patient's age, and family history) can estimate the local wall strength adequately. The model fits the validation data well with shrinkage of only 8.2% and has a significant predictability. This model can be easily combined with our existing 3D AAA wall stress simulation technique to evaluate the potential risk of rupture for a given AAA, and this is the subject of Chapter 10.

9.0 WALL STRENGTH DISTRIBUTION MAPPING FOR INDIVIDUAL AAA

9.1 Introduction

The finite element simulation described in Chapter 7 provided a mapping of AAA wall stress distribution displayed on a reconstructed AAA geometry. The wall stress values were given for each nodal point of the finite element mesh of each individual AAA geometry. To carry out Specific Aim #4 – the estimation of rupture potential index distribution - the wall strength value of the wall at each node is also necessary. In this chapter, the techniques are described to measure the local ILT thickness and local AAA diameter from CT scan images, then use these in Equation 8.16 to estimate the local wall strength value distribution for individual AAA. Demonstrative results are provided for the four AAA which were 3D reconstructed in Chapter 5 and for which the stress distributions were estimated in Chapter 7.

9.2 Methods

9.2.1 Local AAA Diameter and ILT Thickness Calculation

To use Equation 8.16 to predict the wall strength distribution for a AAA patient, two spatially-varying parameters, local AAA diameter and ILT thickness, were measured on each

2D, digitized CT image. The lumen and wall contours were extracted from the CT image as described in Section 5.2.3 and shown here in **Figure 55 A**. The extracted boundary points were converted from Cartesian coordinates to r-θ coordinates and smoothed. Using a custom Mathematica program (see **APPENDIX A**), the thickness of ILT was calculated at 5^o intervals of θ as the difference between the radii for the wall and the luminal contours, as shown in **Figure 55 B**. The local diameter of AAA for a given slice was taken as twice the average of all 72 values of the wall radius. For each image, therefore, the Mathematica program provided one local diameter value and 72 ILT thickness values spaced evenly around the wall contour.

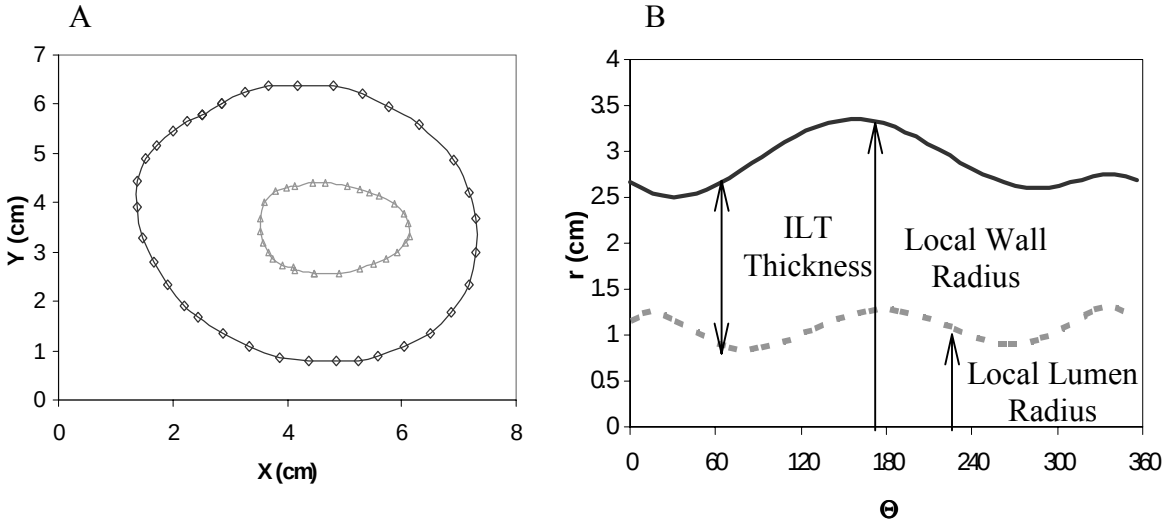

Figure 55 Calculation of local diameter and local ILT thickness in r-θ domain. First, the wall and lumen contours in X – Y space(A) were transferred to the r-θ domin (B). The difference between local wall radius and local lumen radius is the local ILT thickness. It was calculated at 72 evenly spaced points around the perimeter (i.e., at a 5^0 interval). The local diameter was taken as twice the average of all 72 local wall radii values.

9.2.2 Local Strength Calculation

The local AAA wall strength was calculated for each of the 72 spatial points for which ILT thickness was measured in **Figure 55.** This was calculated by equation 8.16 by using local diameter and local ILT thickness values calculated in Section 9.2.1, AAA size, and patient's family history.

9.2.3 Nodal Interpolation of ILT Thickness, Local Diameter and Wall Strength

The stress distribution results obtained in Chapter 7 were given at each node on the surface of the 3D "virtual AAA" mesh. To compare the local wall strength with local wall stress value (the topic of Chapter 10), we need to know the corresponding strength value for every nodal stress value. The nodal strength value was interpolated from the calculated strength values described in Section 9.2.2 using the following finite element interpolation method.

For any given node, the same Mathematica program used in Section 9.2.2 (**APPENDIX A**) transforms its Cartesian (X-Y-Z) coordinates into cylindrical (r-θ-z) coordinates. To facilitate this, the coordinates of the centroid for the closed AAA wall contour at level Z were interpolated from the two neighboring centroids (recall Section 5.2.3) as follows:

$$
\begin{aligned}
X_c &= \left[1-\frac{(Z_{c1}-Z)}{(Z_{c1}-Z_{c2})}\right]X_{c1}+\frac{(Z_{c1}-Z)}{(Z_{c1}-Z_{c2})}X_{c2} \\
Y_c &= \left[1-\frac{(Z_{c1}-Z)}{(Z_{c1}-Z_{c2})}\right]Y_{c1}+\frac{(Z_{c1}-Z)}{(Z_{c1}-Z_{c2})}Y_{c2} \\
Z_c &= Z
\end{aligned}
\qquad (9.1)
$$

where (X_{c1}, Y_{c1}, Z_{c1}), and (X_{c2}, Y_{c2}, Z_{c2}) are the two centroids calculated for the two neighboring cross-sections, and (X_c, Y_c, Z_c) are the coordinates of the interpolated centroid. Using the interpolated centroid as the "origin", coordinates of any given node point (X, Y, Z) is then transformed to the cylindrical coordinates (r, θ, Z) using the following equations

$$\begin{aligned} r &= \sqrt{(X - X_c)^2 + (Y - Y_c)^2} \\ \theta &= 180\pi \sin^{-1}\left(\frac{Y - Y_c}{r}\right) \\ Z &= Z \end{aligned} \tag{9.2}$$

Any four points for which the wall strength is calculated forms a rectangular element with these four points as its nodes. Any node from the surface of the finite element mesh in the stress analysis falls into one of these elements. Since the strength value on the four nodes are known, any points within the element can be estimated using finite element interpolation.

Figure 56 shows an element formed by four nodes with strength values (S_1, S_2, S_3 and S_4) calculated in Section 9.2.2. The local wall strength value of point N inside of this element was linearly interpolated from these four nodal strength values, S_1, S_2, S_3 and S_4, as follows: [215]

$$S = [w_1, w_2, w_3, w_4] \begin{bmatrix} S_1 \\ S_2 \\ S_3 \\ S_4 \end{bmatrix} \tag{9.3}$$

where w_i's are linear shape functions given by: [215]

$$w_1 = \frac{1}{4bh}(2b - \theta + \theta_0)(2h - Z)$$
$$w_2 = \frac{1}{4bh}(\theta - \theta_0)(2h - Z) \qquad (9.4)$$
$$w_3 = \frac{1}{4bh}(\theta - \theta_0)Z$$
$$w_4 = \frac{1}{4bh}(2b - \theta + \theta_0)Z$$

and

$b = 2.5^{o}$ and $h = (Z_2 - Z_1)/2$

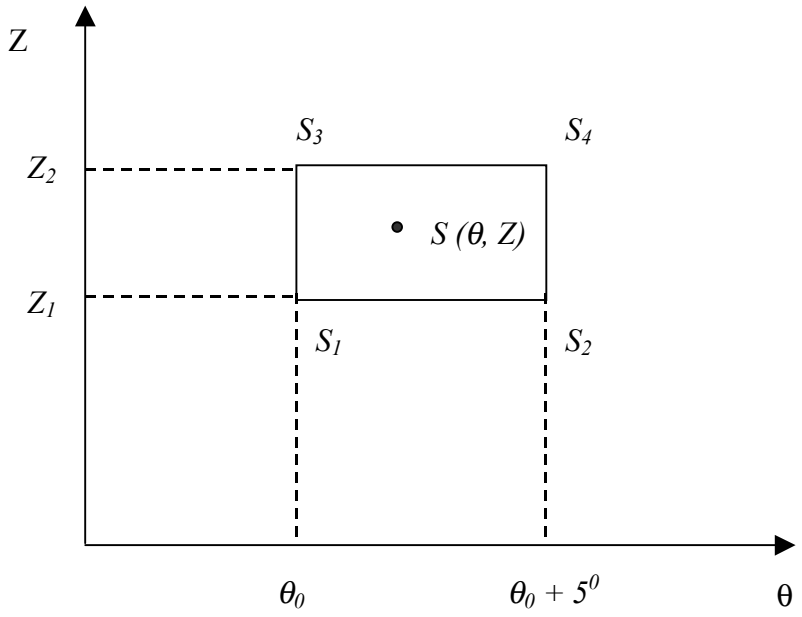

Figure 56 Finite element interpolation of local wall strength. At a given point N at angle θ and level Z, the local wall strength S is interpolated by the four nodal values S_1, S_2, S_3 and S_4.

Combining equation 9.3 and 9.4, the strength value for node N is expressed as

$$S = \frac{1}{4bh}\left[(2b-\theta+\theta_0)(2h-Z)S_1 + (\theta-\theta_0)(2h-Z)S_2 + (\theta-\theta_0)ZS_3 + (2b-\theta+\theta_0)ZS_4\right] \qquad (9.5)$$

The Mathematica code used to carry out the calculation can be found in **APPENDIX A**. The calculation was carried out for all the nodes on the surface of each 3D "virtual AAA" mesh described in Chapter 7. A contour plot of strength distribution was also generated for each AAA similar to the wall stress mapping shown in **Figure 25** using the visualization software Tecplot (Version 8.0, Amtec Engineering, Inc., Bellevue, Washington). A 3D strength plot animation was also generated for that patient in AVI (Advanced Visual Interfaces) format which can be easily viewed and transferred through the Internet.

The procedure is summarized in **Figure 57**. First, 72 local wall strength values were calculated on each CT image slice based on measurements of local ILT thickness and local diameter (Section 9.2.1, **Figure 55**), patient's age, patient's family history, and AAA size using equation 8.16. Then, wall strength at any given point (node) was interpolated from these wall strength values using equation 9.5. Local ILT thickness and local diameter for any given nodal point was calculated based on discrete measurements from the CT images in the same manner. 3D plot animations were generated for viewing local ILT thickness, local diameter, and local wall strength distributions.

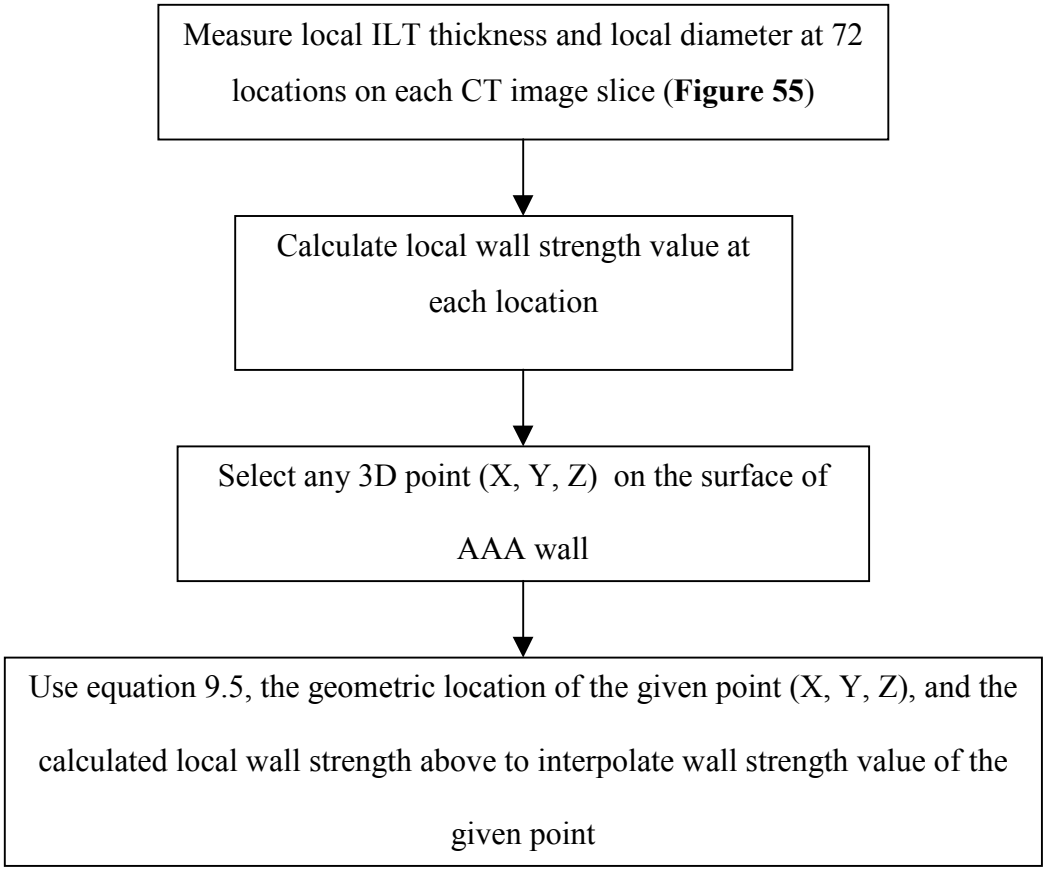

Figure 57 Local wall calculation procedure.

9.3 Results

The local wall strength distributions for the four AAA studied in Chapter 7 and Chapter 8 are plotted in **Figure 58**. Notice the unique pattern for each AAA. In general, wall strength values are higher at both ends and lower in the bulge regions. Local ILT thickness distribution plots for those four AAA are presented in **Figure 59**. The unique patterns are determined by the specific ILT configuration of each AAA. The local diameter is also mapped on each of the four

"virtual" AAA shown in **Figure 60**. The local diameter at the apex of each AAA should correspond to the size (i.e., the maximum diameter) of that AAA.

9.4 Discussion

The finite element stress simulation method described in Chapter 7 provides us nodal values of AAA wall stress. To evaluate the propensity of rupture of individual AAA, it is pivotal to obtain the information on how much stress each location on the wall can sustain, i.e., the corresponding wall strength value at each nodal point. Only when we have this information, can we evaluate the critical value of the ratio of local wall stress to wall strength, i.e., the rupture potential index for that individual AAA. We believe that this index would provide an improved estimation of aneurysm severity. The method developed in this chapter allowed us to evaluate the nodal wall strength for four representative AAA using the mathematical equation developed in Chapter 8 (Equation 8.16).

To use equation 8.16 to predict the wall strength at a given location, five parameters: local ILT thickness, local diameter, patient's age, patient's family history, and AAA size, are needed, and are required to be noninvasively determinable. The last three parameters were easily obtained from the patient's hospital chart. The two locally varying parameters, local IT thickness and local diameter were measured on each cross-sectional CT image, then interpolated` to provide values at nodes that correspond to the finite element mesh. The local strength distribution was then mapped on the 3D reconstructed AAA surface.

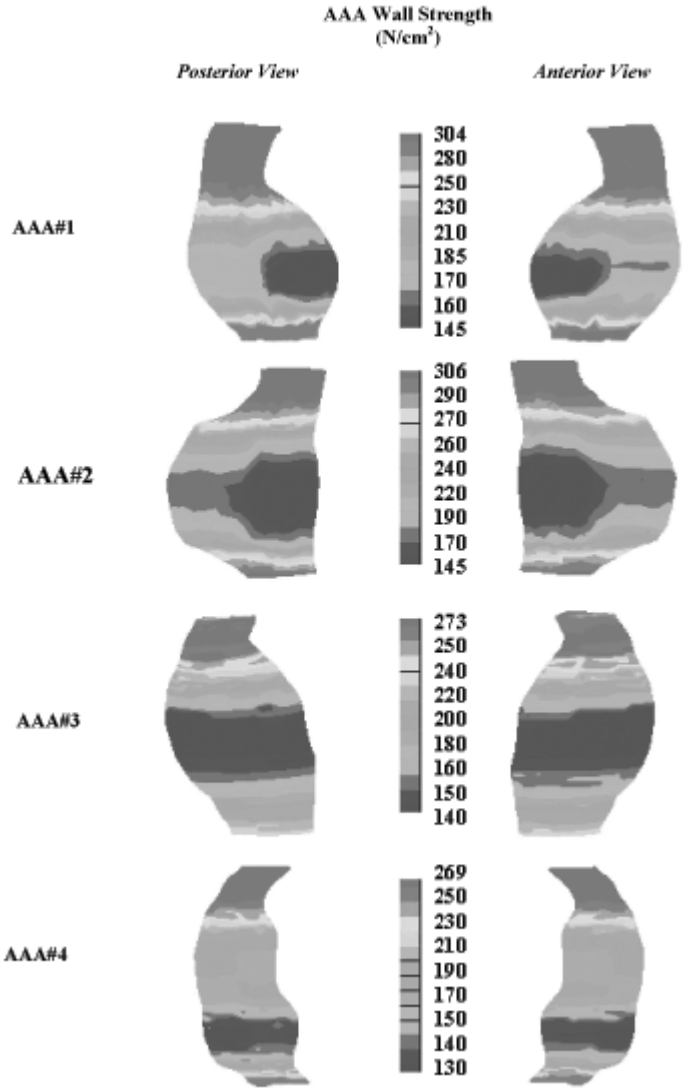

Figure 58 Local wall strength distribution estimated by using the developed statistical model (equation 8.16) for all four AAA studied.

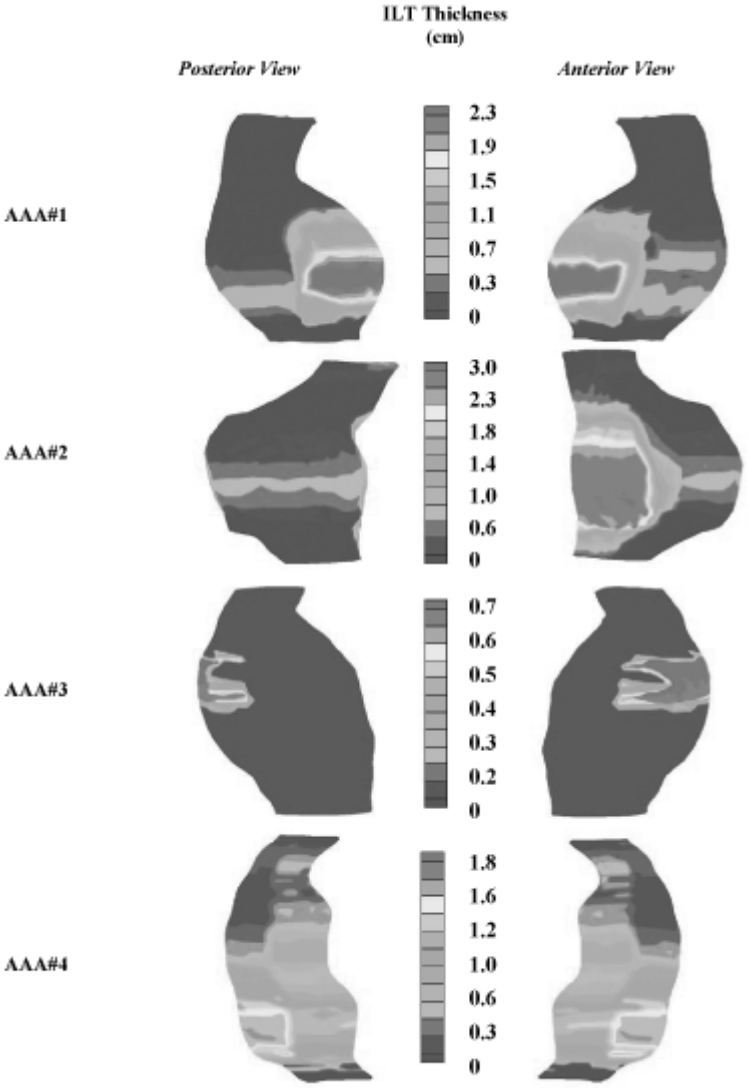

Figure 59 Local ILT thickness distribution for the four AAA studied.

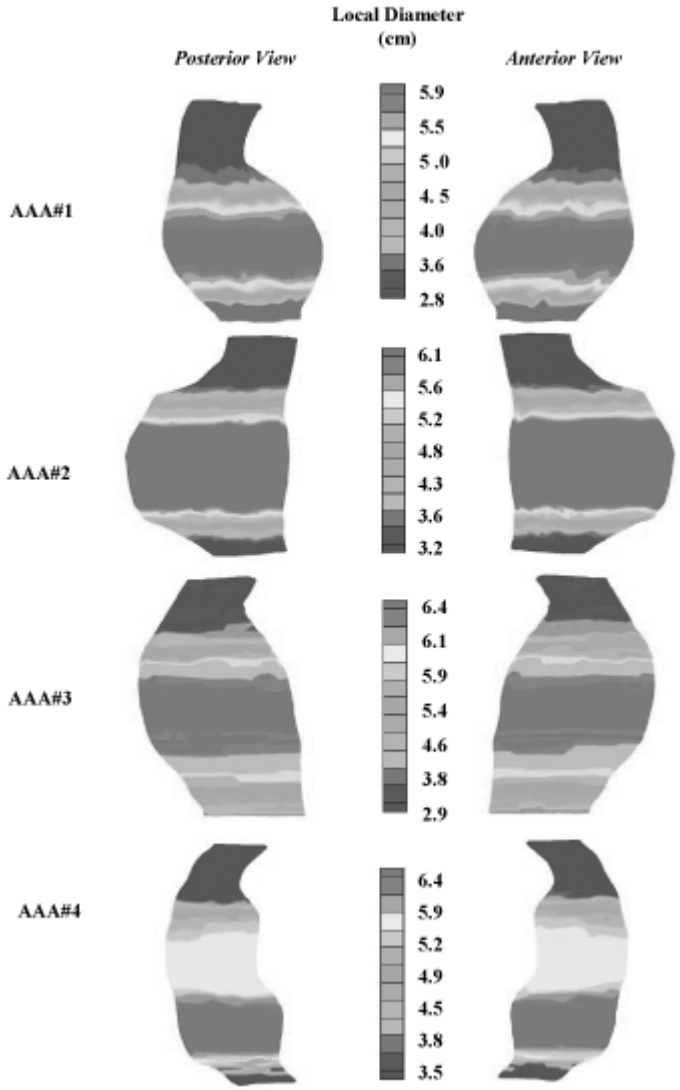

Figure 60 Local diameter distribution for the four AAA studied

Ideally, any prediction technique should be validated against accurate measurements. However, it is impossible to measure nodal wall strength. Nevertheless, there are certain observations and comparisons that can be made that lend themselves to a quasi-validation of our methods. For example, there is a good correspondence between the ILT thickness patterns in **Figure 58** with the actual ILT configurations shown in **Figure 24**, section 5.3, suggesting that our technique be accurate. Likewise, the maximum local diameter shown in **Figure 59** also corresponds well with the maximum diameter (AAA size) listed in each patient's chart, **Table 28**. Paired t-test showed no difference between the measured maximum diameter listed in chart and the interpolated maximum AAA diameter ($p = 0.22$). These findings suggest that our FEM technique is accurate in interpolating local AAA diameter and ILT thickness.

Table 28 Measured AAA size and calculated maximum AAA diameter.

AAA#	Max. Diameter Listed in Chart, (cm)	Max. Diameter from Interpolation (Figure 59), (cm)
1	6.0	5.92
2	6.1	6.08
3	6.4	6.40
4	6.4	6.39

The wall strength distribution in **Figure 57** reveals a unique pattern for each patient. However, some generalized observations can be obtained. The weak points seem to reside in the area with the largest diameter and thickest ILT. The wall strength values are higher towards the

distal and proximal ends where local diameters are smaller and ILT presence is less likely. Comparing **Figure 57** with **Figure 25**, there is no correlation between the location of the highest stress and lowest strength. This underscores the argument that neither maximum stress nor minimum strength location alone can predict a critical location on an AAA. The predicted nodal strength values for the four patients studied range from 130 N/cm^2 to 306 N/cm^2, whereas the measured wall strength values in Chapter 8 range from 39 to 324 N/cm^2. This comparison at least suggests that our technique is reliable. Those ranges are agreeable with previous reported wall strength data ranged from 117 N/cm^2 to 250 N/cm^2. [183] Vorp et al. [62] reported measured AAA wall strength ranged from 54 N/cm^2 to 80 N/cm^2. The noticeable difference between the highest strength value and current measured highest strength value might due to the fact that the current data included wall specimens from the neck regions, which tend to be stronger than that from the dilated regions alone as was the case in the previous study.

The accuracy of the 3D wall strength distribution prediction depends on the accuracy of the mathematical model (Equation 8.16), and the accuracy of the 3D geometry reconstruction. The former was discussed in detail in Chapter 8. The latter is related strongly to the resolution of image collection; i.e., the interval of CT slices. Since the local parameters (ILT thickness and local diameter) are based on the measurements on the CT slices, the more slices, the more accurate their values. The more complex and irregular the ILT configuration, the smaller the pitch needed to accurately capture the ILT configuration and, therefore, the strength distribution. However, there is a practical balance between the exposure of the patient to X-rays and the 3D reconstruction. In general, this technique and the number of images are limited by current clinical protocols for CT imaging.

10.0 RUPTURE POTENTIAL INDEX CALCULATION

10.1 Introduction

For lack of a better approach, the surgical community still predominantly uses the "5-cm diameter criterion" to make the decision on surgical intervention of AAA. The problem of this approach is that some aneurysms smaller than 5 cm in diameter rupture, and other aneurysms larger than 5 cm diameter never do prior to the patient succumbing to other causes. [20, 34] The insufficiency of this approach in predicting the risk of rupture of individual AAA is due to the empirical nature of the approach. The criterion is based on the aggregate population, and it does not necessarily suit every individual.

The goal of this work was to develop a better technique that will provide a more accurate prediction of the risk of rupture for individual AAA. Based on the basic engineering principle that a material fails when the stress applied to it exceeds its strength, our developed approach assumes that AAA ruptures when local wall stress exceeds local AAA strength. We refer to the ratio of the locally acting wall stress divided by local wall strength value at that location as the ***Rupture Potential Index (RPI)***. Therefore, as local RPI approaches a value of 1.0, the value of local wall stress is approaching that of local wall strength, and rupture of that patient's aneurysm is imminent. We believe that a critical RPI value to predict the rupture potential of individual AAA would be more accurate than the "one-size-fits-all" 5-cm diameter criterion. Specific Aim

#4 of this study is to develop a noninvasive technique to estimate RPI for individual AAA. The detailed methodology related to this approach is described in this chapter.

10.2 Methods

Two parameters are needed for RPI calculation: local wall stress and local wall strength. The former was determined for each AAA studied using the methods described in Section 5.2 (3D reconstruction) and, Section 7.2 (computational stress analysis). The wall strength was then estimated at each node of the finite element mesh for stress analysis according to Section 9.2. Dividing the stress acting at the node by the strength estimated for the wall at that node yields the RPI value for that node. A custom Mathematica code was developed to calculated the RPI values for all the nodes (**APPENDIX A**). The step-by-step procedure for this process is shown schematically in **Figure 60**.

Once all the nodal RPI values were determined, a contour plot of RPI distribution was generated for each AAA using the visualization software Tecplot (Version 8.0, Amtec Engineering, Inc., Bellevue, Washington). A 3D RPI plot animation is also generated for that patient in AVI (Advanced Visual Interfaces) format which can be easily viewed and transferred through the Internet.

10.3 Results

The RPI distribution of the four AAA for which stress and strength distribution were

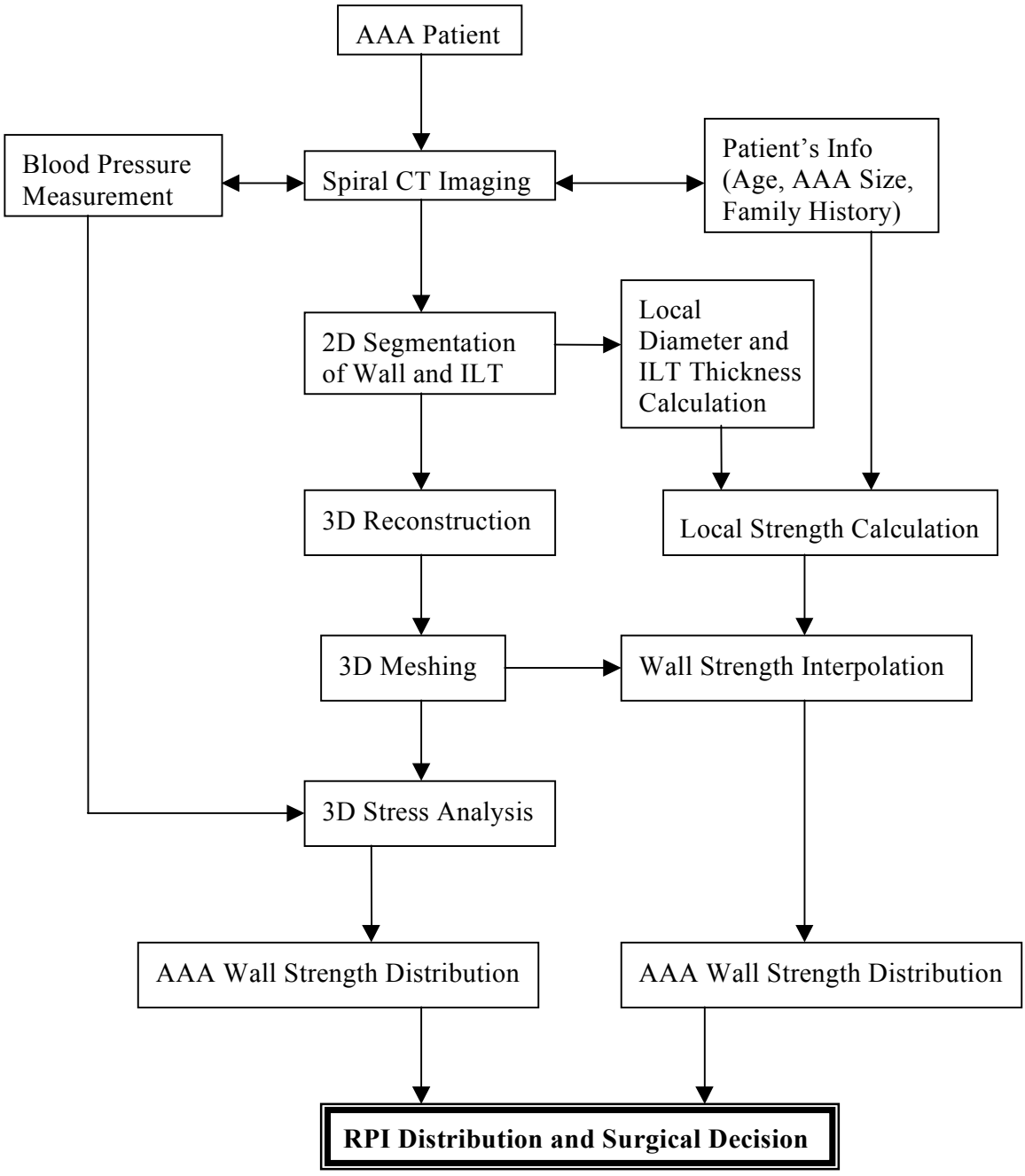

Figure 61 Procedure of determination of rupture potential index (RPI) distribution for individual AAA.

estimated in Chapters 7 and 9, respectively, are shown in **Figure 61**. For each case, the maximum RPI value, the minimum RPI value, and global average RPI value, which is determined by the sum of RPI values of all nodes divided by the total number of nodes, are listed

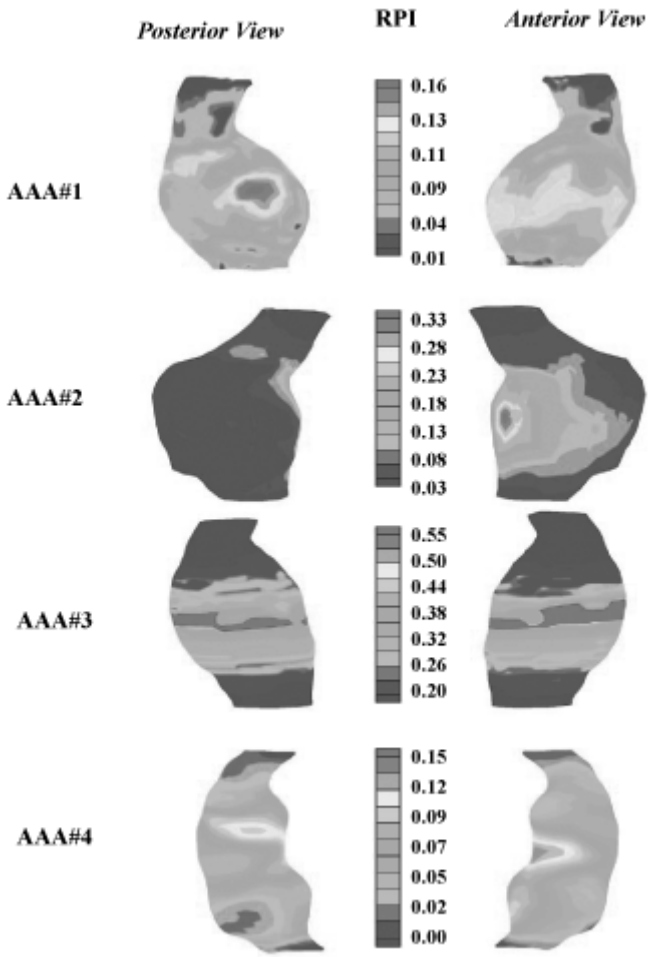

Figure 62 RPI distribution of the four AAA evaluated in this study.

in **Table 29**. None of the peak (maximum) RPI values exceeded a value of 1 for the four cases studied.

Table 29 The maximum, minimum, and average RPI values for the four cases studied.

AAA#	Min. RPI	Max. RPI	Average RPI*
1	0.01	0.16	0.14
2	0.03	0.33	0.17
3	0.20	0.55	0.36
4	0.00	0.15	0.06
Mean	0.06	0.30	0.18
SD	0.09	0.19	0.13

* Calculated from $(\sum_{i=1}^{N} RPI)/N$ where N is the number of nodes.

10.4 Discussion

The RPI distribution plots in **Figure 61** provide a direct visualization of the rupture potential for each individual patient. That is, the location of the peak RPI value – the "hot spot" shown in red in each panel of **Figure 61** – depicts where each AAA might be most prone to rupture. A peak value closer to 1 suggests a higher risk of rupture for that particular AAA. Similar to the 5-cm criterion, we believe that when the peak RPI value exceeds a certain critical

value, the risk of rupture exceeds the risk of intervention. However, unlike the 5-cm diameter criterion, the decision making is tailored to the individual AAA and, we believe, much more accurate. Future clinical studies should verify this belief and also address the question of the critical value of peak RPI for selective surgery.

Comparing **Figure 61** to the stress distribution in **Figure 25** and strength distribution in **Figure 56**, neither peak wall stress nor weak wall strength alone can predict AAA rupture accurately. For example, AAA #4 has the highest peak stress (**Figure 25**) and lowest peak wall strength value (**Figure 57**), but AAA#2 has the highest RPI value (**Figure 59**). This again confirms the importance of calculating RPI value in predicting individual AAA rupture potential.

The fact that all four patient's peak RPI values are lower than 1.0 suggests that our technique is valid. Rigorous validation studies should be carried out before this technique can be applied in clinical settings, however. One way to validate this technique is to follow patients who have been turned down for surgery because of other health related problems. Serial CT scanning could be performed and a retrospective, longitudinal study could be performed on the reconstructed models at the different time points. The RPI value would presumably increase with enlargement of the AAA, and the peak RPI value just before and at the location of rupture should be close to one. A second way to conduct the validation study is to obtain an intact AAA from autopsy. This intact AAA could then be connected to an ex-vivo perfusion loop and undergo CT scanning for 3D reconstruction. Wall strength distribution could be evaluated using the techniques described in Chapter 9. The AAA then could be subjected to an incremental luminal pressure until it ruptures. The stress distribution in AAA wall at the time of rupture would be evaluated using the pressure applied at that time and the FEM simulation method described in Chapter 7. The RPI distribution at the time of rupture would then be evaluated using the protocol

outlined in this chapter. The calculated maximum RPI value should be close to 1 and the location should be close to the site where the rupture of the intact AAA occurs. Similar studies could be conducted on an artificial AAA model made from a material of known strength distribution. The model will be connected to the same ex-vivo perfusion loop and, again, an incremental internal pressure could be applied until it ruptures. Still another possible way to validate our approach might be to utilize a large animal model of AAA, which can be created in vivo by topical application of elastase to the infrarenal aortic segment. [216, 217] Perhaps the elastase could be applied in such a manner as to obtain AAA of different sizes and known wall strength distributions. Longitudinal studies could be conducted to follow the development of AAA and the changes of RPI distribution. The major drawback of this approach is that our strength model was developed for human AAA, not chemically-induced dilations produced in animals. A different and specific strength model would need to be developed for this approach.

11.0DISCUSSION AND CONCLUSION

Some patients have described the feeling of having an AAA as having a "time bomb" inside their body. Even though most AAA patients are asymptotic, every patient's aneurysm is facing a risk of sudden rupture that is a catastrophic event with a very high mortality. [4, 35, 43, 153] This can be prevented by clinical intervention – by endovascular repair or by open surgical repair if the former is not suitable for a particular patient. Neither approach is without risk and complications. [28, 32, 99, 218-220] Plus both approaches are costly. The unique decision must be made for each patient: should he or she undergo surgical intervention? If so, when?

Ideally, one would weigh the risk of rupture for a particular AAA against the risk of repair. If the risk of AAA rupture exceeds the risk of operation, that patient should undergo repair immediately. Otherwise, the patient could be put on a "watchful waiting" list while he or she continues to lead their normal life. Therefore, accurate prediction of the rupture potential of a particular patient's AAA is the key to timely surgical intervention, and hence, improved patient management.

The evaluation of the risk of rupture for each individual AAA is not an easy task. For lack of a better approach, surgeons are still using the 5 cm diameter cutoff criteria to make their surgical decision. In this approach, if the maximum diameter of an individual's AAA exceeds 5 cm, that aneurysm is considered to be at a high risk of rupture. Surgical intervention is then felt to be justified. [35, 36] However, as mentioned, clinical studies have indicated that this practice is not sufficient since some aneurysms smaller than 5 cm diameter do rupture and some aneurysms larger than 5 cm never rupture prior to patient death from other causes. [20, 37, 38] The unreliability of this criterion is due to its empirical nature. Even though a large number of

AAAs larger than 5 cm in diameter do rupture, there are still exceptions to this due to the uniqueness of each AAA. Therefore, it makes sense to evaluate the susceptibility of a particular AAA to rupture on a more individualized basis, so that the clinician can be in better control and obtain higher accuracy in the surgical decision. It is with this need in mind that this work was carried out. That is, the purpose of this work was to develop a technology that would allow the evaluation of the potential risk of AAA rupture on a patient by patient basis.

The approach taken here is based on sound fundamental principles of mechanics. That is, we treat the AAA as a pressure vessel, assuming that rupture occurs when the acting wall stress exceeds the wall strength. To accurately assess rupture potential of a given AAA, local wall stress distribution and local wall strength distribution need to first be assessed. It has been pointed out by us and others [47, 50, 52, 57, 131] that simple geometric characteristics and the law of Laplace can not give us reliable estimates of wall stress distribution. A rigorous method was therefore developed here which includes the reconstruction of the real geometry of AAA including ILT from medical image data (Chapter 5), the testing and quantifying of the material behavior of the AAA wall and ILT (Chapters 2, 3, and 4), and the complex 3D finite element modeling (Chapter 7), all for the accurate determination of the wall stress distribution for a given patient. Then we also noticed that wall strength not only differs from patient to patient, but from location to location for the same aneurysm. [183] To estimate the local wall strength distribution, a statistical model was developed and validated to predict of local wall strength based on four clinical measurable parameters (Chapter 8). Based on the information on local wall stress and local wall strength, a local rupture potential index was calculated for any given location (Chapter 10), and a mapping of RPI values was displayed on the 3D “virtual AAA”. The feasibility of our

technique was demonstrated by computing the RPI distribution for four patients who underwent elective surgical repair.

To the best of our knowledge, this is the first study that evaluates the rupture of AAA in a systematic, biomechanical manner on a patient-by-patient basis. Therefore, this work represents the state of art in this field. Nevertheless, though there are clear advantages of this technique, there are certainly limitations that one must bear in mind. Both of these are summarized in the remainder of this chapter.

11.1 Advantage of the Developed Technique

This study, compared to other methods for the clinical assessment of AAA, has several advantages; e.g., patient specificity, non-invasiveness, and incorporation of sound biomechanical principles. Each of these is discussed in more detail here.

11.1.1 Patient Specificity

Instead of using a generalized rule of thumb approach such as the "5-cm diameter criterion", each AAA was evaluated individually, taking into account its unique characteristics. The unique 3D geometry of each AAA, which plays a critical role in determining the wall stress, [51, 52] was reconstructed individually for each AAA. The wall stress was evaluated using the patient's own blood pressure. The local wall strength distribution was evaluated from a statistical model that uses some variables related to the unique features of each aneurysm. Finally, a

customized plot of the rupture potential index was displayed on the custom reconstructed AAA surface for visualization.

11.1.2 Noninvasive

Great care was taken to ensure that each step of our method was noninvasive. For example, to evaluate the wall stress distribution, the geometry was obtained from the CT scan images, blood pressure was measured through cuff pressure, and the material properties of the AAA wall and ILT were taken as the population mean from previous testing data. To evaluate the wall strength distribution, all the parameters - patient's age, AAA diameter, family history, local ILT thickness, and local diameter - were all obtained noninvasively. No invasive procedure of any kind was required. In our opinion, this makes the technique clinically applicable, feasible and cost effective.

11.1.3 Realistic Approach

As mentioned in Chapter 2, ILT is a solid mass existing in most aneurysms. We hypothesized that the presence of ILT alters the magnitude and distribution pattern of wall stress. The results of Chapter 7 prove that this is indeed the case. By incorporating the real ILT configuration into the AAA wall stress simulation, the result is more realistic and, therefore, more accurate in evaluating both AAA wall stress and rupture potential.

11.1.4 Application of Sound Biomechanical Principles

We believe that a major advantage of our work is the introduction of the concept of rupture potential index (RPI). Many researchers have been focused on evaluating the risk of rupture based solely on the wall stress distribution. [63, 81, 93, 95] However, as we discussed in Chapter 10, high stress does not necessarily mean high rupture potential at a particular point on the AAA wall if the wall strength at that point is much higher. Therefore, it is necessary to evaluate both wall stress and strength, then compare the local stress and strength to give an accurate assessment of the rupture potential. The concept of RPI was introduced as an easy-to-understand means to describe how close the acting wall stress is to wall strength. This index is, by definition, normalized and takes on values ranging from 0 to 1. Because it is based on biomechanical principle, we believe that this approach is more accurate and less subjective than the "5-cm diameter" approach that is popularly used currently.

11.2 General Limitations and Future Work

As discussed within individual Chapters, the developed methodology does have its limitations, mostly due to the shortcomings of contemporary technology, the unavailability of validated theories or information, and the use of a simplified model in an attempt to make it a tractable clinical tool. These limitations are summarized in this section. Like any other technology, development of this technology is and will be an ongoing process. Future work will certainly need to be done to address the more severe of these limitations.

11.2.1 Accuracy of Stress Simulation

For any finite element simulation, the accuracy of the result (output) depends on the accuracy of the following three inputs: geometry, material properties, and boundary conditions. Each of these contain limitations which should be addressed in future studies.

Geometric modeling (3D reconstruction) has the following limitations:

- *Average constant wall thickness*. The wall thickness was assumed to be constant (uniform) throughout each AAA because the local wall thickness variation was not available using the current imaging method. It is likely that wall thickness is spatially variable throughout the entire AAA, varying by a full millimeter in some cases. [126] This is of critical important as wall thickness is a key determinant of local wall stress. [63, 126] Raghavan showed that for the constant wall thickness varying 7.9 %, the peak wall stress could vary up to 12%. Thubrikar et al showed that by increasing uniform wall thickness from 1.31 mm (average thickness throughout entire AAA) to 1.58 mm (wall thickness of undilated section), the peak wall stress decreased from 34 N/cm^2 to 27 N/cm^2. The peak wall stress for the model using the measured local wall thickness was 40 N/cm^2. Future studies should further address this question and improve the current technique by incorporating the using real wall thickness into the 3D-reconstruction and stress analyses.
- *Calcified plaque was not included in the 3D reconstruction and stress analysis.* As shown by Inzoli et al., [55] the presence of calcified plaque can lead up to a 200% increase in peak wall stress. Future studies should further address the question of how much error we introduce to the stress calculation by neglecting calcified plaques and including them if necessary.

- *Average configuration.* The cross-sectional CT images of AAA used for 3D reconstruction are not a snap shot at a certain time point, but rather an average over the period of time over which the image data was collected. The resulting 3D reconstruction is not the geometry at one time point, but rather an "average" during the duration of the procedure. Future studies should address the degree of error introduced and develop possible ways of improving it.

Since our model is static instead of dynamic, it does not mimic the true stress state in vivo. To improve this limitation, one should perform a 3D dynamic simulation. For the in vivo situation, the pulsatile blood flow transmits the pressure through the ILT to the AAA wall. [221] Fluid structure interaction simulation is therefore also necessary. The hyperelastic material properties of wall and ILT used in this work can not be used for this purpose. New constitutive equations should therefore be developed to model the dynamic responses of ILT and AAA wall. Furthermore, if future studies include calcified plaque in the model, the material properties of the plaque also need to be quantified. Finally, we treated both AAA wall and ILT as isotropic, homogeneous material. As shown in **Figure 4**, ILT is not a homogenous material, but laminated with distinct layers. How the homogeneity assumption affects the accuracy of the stress analysis needs to be addressed in future studies. The AAA wall may not be isotropic material and current studies are ongoing in our laboratory to determine this. [222]

Boundary conditions are probably the most difficult to accurately simulate. AAA in vivo is directly connected to other parts of the body. To simplify the problem, we modeled AAA as an isolated part. In order to more closely mimic the in vivo situation, however, every connection or contact should be treated as a boundary condition for the model. This includes inclusion of an axial testing force, contact with the vertebral column, contact with other internal organs, etc.

Residual stress and residual strain should be included in the model as well. Although use of population mean values of ILT and AAA wall material properties does not introduce significant error in stress simulation (Section 7.4.2.2), obtaining patient specific material property values will no doubt increase the accuracy of the result at least incrementally. Moulton et al [223] used magnetic resonance imaging (MRI) tissue-tagging method to determine nonlinear material properties of myocardium. A similar "inverse" technique might apply to estimating patient- and location-specific material properties of the AAA wall and ILT in vivo. Future studies should address these limitations and include at least the most important ones.

11.2.2 Accuracy of Wall Strength Prediction

A detailed description of the limitations of the developed wall strength prediction model can be found in Section 8.4. In summary, due to the restriction of the open surgery procedure, we only collected samples from the anterior region of AAA. Future studies should collect samples from both the anterior and posterior region of AAA. However, due to surgical constraints, this can only be done from autopsy specimens, which of course have their own limitations. Test data from future studies can serve to further validate and update the current model. Since the model is only valid in the range of the data used for model construction, more samples are needed to broaden the allowable range of predictor parameters. Again, the significant predictors chosen here do not explain the mechanisms of wall weakening; they are only selected as a set of clinical variables to adequately predict the local wall strength. Any causal relationship suggested by the model must be based on sound theories. Future studies on the mechanisms of wall weakening will therefore aid the construction of an even better model.

11.2.3 Time Consuming

The tedious and time-consuming 3D-reconstruction and stress analysis procedures prohibit us from performing the analysis on a routine base. The current procedures can take from several hours to several days. Future studies should investigate an automatic 3D-reconstruction method that is less labor- and time-intensive and a computational stress analysis that is less computationally taking. Hopefully, with the advancement of computer technology, this will not be a problem in the future.

11.2.4 Expertise Demanded

From CT images to the final RPI plots, the current protocol uses various commercial as well as custom software. Because the process has not been "streamlined" to minimize ease of use, implementation currently requires significant familiarity and software expertise. For the purpose of clinical use, future studies should develop a user-friendly version that does not require a lot user involvement. A Windows-based application would be ideal.

11.2.5 Proper Failure Theory and the Critical RPI

The exact mechanism of AAA rupture (i.e., the failure theory for the AAA wall) is unknown. For example, it is unknown whether the wall yields first and then ruptures like ductile material, or if rupture happens rather quickly and is more like the failure of brittle material. The

exact nature of material failure should determine the appropriate evaluation criteria (i.e., selection of the appropriate stress and/or strength measure).

The basic underlying assumption of this work is that AAA ruptures when the acting stress exceeds the strength of the wall. However, "stress" is a not a single value, but rather a tensor with 3 normal components and three shear components. Which stress or what combination of the stresses is responsible for the failure of the wall? Is it the maximum principle stress? Or even the maximum principle strain? Is shear stress important at all? The answer to these questions lies in exactly how AAA ruptures. Future structural studies on the region of ruptured AAA wall might shed some light on choosing the proper failure theory. Biaxial or mutliaxial tensile failure testing might also help us to understand the failure of the material. In the current work, we used the von Mises stress index, which is combination of all the three principle stresses, to assess the potential of wall failure. We chose this index simply because there is no other known failure theory for the AAA wall, and this has been used previously for similar purposes. [47, 51, 52, 56, 57, 63, 81]

To evaluate how the choice of failure criterion would affect the stress results and findings in the present study, the maximum principle stress for one subject was plotted and compared to the von Mises stress distribution patterns. The von Mises stress and the maximum principle stress of subject AAA #4 are almost identical (**Figure 62**), though the maximum principle stress is slightly higher (~3%) than von Mises stress. Indeed, a similar comparison results from all the study subjects. **Table 30** lists the peak maximum principle stress and peak von Mises stress for each AAA studied. For all the AAAs studied, the differences between peak von Mises stress and peak maximum principal stress are about 3%. While the best choice of which failure theory is most appropriate deserves further evaluation, within the overall context of determining the risk of rupture, it might make a significant difference which theory is chosen.

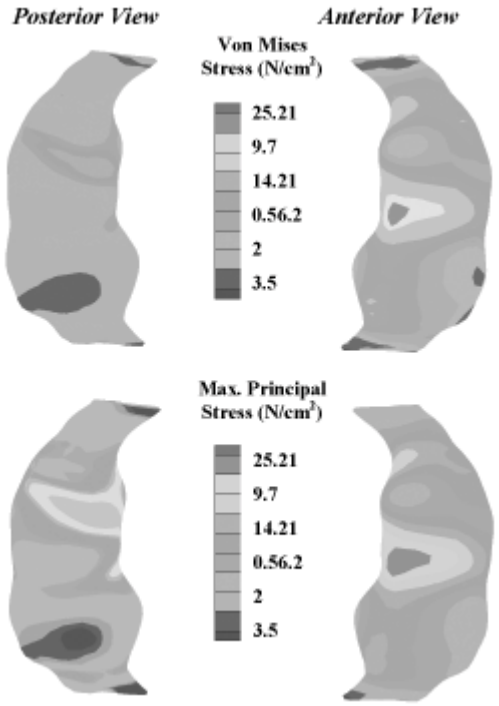

Figure 63 von Mises stress distribution (top) and maximum principal stress distribution (bottom) on AAA #4. Note the similarity between the two stress distribution patterns.

Table 30 Peak von Mises stress and maximum principal stress for each AAA studies. Less than 5% difference was observed between these two peak stress values.

	Peak von Mises Stress (N/cm^2)	**Peak Maximum Principal Stress** (N/cm^2)	**Absolute Difference** (N/cm^2)	**Percentage Difference** (%)
AAA #1	35.3	34.2	1.1	3.1
AAA #2	19.1	18.7	0.4	2.4
AAA #3	38.0	36.5	1.5	4.0
AAA #4	24.5	25.2	0.7	3.0

As discussed in Section 11.2.1, the AAA wall may be anisotropic. This might also hold true respect to the AAA wall strength; i.e., it might be different depending on the direction of the force applied. In the present study, we assumed that the wall strength does not differ between the longitudinal and circumferential directions. We based this assumption on previous data collected in our lab. [62] However, this data, as well as the data used in this work was based on uniaxial loading conditions. In reality, the AAA wall material is loaded in multiple directions. Therefore, it is currently unknown which strength measure should be used. Again, this should be addressed by developing a suitable failure theory for the AAA wall.

Finally, the most practical question is, "what is the critical value of peak RPI"? Is RPI of 0.5 too high or not high enough to warrant surgery? Future clinical studies need to be conducted to address this question before this technology can be realistically and reliably employed in clinical practice.

11.3 Conclusion

Despite the stated limitations, we believe that this study represents a significant advancement in incorporating biomechanical principles in the clinical assessment of AAA rupture potential. Besides being a completely noninvasive approach, the overall methodology required no additional involvement by the patients and is quite feasible in a clinical setting. Ultimately, the scope and utility of this technique will need to be evaluated in clinical trials. The evolution of this technique will be an on-going process. However, the successful implementation of this technique would no doubt benefit both the surgical community and AAA patients alike.

APPENDICES

Appendix A

Mathematica Program For Calculation of Local ILT Thickness, Local Diameter, Local Wall Strength, Local RPI Values, and Interpolation of Nodal ILT Thickness, Nodal Local Diameter, Nodal Wall Strength, and Nodal RPI.

Note: Comments appear in bold.

```
Set directory and input constants
(Th is slice thickness in cm)
MaxDiam is from the patient chart
Nodes is the number of nodes from the (outer?) surface mesh
(from Abaqus)
     SetDirectory["M:\RPI\A13584\wall"];
     Th=0.5;
     Age = 73;
     His = 0;
     MaxDiam = 6.4;
     Nodes=2496;
```

Specify wall filenames

```
WallFnames:=FileNames["a*.txt"]
```

Specify Intraluminal thrombus (lumen) filenames

WallFnames and IltFnames needs to be the same length

```
IltFnames:=FileNames["i*.txt"]
```

Sects is the number of slices for wall and lumen

```
Sects=Length[WallFnames]
```

Initialize the variables for the total length of data for the wall and lumen to 0

```
TLw:=0;
TLi:=0;
```

Calculate the total length of data for wall (Total Length wall) and length for each file (Each length wall) ELw

```
Do[
Walldata[J]=ReadList[WallFnames[[J]],Number, RecordLists->True];
```

Calculate the total length of data for lumen (Total Length Ilt) and length for each file (Each length ilt) ELi

```
Do[
Iltdata[J]=ReadList[IltFnames[[J]],Number, RecordLists->True];
ELi[J]=Length[Iltdata[J]];TLi=TLi+Length[Iltdata[J]], {J,1,Sects}]
TLi
```

```
2587
ELi[1]
44
```

Determines which values of z are being read in

```
Do[Z[J]=Walldata[J][[1]][[3]], {J,1,Sects}];
Table[Z[i],{i,Sects}]
```

Calculates the centroids of each slice for the lumen data in the x-direction (takes an average)

```
Do[AX=0;AY=0;
Do[AX=AX+Iltdata[J][[L]][[1]],
{L,1,ELi[J]}];
CX[J]=AX/ELi[J],
{J,1,Sects}];
```

Calculates the centroids of each slice for the lumen data in the y-direction (takes an average)

```
Do[AY=0;
Do[AY=AY+Iltdata[J][[L]][[2]],
{L,1,ELi[J]}];
CY[J]=AY/ELi[J],
{J,1,Sects}];
```

Converts the lumen data into polar coordinates (theta, r)

```
Do[ILTPol[J]=Table[{0,0},{L,1,ELi[J]}],{J,1,Sects}]
Do[ILTPol[J]=Sort[Table[{Which[
     (Iltdata[J][[L]][[1]]-CX[J])>=0 &&
```

```
          (Iltdata[J][[L]][[2]]-CY[J])>=0,
               90.-ArcTan[(Iltdata[J][[L]][[1]]-CX[J]),
               (Iltdata[J][[L]][[2]]-CY[J])]*180./N[Pi],
          (Iltdata[J][[L]][[1]]-CX[J])>=0 &&
          (Iltdata[J][[L]][[2]]-CY[J])<0,
               90.-ArcTan[(Iltdata[J][[L]][[1]]-CX[J]),
               (Iltdata[J][[L]][[2]]-CY[J])]*180./N[Pi],
          (Iltdata[J][[L]][[1]]-CX[J])<=0 &&  Sects
          (Iltdata[J][[L]][[2]]-CY[J])>=0,
               450.-ArcTan[(Iltdata[J][[L]][[1]]-CX[J]),
               (Iltdata[J][[L]][[2]]-CY[J])]*180./N[Pi],
          (Iltdata[J][[L]][[1]]-CX[J])<=0 &&
          (Iltdata[J][[L]][[2]]-CY[J])<0,
               90.-ArcTan[(Iltdata[J][[L]][[1]]-CX[J]),
               (Iltdata[J][[L]][[2]]-CY[J])]*180./N[Pi]],
     Sqrt[(Iltdata[J][[L]][[1]]-CX[J])^2+
          (Iltdata[J][[L]][[2]]-CY[J])^2]},
     {L,1,ELi[J]}]],{J,1,Sects}]
     Do[Sort[ILTPol[J]],{J,1,Sects}]
```

Converts the wall data into polar coordinates using the centroid data (theta, r)

```
     Do[Pol[J]=Table[{0,0},{L,1,ELw[J]}],{J,1,Sects}]
     Do[Pol[J]=Sort[Table[{Which[
          (Walldata[J][[L]][[1]]-CX[J])>=0 &&
```

```
          (Walldata[J][[L]][[2]]-CY[J])>=0,
               90.-ArcTan[(Walldata[J][[L]][[1]]-CX[J]),
               (Walldata[J][[L]][[2]]-CY[J])]*180./N[Pi],
          (Walldata[J][[L]][[1]]-CX[J])>=0 &&
          (Walldata[J][[L]][[2]]-CY[J])<0,
               90.-ArcTan[(Walldata[J][[L]][[1]]-CX[J]),
               (Walldata[J][[L]][[2]]-CY[J])]*180./N[Pi],
          (Walldata[J][[L]][[1]]-CX[J])<=0 &&  Sects
          (Walldata[J][[L]][[2]]-CY[J])>=0,
               450.-ArcTan[(Walldata[J][[L]][[1]]-CX[J]),
               (Walldata[J][[L]][[2]]-CY[J])]*180./N[Pi],
          (Walldata[J][[L]][[1]]-CX[J])<=0 &&
          (Walldata[J][[L]][[2]]-CY[J])<0,
               90.-ArcTan[(Walldata[J][[L]][[1]]-CX[J]),
               (Walldata[J][[L]][[2]]-CY[J])]*180./N[Pi]],
     Sqrt[(Walldata[J][[L]][[1]]-CX[J])^2+
          (Walldata[J][[L]][[2]]-CY[J])^2]},
     {L,1,ELw[J]}]],{J,1,Sects}]
```

Sets the angle increment to 5 degrees, initialzes k = 1

Recalculates a point for every 5 degrees for the wall data

```
     DT=5;K=1;RTheta=Table[{0,0},{360/DT*Sects}];
     Do[{TX=0;L=1;
          While[TX<360 && L<ELw[J],
          {T1=Pol[J][[L]][[1]];T2=Pol[J][[L+1]][[1]];
```

```
          R1=Pol[J][[L]][[2]];R2=Pol[J][[L+1]][[2]];
          Which[TX<=T1,
               {T1=Pol[J][[ELw[J]]][[1]]-
360;R1=Pol[J][[ELw[J]]][[2]];
               T2=Pol[J][[L]][[1]]; R2=Pol[J][[1]][[2]];
               RTheta[[K]]={TX,(TX-T1)/(T2-T1)*(R2-R1)+R1};
               K=K+1;TX=TX+DT},
          TX>T1 && TX<=T2,
               {TM=T1+0.5*(T1+T2);RM=(R1+R2)/2;
               RTheta[[K]]={TX,(TX-T1)/(T2-T1)*(R2-R1)+R1};
               K=K+1;TX=TX+DT},
          TX>T2,L=L+1]}];
          While[TX<360,
          {T1=Pol[J][[ELw[J]]][[1]];T2=Pol[J][[1]][[1]];
          R1=Pol[J][[ELw[J]]][[2]];R2=Pol[J][[1]][[2]];
          TM=T1+0.5*(T1+T2);RM=(R1+R2)/2;
          RTheta[[K]]={TX,(TX-T1)/(T2-T1)*(R2-R1)+R1};
          K=K+1;
          TX=TX+DT}]},{J,1,Sects}];
     Do[RTA[J]=ListPlot[Table[RTheta[[(J-1)*360/DT+L]],
          {L,1,360/DT}],Ticks->None,PlotJoined->True,
          DisplayFunction->Identity,PlotRange->Automatic,
          GridLines->Automatic],{J,1,Sects}]
```

Sets the angle increment to 5 degrees, initialzes k = 1

Recalculates a point for every 5 degrees for the lumen data

```
     K=1;IltRTheta=Table[{0,0},{360/DT*Sects}];
     Do[{TX=0;L=1;
          While[TX<360 && L<ELi[J],
          {T1=ILTPol[J][[L]][[1]];T2=ILTPol[J][[L+1]][[1]];
          R1=ILTPol[J][[L]][[2]];R2=ILTPol[J][[L+1]][[2]];
          Which[TX<=T1,
               {T1=ILTPol[J][[ELi[J]]][[1]]-
360;R1=ILTPol[J][[ELi[J]]][[2]];
               T2=ILTPol[J][[L]][[1]]; R2=ILTPol[J][[1]][[2]];
               IltRTheta[[K]]={TX,(TX-T1)/(T2-T1)*(R2-R1)+R1};
               K=K+1;TX=TX+DT},
          TX>T1 && TX<=T2,
               {TM=T1+0.5*(T1+T2);RM=(R1+R2)/2;
               IltRTheta[[K]]={TX,(TX-T1)/(T2-T1)*(R2-R1)+R1};
               K=K+1;TX=TX+DT},
          TX>T2,L=L+1]}];
          While[TX<360,
          {T1=ILTPol[J][[ELi[J]]][[1]];T2=ILTPol[J][[1]][[1]];
          R1=ILTPol[J][[ELi[J]]][[2]];R2=ILTPol[J][[1]][[2]];
          TM=T1+0.5*(T1+T2);RM=(R1+R2)/2;
          IltRTheta[[K]]={TX,(TX-T1)/(T2-T1)*(R2-R1)+R1};
          K=K+1;
          TX=TX+DT}]},{J,1,Sects}];
```

Calculates the centroids of each z value for the wall data in the x-direction (takes an average)

```
     Do[AX=0;AY=0;
     Do[AX=AX+Walldata[J][[L]][[1]],
     {L,1,ELw[J]}];
     CWX[J]=AX/ELw[J],
     {J,1,Sects}];
```

Calculates the centroids of each z value for the wall data in the y-direction (takes an average)

```
     Do[AY=0;
     Do[AY=AY+Walldata[J][[L]][[2]],
     {L,1,ELw[J]}];
     CWY[J]=AY/ELw[J],
     {J,1,Sects}];
     Do[Pol[J]=Table[{0,0},{L,1,ELw[J]}],{J,1,Sects}]
     Do[Pol[J]=Sort[Table[{Which[
          (Walldata[J][[L]][[1]]-CWX[J])>=0 &&
          (Walldata[J][[L]][[2]]-CWY[J])>=0,
               90.-ArcTan[(Walldata[J][[L]][[1]]-CWX[J]),
               (Walldata[J][[L]][[2]]-CWY[J])]*180./N[Pi],
          (Walldata[J][[L]][[1]]-CWX[J])>=0 &&
          (Walldata[J][[L]][[2]]-CWY[J])<0,
               90.-ArcTan[(Walldata[J][[L]][[1]]-CWX[J]),
               (Walldata[J][[L]][[2]]-CWY[J])]*180./N[Pi],
```

```
          (Walldata[J][[L]][[1]]-CWX[J])<=0 &&  Sects
          (Walldata[J][[L]][[2]]-CWY[J])>=0,
               450.-ArcTan[(Walldata[J][[L]][[1]]-CWX[J]),
               (Walldata[J][[L]][[2]]-CWY[J])]*180./N[Pi],
          (Walldata[J][[L]][[1]]-CWX[J])<=0 &&
          (Walldata[J][[L]][[2]]-CWY[J])<0,
               90.-ArcTan[(Walldata[J][[L]][[1]]-CWX[J]),
               (Walldata[J][[L]][[2]]-CWY[J])]*180./N[Pi]],
     Sqrt[(Walldata[J][[L]][[1]]-CWX[J])^2+
          (Walldata[J][[L]][[2]]-CWY[J])^2]},
     {L,1,ELw[J]}]],{J,1,Sects}]
     ELw[1]
     44
     L = Length[Pol[1]]
     44
```

Calculates the normalized diameter of the wall data

```
     Do[AXX=0;
     Do[AXX=AXX+Pol[J][[L]][[2]],
     {L,1,ELw[J]}];
     NorD[J]=2*(AXX/ELw[J])/MaxDiam,
     {J,1,Sects}];
```

Writes a file called Thicknss.txt (format: x,y,x, ilt thickness, norm Diam, strength)

```
     FileTh=OpenWrite["Thickness.txt"]
```

```
     Thick=Table[{0,0},{360/DT*Sects}];K=1;
     Do[
     Do[{Thick[[K]]={N[
CX[J]+(RTheta[[K]][[2]]+Th)*Sin[RTheta[[K]][[1]]*\[Pi]/180.],
                4],
          N[CY[J]+(RTheta[[K]][[2]]+Th)*Cos[RTheta[[K]][[1]]*N[P
i]/180],5],
          Z[J],N[RTheta[[K]][[2]]-
IltRTheta[[K]][[2]],4],N[NorD[J],4],
               N[141.26-17.16*(RTheta[[K]][[2]]-
IltRTheta[[K]][[2]])+3.39*
                    Age-257.30*NorD[J]-82.00*His,4]};
     Write[FileTh,Thick[[K]][[1]],"  ",Thick[[K]][[2]],"  ",
          Thick[[K]][[3]],"  ",Thick[[K]][[4]],"
",Thick[[K]][[5]],"  ",
             Thick[[K]][[6]]];
          K=K+1},{L,1,360/DT}],
     {J,1,Sects}];Close[FileTh]
     OutputStream[Thickness.txt,201]
     Thickness.txt
```

Reads in a file called stress.txt

```
     StressFnames:=FileNames["stress.txt"]
     Stressdata=ReadList["stress.txt",Number, RecordLists-
>True];
```

```
Dimensions[Stressdata]
Do[
     u=0;v=0;
     x=Stressdata[[J]][[3]]/Th;
     u=1-IntegerPart[x];
     v=Z[u]/Th-Stressdata[[J]][[3]]/Th;
     NMDia[J]=(1-v)*NorD[u]+v*NorD[u+1];
     NCX[J]=(1-v)*CX[u]+v*CX[u+1];
     NCY[J]=(1-v)*CY[u]+v*CY[u+1],
     {J,1,Nodes}];
Do[NodalP=Table[{0,0},{L,1,Nodes}]];
Do[NodalP=Sort[Table[{Which[
     (Stressdata[[L]][[1]]-NCX[L])>=0 &&
     (Stressdata[[L]][[2]]-NCY[L])>=0,
          90.-ArcTan[(Stressdata[[L]][[1]]-NCX[L]),
          (Stressdata[[L]][[2]]-NCY[L])]*180./N[Pi],
     (Stressdata[[L]][[1]]-NCX[L])>=0 &&
     (Stressdata[[L]][[2]]-NCY[L])<0,
          90.-ArcTan[(Stressdata[[L]][[1]]-NCX[L]),
          (Stressdata[[L]][[2]]-NCY[L])]*180./N[Pi],
     (Stressdata[[L]][[1]]-NCX[L])<=0 &&  Sects
     (Stressdata[[L]][[2]]-NCY[L])>=0,
          450.-ArcTan[(Stressdata[[L]][[1]]-NCX[L]),
          (Stressdata[[L]][[2]]-NCY[L])]*180./N[Pi],
```

```
          (Stressdata[[L]][[1]]-NCX[L])<=0 &&
          (Stressdata[[L]][[2]]-NCY[L])<0,
               90.-ArcTan[(Stressdata[[L]][[1]]-NCX[L]),
               (Stressdata[[L]][[2]]-NCY[L])]*180./N[Pi]],
     Sqrt[(Stressdata[[L]][[1]]-NCX[L])^2+
          (Stressdata[[L]][[2]]-NCY[L])^2]},
     {L,1,Nodes}]]]
```

Interpolates the nodal strength (Strength) from previously calculated wall strength

```
     Do[
     uu=0;vv=0;w=0;s=0;
          y=NodalP[[J]][[1]]/DT;
          x=Stressdata[[J]][[3]]/Th;
               uu=1-IntegerPart[x];
          vv=Z[uu]/Th-Stressdata[[J]][[3]]/Th;
            w=IntegerPart[y];
          s=Mod[NodalP[[J]][[1]],DT]/DT;
           s1=72*(uu-2)+w+1;
        s2=72*(uu-2)+w+2;
       s3=72*(uu-1)+w+1;
        s4=72*(uu-1)+w+2;
          ILT[J]=(1-vv)*(1-s)*Thick[[s1]][[4]]+
             vv*(1-s)*Thick[[s2]][[4]]+(1-
vv)*s*Thick[[s3]][[4]]+
```

```
            vv*s*Thick[[s4]][[4]];
          Strength[J]=(1-vv)*(1-s)*Thick[[s1]][[6]]+
            vv*(1-s)*Thick[[s2]][[6]]+(1-
vv)*s*Thick[[s3]][[6]]+
            vv*s*Thick[[s4]][[6]];
          NMDia[J]=(1-v)*NorD[u]+v*NorD[u+1],
          {J,1,Nodes}];
```

File RPI outputs are interpolated local ilt thickness and interpolated nodal strength which corresponds to nodal stress from FEM simulation

```
     FileRPI=OpenWrite["RPI.txt"]
     Do[
     Write[FileRPI,N[ILT[J],3],"
",N[Strength[J],5]],{J,1,Nodes}];Close[FileRPI]
     OutputStream[RPI.txt,203]
     RPI.txt
```

Appendix B

Sample ABAQUS Program

The following is an ABAQUS input file titled AAA.inp. To conserve space, the mesh information has been shortened.

```
*HEADING
ABAQUS job created on 09-Jun-01 at 13:26:59
**
*RESTART, WRITE, OVERLAY
*NODE
     1,      9.68059,      13.3987,    -0.263817
     2,      9.35018,      13.6632,    -0.285977
~~~~~~~
  13061,      10.2486,       11.069,      -8.8919
  13062,      10.2278,      11.0107,          -9.
*Element, type=C3D10H, ELSET=WALL
   1,    84,    98,   100,   233,  1935,  1934,  1933,  1937,  1936,  1938
~ ~ ~ ~ ~
3706,  1108,   801,   806,   805,  5285,  7713,  6464,  5283,  5287,  7769
```

```
*ELEMENT, TYPE=C3D10H, ELSET=ILT
3707,  1295,   261,  1570,  1767,  8221,  8220,  8219,  8223,  8222,  8224
~ ~ ~ ~ ~
8097,  1838,   491,   493,  1844, 13005,  4198, 12215, 12870,  8708, 12946
** ILT
**
*SOLID SECTION, ELSET=ILT, MATERIAL=ILT
        1.,
**
** WALL
**
*SOLID SECTION, ELSET=WALL, MATERIAL=WALL
        1.,
**
** ILT
**
*MATERIAL, NAME=ILT
**
*DENSITY
        1.,
**
*HYPERELASTIC, N=2
      0.,       2.6,        0.,        0.,       2.6,        0.,        0.
```

```
**
** WALL
**
*MATERIAL, NAME=WALL
**
*DENSITY
         1.,
**
*HYPERELASTIC, N=2
      17.4,        0.,     188.1,        0.,        0.,        0.,        0.
**
** wallfix
**
*BOUNDARY, OP=NEW
       1, 1,,          0.
       1, 2,,          0.
       1, 3,,          0.
    ~ ~ ~ ~ ~
    1294, 1,,          0.
    1294, 2,,          0.
    1294, 3,,          0.
**
** iltfix
```

```
**
*BOUNDARY, OP=NEW
   1555, 1,,         0.
   1555, 2,,         0.
   1555, 3,,         0.
  ~ ~ ~ ~ ~
   1932, 1,,         0.
   1932, 2,,         0.
   1932, 3,,         0.
** Step  1, aaa
** LoadCase, AAA
**
*STEP, AMPLITUDE=RAMP, INC=100, NLGEOM
*STATIC
       0.05,         1.
**
*ELSET, ELSET=AAA
   3711,   4715,   4842,   5033,   5420,   5452,   5453,   5555,
   ~ ~ ~ ~ ~
  7946,   7975,   8002,   8006,   8007,   8046,   8089,   8094
*ELSET, ELSET=AAA_1
   3720,   4444,   4472,   4744,   5020,   5027,   5416,   5457,
   ~  ~ ~ ~ ~
```

```
7994,  8005,  8008,  8012
*ELSET, ELSET=AAA_2
  3862,  4001,  4003,  4064,  4383,  4495,  4501,  4598,
  ~ ~ ~ ~ ~
  7966,  7983,  7985,  7991,  8033,  8067,  8071,  8095
*ELSET, ELSET=AAA_3
  4306,  4611,  4701,  4747,  4793,  4822,  5028,  5079,
  ~ ~ ~ ~ ~
  8051,  8072
**
**
** AAA
**
*DLOAD, OP=NEW
AAA, P1,       1.25
AAA_1, P2,       1.25
AAA_2, P3,       1.25
AAA_3, P4,       1.25
**
*RESTART, WRITE, OVERLAY
*EL PRINT, POSITION=AVERAGED AT NODES
MISES, SP3
*ENDSTEP
```

Appendix C

Sample ABAQUS Status File

ABAQUS VERSION 6.2-1

SUMMARY OF JOB INFORMATION:

STEP	INC	ATT	SEVERE DISCON ITERS	EQUIL ITERS	TOTAL ITERS	TOTAL TIME/ FREQ	STEP TIME	INC OF TIME
1	1	1	0	2	2	0.0500	0.0500	0.05000
1	2	1	0	1	1	0.100	0.100	0.05000
1	3	1	0	2	2	0.175	0.175	0.07500
1	4	1	0	2	2	0.288	0.288	0.1125
1	5	1	0	2	2	0.456	0.456	0.1688
1	6	1	0	3	3	0.709	0.709	0.2531
1	7	2	0	2	2	0.962	0.962	0.2531
1	8	1	0	1	1	1.0	1.0	0.0379

THE ANALYSIS HAS BEEN COMPLETED

Appendix D

Table D1 Wall Strength Data and Related Information for Model Construction Group

PT	Strength	ILT	Size	Age	Local Dia.	Normalized Dia.	Hist	SMK	SEX
	(N/cm^2)	(cm)	(cm)	(yr)	(cm)		(1=Yes)	(1= SMK)	(1=Man)
1	91.08	0.925 (0.90, 0.95)	5.5	71	5.11 (5.15, 5.07)	0.93	1	1	1
1	89.25	0.80 (0.80, 0.80)	5.5	71	4.50 (4.52, 4.48)	0.82	1	1	1
1	246.39	0.30 (0.30, 0.30)	5.5	71	3.05 (3.00, 3.10)	0.55	1	1	1
2	40.46	1.25 (1.30, 1.20)	5	81	4.86 (4.82, 4.90)	0.97	1	1	0
2	66.4	0.88 (0.85, 0.91)	5	81	4.80 (4.68, 4.92)	0.96	1	1	0
2	60.65	0.88 (0.85, 0.91)	5	81	4.30 (4.26, 4.34)	0.86	1	1	0
3	91.08	1.49 (1.40, 1.58)	5.5	57	4.20 (4.23, 4.17)	0.76	0	0	1
3	128.51	1.375 (1.40, 1.35)	5.5	57	3.80 (3.80, 3.80)	0.69	0	0	1
3	172.05	1.20 (1.20, 1.20)	5.5	57	3.20 (3.15, 3.25)	0.58	0	0	1
3	126.66	1.315 (1.3, 1.33)	5.5	57	3.37 (3.30, 3.44)	0.61	0	0	1
4	178.95	0.50 (0.50, 0.50)	4	72	2.10 (2.10, 2.10)	0.53	0	0	0
4	130.45	1.315 (1.30, 1.33)	4	72	3.60 (3.60, 3.60)	0.9	0	0	0
4	224.86	0.85 (0.80, 0.90)	4	72	2.70 (2.72, 2.68)	0.68	0	0	0
4	183.01	1.06 (1.10, 1.02)	4	72	3.10 (3.12, 3.08)	0.78	0	0	0
5	86.59	0.10 (0.10, 0.10)	5	61	4.20 (4.25, 4.15)	0.84	1	0	0
5	136.89	0.07 (0.08, 0.06)	5	61	3.00 (3.10, 2.90)	0.60	1	0	0
6	316.77	0.24 (0.2, 028)	5.4	78	2.26 (2.20, 2.32)	0.42	0	0	1

Table D1 Wall Strength Data and Related Information for Model Construction Group (Continue)

PT	Strength	ILT	Size	Age	Local Dia.	Normalized Dia.	Hist	SMK	SEX
	(N/cm^2)	(cm)	(cm)	(yr)	(cm)		(1=Yes)	(1= SMK)	(1=Man)
6	175.54	1.10 (1.10, 1.10)	5.4	78	4.40 (4.45, 4.35)	0.81	0	0	1
6	233.9	0.57 (0.5, 0.64)	5.4	78	3.00 (3.10, 2.90)	0.56	0	0	1
7	147.53	1.78 (1.80, 1.76)	6.8	69	6.48 (6.40, 6.56)	0.95	0	1	1
7	323.43	0.70 (0.70, 0.70)	6.8	69	3.85 (3.80, 3.90)	0.57	0	1	1
7	152.02	1.32 (1.30, 1.34)	6.8	69	5.26 (5.25, 5.27)	0.77	0	1	1
8	39.07	0.65 (0.60, 0.70)	4	56	2.50 (2.51, 2.49)	0.63	1	0	1
8	100.192	0.19 (0.20, 0.18)	4	56	2.10 (2.10, 2.10)	0.53	1	0	1
8	81.72	0.30 (0.30, 0.30)	4	56	2.30 (2.32, 2.28)	0.58	1	0	1
9	115.2	0.40 (0.40, 0.40)	5.5	75	5.50 (5.60, 5.40)	1.00	0	0	1
9	148.68	0.08 (0.10, 0.06)	5.5	75	5.00 (5.02, 4.98)	0.91	0	0	1
9	123.73	0.08 (0.05, 0.11)	5.5	75	5.30 (5.25, 5.35)	0.96	0	0	1
10	147.95	0.47 (0.50, 0.44)	4.9	76	4.50 (4.56, 4.44)	0.92	0	1	0
10	126.47	0.75 (0.70, 0.80)	4.9	76	4.80 (4.85, 4.75)	0.98	0	1	0
10	200.92	0.44 (0.40, 0.48)	4.9	76	3.76 (3.70, 3.82)	0.77	0	1	0
11	169.14	0.20 (0.20, 0.20)	7.2	68	5.90 (5.86, 5.94)	0.82	0	0	1
11	103.76	0.50 (0.50, 0.50)	7.2	68	6.85 (6.82, 6.88)	0.95	0	0	1
11	73.8	0 (0, 0)	7.2	68	5.80 (5.74, 5.86)	0.81	0	0	1

Appendix E

Table E1 Wall Strength Data and Related Information for Model Validation Group

PT	Strength	ILT	Size	Age	Local Dia.	Normalized Dia.	Hist	SMK	SEX
	(N/cm^2)	(cm)	(cm)	(yr)	(cm)		(1=Yes)	(1= SMK)	(1=Man)
1	99.80	0.20 (0.18, 0.22)	5.7	77	5.50 (5.35, 5.65)	0.96	0	0	1
1	238.57	0.20 (0.20, 0.20)	5.7	77	3.80 (3.92, 3.68)	0.67	0	0	1
1	269.45	0.15 (0.15, 0.15)	5.7	77	3.00 (3.14, 2.86)	0.53	0	0	1
2	98.28	0.60 (0.62, 0.58)	7	66	5.00 (5.05, 4.95)	0.71	1	0	0
2	174.64	0.02 (0.04, 0)	7	66	3.15 (3.13, 3.17)	0.45	1	0	0
2	168.84	0.02 (0.04, 0)	7	66	3.40 (3.42, 3.38)	0.49	1	0	0
3	243.43	0.15 (0.16, 0.14)	5.8	77	5.20 (5.23, 5.17)	0.90	0	0	1
3	255.41	0.14 (0.14, 0.14)	5.8	77	3.40 (3.42, 3.38)	0.59	0	0	1
3	190.79	0.60 (0.62, 0.58)	5.8	77	4.70 (4.82, 4.58)	0.81	0	0	1
4	306.90	0.15 (0.14, 0.16)	6.8	72	2.20 (2.25, 2.15)	0.32	0	0	0
4	306.60	0.18 (0.17, 0.19)	6.8	72	2.25 (2.25, 2.25)	0.33	0	0	0
4	203.50	0.25 (0.26, 0.24)	6.8	72	4.60 (4.50, 4.70)	0.68	0	0	0
5	255.59	0.42 (0.41, 0.43)	5.6	76	3.04 (3.16, 2.92)	0.54	0	0	1
5	210.58	0.62 (0.60, 0.64)	5.6	76	4.06 (4.17, 3.95)	0.73	0	0	1

Table E1 Wall Strength Data and Related Information for Model Validation Group (Continue)

PT	Strength	ILT	Size	Age	Local Dia.	Normalized Dia.	Hist	SMK	SEX
	(N/cm^2)	(cm)	(cm)	(yr)	(cm)		(1=Yes)	(1= SMK)	(1=Man)
5	77.80	1.10 (1.20, 1.00)	5.6	76	5.60 (5.50, 5.70)	1.00	0	0	1
6	173.36	1.37 (1.40, 1.34)	6.5	62	4.00 (4.05, 3.95)	0.62	0	0	1
6	241.00	1.50 (1.50, 1.50)	6.5	62	2.40 (2.45, 2.35)	0.37	0	0	1
6	272.00	0.20 (0.20, 0.20)	6.5	62	2.10 (2.10, 2.10)	0.32	0	0	1
7	69.65	1.00 (1.06, 0.94)	5.3	76	3.50 (3.64, 3.36)	0.66	0	1	1
7	186.78	1.30 (1.32, 1.28)	5.3	76	3.90 (4.02, 3.78)	0.74	0	1	1
7	153.76	2.00 (1.90, 2.10)	5.3	76	4.35 (4.34, 4.36)	0.82	0	1	1

BIBLIOGRAPHY

BIBLIOGRAPHY

[1] STEDMAN, *STEDMAN's Elestronic Medical Dictionary*, 2.0 ed: Williams & Wikins, 1996.

[2] J. White and S. Scovell, *Etiology of Abdominal Aortic Aneurysms: The Structural Basis for Aneurysm Formation*. Philadelphia, PA: W.B. Saunders Company, 1999.

[3] C. Kakos, U. Mukhopadhyay, I. Papakostas, J. Ghosh, G. Thomson, and R. Hughes, "Abdominal Aortic Aneurysm: the role of clinical examination and oppertunistic detection," *European Journal of Vascular and Endovascular Surgery*, vol. 19, pp. 804-817, 2000.

[4] A. I. Holleb, "Vital Statistics of the United States," *CA Cancer J Clin*, vol. 37, pp. 6, 1987.

[5] H. Bengtsson, B. Sonesson, and D. Bergqvist, "Incidence and Prevalence of Abdominal Aortic AneurysmsEestimated by Necropsy Studies and Population Screening by Ultrasound," *Ann. N.Y. Acad Sci*, vol. 800, pp. 1-24, 1996.

[6] J. C. Stanley, R. W. Barnes, C. B. Ernst, N. R. Hertzer, J. A. Mannick, and W. S. Moore, "Vascular Surgery in the United States: Workforce issues. Report of the Society for Vascular Surgery and the International Society for Cardiovascular Surgery, North American Chapter, Committee on Workforce Issues," *J Vasc Surg*, vol. 23, pp. 172-81, 1996.

[7] F. A. Lederle, G. R. Johnson, S. E. Wilson, E. P. Chute, F. N. Littooy, and D. Bandyk, "Prevalence and Associations of Abdominal Aortic Aneurysm Detected Through Screening.," *Ann Intern Med*, vol. 126, pp. 441-9, 1997.

[8] F. A. Lederle, G. R. Johnson, S. E. Wilson, and F. N. Littooy, "Yield of Repeated Screening for Abdominal Aortic Aneurysm after a 4 Year Interval," *Arch Intern Med.*, vol. 160, pp. 1117-1121, 2000.

[9] H. Bengtsson, D. Bergqvist, O. Ekberg, and L. Janzon, "A Population Based Screening of Abdominal Aortic Aneurysms (AAA)." *Eur J Vasc Surg*, vol. 5, pp. 53-57, 1991.

[10] J. W. J. Hallett, J. M. Naessens, and D. J. Ballard, "Early and Late Outcome of Surgical Repair for Small Abdominal Aortic Aneurysm: a Population-based Analysis," *J Vasc Surg*, vol. 18, pp. 684-91, 1993.

[11] L. J. Melton, L. K. Bickerstaff, L. H. Hollier, H. J. Peenen, J. T. Lie, and P. C. Pairolero, "Changing incidence of Abdominal Aortic Aneurysms: A Population-based Study," *Am J Epidemiol*, vol. 120, pp. 379-86, 1984.

[12] M. Heikkinen, J. P. Salenius, and O. Auvinen, "Projected Workload for a Vascular Service in 2020," *Eur J Vasc Endovasc Surg*, vol. 19, pp. 351-5, 2000.

[13] R. N. Limet and A. A. Sakalishasan, "Determination of the Expansion Rate and Incidence of Rupture of Abdominal Aortic Aneurysm," *J vasc Surg*, vol. 14, pp. 540-548, 1991.

[14] J. B. Chang, T. A. Stein, J. P. Liu, and D. M.E., "Risk Factors Associated with Rapid Growth of Small Abdominal Aortic Aneurysms," *Surgery*, vol. 121, pp. 117-22, 1997.

[15] J. L. Cronenwett, S. K. Sargent, and H. Wall, "Variables That Affect the Expansion Rate and Outcome of Small Abdominal Aortic Aneurysms," *Journal of vascular surgery*, vol. 11, pp. 260-268, 1990.

[16] H. M. Pleumeekers, A. W. Hoes, and E. van der Does, "Epidemiology of Abdominal Aortic Aneurysms," *Eur J Vasc Surg*, vol. 8, pp. 119-128, 1994.

[17] A. Hallin, D. Bergqvist, and L. Holmberg, "Literature Review of Surgical Management of Abdominal Aortic Aneurysm," *Eur J Vasc Endovasc Surg*, vol. 22, pp. 197-204, 2001.

[18] K. D. Calligaro, M. J. Dougherty, and L. H. Hollier, *Diagnosis and Treatment of Aortic and Peripheral Arterial Aneurysms*. Philadelphia: W.B. Saunders, 1999.

[19] A. V. Sterpetti, R. D. Schultz, R. J. Feldhaus, S. E. Cheung, and D. J. Peetz, "Factors Influencing Enlargment Rate of Small Abdominal Aortic Aneurysms," *J Surg res*, vol. 43, pp. 211-219, 1987.

[20] R. C. Darling, C. R. Messina, D. C. Brewster, and L. W. Ottinger, "Autopsy Study of Unoperated Abdominal Aortic Aneurysms," *Circulation*, vol. 56, pp. 161-164, 1977.

[21] M. Nevitt, J. Ballard, M. Meissner, and K. Johansen, "Prognosis of Abdominal Aortic Aneurysm," *The New England Journal of Medicine*, vol. 321, pp. 1009-14, 1989.

[22] J. C. Parodi, J. C. Palmaz, and H. D. Barone, "Transfemoral Intraluminal Graft Implantation for Abdominal Aortic Aneurysms," *Ann Vasc Surg*, vol. 5, pp. 491-9, 1991.

[23] F. J. Criado, *Endovascular Intervention : Basic Concepts and Techniques*. NY: Armonk, 1999.

[24] C. P. Cruz, J. C. Drouilhet, F. N. Southern, J. F. Eidt, R. W. Barnes, and M. M. Moursi, "Abdominal Aortic Aneurysm Repair," *Vascular Surgery*, vol. 34, pp. 600-5, 2001.

[25] W. D. Turnipseed, S. C. Carr, G. Tefera, C. W. Acher, and J. R. Hoch, "Minimal Incision Aortic Surgery," *Journal of Vascular Surgery*, vol. 34, pp. 47-53, 2001.

[26] D. C. Brewster, "Presidential Address: What Would You Do if It Were Your Father? Reflections on Endovascular Abdominal Aortic Aneurysm Repair," *Journal of Varcualr surgery*, vol. 33, pp. 1139-47, 2001.

[27] G. A. Sicard, B. G. Rubin, L. A. Sanchez, C. A. Keller, M. W. Flye, D. Picus, D. Hovsepian, E. T. Choi, P. J. Geraghty, and R. W. Thompson, "Endoluminal Graft Repair for Abdominal Aortic Aneurysms in High-Risk Patients and Octogenarians: Is it Better Than Open Repair?," *Annals of Surgery*, vol. 234, pp. 427-437, 2001.

[28] U. Blum, G. Voshage, J. Lammer, F. Beyerdorf, D. Tollner, and G. Kretschmer, "Endoluminal Stent Grafts for Infrarenal Abdominal Aneurysms," *N Engl J Med*, vol. 336, pp. 13-20, 1997.

[29] P. Cuypers, J. Buth, P. Harris, E. Gevers, and R. Lahey, "Realistic Expectations for Patients with Stent-graft Treatment of Abdominal Aortic Aneurysms: Results of a European Multicentre Registry," *Eur J Vasc Endovasc Surg*, vol. 17, pp. 507-16, 1999.

[30] W. S. Moore and R. B. Rutherford, "Transfemoral Endovascular Repair of Abdominal Aortic Aneurysm: Results of the North American EVT Phase I Trial," *J Vasc Surg*, vol. 23, pp. 543-53, 1996.

[31] R. A. Wain, M. L. Marin, T. Ohki, L. A. Sanchez, R. T. Lyon, and A. Rozenblit, "Endoleaks After Endovascular Graft Treatment of Aortic Aneurysms: Classification, Risk Factors, and Outcome," *J Vasc Surg*, vol. 27, pp. 69-80, 1998.

[32] C. K. Zarins, R. A. White, K. J. Hodgson, D. Schwarten, and T. J. Fogarty, "Endoleak As a Predictor of Outcome Following Endovascular Aneurysm Repair: AneuRx Multicenter Clinical Trial.," *J Vasc Surg*, vol. 32, pp. 90-107, 2000.

[33] M. Dryjski, R. C. Driscoll, M. A. Blair, M. A. McGurrin, F. J. Dagher, M. Ceraolo, O'Donnell, and W. Blackshear, "The Small Abdominal Aortic Aneurysm: the Eternal Dilemma," *Journal of cardiovascular Surgery*, vol. 35, pp. 95-100, 1994.

[34] G. Gerouolakos and A. Nicolaides, "Infrarenal Abdominal Aortic Aneurysms Less Than Five Centimeters in Diameter: The Surgon's Dilemma," *Eur J Vasc Surg*, vol. 6, pp. 616-622, 1992.

[35] S. A. Choksy, C. R. Quick, and A. B. M. Wilmink, "Ruptured Abdominal Aortic Aneurysm in the Huntingdon District: a 10 Year Experience," *Ann of the royal collage of surgeons of England*, vol. 81, pp. 27-31, 1999.

[36] A. J. Hall, E. F. G. Busse, D. J. McCarville, and J. J. Burgess, "Aortic Wall Tension as a Predictive Factor for Abdominal Aortic Aneurysm Rupture: Improving the Selection of Patients for Abdominal Aortic Aneurysm Repair," *Ann Vasc Surg*, vol. 14, pp. 152-157, 2000.

[37] K. W. Johnston, R. B. Rutherford, and M. D. Tilson, "Suggested Standard for Reporting on Arterial Aneurysms," *Journal of vascular surgaery*, vol. 21, pp. 945-952, 1995.

[38] D. J. Katz, J. C. Stanley, and G. B. Zelenock, "Operative Mortality Rates for Intact and Ruptured Abdominal Aortic Aneurysm in Michigan: An Eleven Year Statewide Experience," *J. Vasc Surg*, vol. 19, pp. 804-817, 1994.

[39] K. Ouriel, R. M. Green, C. Donayree, C. K. Shortell, J. Elliot, and J. A. DeWeese, "An Evaluation of New Methods of Expressing Aortic Aneurysm Size: Relationship to Rupture," *J Vasc Surg*, vol. 15, pp. 12-20, 1992.

[40] Y. G. Wolf, W. S. Thomas, F. J. Brennan, W. G. Goff, and E. F. Bernstein, "Computer Topography Scanning Findings Associated with Rapid Expansion of Abdominal Aortic Aneurysms," *J Vasc Surg*, vol. 20, pp. 529-35, 1994.

[41] J. L. Cronenwett, T. F. Murphy, and G. B. Zelenock, "Actuarial Analysis of Variables Associated with Rupture of Small Abdominal Aortic Aneurysm," *Surgery*, vol. 98, pp. 472-483, 1985.

[42] L. C. Borwn and J. T. Powell, "Risk Factors for Aneurysm Rupture in Patients Kept Under Ultrosound Surveillance.," *Annals of surgery*, pp. 230-233, 1999.

[43] H. Bengtsson and D. Bergqvist, "Ruptured Abdominal Aortic Aneurysm: A Population-based Study," *J Vasc Surg*, vol. 18, pp. 74-80, 1993.

[44] E. M. Guirguis and G. G. Barber, "The Natural History of Abdominal Aortic Aneurysms," *The American Journal of Surgery*, vol. 162, pp. 481-483, 1991.

[45] T. Hatakeyama, S. Hiroshi, and M. Tetsuichiro, " Risk Factors for Rupture of Abdominal Aortic Aneurysm Based on Three-dimensional Study," *Journal of Vascular Surgery*, vol. 33, pp. 453-461, 2001.

[46] J. Stebaek, B. Kalin, and J. Swedenborg, "Growth of Thrombus May Be a Better Predictor of Rupture Than Diameter in Patients with Abdominal Aortic Aneurysm," *Eur J Vasc Endovasc Surg*, vol. 20, pp. 466-469, 2000.

[47] J. Hua and W. R. Mower, "Simple Geometry Characteristics Fail to Reliably Predict Abdominal Aortic Aneurysm Wall Stress," *Journal of Vascular Surgery*, vol. 34, pp. 308-15, 2001.

[48] P. B. Dobrin, "Pathophysiology and Pathogenesis of Aortic Aneurysms: Current Concepts," *Surgical Clinics of North Americ*, vol. 69, pp. 687-703, 1989.

[49] M. M. Stringfellow, P. F. Lawrence, and R. G. Stringfellow, "The Influence of Aorta-aneurysm Geometry Upon Stress in the Aneurysm Wall," *J Surg Res*, vol. 42, pp. 425-33, 1987.

[50] W. R. Mower, L. J. Baraff, and J. Sneyd, "Stress Distributions in Vascular Aneurysms: Factors Affecting Risk of Aneurysm Rupture," *J Surg Res*, vol. 55, pp. 155-161, 1993.

[51] D. F. Elger, D. M. Blackketter, R. S. Budwig, and K. H. Johansen, "The Influence of Shape on the Stresses in Model Abdominal Aortic Aneurysms," *Neurourol Urodyn*, vol. 118, pp. 326-332, 1996.

[52] D. A. Vorp, M. L. Raghavan, and M. W. Webster, "Mechanical Wall Stress in Abdominal Aortic Aneurysm:Influence of Diameter and Asymmetry," *Journal of Vascular Surgery*, vol. 27, pp. 27, 1998.

[53] M. L. Raghavan, "Mechanical Wall Stress in Abdominal Aortic Aneurysm: Towards the Development of a Clinical Tool to Predict Rupture," in *Bioengineering Dept.* Pittsburgh: University ogf Pittsburgh, 1998.

[54] L. P. Harter, "Ultrasonic Evaluation of Abdominal Aortic Thrombus," *J. Ultra. Med*, vol. 1, pp. 315-318, 1982.

[55] F. Inzoli, F. Boschetti, M. Zappa, T. Longo, and R. Fumero, "Biomechanical Factors in Abdominal Aortic Aneurysm Rupture," *Eur J Vasc Surg*, vol. 7, pp. 667-74, 1993.

[56] E. Di Martino, S. Mantero, F. Inzoli, G. Melissano, D. Astore, R. Chiesa, and R. Fumero, "Biomechanics of Abdominal Aortic Aneurysm in the Presence of Endoluminal Thrombus: Experimental Characterization and Structural Static Computational Analysis," *Eur J. Vasc. Endovasc. Surg*, vol. 15, pp. 290-299, 1998.

[57] W. R. Mower, W. J. Quinones, and S. S. Gambhir, "Effect of Intraluminal Thrombus on Abdominal Aortic Aneurysm Wall Stress," *J Vas Surg*, vol. 26, pp. 602-608, 1997.

[58] D. H. J. Wang, M. S. Makaroun, M. W. Webster, and D. A. Vorp, "Mechnaical Properties and Microstructure of Inraluminal Thrombus From Abdominal Aortic Aneurysm," *J. Biomechanical Engineering*, vol. 123, pp. 536-539, 2001.

[59] D. A. Vorp, J. Gorcsan, W. A. Mandarino, and M. W. Webster, "The Potential Influence of Intraluminal Thrombus on Abdominal Aortic Aneurysm as Assessed by a New Noninvasive Method," *Cardiovasc Surg*, vol. 4, pp. 732-739, 1996.

[60] M. L. Raghavan, M. W. Webster, and D. A. Vorp, "Ex-vivo Biomechanical Behavior of Abdominal Aortic Aneurysm: Assessment Using a New Mathematical Model," *Ann Biomed Eng*, vol. 24, pp. 573-582, 1996.

[61] A. Higdon, E. H. Olsen, W. B. Stiles, J. A. Weese, and W. F. Riley, *Mechanics of Materials*. New York: John Wiley and Sons, 1985.

[62] D. A. Vorp, M. L. Raghavan, S. C. Muluk, M. S. Makaroun, D. L. Steed, and M. W. Webster, "Wall Strength and Stiffness of Aneurysmal and Nonaneurysmal Abdominal Aorta," *Ann. NY Acad. Sci*, pp. 274-277, 1996.

[63] M. L. Raghavan and D. A. Vorp, "Toward a Biomechanical Tool to Evaluate Rupture Potential of Abdominal Aortic Aneurysm: Identification of a Finite Strain Constitutive Model and Evaluation of Its Applicability," *Journal of Biomechanics*, vol. 33, pp. 475-482, 2000.

[64] R. Adolph, D. A. Vorp, D. L. Steed, M. W. Webster, K. MV., and W. SC., "Cellular Content and Permeability of Intraluminal Thrombus in Abdominal Aortic Aneurysm," *J. Vasc. Surg.*, vol. 25, pp. 916-926, 1997.

[65] J. D. Humphrey, "Mechanics of the Arterial Wall: Review and Directions," *Critical Review in Biomedical Engineering*, vol. 23, 1995.

[66] H. J. C. de Vries, D. N. H. Enomoto, J. van Marle, P. P. M. van Zuijlen, J. R. Mekkes, and J. D. Bos, "Dermal Organization in Scleroderma: The
Fast Fourier Transform and the Laser Scatter Method Objectify Fibrosis in Nonlesional as well as Lesional Skin," *Laboratory Investigation*, vol. 80, pp. 1281-1289, 2000.

[67] S. J. Jones, A. Boyde, and J. B. Pawley, "Osteoblasts and Collagen Orientation," *Cell Tissue Research*, vol. 159, pp. 73-80, 1975.

[68] J. Millard, P. Augat, M. Kothari, D. C. Newitt, H. K. Genant, and S. Majumdar, "Power Spectral Analysis of Vertebral Trabecular Bone Structure from Radiographs: Orientation and Correlation with Bone Mineral Density and Mechanical Properties," *Calcified Tissue International*, vol. 63, pp. 482-489, 1998.

[69] L. Pannarale, P. Braidotti, and G. E. d'AlbaL, "Sacnning Eletron Microscopy of Collagen Fiber Orientation in the Bone Lamellar in Non-decalcified Humna Samples," *acta Anat*, vol. 151, pp. 36-42, 1994.

[70] A. M. Higgins and R. A. L. Jones, "Anisotropic spinodal dewetting as a route to self-assembly of patterned surfaces," *Nature*, vol. 404, pp. 1281-1289, 2000.

[71] M. S. Sacks and C. J. Choung, "Biaxail Mechanical Properties of Passive Right Ventricular Free Wall Myocardium," *J. Biomech. Eng.*, vol. 115, pp. 202-205, 1993.

[72] Y. C. Fung, *Biomechanics --Mechanical Properties of Living Tissue*, 2 ed: Springer, 1993.

[73] J. K. Suh and R. Spilker, "Indentation Analysis of Biphasic Articular Cartilage: Nonlinear Phnomena Under Finite Deformation," *Jounal of Biomechanical Engineering*, vol. 116, pp. 1-9, 1994.

[74] J. B. Duguid, "Abdominal Aortic Aneurysm Pathology," *Journal of Pathology and Bacteriology*, vol. 58, pp. 207-212, 1946.

[75] R. Rodney and R. Pflanzer, *Human Physiology*, 3rd ed. Fort Worth, TX: Saunders College Pub.,, 1996.

[76] G. M. Fischer and J. G. Llaurando, "Collagen and Elastin Content in Canie Arteries Selected from Functionally Different Vascular Beds," *Circ Res.*, vol. 19, pp. 394-9, 1966.

[77] S. Y. Woo and j. Buckwater, *Injury and Repair of the Musculoskeletal Soft Tissue*. New York: Americam Academy of Orthopedic Surgeons, 1988.

[78] J. Humphrey, *Cardiovascular Solid Mechanics*. New York: Springer-Verlag, 2001.

[79] Y. C. Fung, "Elasticity of Soft Tissue in Simple Elongation," *Am. J. Physiol.*, vol. 213, pp. 1532-1544, 1967.

[80] E. S. da Silva, A. J. Rodrigues, E. M. C. de Tolosa, C. J. Rodrigus, G. Villas Boas do Prado, and J. C. Nakamoto, "Morphology and Diameter of Infrarenal Aortic Aneurysms: A Prospective Autopsy Study," *Cardiovascular Surgery*, vol. 8, pp. 526-532, 2000.

[81] M. L. Raghavan, D. A. Vorp, M. P. Federle, M. S. Makaroun, and M. W. Webster, "Wall Stress Distribution on Three-dimensionally Reconstructed Models of Human Abdominal Aortic Aneurysm," *Journal of Vascular Surgery*, vol. 31, pp. 760-769, 2000.

[82] R. S. Rivlin and D. W. Saunders, "Large elastic deformation of isotropic material, VII. Experiments on the deformation of rubber," *Phil. Trans. Roy. Soc.*, vol. A243, 1951.

[83] A. J. M. Spencer, *Continuum Mechanics*, 1980.

[84] J. D. Humphrey, R. K. Strumpf, and F. C. Yin, "Determinaation of a Constitutive Relation for Passive Myocardium: II. A New Functional Form," *j. Biomech. Eng.*, vol. 112, pp. 340-346, 1993.

[85] M. S. Sacks, D. A. Vorp, M. L. Raghavan, M. P. Federle, and M. W. Webster, "In-vivo 3D Surface Geometry of Abdominal Aortic Aneurysm," *Ann. Biomed. Eng.*, vol. 27, pp. 469-479, 1999.

[86] D. L. Serna, A. Y. Lee, H. Pham, D. Chang, J. Boos, and S. E. Wilson, "Helical CT Angiography Replaces Conventional Aortography in the Preoperative Evaluation of Abdominal Aortic Aneurysm. Vascular & Endovascular Surgery|Vascular Surgery," *Vascular & Endovascular Surgery and Vascular Surgery*, vol. 33, pp. 351-355, 1999.

[87] B. D. Toombs and J. Jing, "Current Concepts in the Evaluation of Vascular Disease: Magnetic Resonance and Computed Tomographic Angiography," *Texas Heart Institute Journal*, vol. 27, pp. 170-192, 2000.

[88] B. Schouchoff, "Endovascular Aortic Aneurysm Repair: An Alternative Approach," *Critical Care Nursing Quarterly*, vol. 23, pp. 35-41, 2000.

[89] O. C. Velazquez, R. A. Larson, R. A. Baum, J. P. Carpenter, M. A. Golden, M. E. Mitchell, A. Pyeron, C. F. Barker, and R. M. Fairman, "Gender-related Differences in Infrarenal Aortic Aneurysm Morphologic Features: Issues Relevant to Ancure and Talent endografts.," *Journal of Vascular Surgery*, vol. 33, pp. S77-84, 2001.

[90] M. Prinssen, J. J. Wever, W. P. Mali, B. C. Eikelboom, and J. D. Blankensteijn, "Concerns for the Durability of the Proximal Abdominal Aortic Aneurysm Endograft Fixation from a 2-year and 3-year Longitudinal Computed Tomography Angiography Study," *Journal of Vascular Surgery*, vol. 33, pp. S64-9, 2001.

[91] J. P. Henretta, L. A. Karch, K. J. Hodgson, M. A. Mattos, D. E. Ramsey, R. McLafferty, and D. S. Sumner, "Special Lliac Artery Considerations During Aneurysm Endografting," *American Journal of Surgery*, vol. 178, pp. 212-8, 1999.

[92] S. E. Birch, D. R. Stary, and A. R. Scott, "Endovascular Stent-Grafts," *Journal of Vascular & Interventional Radiology*, vol. 12, pp. 270-2, 2001.

[93] M. F. Fillinger, "New Imaging Techniques in Endovascular Surgery," *Surg Clin North Am*, vol. 79, pp. 451-75, 1999.

[94] R. A. Peattie, C. L. Asbury, E. I. Bluth, and T. J. Riehle, "Steady Flow in Models of Abdominal Aortic Aneurysm: Part II: Wall Stresses and Their Implication for in Vivo Thrombosis and Rupture," *J. Ultrasound Med.*, vol. 15, pp. 689-696, 1996.

[95] M. L. Raghavan, M. F. Fillinger, S. P. Marra, and F. E. Kennedy, "An Automated Methodology for Investigating the Correlation between Abdominal Aortic Aneurysm Wall Stress and Risk of Rupture," presented at 2001 ASME Internatinal Mechanical Engineering Congress and Exposistion, New York, New York, 2001.

[96] B. I. Tropea, S. P. C. Schwarzacher, A., C. Asvar, P. Huie, and R. K. Sibley, "Reduction of Aortic Wall Motion Inhibits Hypertension-mediated Experimental Atherosclerosis," *Arterioscler Thromb Vasc Biol*, vol. 20, 2000.

[97] H. Masuda, Y. J. Zhuang, T. M. Singh, K. Kawamura, M. Murakami, and C. K. Zarins, "Adaptive Remodeling of Internal Elastic lamina and Endothelial Lining During Flow-induced Arterial Enlargement," *Arterioscler Thromb Vasc Biol*, vol. 19, pp. 2298-307, 1999.

[98] C. Taylor, T. Hughes, and C. K. Zarins, "Finite Element Modeling of 3-dimensional Pulsatile Flow in the Abdominal Aorta: Relevance to Atherosclerosis. Annals of Biomedical Engineering," *Annals of Biomedical Engineering*, vol. 26, pp. 1-13, 1998.

[99] G. B. Torsello, E. Klenk, B. Kasprzak, and T. Umscheid, "Rupture of Abdominal Aortic Aneurysm Previously Treated by Endovascular Stent Graft," *J Vasc Surg*, vol. 28, pp. 184-7, 1998.

[100] D. F. Leotta, M. Paun, K. Beach, T. R. Kohler, R. E. Zierler, and Strandness D. E., "Measurement of Abdominal Aortic Aneurysms with Three-dimensional Ultrasound Imaging: Preliminary Report," *Journal of Vascular Surgery*, vol. 33, pp. 700-707, 2001.

[101] A. N. Shetty, A. Shirkhoda, K. G. Bis, and A. Alcantara, "Contrast-enhanced Three-dimensional MR Angiography in a Single Breath-hold: A Novel Technique," *AJR Am J Roentgenol.*, vol. 165, pp. 1290-1292, 1995.

[102] J. A. Kaufman, S. C. Geller, M. J. Petersen, R. P. Cambria, M. R. Prince, and A. Waltman, "MR Imaging (including MR angiography) of Abdominal Aortic Aneurysms: Comparison with Conventional Angiography," *AJR Am J Roentgenol*, vol. 163, pp. 203-210, 1994.

[103] D. Smith, M. Sacks, D. Vorp, and M. Thornton, "Surface Geometric Analysis of Anatomic Structures Using Biquintic Finite Element Interpolation.," *Ann Biomed Eng*, vol. 28, pp. 598-611, 2000.

[104] B. Tsagaan, A. Shimizu, H. Kobatake, K. Miyakawa, and Y. Hanzawa, "Segmentation of Kidney Using a Deformable Model," presented at Proceedings of the IEEE, 2001.

[105] H. Rifa, I. Bloch, S. Hutchinson, J. Wiart, and L. Garnero, " Segmentation of the Skull in MRI Volumes Using Deformable Model and Taking the Partial Volume Effect into Account," Medical Image Anal. vol. 4 pp. 219-33, 2000.

[106] P. J. Yim, J. J. Cebral, R. Mullick, M. Skopec, and P. L. Choyke, " Vessel Surface Reconstruction With A Tubular Deformable Model," *IEEE Trans Med Imaging*, vol 109, pp. 472-81, 2002.

[107] G. Pillari, J. B. Chang, J. Zito, J. R. Cohen, K. Gersten, A. Rizzo, and A. M. Bach, "Computed Tomography of Abdominal Aortic Aneurysm," *Arch. Surg.*, vol. 123, pp. 727-32, 1988.

[108] C. L. Siegel, R. H. Cohan, M. Korobkin, M. B. Alpern, D. L. Courneya, and R. A. Leder, "Abdominal Aortic Aneurysm Morphology: CT feature in Patients with ruptured and nonruptured aneurysms," *Am J Roentgenol*, vol. 163, pp. 1123-9, 1994.

[109] A. Senapati, P. Hurst, M. L. Thomas, N. L. Browse, and K. G. Burnard, "Diferrentiation of Ruptured Aortic Aneurysm from Acute Expansion by CT," *J. Cardiovasc Surg*, vol. 27, pp. 719-722, 1986.

[110] C. L. Asbury, J. W. Ruberti, E. I. Bluth, and R. A. Peattie, "Experimental Investigation of Steady Flow in Rigid Models of Abdominal Aortic Aneurysms," *Annals of Biomedical Engineering*, vol. 23, pp. 29-39, 1995.

[111] D. H. Bergel, "The Visco-elastic Properties of the Arterial Wall," University of London, 1960.

[112] J. Vossoughi, Z. Hedjazi, and F. S. Borris, "intimal residual stress and strain in large arteries," presented at 1993 ASME Advances in bioengineering, 1993.

[113] R. N. Vaishnav and J. Vossoughi, "Residual Stress and Strain in Aortic Segments," *J. Biomech.*, vol. 20, 1987.

[114] T. Kang and J. D. Humphrey, "Finite deformation of an Inverted Artery," presented at 1991 ASME advances in Bioengineering, new York, 1991.

[115] C. J. Chuong and Y. C. Fung, "Compressibility and Constitutive Equation of Arterial Wall in Radial Compression Experments," *J. of Biomech.*, vol. 17, pp. 35-40, 1984.

[116] Y. C. Pao, E. L. Ritman, and E. H. Wood, "Finite Elent Analysis of Left Ventricular Myocardial Stresses," *Journal of Biomechanics*, vol. 7, pp. 469-77, 1974.

[117] T. W. Taylor and T. Yamaguchi, "Three-dimensional simulation of blood flow in an abdominal aortic aneurysm--steady and unsteady flow cases," *J Biomech Eng*, vol. 116, pp. 89-97, 1994.

[118] R. Budwig, D. Elger, H. Hooper, and J. Slippy, "Steady Flow in Abdominal Aortic Aneurysm Models," *J Biomech Eng*, vol. 115, pp. 418-423, 1993.

[119] E. Hinton and D. R. J. Owen, *An Introduction to Finite Element Computations*, 1st ed. Swansea, U.K: Pineridge Press Ltd, 1979.

[120] R. D. Cook, D. S. Malkus, and M. E. Plesha, *Concepts and Applications of Finite Element Analysis*, 3rd ed. New York: Wiley, 1989.

[121] V. Adams and A. Askenazi, *Building Better Products WIth Finite Element Analysis*. Santa Fe, NM: Onward Press, 1999.

[122] J. P. Fielding, *Introduction to Aircraft Design*. London, UK: Cambridge University Press, 1998.

[123] X. Gong and A. R. Pelton, "ABAQUS Analysis on Nitinol Medical Applications," presented at 2002 ABAQUS Users' Conference, Newport, RI, 2002.

[124] W. Z. Kong, V. K. Goel, and L. G. Gilbertson, "Prediction of Biomechanical Parameters in the Lumbar Spine During Static Sagittal Plane Lifting," *J. Biomechanical Engineering*, vol. 120, pp. 273-280, 1998.

[125] J. D. Humphery and F. C. Yin, "On Constitutive Relations and Finite Deformation of Passive Cardiac Tissue I: A Pseudostrain-energy Function," *J. Biomech. Eng.*, vol. 109, pp. 298-304, 1987.

[126] M. J. Thubrikar, J. J Al-Soudi, and F. Robicsek, "Wall Stress Studies of Abdominal Aortic Aneurysm in a Clinical
Model," *Annals of Vascular Surgery*, vol. 15, pp. 355-366, 2001.

[127] D. A. Vorp, D. H. J. Wang, M. W. Webster, and W. J. Federspiel, "Effect of Intraluminal Thrombus Thickness and Bulge Diameter on the Oxygen Flow in Abdominal Aortic Aneurysm," *J. Biomech. Eng.*, vol. 120, pp. 579-583, 1998.

[128] G. W. H. Schurink, N. J. M. Aarts, and J. H. van Bockel, "Endoleak after stent graft treatment of abdominal aortic aneurysm: a meta-analysis of clinical studies," *Br J Surg*, vol. 86, pp. 581-7, 1999.

[129] G. W. H. Schurink, J. H. van Bockel, M. J. T. Visser, and J. H. Van Bockel, "Thrombus within an Aortic Aneurysm Does Not Reduce Pressure on the Aneurysmal Wall," *J. Vasc Surg*, vol. 31, pp. 501-6, 2001.

[130] M. J. Thubrikar, F. Robicsek, M. Labrosse, V. Chervenkoff, and B. L. Fowler, "Effect of Thrombus in AAA on Pressure and Dilation Experienced by the Aneurysm Wall," presented at 2001 ASME Internatinal Mechanical Engineering Congress and Exposistion, New York, New York, 2001.

[131] D. H. J. Wang, M. S. Makaroun, M. W. Webster, and D. A. Vorp, "Effect of Intraluminal Thrombus on Wall Stress in Patient Specific Models of Abdominal Aortic Aneurysm," *Journal of Vascular surgery*, vol. In press, 2002.

[132] A. Manual, "ABAQUS Manual, V. 6.2."

[133] O. C. Zienkiewicz, *The Finite Element Method in Engineering Science*: McGraw-Hill, 1971.

[134] M. L. Raghavan and D. A. Vorp, "Indentification and Evaluation of a Finite Strain Constitutive Law for AAA," *J. Biomech.*, 1999.

[135] E. S. Di Martino, D. H. J. Wang, A. Redaelli, M. S. Makaroun, and D. A. Vorp, "Effect Variations in Intraluminal Thrombus Constitutive Properties on Abdominal Aortic Aneurysm Wall Stress: A Parameter Study," Advances in Bioengineering, BED-Vol. 51, pp. 250-252, ASME winter Conference, New York, New York, 2001.

[136] A. P. Boresi, R. J. Schmidt, and O. M. Sidebottom, *Advanced Mechanics of Materials*. New York: John Wiley & Sons, Inc., 1993.

[137] S. P. Timoshenko and J. N. Goodier, *Theory of Elasticity*. New York: McGraw-Hill, 1970.

[138] G. C. Cheng, H. M. Loree, R. D. Kamm, F. M.C., and R. T. Lee, "Distribution of Circumferential Stress in Ruptured and Stable Atherolerotic Lesions," *Circulation*, vol. 87, pp. 1179-87, 1992.

[139] H. C. Han and Y. C. Fung, "Longitudinal Strain of Canine and Porcine aortas.," *J Biomech*, vol. 28, pp. 637-41, 1995.

[140] A. Delfino, N. Stergiopulos, J. E. Moore, and J.-J. Meister, "Residual Strain Effects on the Stress Field in a Thick Wall Finite Element Model of the Human Carotid Bifurcation," *Journal of Biomechanics*, vol. 30, pp. 777-786, 1997.

[141] A. C. Burton, "Relation of Stuctural to Function of the Tissues of the Wall of Blood Vessels," *Physiol. Rev.*, vol. 34, pp. 619-42, 1954.

[142] P. Dobrin, "Mechanics of Normal and Diseased Blood Vessels," *Ann. Vasc. Surg.*, vol. 2, pp. 283-294, 1988.

[143] A. Ghorpade and T. B. Baxter, "Biochemistry and Molecular Regulation of Matrix Macromolecules in Abdominal Aortic Aneurysms," *Ann. N.Y. Acad. Sci.*, vol. 800, pp. 138-150, 1996.

[144] M. P. Jacob, B.-C. C, V. Fontaine, Y. Benazzoug, L. Feldman, and J. B. Michel, "Extracellular Matrix Remodeling in the Vascular Wall," *Pathol Biol*, vol. 49, pp. 326-32, 2001.

[145] S. Menashi, J. S. Campa, and R. M. Geenhalgh, "Collegan in Abdominal Aortic Aneurysm: Typing, Content, and Degradation," *J. Vas. Surg.*, vol. 6, pp. 578-82, 1987.

[146] N. Sasaki and A. Enyo, "Viscoelastic Properties of Bone as a Function of Water Content," *Journal of Biomechanics*, vol. 28, pp. 809-815, 1995.

[147] N. Sakalihasan, A. Heyeres, B. V. Nusgens, R. Limet, and C. M. Lapiere, "Modifications of the Extracellular Matrix of Aneurysmal Abdominal Aorta as a Function of Their Size," *Eur J Vasc Surg*, vol. 7, pp. 633-37, 1993.

[148] K. A. Vardulaki, T. C. Prevost, N. M. Walker, N. E. Day, A. B. M. Wilmink, C. R. G. Quick, H. A. Ashton, and R. A. P. Scott, "Growth Rates and Risk of Rupture of Abdominal Aortic Aneurysms," *British Journal of Surgery*, vol. 85, pp. 1674-1680, 1998.

[149] A. Kazmiers, L. Jacobs, A. Perkins, S. M. Lindenauer, and E. Bates, "Abdominal Aortic Aneurysm Repair in Veterans Affairs Medical Centers," *J Vasc Surg*, vol. 23, pp. 191-200, 1996.

[150] C. K. Schewe, H. P. Schweikart, and G. Hammel, "Influence of Selective Management of the Prognosis and the Risk of Rupture of Abdominal Aortic Aneurysm," *Clin Invest*, vol. 72, 1994.

[151] L. N. Sampson and J. L. Cronenwett, "Abdominal Aortic Aneurysms," *Probl Gen Surg*, vol. 11, pp. 385-417, 1994.

[152] H. G. Alcorn, S. K. Wolfson, and K. Sutton-Tyrrell, "Risk Factors for Abdominal Aortic Aneurysms in Older Adults Enrolled in the Cardiovascular Health Study," *Arterioscler Thromb Vasc Biol*, vol. 16, pp. 963-70, 1996.

[153] R. F. Gillum, "Epidemiology of aortic aneurysm in the United States," *J Clin Epidemiol*, vol. 48, pp. 1289-1298, 1995.

[154] D. E. Lillienfeld, P. D. Gunderson, J. M. Sprafka, and C. Vargas, "Epidemiology of aortic aneurysms. I. Mortality trends in the United State, 1951 to 1981," *Aterioscleros*is, vol. 7, pp. 637-643, 1987.

[155] M. McFarlane, "The epidemiologic necropsy for abdominal aortic aneurysm," *JAMA*, vol. 265, pp. 2085-8, 1991.

[156] T. B. Baxter and B. G. Halloran, "Matrix Metabolism in Abdominal Aortic Aneurysms," in *Aneurysms: new findings and treatments*, P. W. Yao JST, Ed. East Norwalk, Conn: Appleton and Lange, 1994, pp. 25-34.

[157] C. M. He and M. R. Roach, "The Composition and Mechanical Properties of Abdominal Aortic Aneurysms," *J Vasc Surg*, vol. 21, pp. 6-13, 1994.

[158] S. T. MacSweeney, G. Young, R. M. Greenhalgh, and J. T. Powell, "Mechanical Properties of the Aneurysmal Aorta," *British Journal of Surgery*, vol. 79, pp. 1281-1284, 1992.

[159] R. J. Rizzo, W. J. McCarthy, S. N. Dixit, M. P. Lilly, V. P. Shively, W. R. Flinn, and J. S. T. Yao, "Collagen Types and Matrix Protein Content in Human Abdominal Aortic Aneurysms," *J Vasc Surg*, vol. 10, pp. 365-73, 1989.

[160] D. S. Summer, D. E. Hokanson, and D. E. Strandness, "Stress-strain characteristics and colagen-elastin content of abdominal aortic aneurysms," *Surg Gynecol and Obstet*, 1970.

[161] R. W. Busuttil, H. Rinderbreicht, A. Flesher, and C. Carmack, "Elastase Activity: The Role of Elastase in Aortic Aneurysm Formation," *J Surg Res*, vol. 32, pp. 214-7, 1982.

[162] D. J. Cannon and R. C. Read, "Blood Elastolytic Activity in Patients with Aortic Aneurysm.," *Ann Thorac Surg*, vol. 35, pp. 10-15, 1982.

[163] J. Cohen, C. Mandell, J. Chang, and L. Wise, "Elastin Metabolism of the Infrarenal Aorta," vol. 7, pp. 210-4, 1988.

[164] A. Rijbroek, Moll FL., von Dijk HA, Meijer R, Jansen JW.,, "Inflammation of the Abdominal Aortic Aneurysm Wall," *Eur. J. Vasc. Surg.*, vol. 8, pp. 41-46, 1994.

[165] K. M. Newman, J. Jean-Claude , L. S. Hong, J.V., Y. Ogata, and H. Nagase, "Cellular Localization of Matrix Metalloproteinases in the Abdominal Aortic Aneurysm Wall.," *Eur J Vasc Endovasc Surg*, vol. 20, pp. 814-820, 1994.

[166] K. Newman, malon AM, Shin RD, Scholes JV, Ramey WG, Tilson MD,, "Matrix metalloproteinases in abdominal aortic aneurysm: characterization, purification, and their possible sources," *Connect. Tissue. Res*, vol. 30, pp. 265-276, 1994.

[167] W. D. McMillan, B. K. Patterson, R. R. Keen, and W. H. Pearch, "In Situ Localization and Quantification of Seventy-Two–kilodalton Type IV Collagenase in Aneurysmal, Occlusive, and Normal Aorta.," *J Vasc Surg*, vol. 22, pp. 295-305, 1995.

[168] P. B. Dobrin, W. H. Baker, and W. C. Gley, "Elastolytic and Collagenolytic Studies of Arteries: Indications for the mechnical Properties of Aneurysms," *Arc surg*, vol. 119, pp. 405-409, 1984.

[169] Z. J. Samila and S. A. Carter, "The Effect of Age on the Unfolding of Elastin Lamellae and Collagen Fibers With Stretch in Human Arteries," *Can J Physiol Pharamacol*, vol. 59, pp. 1050-1057, 1981.

[170] E. G. Lakatta, J. H. Mitchell, A. Pomerance, and G. Rowe, "Human Aging: Changes in Structure and Function," *J Am Coll Cardiol*, vol. 10, pp. 42A-47A, 1987.

[171] E. G. M. Lakatta, "Cardiovascular Aging Research: The Next Horizons," *Journal of the American Geriatrics Society*, vol. 47, pp. 613-625, 1999.

[172] R. S. Reneman, T. van Merode, P. Hick, A. M. Muytjens, and A. P. Hocks, "Age-related Changes in Carotid Artery Wall Properties in Men," *Ultrasound Med Biol.*, vol. 12, pp. 465-471, 1986.

[173] T. Kawasaki, S. Sasayama, S. Yagi, T. Asakawa, and T. Hirai, "Non-invasive Assessment of the Age Related Changes in Stiffness of Major Branches of the Human Arteries.," *Cardiovasc Res.*, vol. 2, pp. 678-687, 1987.

[174] A. Benetos, S. Laurent, A. P. Hoeks, P. H. Boutouyrie, and M. E. Safar, "Arterial Alterations with Aging and High Blood Pressure: A Noninvasive Study of Carotid and Femoral Arteries," *Arterioscler Thromb*, vol. 13, pp. 90-97, 1993.

[175] M. F. O'Rourke and G. Mancia, "Arterial Stiffness," *J Hypertens*, vol. 17, 1999.

[176] M. Groenink, S. E. Langerak, E. Vanbavel, E. van der Wall, B. J. Mulder, A. C. van der Wal, and J. A. Spaan, "The Influence of Aging and Aortic Stiffness on Permanent Dilation and Breaking Stress of the Thoracic Descending Aorta," *Cardiovascular Research*, vol. 43(2), pp. 471-80, 1999.

[177] J. F. Blanchard, "Epidemiology of Abdominal Aortic Aneurysms," *Epidemiologic Reviews*, vol. 21, pp. 207-221, 1999.

[178] B. Sonesson, F. Hansen, H. Stale, and T. Lanne, "Compliance and Diameter in the Human Abdominal Aorta-the Influence of Age and Sex," *Eur J Vasc Surg*, vol. 7, pp. 690-7, 1993.

[179] B. Sonesson, F. Hansen, H. Stale, and T. Länne, "Sex Difference in the Mechanical Properties of the Abdominal Aorta in Human Beings," *J Vasc Surg*, vol. 20, pp. 959-69, 1994.

[180] W. Milnor, "Cardiovascular System," in *Medical physiology*, M. VB, Ed. St. Louis: CV Mosby, 1974, pp. 839-48.

[181] H. Wolinsky, "A Proposal Linking Clearance of Circulating Lipoproteins to Tissue Metabolic Activity as a Aasis for Understanding Atherogenesis," *Circ Res*, vol. 1980, pp. 301-11, 1980.

[182] G. Gabbela, "Structural Changes in Smooth Muscle Cells During Isotonic Contraction," *Cell. Tiss. Ers.*, vol. 170, pp. 187-201, 1976.

[183] D. A. Vorp, P. C. Lee, D. H. J. Wang, M. S. Makaroun, E. M. Nemoto, S. Ogawa, and M. W. Webster, "Association Of Intraluminal Thrombus in Abdominal Aortic Aneurysm With Local Hypoxia and Wall Weakening," *J. Vasc. Surg*, vol. in press, 2001.

[184] W. D. McMillan, N. A. Tamarina, M. Cipollone, D. A. Johnson, M. A. Parker, and W. H. Pearce, "Size Matters: The Relationship Between MMP-9 Expression and Aortic Aiameter.," *Circulation*, vol. 96, pp. 2228-32, 1997.

[185] W. C. Cole, G. B. Hill, and A. G. Bouchard, "Are Aortic Aneurysms Caused by Atherosclerosis?," *Atherosclerotic risk factors in abdominal aortic aneurysm and peripheral vascular occlusive disease*, vol. Chronic Dis Can, pp. 120-2, 1994.

[186] W. W. LaMorte, T. E. Scott, and J. O. Menzoian, "Racial Differences in the Incidence of Femoral Bypass and Abdominal Aortic Aneurysmectomy in Massachusetts: Relationship to Cardiovascular Risk Factors.," *J Vasc Surg*, vol. 21, pp. 422-31, 1995.

[187] T. J. O'Kelly and B. P. Heather, "General Practice-based Population Screening For Abdominal Aortic Aneurysms: A Pilot Study," *Br J Surg*, vol. 76, pp. 479-80, 1989.

[188] D. P. Strachan, "Predictors of Death From Aortic Aneurysm Among Middle-aged Men: The Whitehall Study," *Br. J Surg*, vol. 79, pp. 401-404, 1991.

[189] J. T. Powell, P. Worrell, S. T. R. MacSweeney, P. J. Franks, and R. M. Greenhalgh, "Smoking As a Risk Factor for Abdominal Aortic Aneurysm," *Ann. N.Y. ACAD. Sci.*, vol. 800, pp. 246-248, 1996.

[190] M. P. Pellegrini, D. E. Newby, S. Maxwell, and D. J. Webb, "Short-term Effects of Transdermal Nicotine on Acute Tissue Plasminogen Activator Release in vivo in Man.," *Cardiovasc Res.*, vol. 52, pp. 321-7, 2001.

[191] Q. Wang, H. Zhou, M. Sun, and Z. Jia, "Effects of Smoking on Oxygen Free Radicals and Fibrinolytic System," *Hunan Yi Ke Da Xue Xue Bao*, vol. 22, pp. 149-52, 1997.

[192] S. F. Smith, A. Guz, N. T. Cooke, G. H. Burton, and T. D. Tetley, "Extracellular Elastolytic Activity in Human Lung Lavage: A Comparative Study Between Smokers and Non-smokers.," *Clin Sci*, vol. 69, pp. 17-27, 1985.

[193] W. L. Coudon and J. O. Harris, "Human Alveolar Macrophage Proteolytic Enzyme Activities in Chronic Obstructive Pulmonary Disease. Lack of Correlation with Functional Abnormalities," *Chest*, vol. 73, pp. 364-70, 1978.

[194] A. Cucina, P. Sapienza, V. Corvino, V. Borrelli, B. Randone, L. Santoro-D'Angelo, and A. Cavallaro, "Nicotine Induces Platelet-derived Growth Factor Release and Cytoskeletal Alteration in Aortic Smooth Muscle Cells," *Surgery*, vol. 127, pp. 72-8, 2000.

[195] B. Sonesson, A. R. Ahlgren, L. Lazer, and T. Lanne, "Does Long-term Smoking Affect Aortic Stiffness More in Women Than in Men?," *Clin Physiol*, vol. 17, pp. 439-47, 1997.

[196] R. C. Darling, D. C. Brewster, and G. m. LaMuaglia, "Are Familial Abdominal Aortic Aneurysm Different?," *J Vasc Surg*, vol. 10, pp. 39-43, 1989.

[197] C. W. Cole, G. G. Barber, and A. G. Bouchard, "Abdominal Aortic Aneurysm: Consequences of a Positive Family History," *Can J Surg*, vol. 32, pp. 117-20, 1989.

[198] P. Fitzgerald, D. Ramsbottom, and P. Burke, "Abdominal Aortic Aneurysm in the Irish Population: A Familial Screening Study," *Br J Surg*, vol. 32, pp. 117-20, 1989.

[199] K. Johansen and T. Koepsell, "Familial Tendency for Abdominal Aortic Aneurysms," *JAMA*, vol. 256, pp. 1934-6, 1986.

[200] M. W. Webster, R. E. Ferrell, and P. L. St. Jean, "Ultrasound Screening of First-degree Relatives of Patients with An Abdominal Aortic Aneurysm," *J Vasc Surg*, vol. 13, pp. 9-13, 1991.

[201] M. W. Webster, P. L. St. Jean, and D. L. Steed, "Abdominal Aortic Aneurysm: Results of a Family Study," *J Vasc Surg*, pp. 366-72, 1991.

[202] D. A. Axelrod, P. K. Henke, T. W. Wakefield, J. C. Stanley, L. A. Jacobs, L. M. Graham, L. J. Greenfield, and G. R. Upchurch, "Impact of Chronic Obstructive Pulmonary Disease on Elective and Emergency Abdominal Aortic Aneurysm Repair," *Journal of Vascular Surgery*, vol. 33, pp. 72-6, 2001.

[203] L. C. Brown and J. T. Powell, "Risk Factors for Aneurysm Rupture in Patients Kept Under Ultrosound Surveillance.," *Annals of surgery*, vol. 230, pp. 289, 1999.

[204] S. Laurent, P. Lacolley, X. Girerd, P. Boutouyrie, Y. Bezie, and M. Safar, "Arterial Stiffening: Opposing Effects of Age- and Hypertension-associated Structural Changes.," *Can J Physiol Pharamacol*, vol. 76, pp. 842-849, 1996.

[205] N. R. Drapper and H. Smith, *Applied Regression Analysis*, 2nd ed. New York: Wiely, 1981.

[206] S. Chatterjee and B. Price, *Regression Analysis by Example*: John Wiley & Sons, 1977.

[207] D. G. Klienbaum, L. L. Kupper, K. E. Muller, and A. Nizam, *Applied Regression Analysis and Other Multivariable Methods*, 3rd ed: Duxbury Press, 1988.

[208] B. L. Bowerman and R. T. O'connel, *Linear Stastical Models: An Applied Approach*. Boston: Duxbury Press, 1986.

[209] SAS/STAT, "Software: Change and Enhancements, Release 6.07," SAS Institution, Inc. Cary, N.C. 1992.

[210] E. J. Pedhazur, *Multiple Regression in Behavioral Research*. Orlando, FL: Harcourt Brace, 1997.

[211] J. Cohen and P. Cohen, *Applied multiple regression/correlation analysis for the behavioral sciences*. Hillsdale, NJ: Lawrence Erlbaum Associates, Inc, 1992.

[212] T. P. Ryans, *Modern Regression Methods*: John Wiely & Sons, Inc., 1997.

[213] J. Satta, E. Laara, and T. Juvonen, "Intraluminal Thrombus Predicts Rupture of an Abdominal Aortic Aneurysm.," *J Vasc Surg*, vol. 23, pp. 737-9, 1996.

[214] D. H. J. Wang, M. S. Makaroun, M. W. Webster, S. R. Wisniewski, and D. A. Vorp, "Influence of Family History on Abdominal Aortic Aneurysm Wall Strength," presented at EMBS-BMES2002 - Second Joint Meeting of BMES and IEEE-EMBS, Houston, TX, 2002.

[215] D. L. Logan, *A First Course in the Finite Element Method*. Boston: PWS Engineering, 1986.

[216] J. V. White, "Aneurysm Formation in Vivo by the Topical Degradation of Adventitial Elastin," *J. Vasc. Surg.*, vol. 20, 1994.

[217] J. V. White and S. L. Mazzacco, "PAthogenesis of Aortic Aneurysms: Development of a Large Animal Model," in *Current critical problems in vascular surgery*, vol. 7, V. F., Ed. St. Louis, MO: Quality Medical Publishing, 1996.

[218] C. K. Zarins, R. A. White, and T. J. Fogarty, "Aneurysm Rupture After Endovascular Repair Using the AneuRx Stent Graft," *J Vasc Surg*, vol. 31, pp. 960-70, 2000.

[219] E. W. Steyerberg, J. Kievit, J. C. A. de Mol Van Otterloo, J. H. van Bochel, M. J. C. Eijkemans, and J. D. F. Habbema, "Perioperative Mortality of Elective Abdominal

Aortic Aneurysm Aurgery: A Clinical Prediction Rule Based on Literature and Individual Patient Data," *Arch Intern Med*, vol. 155, pp. 1998-2004, 1995.

[220] W. M. Castlden and J. C. Mercer, "Abdominal Aortic Aneurysms in Western Austrilia: Descriptive Epidemiology and Patterns of Rupture," *Br. J Surg*, vol. 72, pp. 109-112, 1985.

[221] M. Wassef, B. T. Baxter, L. Chisholm, R. L. Dalman, and M. F. Fillinger, "Pathogenesis of Abdominal Aortic Aneurysms: A Multidisciplinary Research Program Supported by the National Heart, Lung, and Blood Institute," *Journal of Vascular Surgery*, vol. 34, pp. 730-738, 2001.

[222] D. A. Vorp, M. S. Sacks, and M. S. Makaroun, "Biaxial Mechanical Behavior of Aneurysmal and Nonaneurysmal Human Abdominal Aorta: Preliminary Results," presented at IMECE 2000, Orlando, FL, 2002.

[223] M. J. Moulton, L. L. Creswell, S. W. Downing, R. L. Actis, R. A. Szabo, and M. K. Pasque, "Myocardial Material Property Determination In The In Vivo Heart Using Magnetic Resonance Imaging," *Int J Card Imaging*, vol. 12, pp. 153-67, 1996.